A Thesis

entitled

~~THE~~ DEVELOPMENT OF A LIQUID HYDROGEN BUBBLE CHAMBER, AND ITS USE IN THE STUDY OF LOW ENERGY-NEUTRON PROTON INTERACTIONS

by

Robert Brian Palmer, B.Sc., A.R.C.S.

Submitted for the
Degree of Doctor of Philosophy
of the University of London

Imperial College of Science and Technology
London
1960

ABSTRACT

The first part of this thesis is devoted to a description of the requirements, construction and operation of a $3\frac{1}{2}$-inch diameter liquid hydrogen bubble chamber. In the second part of the thesis the details and results of an experiment performed with this bubble chamber are given.

Part I: The Hydrogen Bubble Chamber

In order that the consumption of liquid hydrogen be small, the heating of the chamber during a cycle of expansion and compression must also be small. It is shown theoretically and experimentally that the above condition requires a cycle of short duration and an initial pressure and temperature somewhat higher (8 atmospheres, 29°K) than has commonly been used.

The chamber, described, employed a piston in a 'reversible flow gas expansion system' capable of performing a cycle of 10 m.sec. duration at a repetition rate of 33 cycles per minute. Tracks produced in the chamber were illuminated by light from a diffuse source focussed by a condenser lens between the lenses of a stereo camera.

Part II. The Study of Neutron-Proton Interactions

The liquid hydrogen bubble chamber was placed in a

beam of neutrons, whose energy spectrum was peaked at 50 MeV, and which was obtained from a lithium deuteride target placed in the Harwell 170 MeV cyclotron. From the photographs obtained of neutron scattered proton tracks the neutron energy spectrum was obtained. The primary object of the experiment was, however, to observe the neutron capture reaction

$$n + p \rightarrow d + \gamma$$

at the medium energy of 50 MeV. This reaction was observed despite its total reaction cross-section being only 1/10,000 of the n-p scattering cross-section. The measured total neutron-capture cross-section was

$$\sigma_T \text{ (50 MeV)} = 66 \pm 46 \ \mu B$$

C O N T E N T S

Part I
THE LIQUID HYDROGEN BUBBLE CHAMBER

Page

Chapter 1: Introduction

1.1 Introduction 8
1.2 Bubble Chambers 10
1.3 Design Considerations 16

Chapter 2: Description of Apparatus

2.1 Introduction 21
2.2 Chamber and Cryostat 25
2.3 Photography 30
2.4 The Expansion System 37
2.5 Timing Circuits 48
2.6 Instrumentation 51
2.7 Safety 59

Chapter 3: Chamber Performance

3.1 Introduction 63
3.2 Choice of Operating Conditions 64
3.3 Chamber Performance 69

Part II
THE STUDY OF NEUTRON PROTON INTERACTIONS

Chapter 1: Introduction and Theory

1.1 Introduction 78
1.2 Two Nucleon Interactions 80
1.3 Detailed Balance 86
1.4 Neutron Capture Theory 94
1.5 Neutron Capture Kinematics 97

	Chapter 2: The Experiment	Page
2.1	The Choice of Experiment	105
2.2	Identification of Events	119
2.3	Neutron Energy Spectrum Requirement	127
2.4	The Production of a Neutron Beam	131
2.5	The Target	136
2.6	Hardening	148
2.7	Collimation	158
2.8	The Experimental Runs	168
	Chapter 3: Measurements on the Film	
3.1	Corresponding and Non-Corresponding Methods of Reconstruction	170
3.2	Measurement and Scanning	178
3.3	Reconstruction Formulae	185
3.4	The Calculation Programme	190
3.5	Derivation of Reconstruction Constants	194
	Chapter 4: Results	
4.1	Measurement Errors	197
4.2	Neutron Energy Spectrum	204
4.3	Ancillary Results	223
4.4	Determination of Neutron-Capture Cross-Section	229
4.5	Conclusion	247
	Appendices	
A	Work Done During Cycle	249
B	Electronic Circuits	252
C	Reconstruction Errors	261
D	The Effect on Reconstruction of Glass Windows and Liquid Hydrogen	267
E	Reconstruction Computor Programme	273

		Page
F	Probability of Selection used in 'Starting and Stopping Tracks Scan'.	288
G	Probability of Selection Computor Programmes	296
H	Probability of Selection of Small Angle Tracks	302
I	Notation Used in Part II, Chapters 3 and 4	312
	Acknowledgements	316

PART I

THE LIQUID HYDROGEN BUBBLE CHAMBER.

CHAPTER 1

INTRODUCTION.

1.1 INTRODUCTION.

The first part of this Thesis will be devoted to a brief description of a small liquid hydrogen bubble chamber. The work was started at Imperial College under the leadership of Mr. Barford in early 1956. The writer joined the group in the Summer of that year and has worked with the bubble chamber throughout its development and operation.

The chamber, which was intended as a phototype, was first operated in December 1957, and was the first to do so outside the U.S.A. and U.S.S.R. In the summer of 1958 the chamber was taken from Imperial College to the Atomic Energy Establishment at Harwell. There the chamber could be exposed to particle beams from the 170 MeV Cyclotron, and a simple p-p scattering experiment was performed in October 1958. A description of this experiment and of the apparatus at that time will be given in a Thesis by D. Reed.

The chamber, as has been said, was developed as a prototype. It was not, in October 1958, capable of the sustained operation necessary, if it were to be used in a serious nuclear experiment. It was decided

then, to develop the chamber further with a view to performing the experiment that will be described in part II of this thesis.

The expansion system was completely changed and a number of other improvements made before this was possible. A general description of the chamber in its present state, with particular emphasis on the modified expansion system, will be given in Chapter 2.

In the following sections of this chapter the basic principles of a bubble chamber, and the reason for the choice of hydrogen as operating liquid will be given. The basic design considerations will then be discussed.

1.2 BUBBLE CHAMBERS

1.2.1 The Principle of operation.

The principle of a bubble chamber was first proposed by D.A. Glaser in 1952 (Phys. Rev. 87 665, 1952). When a liquid is brought into a suitable condition of superheat, boiling is found to occur, and bubbles form, along the path of any ionizing particle that passes through the liquid. Figure ((1.2)1) shows a photograph of such bubble 'tracks' in the chamber to be described. The bubbles appear as white dots and are seen to lie along straight lines. In this case the lines are the paths of protons in the chamber. It is believed that these bubbles form for the following reason.

Consider a small bubble of radius r in a liquid. Inside the bubble is the normal vapour pressure ($P_{vap}(T)$) corresponding to the temperature (T) of the liquid : this pressure may be regarded as trying to make the bubble grow larger. Opposing this are both the pressure applied to the liquid from outside (P_{app}) and an effective pressure (P_{st}) due to the surface tension of the wall of the bubble. This effective pressure (P_{st}) will be proportional to $1/r$, let

$$P_{st} = \frac{k}{r} .$$

Figure (1.2)1 Photograph of Hydrogen Bubble Chamber Tracks.

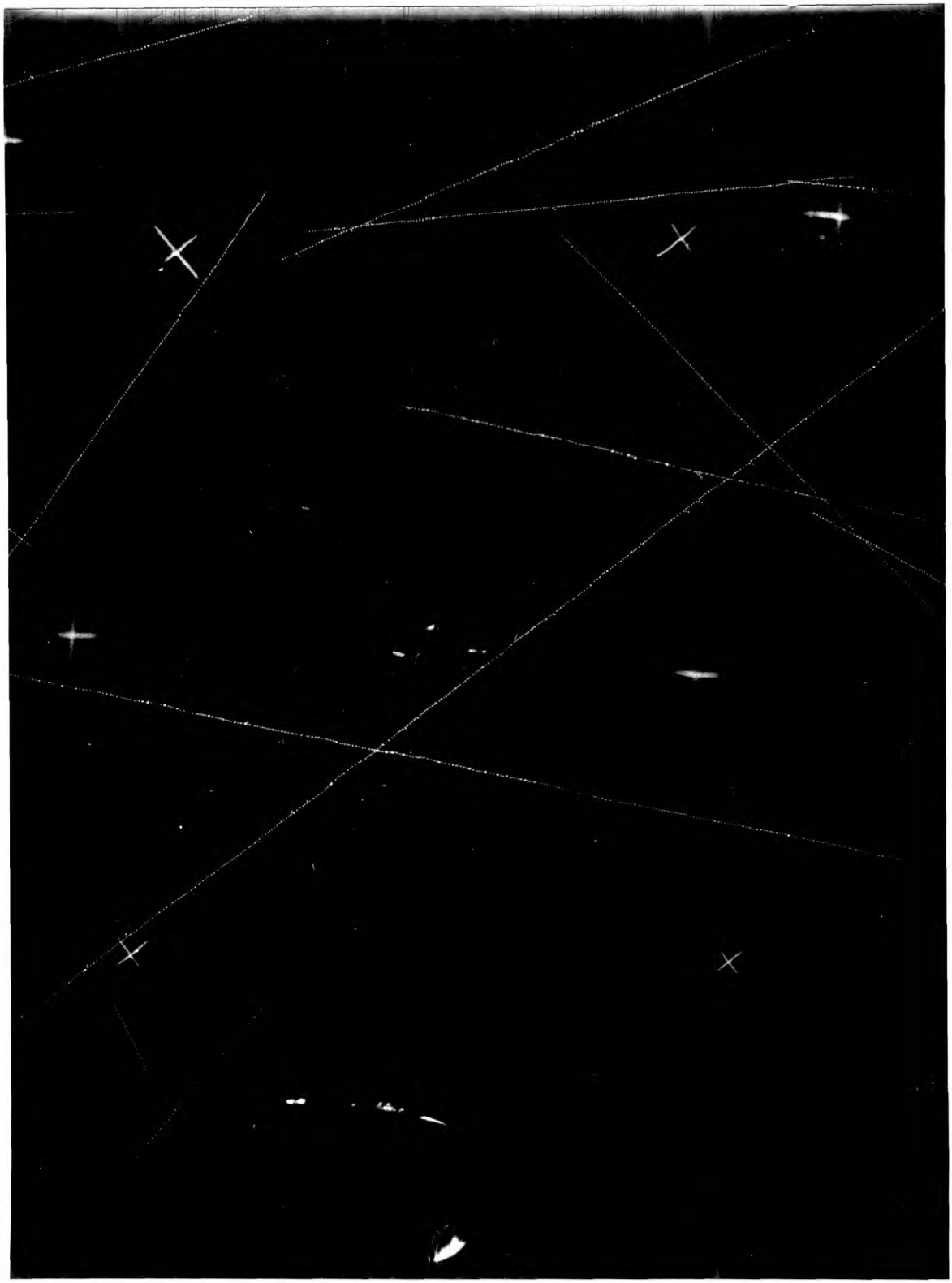

The bubble will grow if :

$$P_{vap} > P_{app} + \frac{k}{r}, \qquad 1.2/1$$

and shrink if the reverse is true. Clearly r cannot be negative. From 1.2/1 it then follows that in order for the bubble to grow, $P_{vap}(T)$ must be greater than P_{app}. This is the condition that the liquid be superheated.

From 1.2/1, and defining $r_o(T)$:

$$r > \frac{k}{P_{vap} - P_{app}} = r_o(T) \qquad 1.2/2$$

must be satisfied if the bubble is to grow. From this it is seen that in order for a liquid to boil bubbles must first be produced with radii greater than the critical radius $r_o(T)$. Due to the thermal motion of the liquid molecules, transitory spaces without molecules or pseudo-bubbles will be formed whose effective radii ($r_e(T)$) will be larger if the temperature T is higher. When an ionizing particle passes through a liquid much of the energy lost by the particle becomes concentrated at the ends of short scattered electron tracks (δ rays). Here the particle produces 'hot spots' where the liquid temperature is locally raised. Due to the higher local temperature, the effective radii ($r_e(T)$) of the pseudo-bubbles

may become larger than the critical radius ($r_o(T)$), thus allowing these pseudo-bubbles to grow into real and visible bubbles. These bubbles will be located near to the path of the ionizing particle and thus give a visual indication, or track, of the particle's trajectory.

The simplest way of bringing a liquid into a super heated state is to heat it to near its boiling point and then reduce the pressure applied to it. This is what is done in a bubble chamber. In practice boiling starts on the walls of the chamber immediately after the pressure has been reduced, whether or not any ionizing particles are present, and rapidly spreads throughout the liquid. If the chamber is to be operated with an accelerator then this effect is of little consequence since it can be arranged that the particles enter the chamber just after the 'expansion' when the pressure is reduced, and the bubble tracks photographed before general boiling develops. Afterwards the pressure may be re-applied, in the 'compression' and further boiling stopped.

1.2.2 The choice of liquid

Many different liquids may be used in a bubble chamber, provided suitable conditions of temperature and pressure are chosen. In general it is found that the initial pressure should be about $^2/_3$ of the critical pressure of the gas. The temperature should then be near

the boiling point at this pressure. D. Glaser has operated chambers with a great many liquids including xenon and even beer! The most convenient liquids are, however volatile organic compounds such as ether and pentane, whose operating temperatures are near room temperature. The choice of liquid hydrogen in this, and many chambers, is made purely on grounds of the nuclear physics that may be studied with the completed chamber.

Consider for instance a particle (A) that enters the chamber and is seen, by the tracks left, to have made a nuclear interaction. From the appearance of the tracks it is not necessarily possible to tell with what nucleus (B) the particle (A) has interacted.

If the liquid consists of a pure element, however, then the interaction must have been with a nucleus of that element. It is thus desirable to use a pure element as the liquid. If the object of the chamber is to study the interactions of the initial particle with the nuclei of the element, then that element must be chosen for the interest of the interaction with its nuclei. At the present state of knowledge only interactions with simple nuclei give much useful information. Of all elements hydrogen has the simplest nucleus - a proton - and is thus often chosen.

The range of pressures and temperatures for which liquid hydrogen is sensitive will be given in section 3.2. It

will be shown there that an initial pressure from four atmospheres upwards may be used but that there are certain advantages in using a fairly high pressure such as seven or eight atmospheres. At such pressures the boiling point of hydrogen is about 30° K. Similar temperatures and pressures are required for liquid deuterium and in fact the present chamber could have been operated with this liquid. The liquid will, howevever, always be referred to as 'hydrogen'.

In order to maintain temperatures in the region of 30°K the chamber must, of course, be kept in a vacuum cyrostat and be cooled with supplies of liquid hydrogen and nitrogen.

1.2.3 History

The first bubble chamber was built by D.A. Glaser (Phys. Rev. 87 665, 1952) using diethyl ether. The first hydrogen bubble chamber was made Hilderbrand and Nagle (Phys. Rev. 92 517, 1953). A later chamber, 4 inches diameter, built at Berkeley, California (Parmentier and Schwemin, 1955 Rev. Sci. Inst. 26, 954.), was in many ways the basis of the present chamber. A bubble chamber 72" long is now operating at Berkeley and several other large chambers are being built.

In the next section more consideration will be given to the detailed requirements of the design. Naturally some of the observations will have come from the work of other groups working in this field.

1.3 DESIGN CONSIDERATIONS

1.3.1 Chamber heating

Tracks of charged particles may be produced in liquid hydrogen, if it is heated to near its boiling point at a suitable initial pressure and the pressure is then rapidly reduced. The pressure must be reduced by some 'expansion system' which may also re-apply the pressure after the tracks have been formed. The requirements of this expansion system will now be discussed.

Any heat introduced into a hydrogen bubble chamber, either when it is static or during a cycle of expansion and compression, has to be removed by boiling liquid hydrogen at some point. The cost of production of the liquid is quite high and thus the cost of removing heat from the chamber is significant. In the present case this cost was approximately £1/10/- per watt per day of operation. It is thus important to consider the causes of heating the chamber.

In order to stop heat from the surroundings reaching the chamber, it must be surrounded by a vacuum cryostat. This must consist of a large vacuum case, to stop conduction of heat, and shields held at an intermediate temperature, to reduce radiation. There will always, however, be some heating of the chamber, by radiation, and conduction in supports. This heating, since it will continue

whether the chamber is 'cycled' or not, will be called the 'static' heating (5 watts in the chamber described) and will produce a corresponding static boil-off of hydrogen. If the chamber is cycled, there will be other 'dynamic' causes of heating. In particular, any mechanical work done on the hydrogen will generate heat in it.

If no boiling occurred in the chamber and the expansion and compression were rapid enough to be purely adiabatic, then the cycle would be reversible and no work would be done. If, however, after the expansion some of the liquid boils and gives a volume U' of gas then on compression extra work (W) will have to be done to compress this gas. The cycle would then be irreversible with the work (W) being done on the liquid of each cycle. It may be shown (see appendix A) that if Δp is the change in pressure, assumed small, and γ is the ratio of specific heats (1.4 for hydrogen) then

$$W = \frac{\Delta p}{\gamma} U' \qquad 1.3.1$$

If, for example, only 1 cc of liquid boils during the cycle, and there are 20 cycles per minute then 10 Watts of heating result. It is very important that the amount of boiling occurring be small. The most general way of keeping it so is to have the shortest time during which the pressure is low, that is, to have a rapid cycle. The methods of producing the cycle will now be considered.

1.3.2 Expansion mechanisms

There are broadly three different ways of expanding a bubble chamber (see fig. (1.3)1). The first (a) uses a piston or bellows in contact with the liquid itself. Such a liquid expansion system requires moving parts at liquid hydrogen temperatures.

The second system (b), used in the present chamber, employs a piston at room temperature, acting on the gas above the liquid. This reversible flow expansion system requires the rapid motion of a piston, large compared with that used in a liquid expansion system.

In the third system (c) the gas pipe from the chamber is joined through two valves to high and low pressure vessels. The pressure on the chamber is changed by closing one valve and opening the other. This cyclic flow system requires a compressor to pump the gas from the low to the high pressure vessel.

Consider now the three systems from the point of view of possible heating. In the liquid expansion system, no new sources of heating have been introduced. In the second system cold gas from above the liquid surface will, during the expansion, be drawn up into the room temperature cylinder. Here it may be warmed before being sent back down the pipe and possibly give up some heat to the liquid hydrogen. In the last system the gas used for recompression

Figure (1-3) 1

Types of Expansion

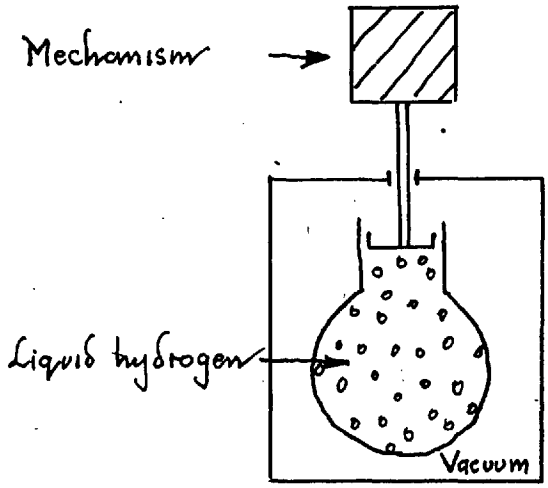

(a) Liquid Expansion

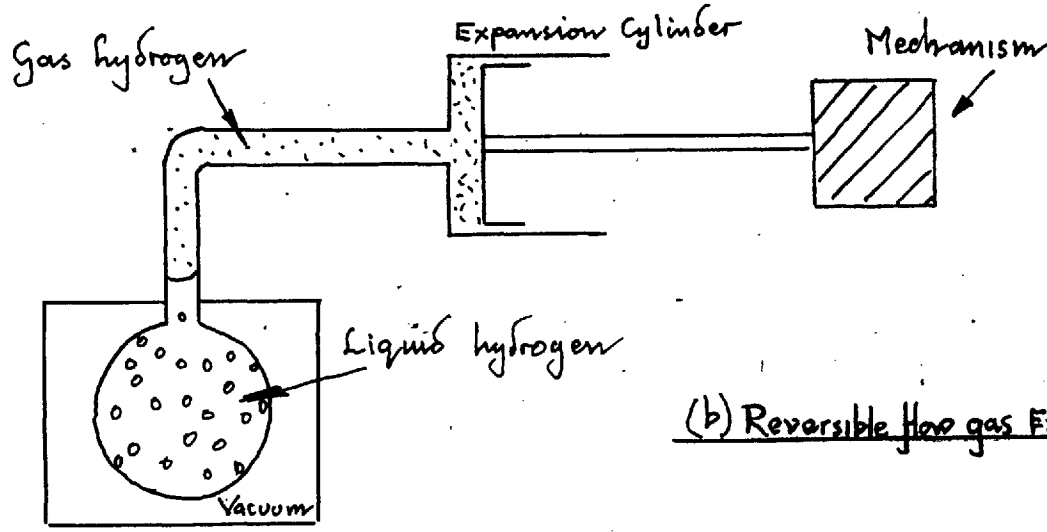

(b) Reversible flow gas Expansion

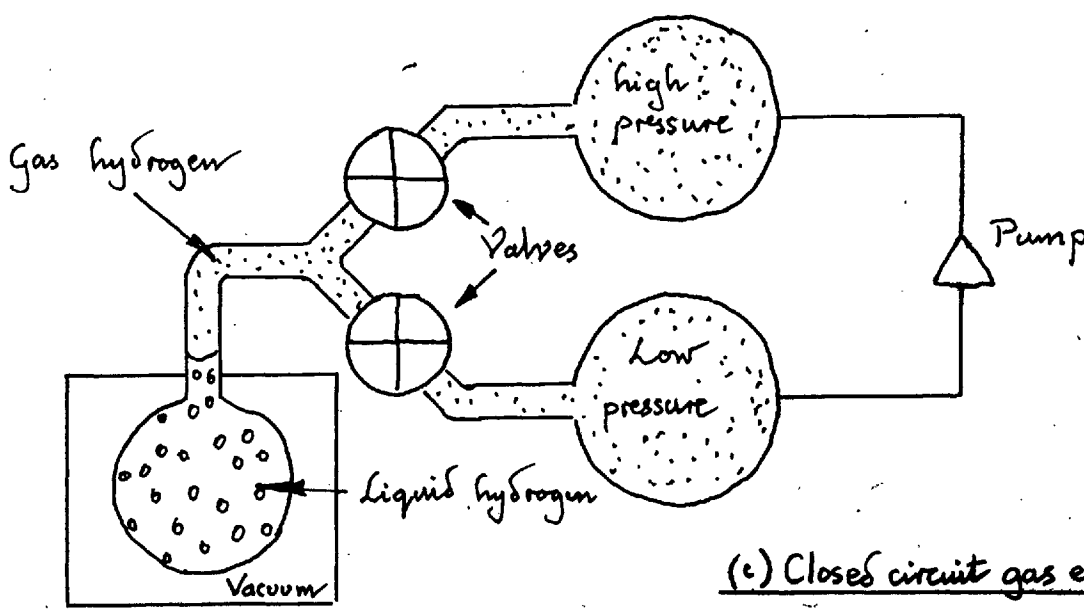

(c) Closed circuit gas expansion

comes from a separate room temperature vessel and may, as above, give up some of its heat to the liquid. The heating in both the latter cases can be reduced if the mixing of the gas in the pipe can be reduced. It will be shown in section 3.3.2 that in the present chamber this heating was certainly not larger than that due to boiling. If such heating is small, then there seems little advantage in using a liquid expansion system. The piston type gas expansion instead of the valve type, was chosen, partly to avoid the use of a hydrogen compressor, and partly because it had been believed that less heating of the liquid would result. A description of the system adopted will be given in the next chapter.

CHAPTER 2

DESCRIPTION OF APPARATUS

2.1 Introduction

The essential components of the bubble chamber may be illustrated as shown in the following figure.

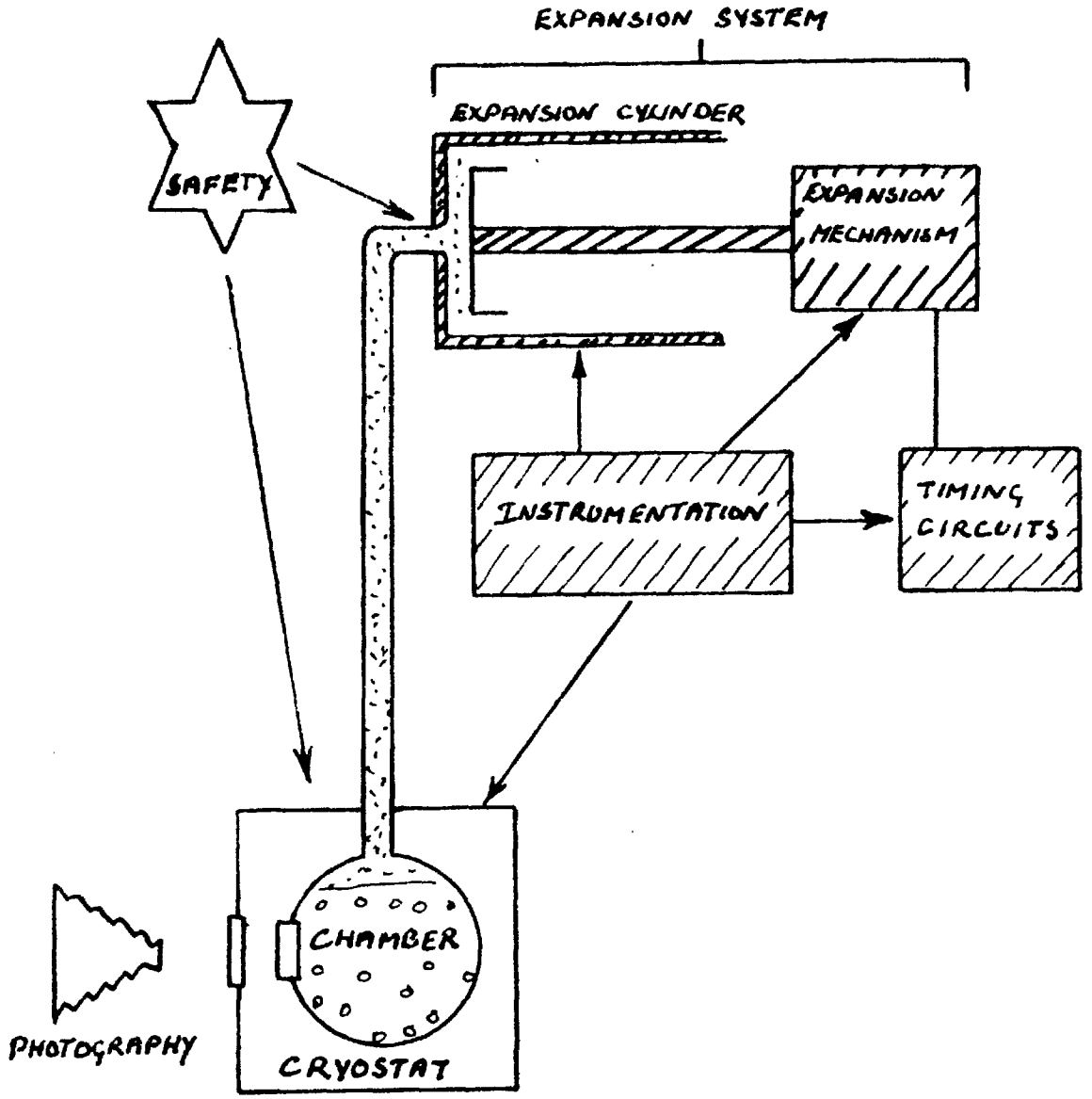

The chamber had to be placed in a cryostat, with windows for photography and illumination. From the chamber, an expansion pipe led to an expansion cylinder, in which a piston was moved by a mechanism. The timing of this movement was controlled with the aid of electronic circuits. Instrumentation was provided to indicate the state and functioning of the parts. A complication arises due to the extreme inflammability of hydrogen gas. One of the safety precautions taken was to make the whole operation of the chamber remote. The chamber and expansion system which formed what will be referred to as the 'rig' (figure (2.1)1), could be separated by up to thirty metres from the 'control station' (figure (2.1)2).

In the sections that follow the various parts of the apparatus will be discussed. References to illustrations will sometimes be given by numbers that refer to particular parts of the apparatus in whichever illustration they appear, e.g. (15) will refer to the vacuum tank in figures (2.1)1, (2.3)4, and (2.4)3. Less detailed description will be given of those parts of the apparatus that will be described in Mr Reed's thesis. For further details, this thesis should be consulted. A number of electronic circuits will be included in appendix B.

Figure (2.1)1 Rear of Chamber Rig.

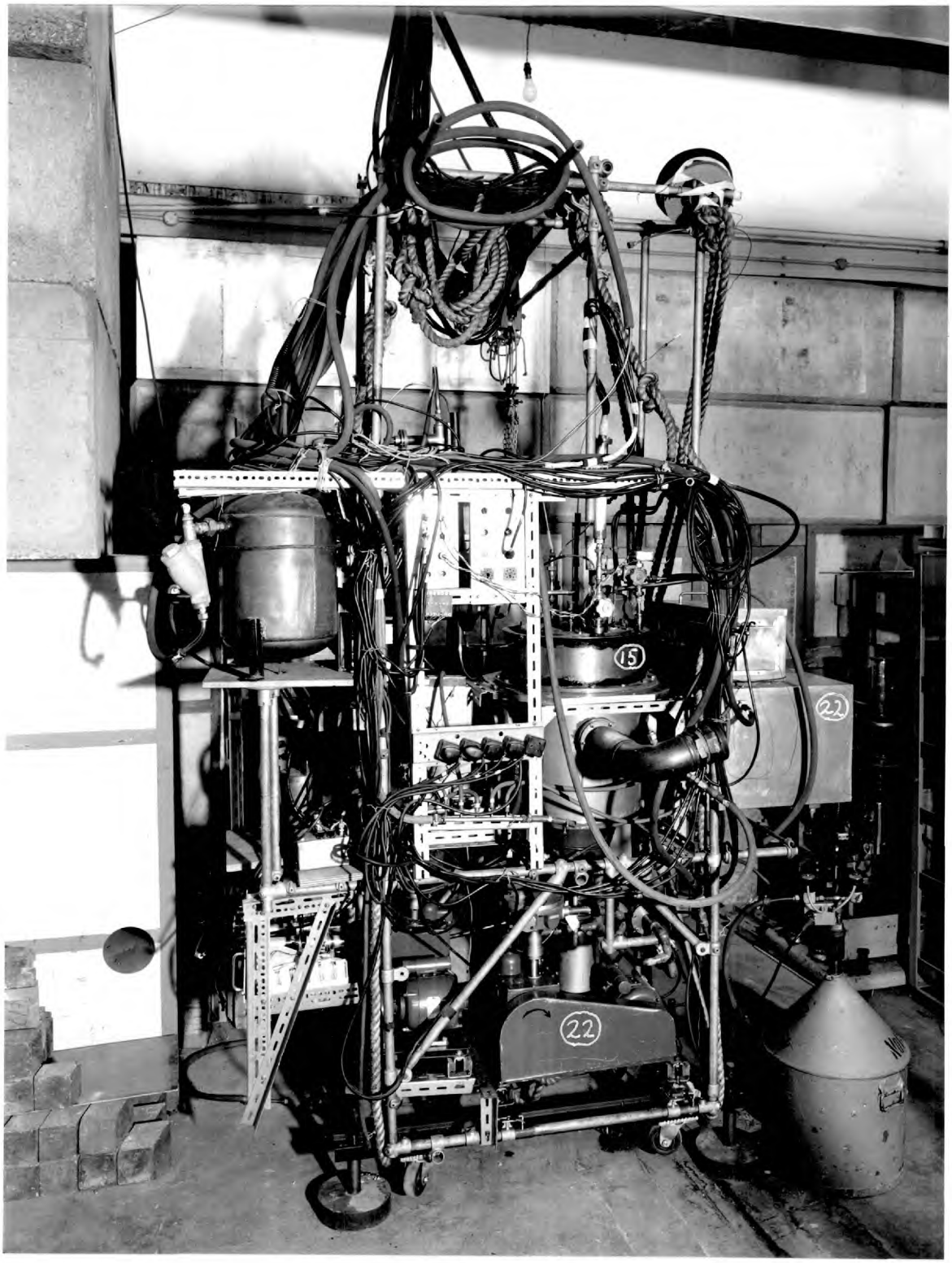

Figure (2.1)2 Control Station.

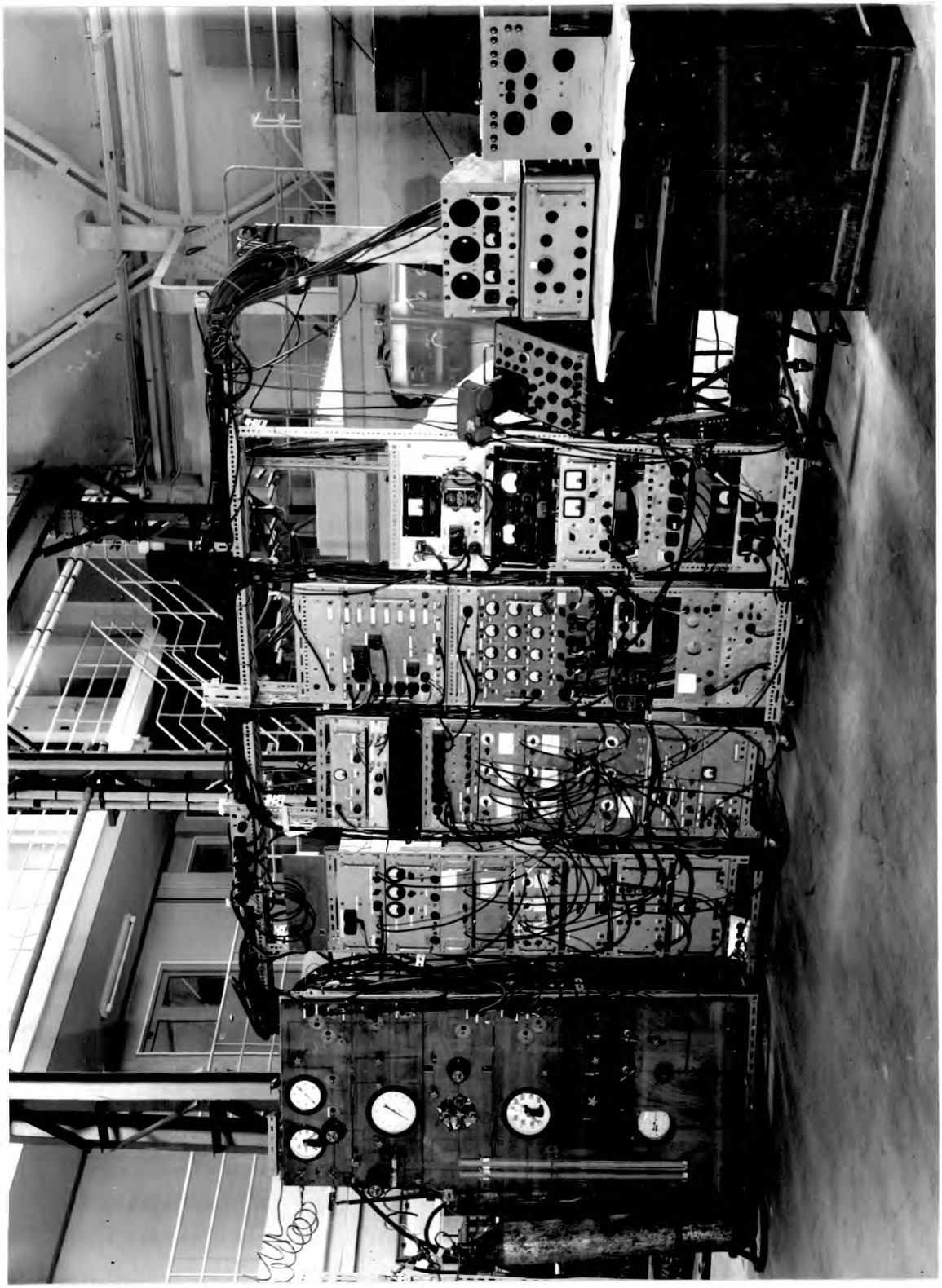

2.2 CHAMBER AND CRYOSTAT

In Chapter one it was stated that the operating conditions for a liquid hydrogen bubble chamber require an initial pressure of up to eight atmospheres and a temperature of about 29°K. The chamber, with its windows, must be able, therefore, to withstand such a pressure at this temperature. The chamber itself (11) was made of a copper tube, at either end of which were brazed heavy brass clamping rings to hold the glass windows (16). The windows were sealed with lead-copper gaskets, designed by Mr Barford, a cross-section of which can be seen in figure (2.2)1b(54).

The chamber was cooled by providing a heat path (12) between it and a tank (9) full of liquid hydrogen, boiling at atmospheric pressure. In order that this hydrogen should not be boiled off too fast, it and the chamber were shielded as far as possible from all sources of external heat. In order to stop radiation falling on them they were surrounded by polished copper shields kept cold by boiling liquid nitrogen in tanks (4) and (5). In order to stop conduction of heat to the chamber, and hydrogen and nitrogen tanks, they were all enclosed in a vacuum tank (15) pumped by an oil diffusion pump (21) and a rotary backing pump. It was found that this vacuum had to be better than 2.10^{-6} mm of

Figure(2.2)1 The Chamber

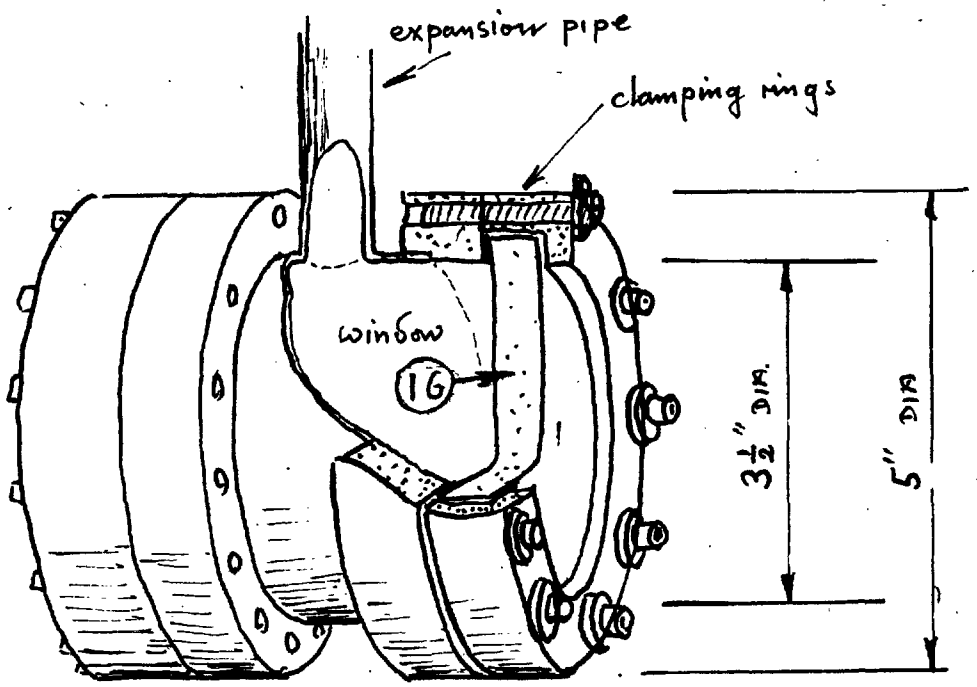

½ Scale

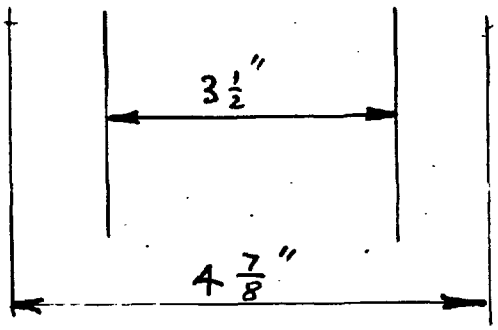

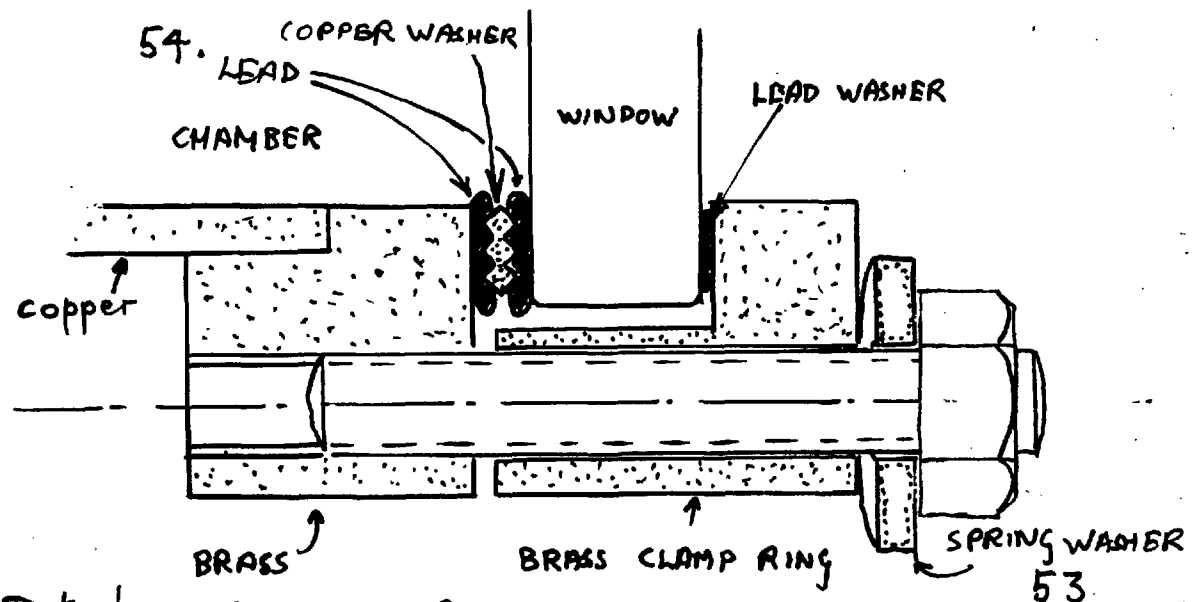

Detail SCALE ×2

Figure (2.2)2

CHAMBER & SHIELDS

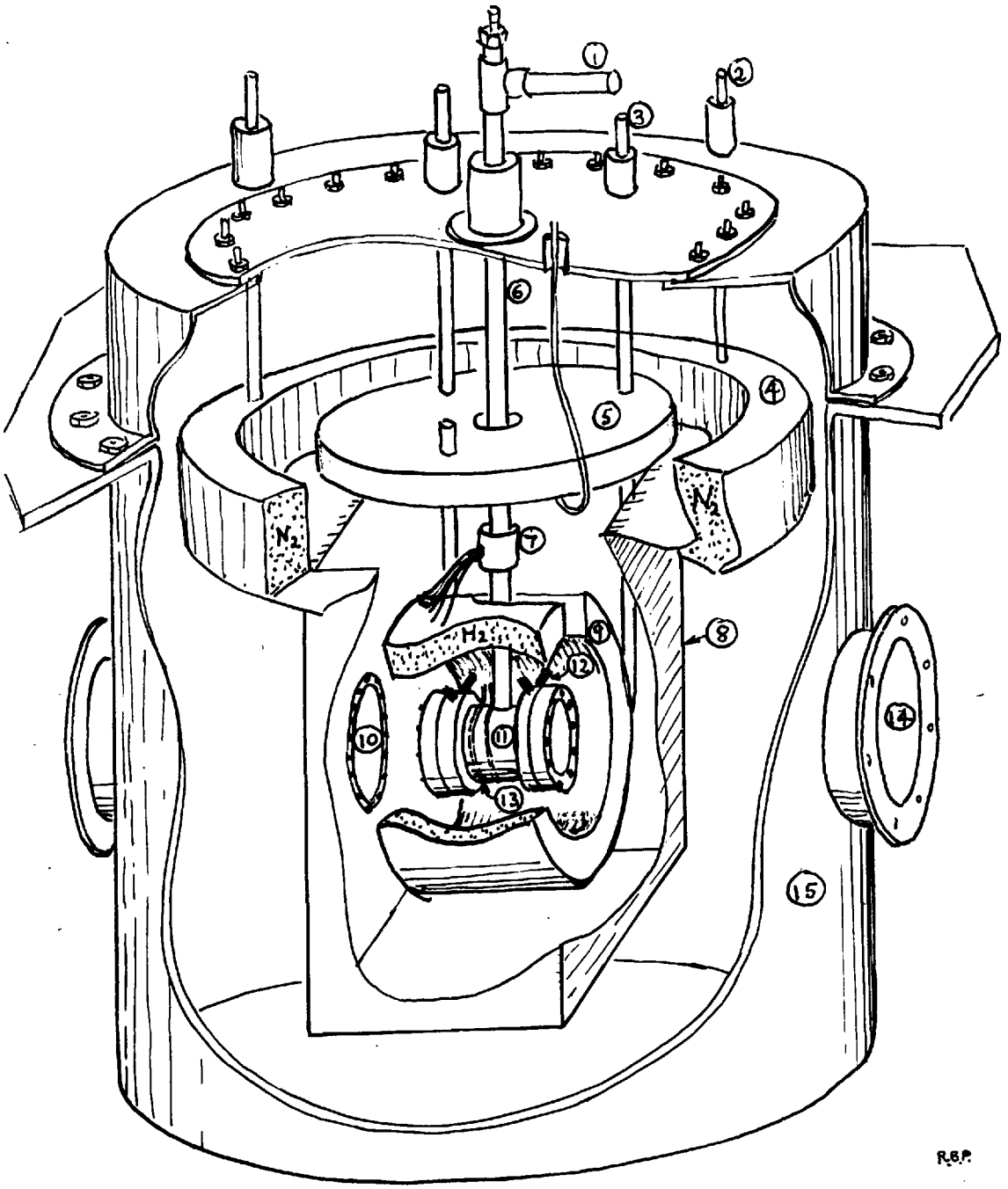

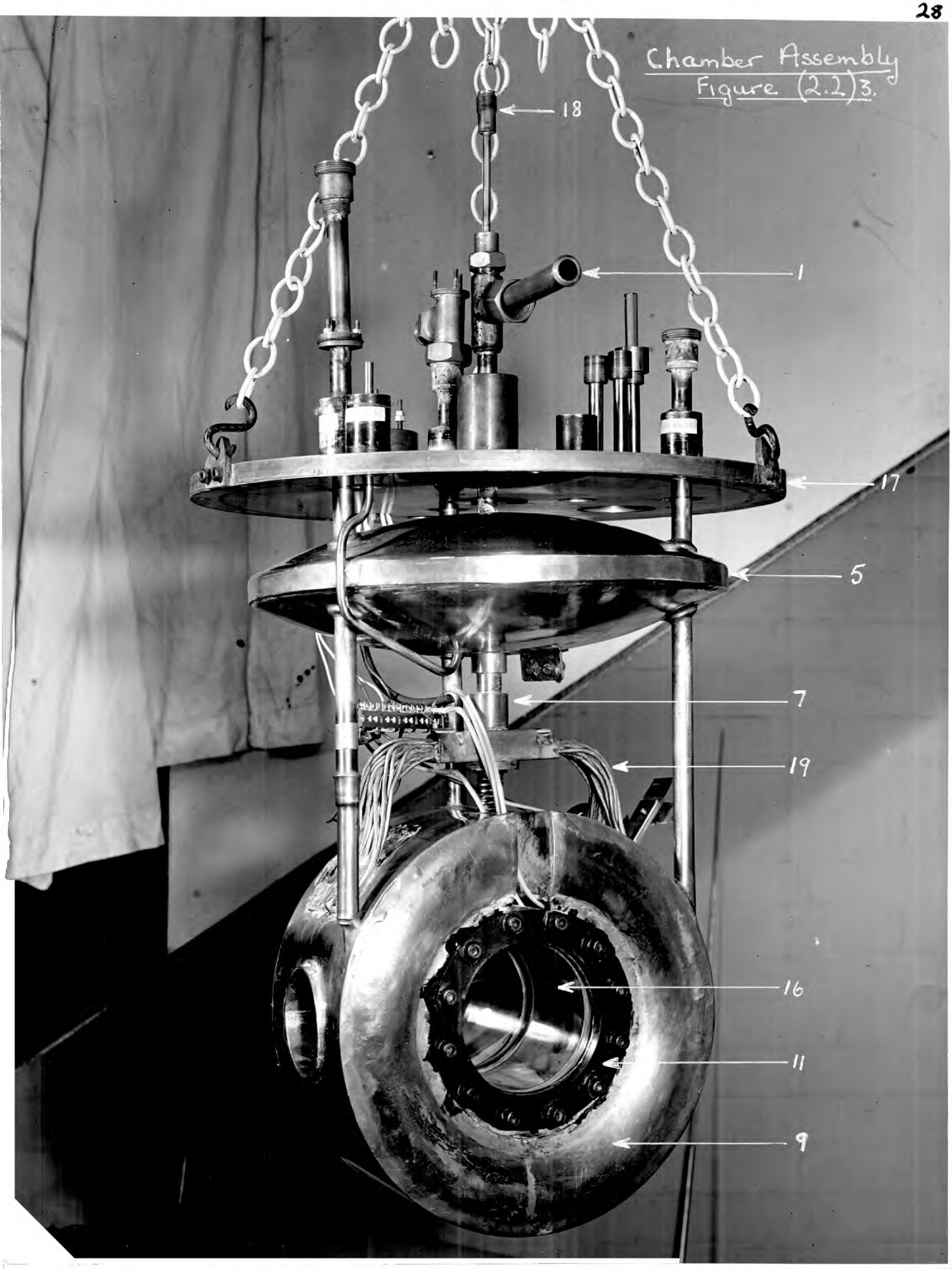
Chamber Assembly
Figure (2.2)3.
18
1
17
5
7
19
16
11
9

mercury to avoid the residual gas freezing on the chamber windows and obscuring the photography of the chamber.

Due to the finite thermal resistance of the heat path (12), any heat dissipated in the chamber raised its temperature above that of the boiling hydrogen (20.4 ^{o}K) in the hydrogen tank (9). Such heat could be provided by an electrical heater (13) wound round the chamber, and thus the temperature of the chamber could be controlled. A pipe (6) from the top of the chamber led up and out of the vacuum case to the expansion cylinder. At a point just above the chamber (7) the pipe was cooled to the temperature of the hydrogen tank by joining the pipe to the tank by wires (19). Since the chamber was maintained at a pressure higher than atmospheric, the hydrogen was liquid at this point, and the liquid level was thus kept above the point and well away from the chamber. This was found to reduce some violent changes of temperature in the chamber whenever it was expanded.

Windows were provided on both sides of the chamber (11), nitrogen shield (10), and vacuum case (14). Those on one side were for illumination and those on the other for photography. The details of the optics will be given in the next section and a description of the expansion system left till the section after it.

2.3 PHOTOGRAPHY

One problem involved in photographing bubbles in liquid hydrogen arises from the liquid's small refractive index (1.078). The intensity of light scattered by a single bubble falls off rapidly with the angle (θ) between scattered and initial directions, (see figure (2.3)1; results taken from calculations by Dr Welford; see: Barford, Progress in Cryogenics, 2, 1960; to be published)

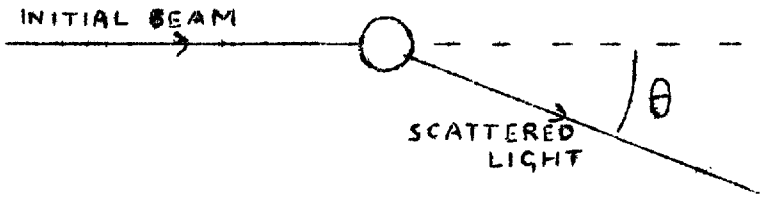

There are two consequences of this. Firstly, if a bubble is observed with a large angle (θ) the intensity of light seen is very small. Secondly, if two bubbles are observed, illuminated by the same light flux, but observed with slightly different angles (θ) then the two bubbles will appear with very different intensities. The relative difference in intensities $\frac{\delta I}{I}$ for a given difference in angle ($\delta\theta$), i.e. $\frac{1}{I}\frac{\delta I}{\delta\theta}$, is plotted on graph (2.3)2 . It is seen to have a minimum at the rather small angle of about one degree.

It is clearly desirable that the camera should 'see' bubbles in different parts of the chamber with equal

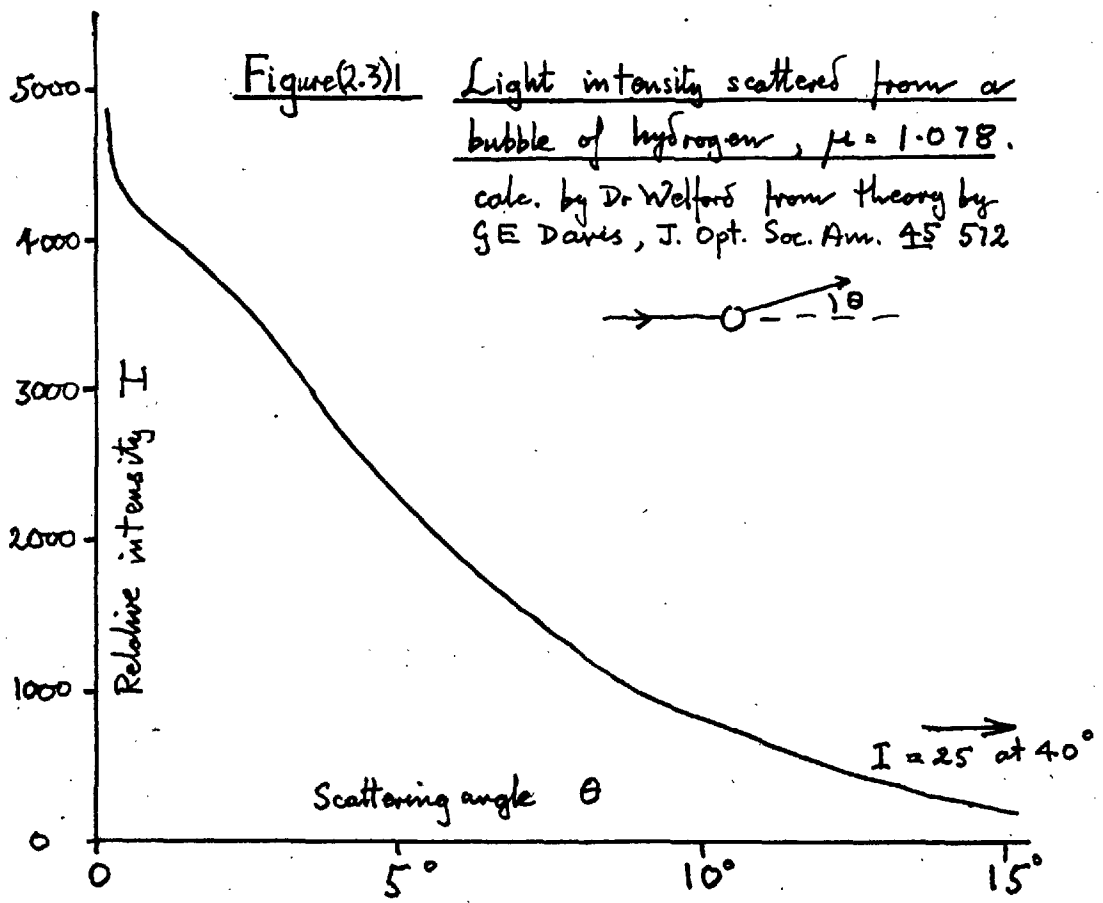

Figure(2.3)1 Light intensity scattered from a bubble of hydrogen, $\mu = 1.078$.
calc. by Dr Welford from theory by G E Davies, J. Opt. Soc. Am. 45 572

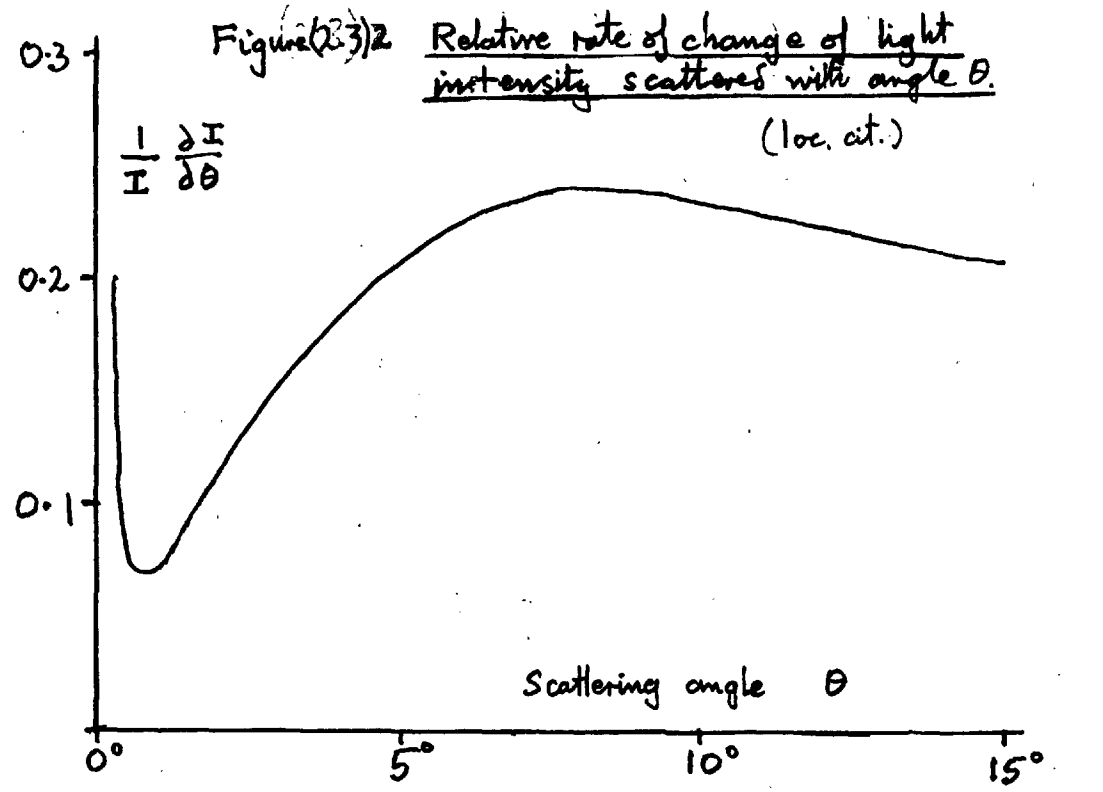

Figure(2.3)2 Relative rate of change of light intensity scattered with angle θ.
(loc. cit.)

intensity, and that this intensity should be high. This demands that as seen by the camera the scattering angles θ for all bubbles should be constant (for equality of intensity), and small (both for equality and magnitude of intensity). It is seen (figure (2.3) 3a) that these conditions are approximately satisfied if the image of a point source of illumination is brought to a focus near to, and in the plane of, the camera lens; ($\alpha_1 \doteq \alpha_2$, and α is small). Such a system has the disadvantage that the slight reflections from the glass surfaces produce point secondary images in the field of the camera (I_2 in fig. (2.3)3b). This problem can be overcome by using a plane diffuse source instead of a point source. The condition of equality of scattering angles is still satisfied and the intensity of bubbles in the chamber will be equal if light leaving the diffuse source is isotropic. The arrangement of figure (2.3)3c, which did not give sufficiently even illumination, was improved by the insertion of an extra condenser lens, (fig. (2.3)3d). In this, the final arrangement, parallel light fell on a circular diffusing screen, that was imaged between two stereo camera lenses. The scattering angles used varied from 4° to 12°. Imperfection in the condenser made it impracticable to use angles less than 4°. In fact, only light scattered through the smaller scattering angles will

Figure (2.3)3

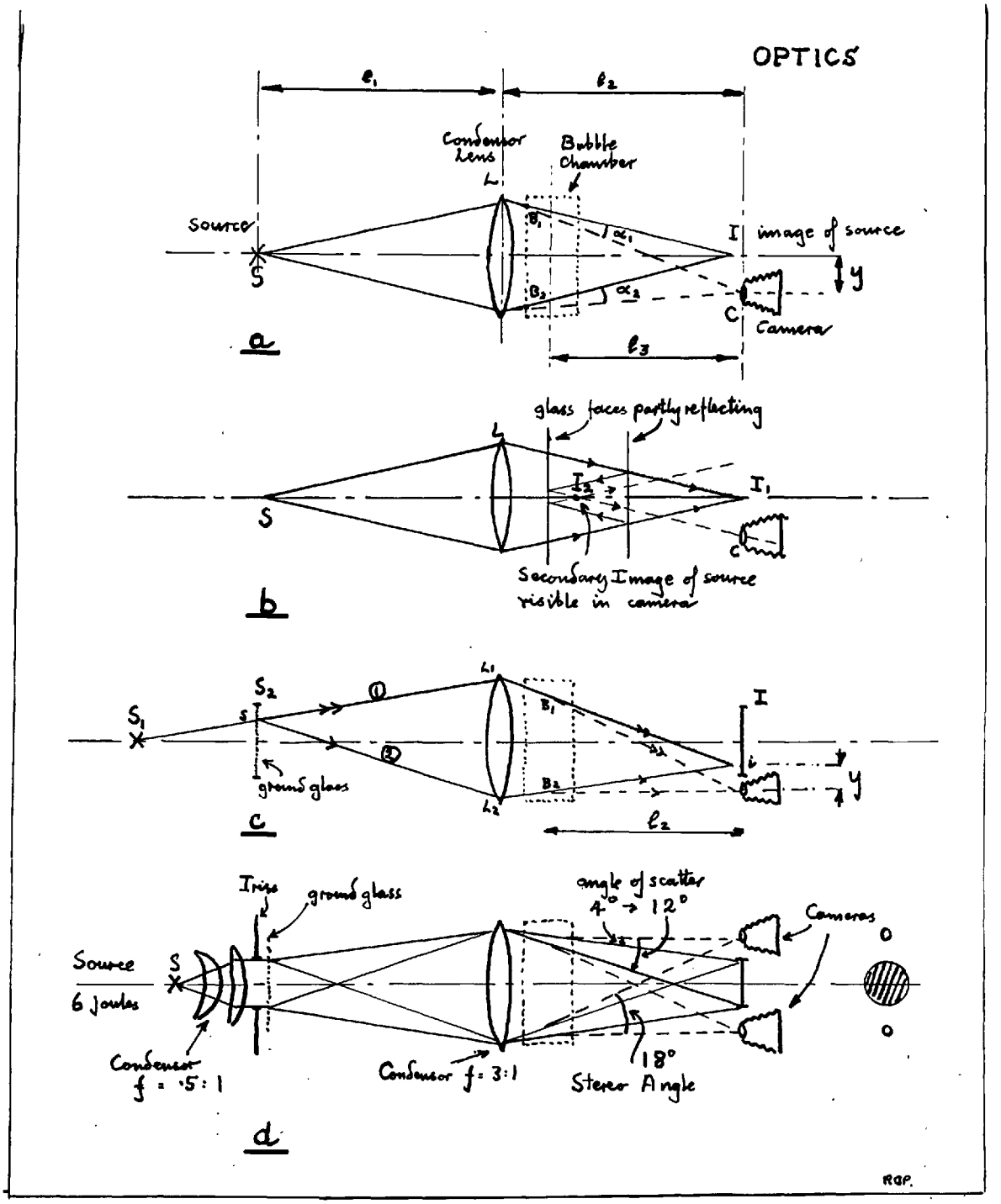
OPTICS
ℓ_1
ℓ_2
Condensor lens
L
Bubble Chamber
Source
S
B_1
B_2
α_1
α_2
I
image of source
y
C
Camera
ℓ_3
a
glass faces partly reflecting
I_2
I_1
Secondary Image of source visible in camera
b
L_1
L_2
S_1
S_2
ground glass
ℓ_2
c
Iris
ground glass
angle of scatter
4° → 12°
Cameras
Source
6 Joules
Condensor f = ·5 : 1
Condensor f = 3:1
18°
Steree Angle
d
RGP.

contribute significantly to the image of a bubble in the camera. This is due to the rapid drop in intensity of scattered light with scattering angle. A logical development of this system is to use a plane diffuse ring source imaged round each camera lens. This, because it uses small, and more nearly constant angles of scatter, will give the maximum intensity of image for given illumination. It may be observed that displacements of the circular image due to imperfections in the condenser will, to a first approximation, not alter the mean scattering angle, and thus not alter the intensity of illumination. This system has been adopted and developed for the British National Bubble Chamber by Dr Welford and Mr Barford.

Returning to a description of the system adopted in the present chamber, a few details of the actual arrangement should be given. The camera took two stereo-photographs on the same film, with a stereo angle of 15°. For the camera lenses, a balance had to be struck between good resolution, requiring a large aperture, and depth of focus requiring a small aperture. In fact f = 32:1 was chosen, which gave a depth of focus not quite equal to the depth of the chamber, but good resolution. The film in the camera could be wound on automatically. In order to identify the photographs, a number on an electric counter (24) was photographed on each frame. The camera lenses remained

Figure (2.3)4 Front of Chamber Rig.

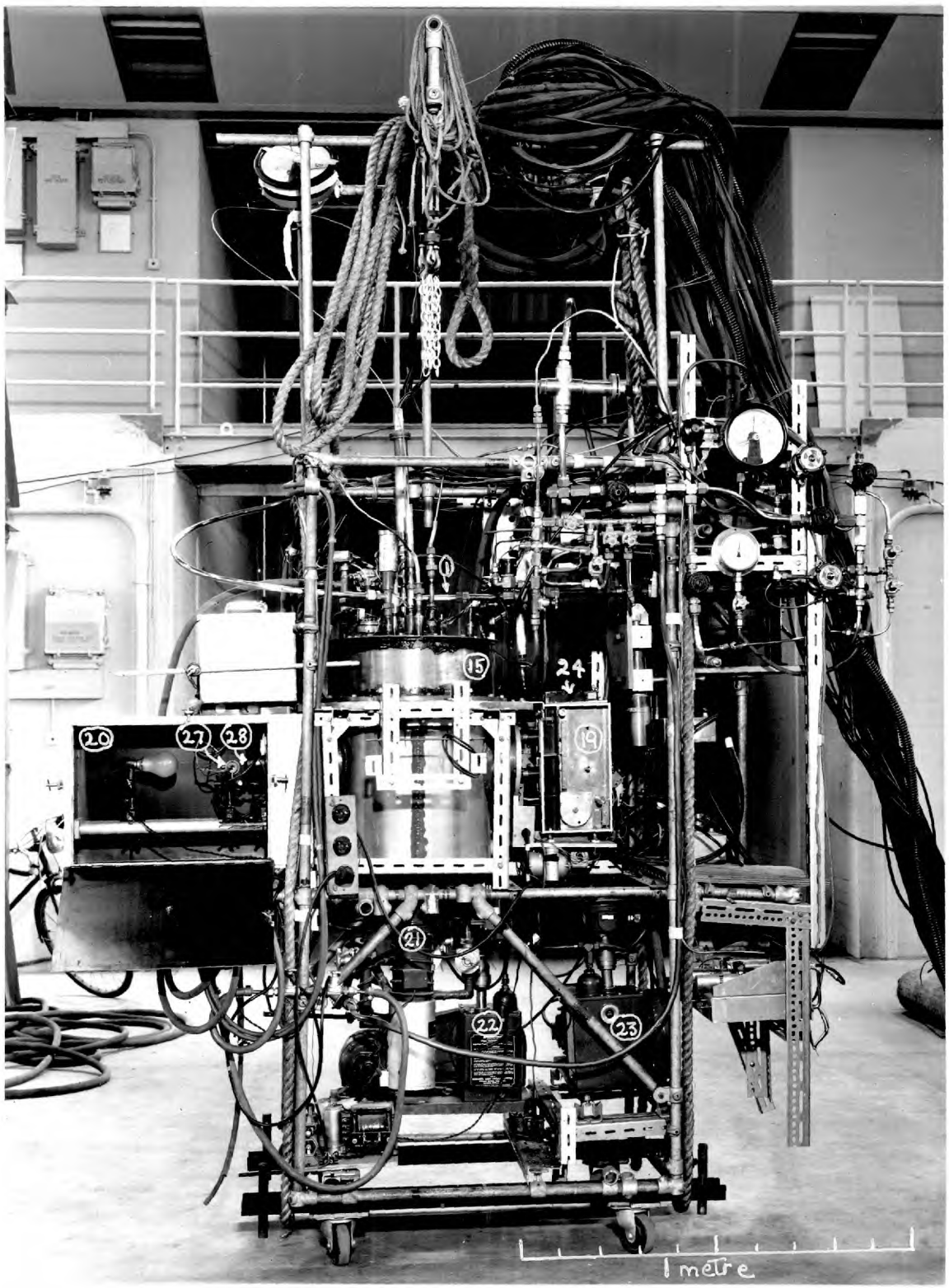

open all the time, photographs being taken only when the source, an electronic flash (27)was fired. It was mounted outside the vacuum tank in a gas tight box (20). The flash tube was fired by discharging a 2μF condenser at 4 kV through it. The circuit used to trigger it is shown in appendix B.1.

An example of the quality of photograph obtained with the system has been shown in fig.(1.2)1. In the experiment described in part II it was found desirable to photograph three expansions on the same film. This gave three times the background illumination but only the same track intensity. The photographs obtained were naturally inferior but still reasonable. See figure (2.1)5 of part II. The description must now return to the expansion system.

2.4 EXPANSION SYSTEM

In order to keep the heating of the chamber small, the duration of a cycle had to be kept short. The reduction of pressure produced by the expansion had to be reproducible, in order to bring the liquid, at each expansion, into the same state. If a serious experiment was to be undertaken the expansion system had to be reliable enough to operate for tens of thousands of cycles without fault.

The system adopted employed an effectively free piston moving in the expansion cylinder, driven back and forwards by the gas pressures on its front and back surfaces. When in its normal position the piston is sealed against a rubber O-ring (46) on the cylinder head. (See the figure overleaf). With the valves 47 and 48 open the forces applied to the piston were as follows:-

From the left: the chamber pressure ($p_1 \doteq 8$ atmospheres) acting over the small area (A_1) inside the O-ring: $p_1 A_1$; and a low pressure ($p_2 \doteq 1$ atmosphere) acting over the large area (A_2) outside the gasket: $p_2 A_2$.

From the right: the medium pressure ($p_3 \doteq 1.5$ atmospheres) acting over the whole piston area (A_3) : $p_3 A_3$.

The piston will remain to the left if

$$p_3 A_3 \geqslant p_1 A_1 + p_2 A_2 \qquad 2.4/1$$

Due to A_1 being small compared to A_2 the relatively slight excess of pressure p_3 over p_2 (0.5 atmospheres) was sufficient to hold the piston to the left, against the chamber pressure.

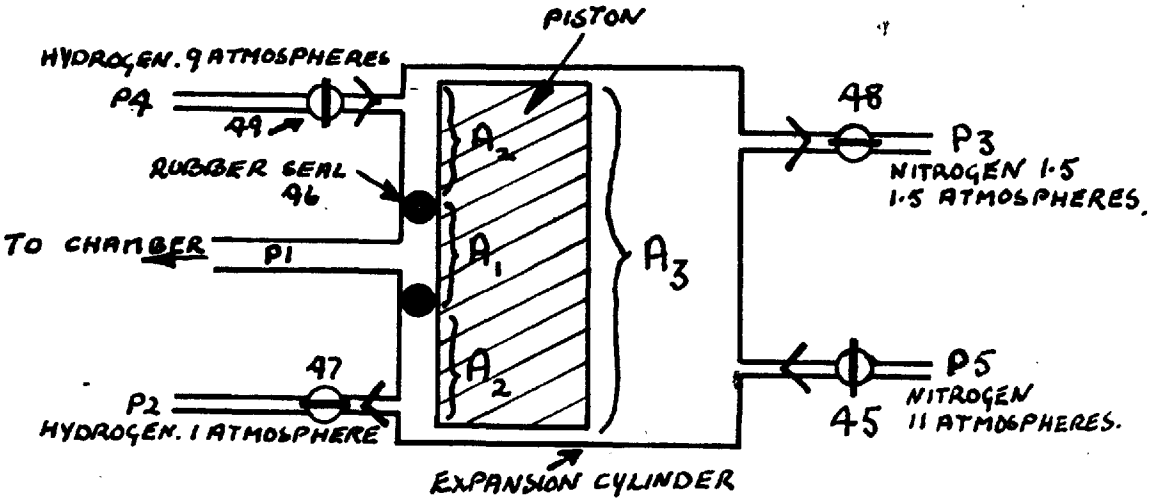

When it was required to expand the chamber, for which the piston had to be moved to the right: first, (a) the valves 47 and 48 were closed, then (b) the expansion valve, 49, was opened momentarily and a small quantity of purified hydrogen gas at a high pressure (p_4) allowed to enter the small space at the head of the cylinder, outside the O-ring. The consequent rapid rise of pressure in this space destroyed the condition (2.4/1) holding the piston to the left, and gave a force on the piston towards the right.

Figure (2.4)1 Expansion System

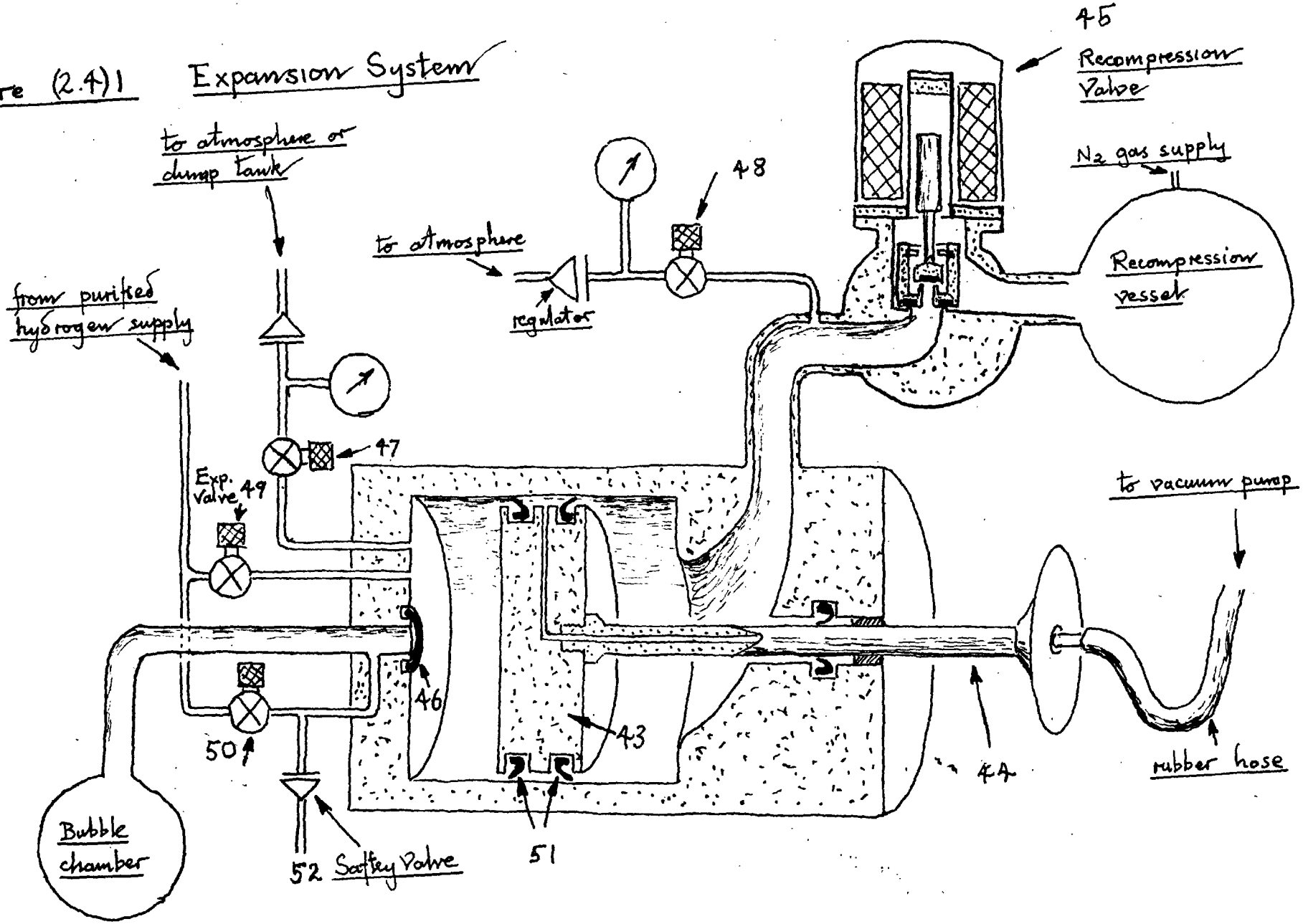

The piston then started moving, thus breaking the seal at the O-ring, and allowing the high chamber pressure (p_1) to act over the entire front area of the piston. This rapidly drove the piston to the right, against the medium pressure, p_3. This motion of the piston resulted in a lowering of the chamber pressure which continued until the compression was initiated.

The compression (c) was started by momentarily opening a large compression valve (45) which allowed very high pressure (p_5 = 11 atmospheres) nitrogen gas to pass into the rear of the cylinder. Since this pressure was greater than the chamber pressure the piston was driven to the left, back to the cylinder head. The motion was as shown in the following diagram.

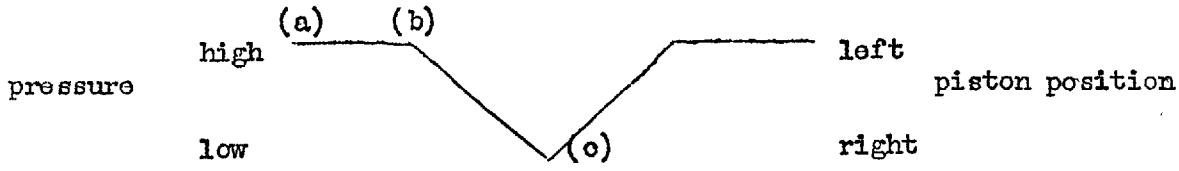

In order to return the system to its original condition: first (d) valve 47 was opened and the pressure on the piston, outside the O-ring, lowered to its original pressure (p_2) ; then (e), the valve 48 was opened and the pressure on the back of the piston lowered to its original medium pressure (p_3). The system was then ready for the next cycle.

In order that the start of the recompression be rapid, the recompression valve (45) must have a large port and the volume behind the piston must be small. The arrangement is shown in figure (2.4)1. The piston was guided by a rod (44) and sealed against the cylinder walls by rubber U-seals. In order that the piston motion be rapid, its weight was cut to the minimum. Both the piston (made of aluminium) and the rod (of stainless steel) were, therefore, bored out. See figure (2.4)2, which shows the parts of the piston, and the rod. A general view of the system is shown in figure (2.4)3.

It was found important that none of the compression nitrogen gas should become mixed with the hydrogen on the chamber side of the piston. If it did, it solidified in the chamber to form a fine white mist, which obscured photography. In order, therefore, to stop this nitrogen passing the piston, double rubber U-seals were employed. The space between the seals was connected via the bored out piston rod and a rubber hose to a vacuum pump. Surprisingly, this rubber hose survived the jerks produced by over 100,000 expansions.

All the valves referred to in the system were electromagnetically operated valves. The expansion (49) and compression (45) valves were opened rapidly by discharging condensers through their low impedance coils. The circuit used is shown in appendix B,(B/2). Both

Figure (2.4)2 Parts of Expansion Piston and Rod.

Figure (2.4)3 Expansion System.

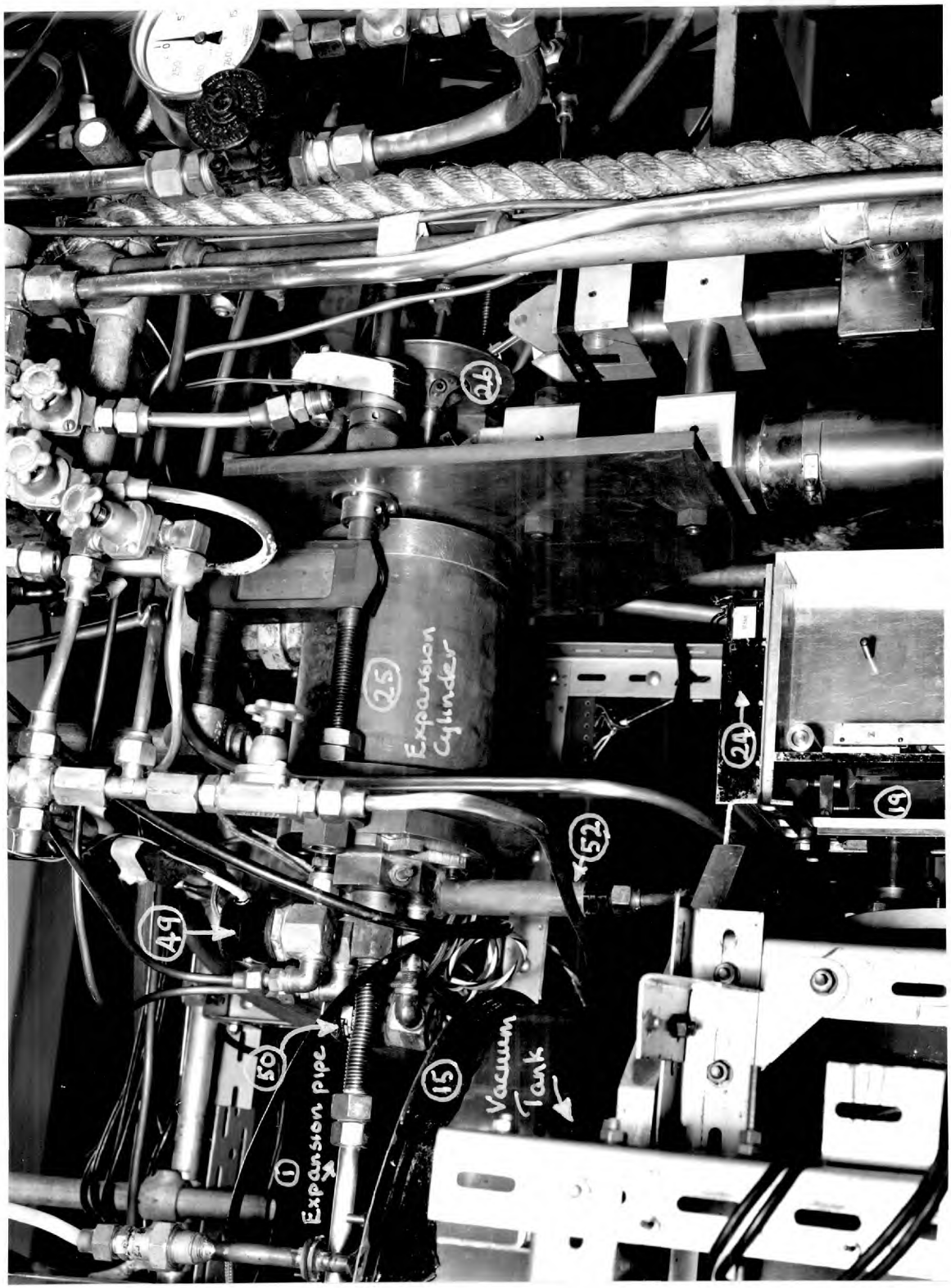

valves were modified commercial valves made by Alexandra Controls Ltd. The expansion valve (49) being 'type ACO_+' and the compression valve (45) being 'type ACP 7'.

Since the expansion and compression were initiated separately, by varying the time between them, the stroke length and thus the pressure drop could be adjusted. Traces, showing the variation of the pressure and piston position with time are given in figure (2.4)4. The pressure is seen to be below its initial value for only 11 m/sec. The length of the pressure drop could be held constant within 5% over long periods and the complete system, in the main experimental run, operated for 50,000 expansions without a fault. The expansion system did, therefore, satisfy the requirements of speed, reproducibility and reliability, that had been aimed at.

Between the cycles the pressure in the chamber was controlled by opening a valve (50) between it and a purified, pressure regulated, hydrogen supply, brought from the control station. This supply was also used when condensing hydrogen in the chamber to fill it. The hydrogen was purified by passing it through carbon and silica gel at a temperature of liquid nitrogen. It was found important that the hydrogen should not be passed through too fast, and also that, between use, the carbon and silica should be thoroughly cleaned. This was done

FIGURE (2.4)4 Oscilloscope traces from the pressure, piston position and beam indicators.

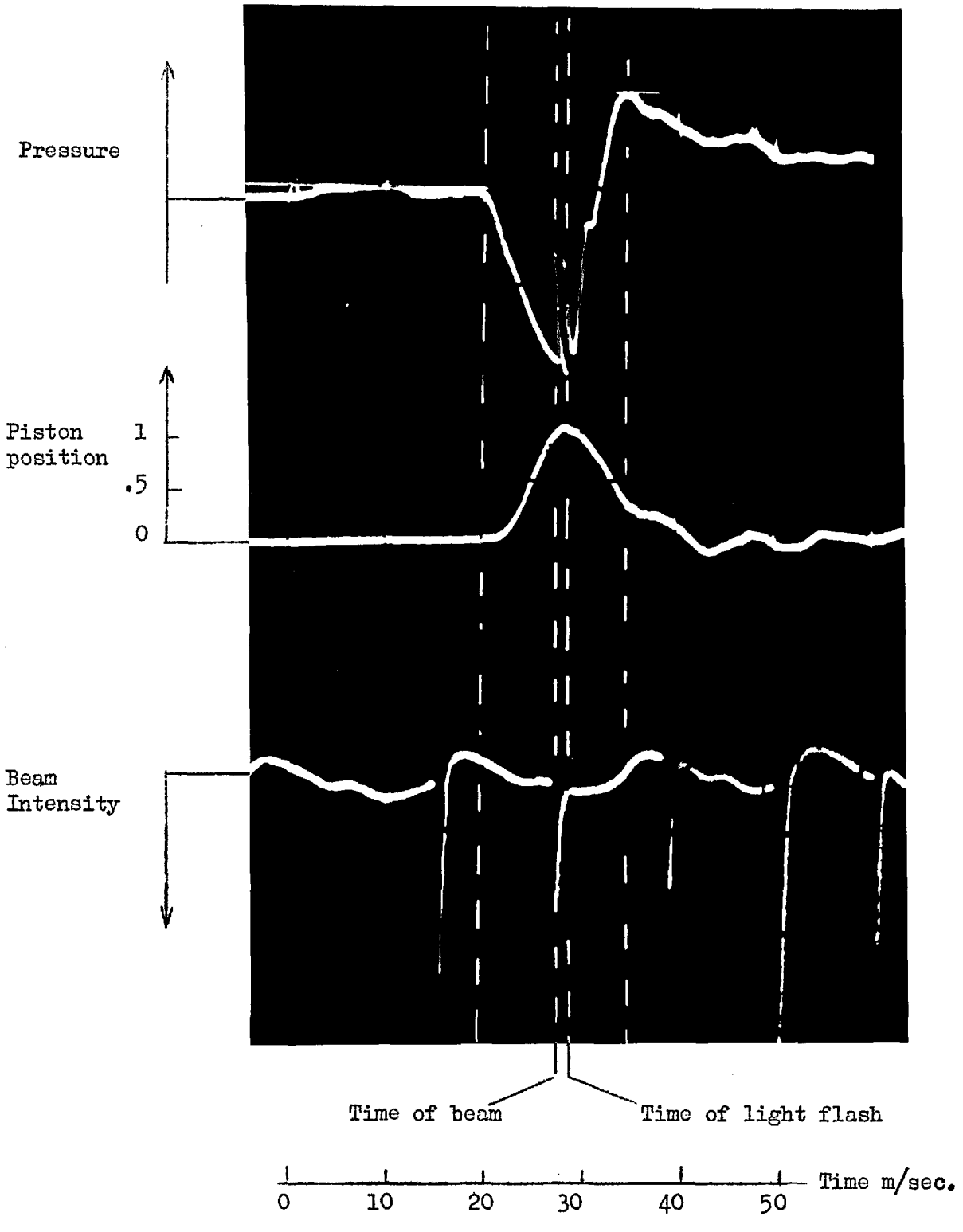

by heating it to 300° C and pumping with a vacuum pump for 36 hours. When such care was not taken impurities solidified in the chamber and obscured the photography.

The complete gas circuit is shown in figure (2.4)5. By the directions of the lines across the valves their normal positions between cycles have been indicated. The magnetically operated valves are shown shaded. They are closed when the current is off except those marked with an R, which are 'reverse acting'. The reason for their use is given in section 2.7.

The timing of the various operations referred to, were controlled by electronic circuits which will be described in the next section.

Figure(2.4)5 Gas circuit

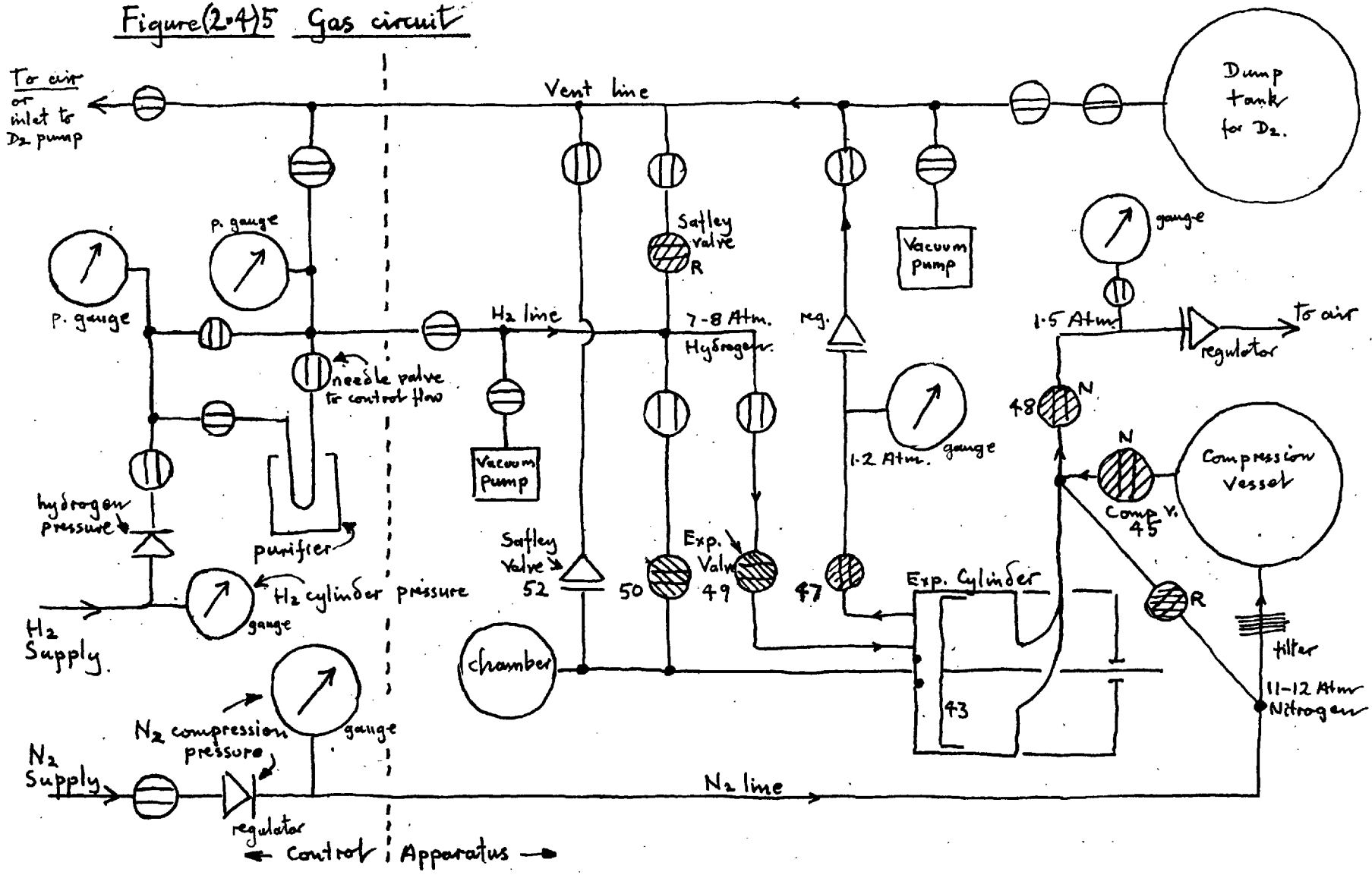

2.5 TIMING CIRCUITS

Circuits had to be provided to perform the sequence of operations outlined in the last section, and to time these operations with respect to the moment when a burst of particles was produced by the cyclotron. It was essential for the experiment described in part II that between the chamber cycles as few bursts of particles as possible should occur. The cyclotron radio frequency power was therefore switched on only long enough to ensure that at least one of the few bursts produced, occurred during the sensitive period of the cycle. When the chamber was ready for a cycle a pulse was sent to the cyclotron and the power was switched on long enough for a few bursts of particles to be produced. The exact times when these bursts occurred was determined by the position of the moving vane of a rotating variable condenser whose purpose was to alter the radio frequency of the accelerating field of the cyclotron (see part II, section 2.5). The precise moment when the expansion of the chamber was to occur was therefore controlled from an electric pulse which was sent from the condenser vane to the chamber, the pulse occurring when the vane was in a certain position during its rotation.

The electronic flash (see section 2.3) was timed, more accurately, from a pulse obtained from the cyclotron

only at the moment of a beam.

The camera could, as required in the experiment (part II, section 2.6), be wound on only once in a number of expansion cycles.

The requirements, outlined above, were achieved with the aid of a number of delay units and gates, a block diagram of which is given in figure (2.5)1. The individual circuits, though sometimes modified by the author, were designed by Dr. G. Cescotti, or taken from other sources. The main circuits used are given in Appendix B:3, 4, and 5.

Figure(2·5)1 Timing electronics.

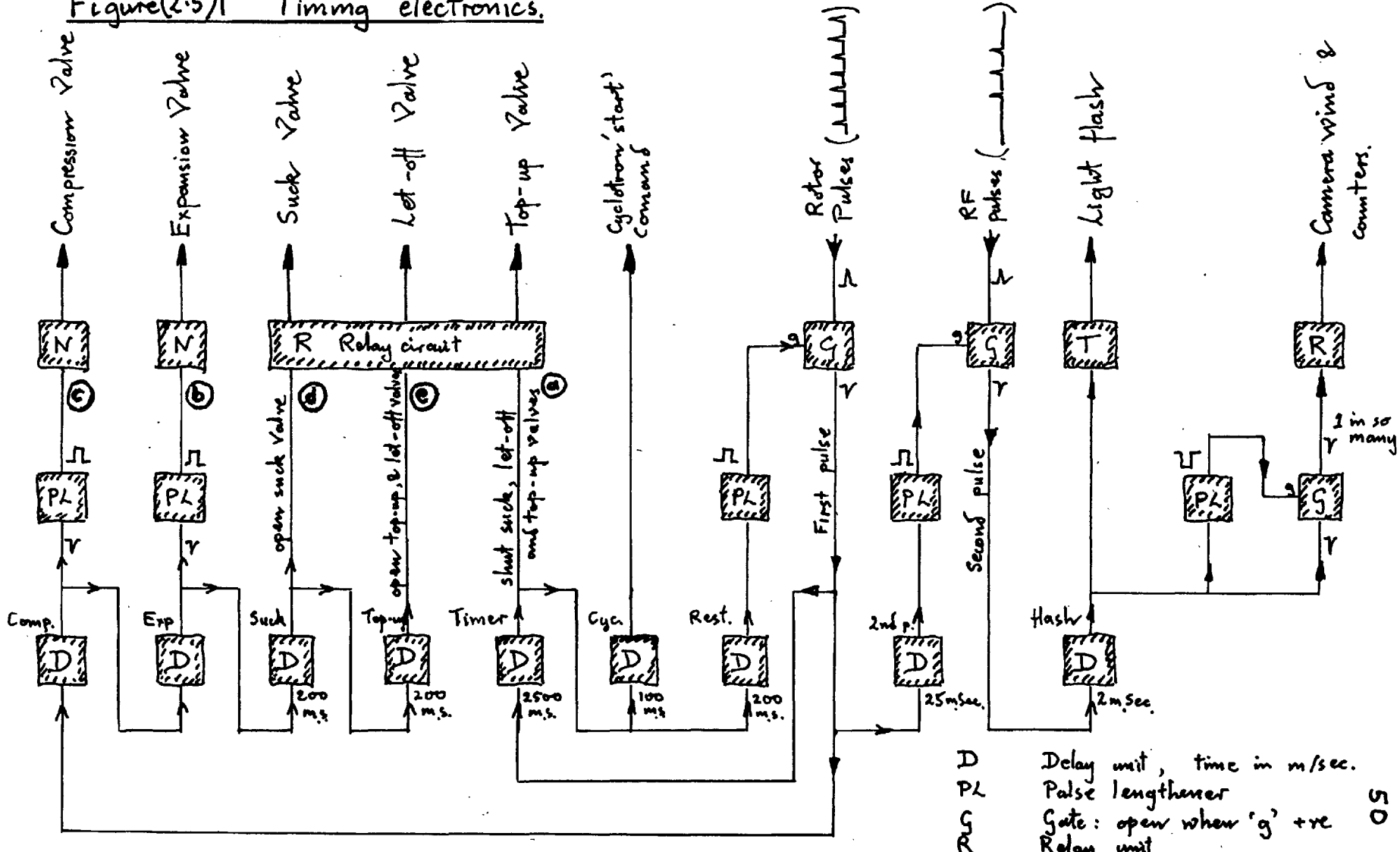

2.6 INSTRUMENTATION

2.6.1 General

Those instruments directly measuring the chamber operating conditions will first be described, and then other instruments with more general uses will be mentioned.

2.6.2 Temperature

The chamber's sensitivity depends on the temperature and pressure of the liquid. Only the initial temperature was measured, and this was done by a hydrogen vapour pressure thermometer, placed inside the chamber on a movable probe. With this, both the actual temperature and its vertical gradient (less than 0.01°K per cm.) could be measured. A large gradient (0.2°K per cm.) had previously produced non-uniform sensitivity, and had to be investigated and overcome.

2.6.3 Pressure Indicator

The initial pressure of gas in the chamber could be read on an ordinary, but well calibrated, Budenberg gauge. In order to know the operating conditions during a cycle, the variations in the pressure with time had to be determined.

These variations in pressure were observed by the variations of resistance in a constantan strain gauge wound round the chamber. The resistance was balanced on a bridge and the difference voltage amplified. This relative change in resistance was so small ($3 \cdot 10^{-5}$) that a DC amplifier was not stable enough to be used.

An A C (500 k/c) bridge was therefore designed, with a wide band amplifier, detector, and final DC amplifier. A block diagram is given in figure (2.6)2 and its circuit in appendix B6. A typical output from it, photographed from an oscilloscope, has been shown in figure (2.4)4. It was not found possible to give an absolute calibration of indicated pressure, because of a drift of sensitivity with both chamber temperature and time. Its linearity, and speed of response, were however, good and it served its main purpose of indicating when the pressure was at a minimum and the chamber at its most sensitive.

2.6.4 Piston Position Indicator

Knowledge of temperature and pressure are all that are needed to monitor the chamber operating conditions. In order to gain knowledge of how the mechanism was working it was desirable to know the motion and timing of the expansion mechanism as well. The position

of the piston was, therefore, indicated with the aid of a lamp and photo-cell. The arrangement is illustrated in figure (2.6)1, and an output has been shown in figure (2.4)4.

2.6.5 Beam monitor

The pressure indicator, described above, gave an indication of the short period over which the chamber was sensitive. The cycle had to be operated so that this period coincided with the beam of particles from the accelerator. It was clearly desirable to have an indication of the exact moment, and incidentally of the strength, of this beam. Such indication was provided by a large scintillation counter of conventional type, that was built by Dr. Tollini. It will not, therefore, be further described. Its output has also been shown on figure (2.4)4.

2.6.6 Mixer

In order to help in the timing of the sequence of events that made up a cycle, a mixer and pulse lengthener was designed (see appendix B7). Pulses from any part of the sequence could be fed into this unit, mixed with the output from the pressure monitor and then viewed on a

Figure (2.6)1

Piston position Indicator

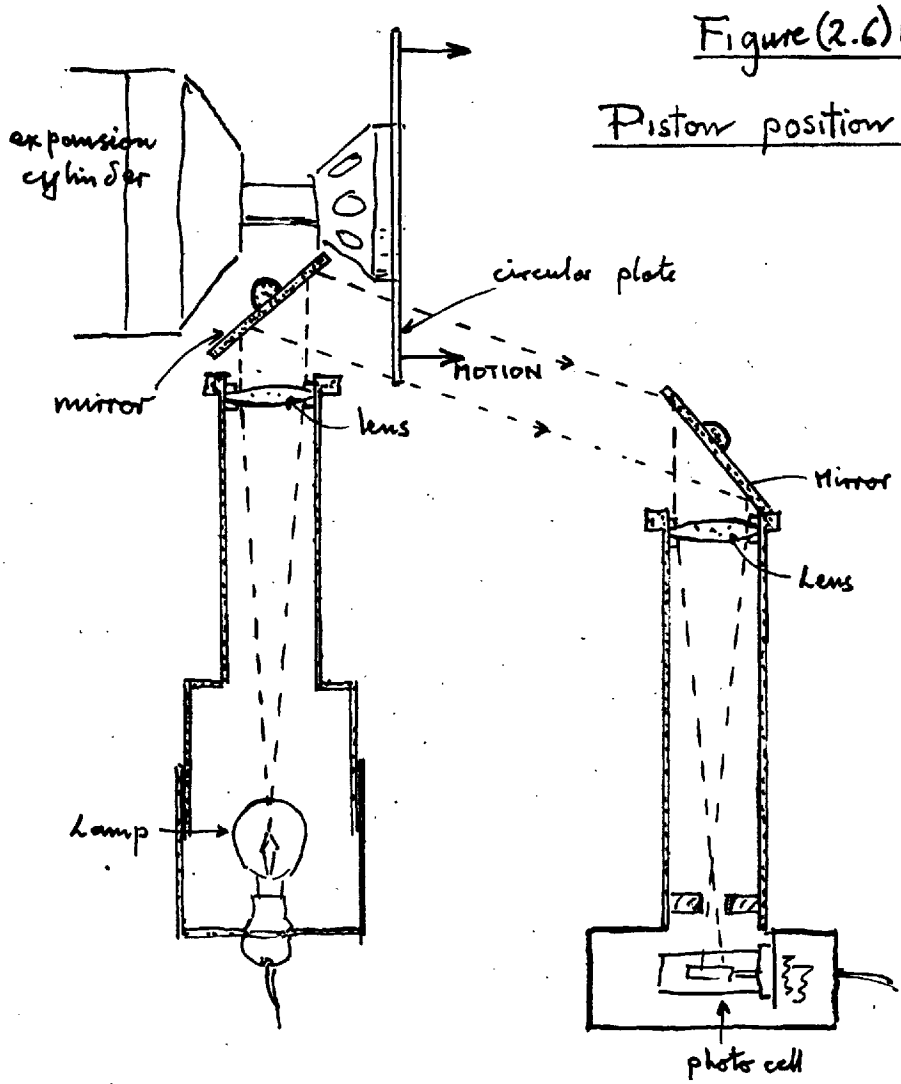

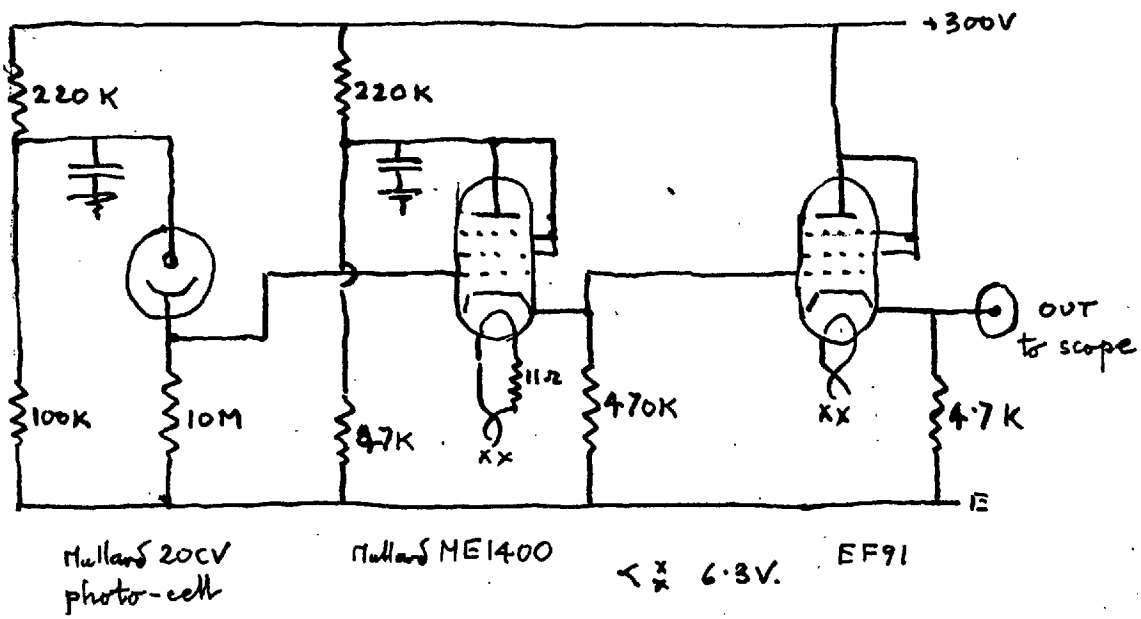

double beam oscilloscope. On the pressure trace of figure (2.4)4 two output pulses from the mixer, representing the time of the beam and flash, can be seen. A block diagram of the instruments referred to is shown in figure (2.6)2.

2.6.7 Depth gauges

In order to be able, remotely, to re-fill the liquid hydrogen and nitrogen tanks in the vacuum case, some form of depth gauge was required. A liquid sensitive element, operating by its measurement of thermal conductivity, was therefore developed. The element consisted of a small five ohm constantan heater coil in which half a watt was dissipated. The temperature this reached depended on whether it was in or out of the liquid, and was measured by a five ohm copper resistance thermometer, consisting of a coil wound over the heater. The complete element was placed inside a 'bucket', in order to shield it from draughts. An arrangement of two elements is shown in figure (2.6)3. A circuit was devised such that when the liquid level in a tank fell below the lower depth gauge then the tank was filled until the level reached the upper gauge. Another element indicated when the supply dewar was empty and should be changed. The circuit used is given in appendix B8.

Figure (2·6)2 Monitoring electronics

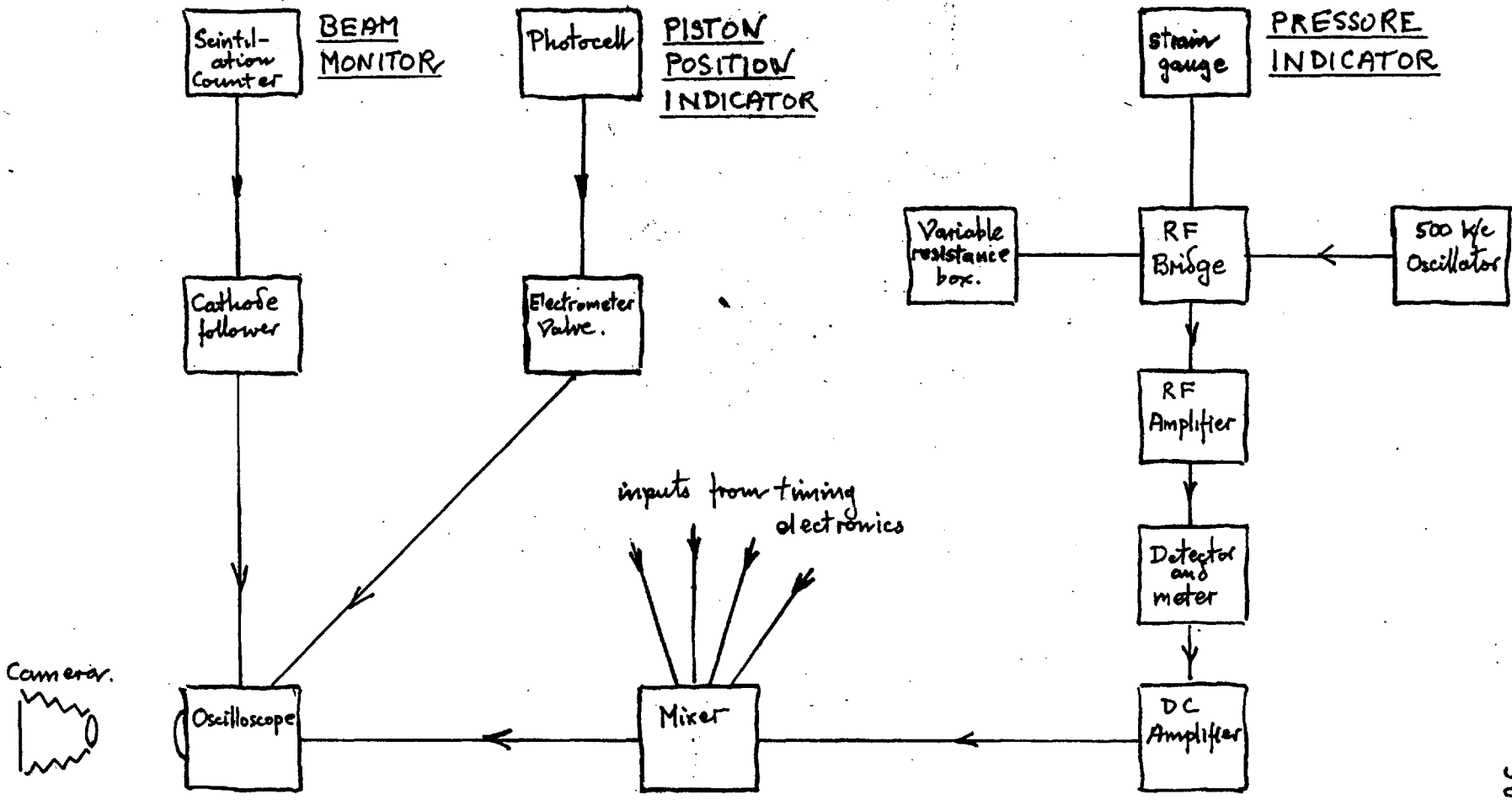

Fig. (2.6)33 Depth Gauge

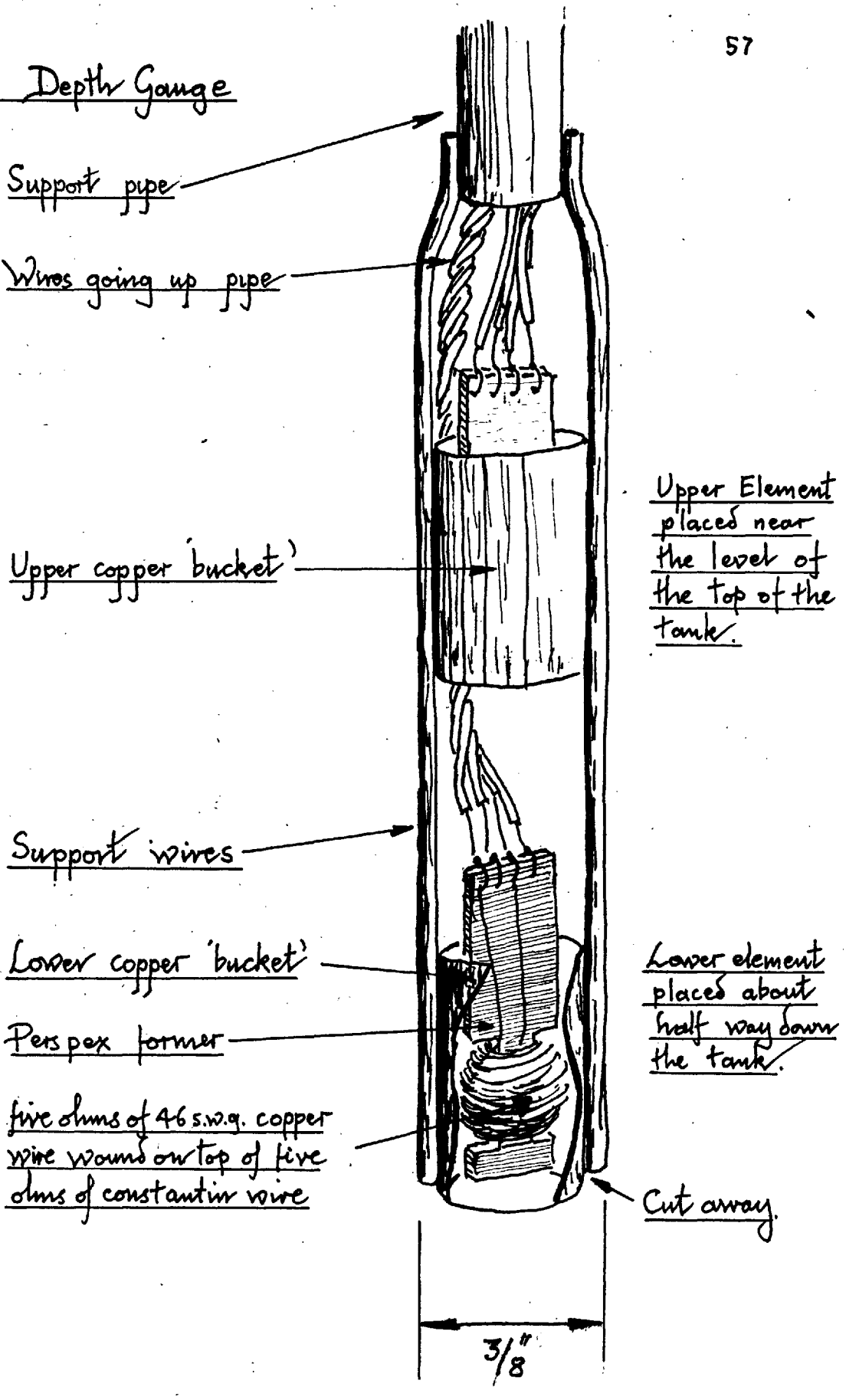

The electronic units associated with these instruments were all mounted at the control station. A few instruments such as vacuum gauges and a gas meter to measure hydrogen boil off were also mounted at the control station, plus the safety interlocks which will be mentioned in the next, and last section of this chapter.

2.7 SAFETY

Hydrogen mixed with air in proportions ranging from 4% to 80% is highly explosive. The fear is always that for some reason the liquid hydrogen will be suddenly heated and give off large quantities of gas, possibly at a high pressure.

The possibility of the chamber windows breaking and liquid hydrogen pouring out on to the warm vacuum case must be considered. A three inch diameter pipe, initially filled with nitrogen, was provided to take the resultant hydrogen gas from the vacuum tank to a gas flame. The burner, figure (2.7)1, had to be designed so that the rush of nitrogen gas preceding the hydrogen would not blow the flame out. A system of baffles, illustrated in figure (2.7)2 were employed to avoid this, and they proved effective when the burner was tested. A spark to light the gas flame and a remote indicator to show whether the gas was alight were provided together with a second indicator which was intended to register the breakage of a window. In the event of such a breakage or in the event of a number of other emergencies most of the electrical supplies were automatically turned off. The gas circuit shown in figure (2.4)5 was so designed that the effect of this was to reduce pressure on the chamber and leave everything in a safe condition.

Figure (2.7)1 Safety Burner.

Figure(2.7)2 Safety Burner

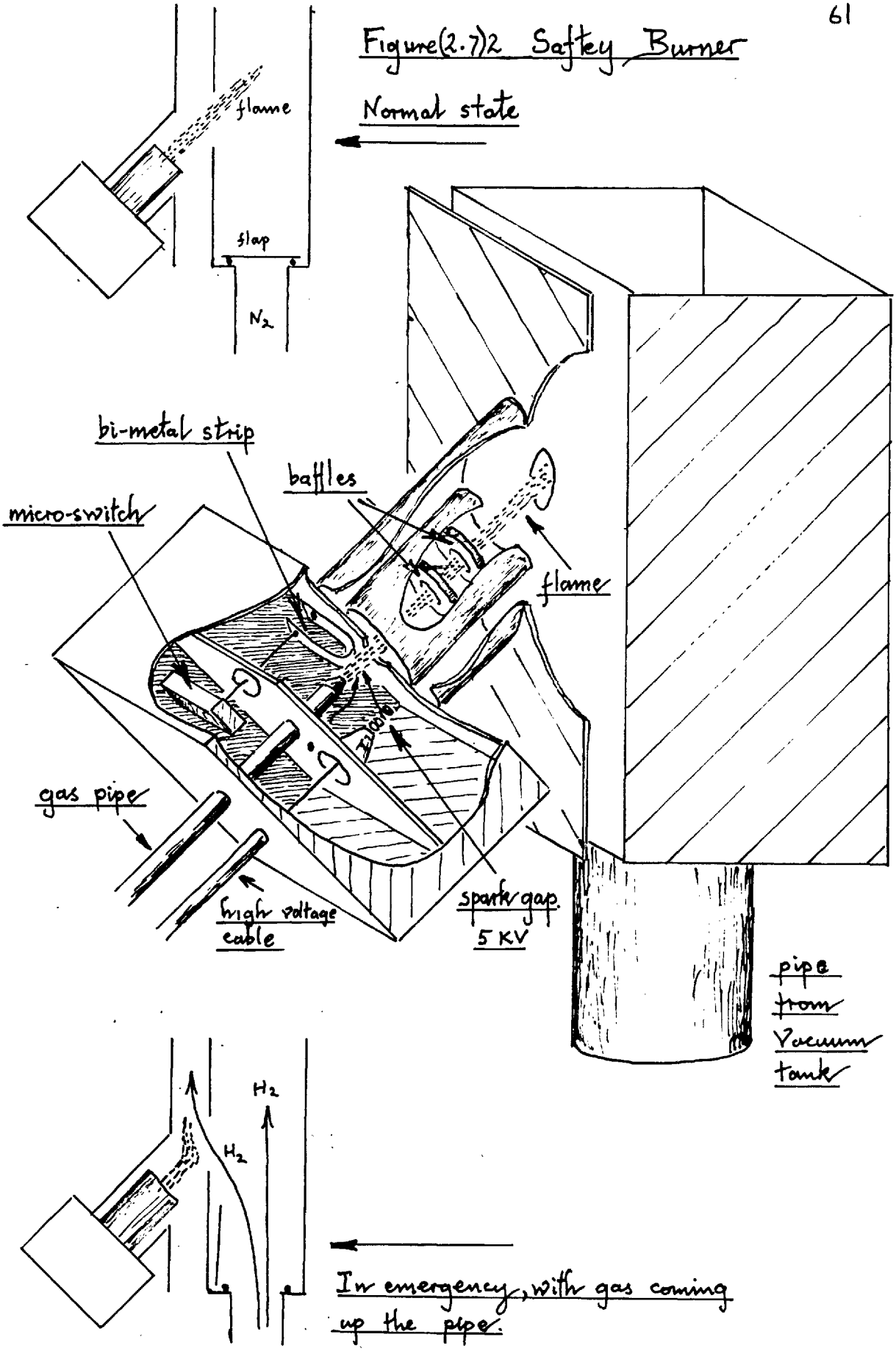

In case hydrogen gas did escape in the neighbourhood of the apparatus, all switches near the vacuum case, together with the electronic flash box were filled with nitrogen gas. The only other, and very general, precaution that was taken was that no one was allowed near the chamber unless absolutely necessary.

CHAPTER 3

CHAMBER PERFORMANCE

3.1 INTRODUCTION

When the chamber first operated in December 1957 a considerable difference of temperature between the top and bottom (2^{o}) resulted in uneven sensitivity. When this problem was solved two new problems arose. Firstly the prototype expansion mechanism was found to be insufficiently reliable to allow long experimental runs; and secondly, when long runs were attempted a mist formed inside and outside the chamber windows which spoilt the photography. By June 1959, the expansion system had been made more reliable and the mists removed by improving the hydrogen purification and the cryostat vacuum.

With the new expansion system it was soon found that the 'dynamic' chamber heating had been much reduced. This improvement was used to speed up the rate at which the chamber could be expanded, from its previous value of 6 cycles per minute to a maximum of 33 cycles per minute.

It was found that the rate of heating depended very considerably on the initial temperatures and pressures used. In the next section some arguments will be given as to why this may be so.

3.2 CHOICE OF OPERATING CONDITIONS

The object of this section is to consider what operating conditions might be expected to produce the minimum boiling, and thus minimum dynamic heating, of the chamber (see section 1.3.1.).

On graph (3.2)1 are shown the states of temperature and pressure at which various bubble chambers have been successfully operated.

Above the region of sensitivity the degree of superheat is presumably not sufficient to produce tracks. It is not possible to work below the region due to spontaneous boiling of the liquid. No bubble chamber has been successfully operated below 26° Kelvin and it is concluded that at lower temperatures spontaneous boiling occurs before sufficient superheat has been achieved to produce tracks. Conjectured lines bounding the sensitive region have been drawn in on graph (3.2)1. The lower line will be referred to as the 'spontaneous boiling line'. For convenience, the graph is repeated without the individual points in figure (3.2)2.

It is well known that a superheated liquid, even if above the 'spontaneous boiling line' will start boiling on rough surfaces. It might be expected, however, that such boiling would be less, the further the state of the liquid was from this line. Referring now to figure (3.2)2;

Fig (3.2)1. Regions of operation

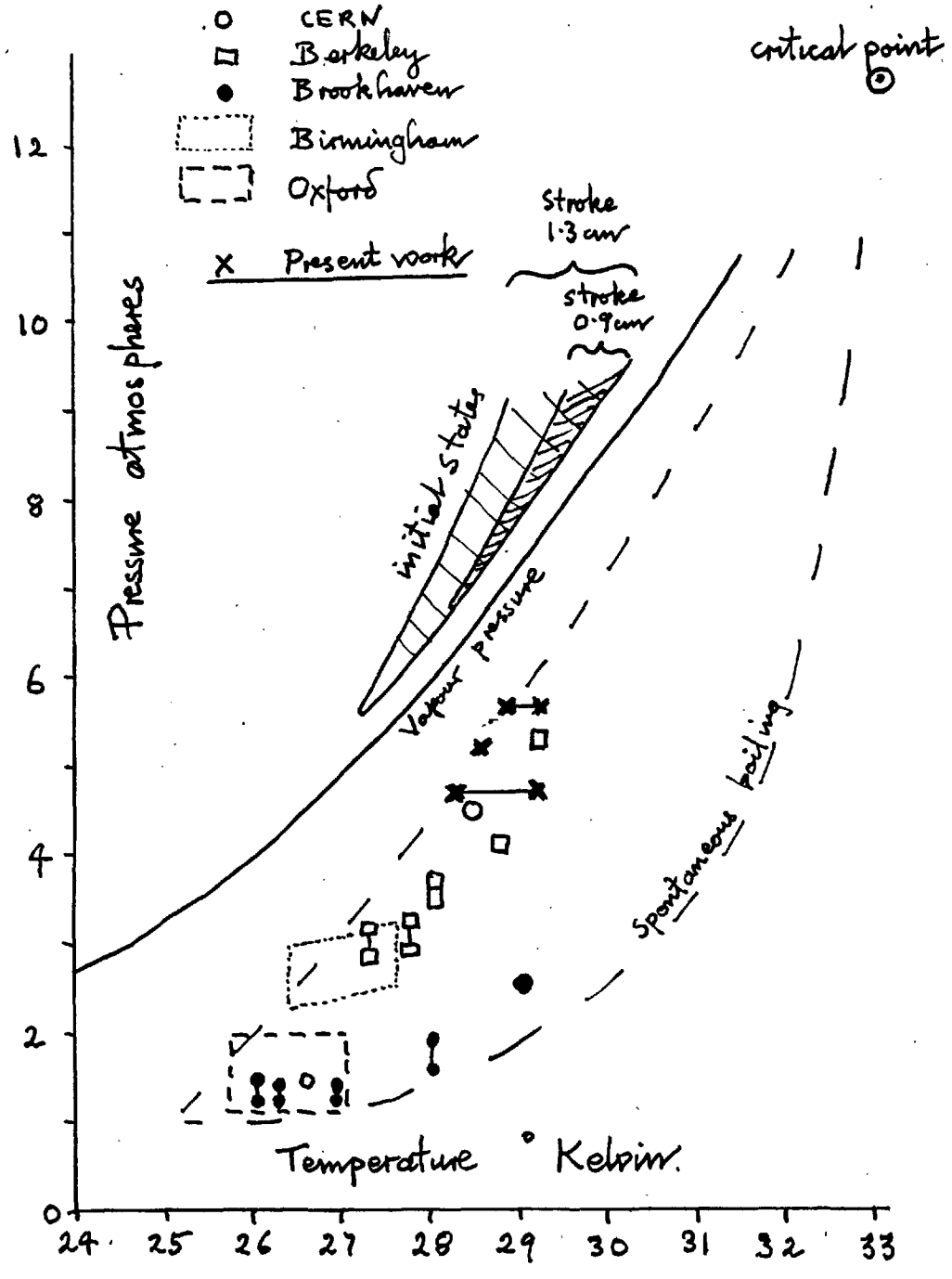

Figure (3.2)2 Sensitive Region

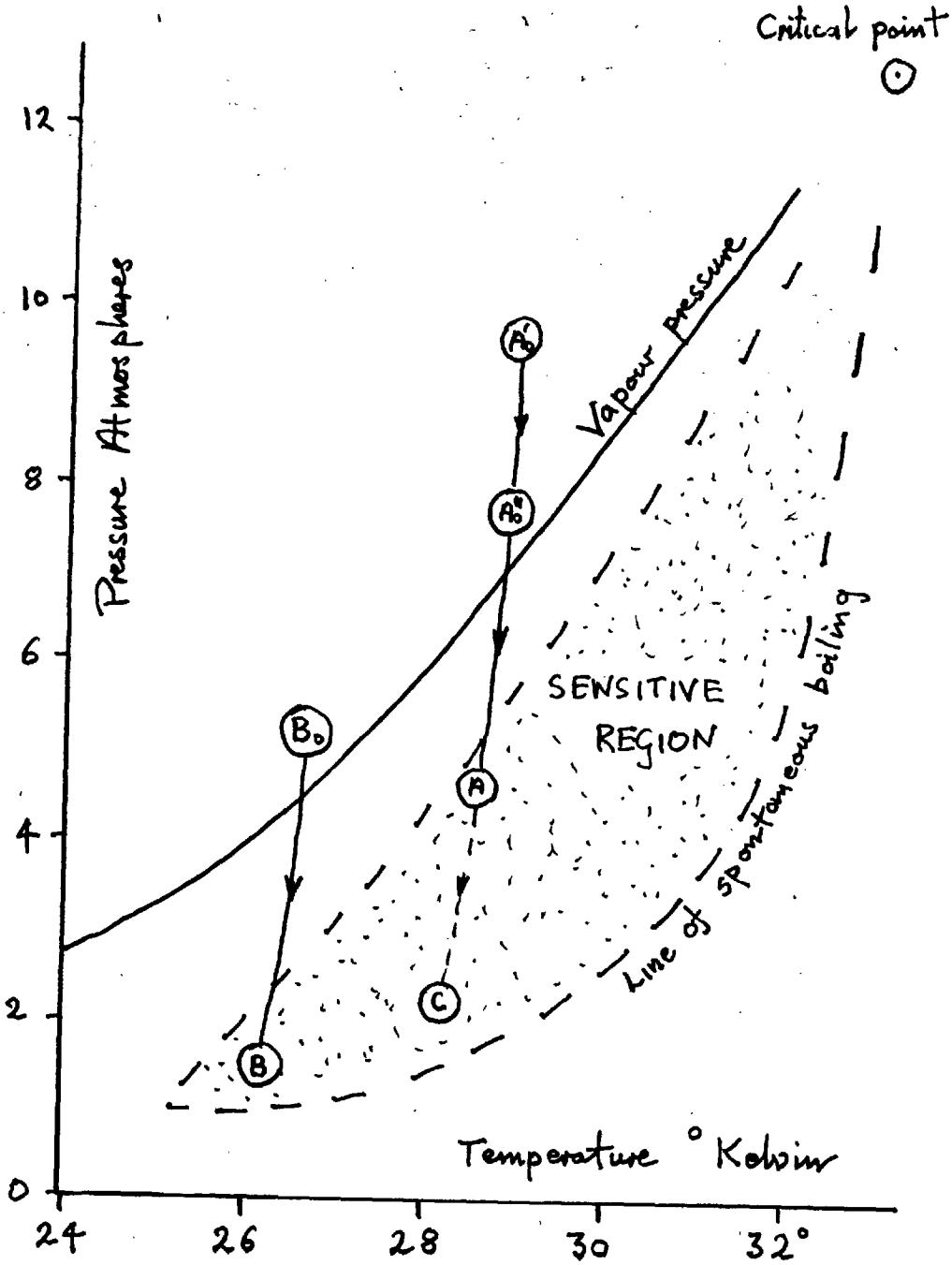

if the above is true then less boiling would be expected in the state marked A than B, although both are in the sensitive region. Similarly less boiling would occur at A than C. Now the best operating conditions from the point of view of heating are those where there is least boiling. Providing then, that satisfactory tracks are obtained, the best condition is one represented by a point near the top of the sensitive region, with the temperature at a value about half way (29.4° K) between the minimum (at 25.5° K) and the critical point at (33.3° K). This temperature of 29.4° K is high by comparison with those that have so far been used (see figure (3.2)1).

A place in which the liquid in a chamber is particularly likely to boil is at the liquid surface. The liquid here, will be near equilibrium with the gas above it and thus its temperature will be near that of the boiling point of the liquid at the applied initial pressure. If the initial pressure is higher than the vapour pressure at the chamber temperature, then the liquid at the surface will be hotter than that in the chamber, and consequently more likely to boil when the pressure is dropped. It is thus better to have an initial pressure not much higher than the chamber vapour pressure. Referring again to figure (3.2)2, this implies

having an initial state near to the vapour pressure line: (initial state A'_o is better than A''_o).

Writing the above conclusions in a different form; for the minimum of general boiling, and thus heating:

a) a high initial pressure should be used;

b) the temperature should be such that the liquid, initially, is as near boiling as possible.

c) the minimum drop of pressure that will produce satisfactory tracks should be employed.

In the next section the observed characteristics of the chamber operation will be described.

3.3 CHAMBER PERFORMANCE

3.3.1 Operating Conditions

Tracks were successfully obtained using initial pressures between 5.7 and 8.4 atmospheres (70 - 110 p.s.i.g.). The regions of initial temperature and pressure over which tracks were observed, with piston stroke lengths of 0.9 and 1.3 cms., have been indicated on graph (3.2)1. The maximum expanded pressures for which tracks were obtained at three different temperatures were also plotted on the same graph. These expanded pressures were obtained from the output of the pressure indicator which was calibrated by a method described below.

In support of the arguments given in the last section, it was found that less heating of the chamber was obtained using higher initial pressures, and using chamber temperatures near to the boiling point. For instance, with an initial pressure of 7.7 atmospheres (100 p.s.i.g.), the heating could be reduced to about $^1/_3$ of the minimum attainable using a pressure of 6.3 atmospheres (80 p.s.i.g.). At any initial pressure, the maximum temperature that could be used was 0.3° below the boiling point at that pressure.

The highest pressure for which the chamber was designed was 7.7 atmospheres, and this pressure was

normally used. The temperature was maintained in region just below the boiling point (29.1° → 29.6° K). Oscilloscope traces of pressure and piston position for three different stroke lengths under these conditions are given in figure (3.3)1.

3.3.2 Calibration of Pressure

Unfortunately it was not possible to calibrate the pressure indicator by any direct method. The scale on the pressure trace in figure (3.3)1 was added on the basis of an argument that will follow. The piston monitor was calibrated by a series of static measurements, which gave the scale on figure (3.3)1 with an estimated accuracy of 10%. The time scale is accurate to 5%. If no boiling occurred in the chamber then the pressure drop could be calculated from the piston stroke and dimensions of the system, and thus the pressure indicator could be calibrated. It is seen from the pressure traces, however, that the final pressure is higher than the initial pressure. This indicates that there must, in fact, have been some boiling during the cycle. The compression is seen to be more rapid than the expansion, so it may be hoped, therefore, that a negligible part of this boiling occurred during the compression. The pressure indicator can then be provisionally cali-

Figure (3·3)1 Typical Cycles with initial pressure 7·7 At, temp 29·4 °K.

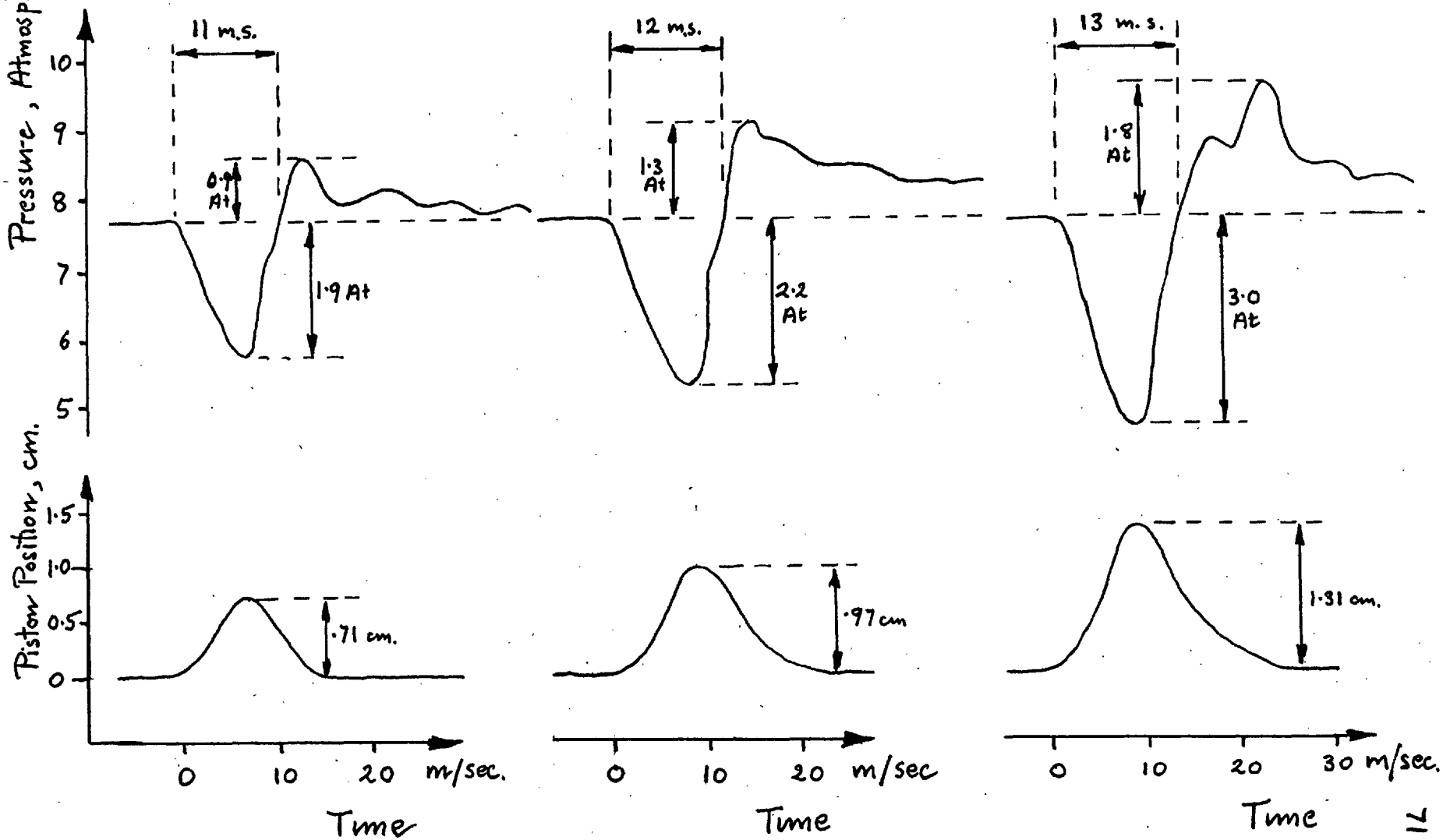

brated by relating the total rise of pressure on re-compression with the piston stroke. If the calibration is valid, it should be the same when derived from different stroke lengths. On graph (3.3)2 it is plotted for the three lengths considered and seen to be substantially constant. On this basis the pressure scale in figure (3.3)1 was marked.

The pressure drop, calibrated by the above method is plotted against stroke length on graph (3.3)3, together with the results from the prototype expansion system. As would be expected, the pressure drop is proportional to the stroke for short strokes where no boiling occurs, it then rises less steeply and eventually reaches a maximum. When this maximum is reached further piston motion is compensated for by more boiling. It appears from the graph, that due to the higher velocity of the piston in the new system, larger pressure drops may be obtained than was formerly possible.

3.3.3 Chamber heating

On graph (3.3)4 is plotted the measured heat given to the chamber per expansion, due to its being expanded. With a stroke of 0.7 cm, there was a dynamic hydrogen boil-off of 1.2 litres per hour when the chamber was being cycled 33 times a minute. This can be com-

Figure(3.3)2 Variation of pressure calibration

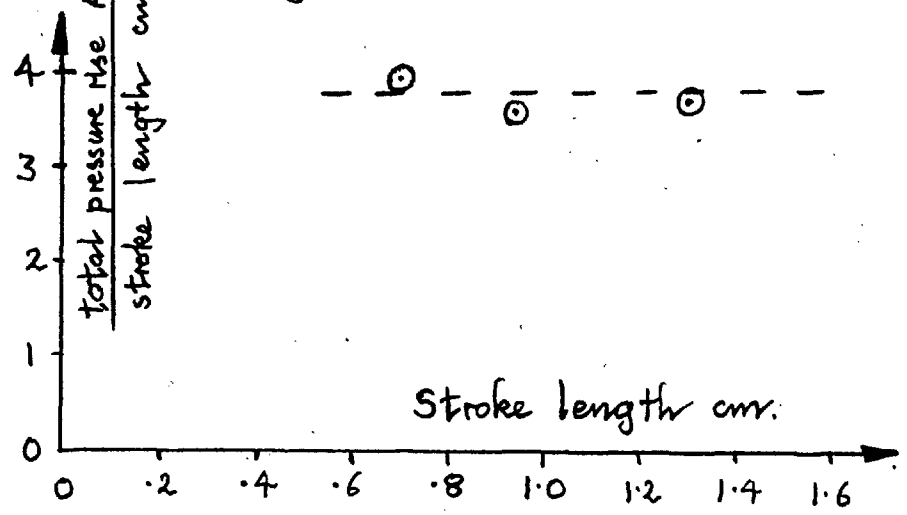

Figure(3.3)3 Pressure drop due to expansion

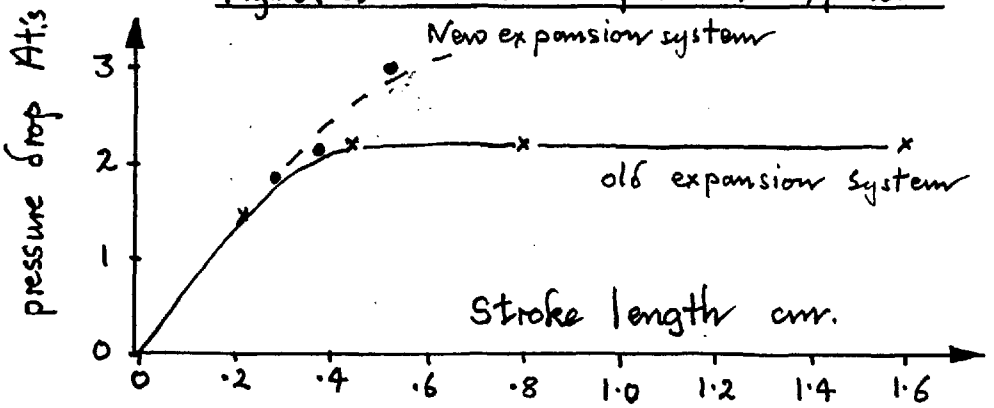

Figure(3.3)4 Dynamic heating

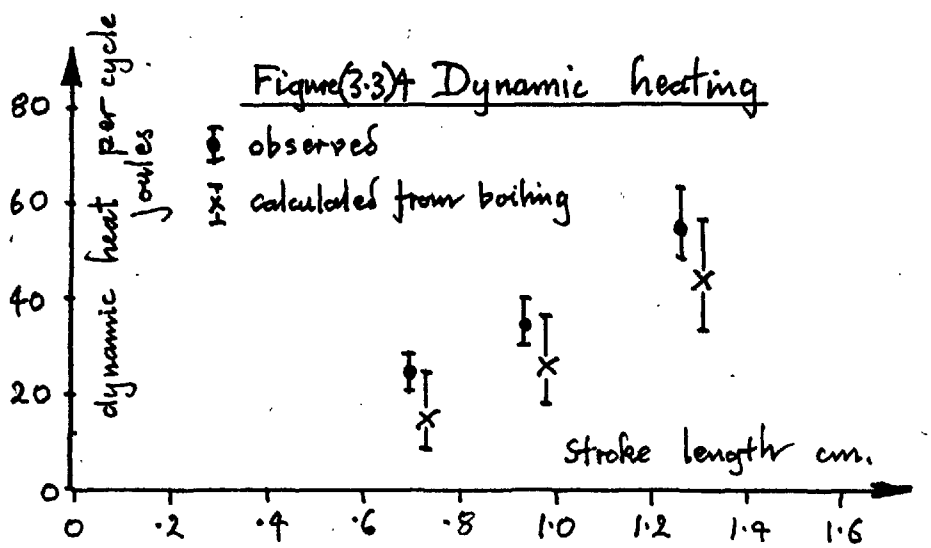

pared with that obtained with the prototype expansion system of 1.5 litres per hour with a rate of only 6 expansions per minute. Using so short a stroke the temperature had to be held within the rather close limits of about 0.3° K. A slightly longer stroke of 0.9 cm. was therefore used, with which satisfactory tracks were obtained over the wider range of about 0.6° K. The same dynamic boil-off of 1.2 litres per hour was then obtained with 20 expansions per minute. In order to obtain the total consumption of liquid hydrogen, the static boil-off of 0.5 litres per hour and the losses in transferring, about 25%, must be added. The total consumption was about 2.1 litres per hour.

In section 1.3.1 it was argued that the heat given to the chamber can be due either to warm gas being carried down the expansion pipe during compression, or due to work done on the fluids. As has been already noted, there is an overshoot of pressure at the end of a cycle due to the volume (v') of gas boiled from the hydrogen during the cycle. From the height of this overshoot the volume v' of gas that had been produced can be calculated. In appendix A it is shown that such boiling should result in an amount of work W being done on the chamber, each cycle; where

$$W = U' \frac{\Delta P}{\gamma}$$

Δp is the change of pressure on compression and γ the ratio of specific heats. W has been calculated and plotted on graph (3.3)4 together with the measured heating. The difference between total heating and W should give the heating due to warm gas carried down the pipe. As a result of the large errors in the measurements it is only possible to say that this heating due to gas carried down the pipe is not more than half of the total heating.

3.3.4 Conclusion

Although the chamber was originally designed as a prototype it was successfully developed for use in a serious experiment. In part II of this thesis an experiment that has, in fact, been performed with the chamber will be described.

In this chapter it has been shown that variation of the operating conditions have a very large effect on the resultant heating of the chamber. Evidence and a theoretical argument have suggested that minimum heating is obtained by using a temperature rather higher than has

normally been used in hydrogen bubble chambers. Using the reasonably high temperature of about 29° K good tracks have been obtained with a heating of only 24 joules per cycle. Such heating in a chamber of 570 cc. volume is surprisingly low and enabled the chamber to be operated at the high rate of 33 cycles per minute.

PART II

THE STUDY OF NEUTRON-PROTON INTERACTIONS

CHAPTER 1.

INTRODUCTION AND THEORY.

1.1 INTRODUCTION.

The main aim of the experiment, to be described, was to observe radiative neutron-capture ($n + p \rightarrow d + \gamma$) at a medium neutron laboratory energy of about 50 MeV, and determine the total cross section of the reaction. The reaction was produced by bombarding protons of the liquid hydrogen in the bubble chamber, with a neutron beam of 50 MeV. The reaction was observed by the track of the emitted deuteron in the chamber. The neutron beam was obtained by bombarding a target with protons from the Harwell cyclotron.

The neutron-capture reaction had, previously, only been observed at very low, thermal, neutron energies of the order of 0·025 eV. By the theory of detailed balance, however, the reaction cross section at medium energies may be predicted from measurements made on the reverse process of deuteron photo-disintegration ($\gamma + d \rightarrow n + p$). The observation, and determination of the the cross section, of neutron-capture at medium energies can, therefore, be used to check the theory of detailed balance. This theory will be outlined in section (1.3).

Besides being a check on the theory of detailed balance, the observation of the neutron-capture reaction has a particular significance in the more general investigation of the two neucleon interaction. Its observation is a first step towards an experiment that may be of considerable importance in this investigation. In order to show this, the next section will be devoted to a short description of the state of theory and experiments on the two nucleon interaction.

Following the section on the two nucleon interaction, will be given an outline of detailed balance, that has already been referred to. A few points will then be made on the theory of the neutron-capture reaction followed by a section in which the kinematics of the reaction are calculated. The kinematic properties of the reaction calculated in this section will be used in later chapters when the appearance and identification of the capture events are discussed.

The reasons for choosing this experiment, and the choice of beam and energy will be left to the next chapter.

The symbols n and p will be used to signify neutron and proton respectively. When the energy of a reaction is referred to it will be the laboratory kinetic energy of the bombarding particle unless stated otherwise.

1.2 TWO NUCLEON INTERACTIONS.

In this section a brief outline of the present state of the theory of the two nucleon interaction will be given. The object is to give the reason for particular interest in observing the neutron-capture reaction, even if the accuracy, and immediate theoretical interest in the total cross section obtained, is small. A slightly more detailed account of the theory of neutron-capture itself will be left till section 1.4.

Yukawa suggested in 1935 that the interaction between any two nucleons was due to the exchange of particles with mass about 300 electron masses. Later the pion (π meson) was discovered with a suitable mass and the required strong muclear interaction. Since that time it has been generally believed that nuclear interactions are due to the exchange of these π mesons, with perhaps some slight effects from the exchange of other more massive mesons at very short ranges.

When the two nucleons are sufficiently far apart the probability of more than one pion being exchanged at a time is small. The effect of such a single pion exchange on the interaction can then be calculated, and applied to predict certain parts, or aspects, of the two nucleon interaction. For instance, Chew has predicted that certain n-p and p-p differential scattering cross sections, if extrapolated to small imaginary

negative angles should give the corresponding π-nucleon coupling constants (Chew, U.C.R.L. Report number 8283). If a phenomenological model of a two mucleon interaction is constructed then pion theory can be used to predict the long range part of that model.

A simple form of phenomenological model of a two nucleon interaction is that of a potential that may be dependent on the distance between the two nucleons ($\underline{r}$), their isotopic spins ($\underline{\tau}$), spins ($\underline{\sigma}$), and momentum ($\underline{p}$). It is only possible to construct such a potential from all possible experimental results if certain assumptions are made. If, for instance, the potential is assumed to have rotation, parity, time, and charge invariance and if it is not a function of any power of $\underline{p}$, then it has been shown by Eisenbud and Wigner that the potential must be some linear combination of the following potentials, or the same potentials multiplied by $(\underline{\tau}_1 . \underline{\tau}_2)$:

$$\left.\begin{aligned} V_1 &= V(r) \\ V_2 &= \underline{\sigma}' . \underline{\sigma}^2 \; V(r) \\ V_3 &= \left\{ \frac{3(\underline{\sigma}' . \underline{r})(\underline{\sigma}^2 . \underline{r})}{r^2} - \underline{\sigma}' . \underline{\sigma}^2 \right\} V(r) \\ V_4 &= \frac{1}{2} \; \underline{r} \wedge \underline{p} \; (\underline{\sigma}' + \sigma^2) \; V(r) \end{aligned}\right\} \quad 1.2/1$$

It is naturally simpler to assume that the latter terms V_3 and V_4, in the sum, are negligible, and this was at first assumed. On the basis then of potentials of the form of V_1 and V_2, which are 'central' potentials, it was found possible to give reasonable fits to all scattering data up to 10 MeV. The ground state of the deuteron, the only two nucleon bound state, was predicted to be $^3S_1$ and found to be substantially so. Certain other data, such as that from photo-disintegration ($\gamma + d \rightarrow n + d$), was also fitted up to 10 MeV.

One consequence of assuming the potential to be only central is that there should be no polarization effects in nucleon-nucleon scattering. There is, in fact, found to be negligible polarization at energies below 10 MeV, but at higher energies such as 40 MeV it becomes considerable. To fit this polarization the tensor potential (V_3) has to be included. Radio frequency spectroscopy has shown that the deuteron is not a pure $^3S_1$ state, but has an admixture of about 5% $^3D_1$. To explain this, also, a non-central potential has to be included.

In order to fit nucleon-nucleon scattering data up to 300 MeV it is maintained that both the spin-orbit potential V_4 and the tensor potential V_3, have to be included. Thus, all four of the above possible potentials have to be considered and the functions V(r) chosen, either purely phenomenologically, or with the help of pion theory, to fit the data. The theory of single

pion exchange gives the form of the central and tensor potentials for large (r), but leaves the form of the rest of these potentials , and the whole of the spin-orbit potential, to phenomenological choice. Since there are eight potentials, it is not easy to guess forms of them that will fit the data. Some help is provided, however, by first obtaining a phase shift analysis of nucleon-nucleon scattering, and then observing what particular characteristics of the potential are needed to obtain certain of the phase shifts.

A phase shift analysis consists, in principle, of giving the amplitudes of all the quantised waves scattered from one nucleon by a plane wave representing the other nucleon. Each phase shift represents the amplitude of one particular state of the outgoing wave. Only when the results of a sufficient number of experiments at a given energy, are available, is it possible to perform a phase shift analysis at that energy. These experiments may not only include scattering, but can also include photo-disintegration, electron-deuteron scattering, and the reaction ($p + n \rightarrow \pi + d$).

As a result of the considerations outlined above, two sets of potentials have been derived, both of which give reasonable fits to all known data. That of Gammel and Thaler (GT) is entirely phenomenological, while that of Signell and Marshak (SM) is partly based on pion theory. They are similar,

but not identical, both in form and in their predictions of certain unmeasured data. In particular, their predictions differ as to the results of the following experiments:

(a) Certain 'triple scattering' experiments; in which the polarization of a particle scattered from a beam, already polarized by a first scattering, is determined by the assymetry in a third scattering.

(b) An experiment to determine the polarization of photo-disintegration ($\gamma + d \rightarrow n + p$) or its converse ($n + p \rightarrow \gamma + d$). The cross sections and polarization of these two reactions are related by the theory of detailed balance (see section 1.3).

The results of these experiments are 'sensitive' to the details of the nuclear interaction and are of particular interest. Of the two experiments mentioned above only the former is being performed at present. The possibilities of performing the latter, are, therefore, of importance.

To measure the polarization of photo-disintegration, either a polarized photon beam, or nuclear aligned deuterium is required. Neither of these is at present available. The neutron-capture process ($n + p \rightarrow \gamma + d$) has not previously been observed at all at medium energies. This is because its total cross section is small compared with n-p scattering ($n + p \rightarrow n + p$): (1/10,000). There is, however, no difficulty in obtaining polarized neutron beams; and if the reaction can

be observed, there is no fundamental reason why its polarization should not be measured. The first step is, clearly, to observe the reaction and attempt to measure its total cross section. It is this first step that has been attempted in the present work. The total cross section measured can be checked against the corresponding photo-disintegration cross section, with the aid of the theory of detailed balance, alternatively the experimental results may be regarded as a check on the validity of the theory. This theory of detailed balance will be outlined in the next section.

1.3 DETAILED BALANCE.

One of the objects of the experiment was to measure the total neutron-capture cross section at a medium energy of about 50 MeV. If the validity of the theory of detailed balance is assumed, then this cross section may be calculated from the total photo-disintegration cross section at a corresponding energy. Photo-disintegration cross sections have been measured in the appropriate energy range by a number of workers (see section 1.5). The capture cross section at 50 MeV calculated from their results has a far higher accuracy than that determined from the present experiment. If the theory of detailed balance is assumed, therefore, the present determination cannot be regarded as a useful contribution to knowledge. It can, however, be regarded as a check on the validity, and applicability, of the theory of detailed balance in this case. A brief outline will now be given of this theory.

The theorem of detailed balance is not universally valid. It can, however, be shown to apply in first order perturbation theory, when time reversal is assumed. The condition that first order perturbation theory should be applicable is that the interaction be 'weak'. Since neutron-capture is fundamentally an electromagnetic interaction and the coupling constant between radiation and matter is weak, the use of perturbation theory is justified. For simplicity it will be assumed that the

interaction takes place in a fixed volume U with infinite potential boundaries. The result will be independent of this volume which can be allowed to go to the limit $U \to \infty$, thus approximating free space. Consider, that in the box there are either two particles A' and B' travelling with equal and opposite momenta but not interacting, or two different particles A" and B", also not interacting. Let a stationary 'plane wave' state representing particles A' and B' be $|\alpha'\rangle$ and those representing A" and B" be $|\alpha''\rangle$, and let both of these states be eigenslates of the same free particle Hamiltonion E. Thus

$$E|\alpha'\rangle = E'|\alpha'\rangle \quad , \qquad E|\alpha''\rangle = E''|\alpha''\rangle \quad . \qquad 1.3/1$$

In order to calculate the approximate probability of a transition between states $|\alpha'\rangle$ and $|\alpha''\rangle$, an interaction between particles A' and B' is considered which introduces a small interaction Hamiltonion, V. Let the initial state at t = 0, under the Hamiltonion H = (E + V) be $|\alpha'\rangle$. Due to V this will not be a stationary state. Let the state at time t be

$$|\alpha(t)\rangle = T(t)|\alpha'\rangle$$

then T must satisfy the equation

$$i\hbar \frac{\partial T}{\partial t} = (E+V)\,T \quad . \qquad 1.3/2$$

The probability of the system being the state $|\alpha''\rangle$ at time t will be

$$P(t)(\alpha'\alpha'') = |\langle\alpha''|T(t)|\alpha'\rangle|^2 \quad . \qquad 1.3/3$$

If $V \ll E$, then equation (2) can be solved approximately to give (Dirac 4th ed. p. 174)

$$P(t)(\alpha'\alpha'') = \frac{1}{\hbar^2}\left|\int_0^t \langle\alpha''|\forall(t')|\alpha'\rangle\, dt'\right|^2 \qquad 1.3/4$$

where $\forall(t') = \exp\left(\frac{iEt'}{\hbar}\right) V \exp\left(\frac{-iEt'}{\hbar}\right)$

Further, if V is independent of time (Dirac p. 178)

$$P(t)(\alpha'\alpha') = \frac{2t^2}{\hbar^2}|\langle\alpha''|V|\alpha'\rangle|^2\left(\frac{1-\cos x}{x^2}\right) \qquad 1.3/5$$

where $x = \dfrac{(E'' - E')t}{h}$.

Consider now the probability, $P(\alpha', \Sigma\alpha''(E'',\theta))\delta\Omega$, of the transition into all possible states $|\alpha''(E'',\theta)\rangle$ that give particle A'' in solid angle $\delta\Omega$. Where the number of such states in the energy angle, interval $\delta E\,\delta\Omega$ is $\rho(E,\theta)\delta E\,\delta\Omega$, and θ is the centre of mass angle between one particle of state $|\alpha'\rangle$ and one of state $|\alpha''\rangle$.

Due to the term $\dfrac{1-\cos x}{x^2}$ in equation 1.3/5 the probability will be small for all transitions but those with E'' $\doteq$ E'. If the matrix element $\langle\alpha''(E'',\theta)|V|\alpha'\rangle$ does not vary too

rapidly with E", for fixed θ; and if the volume U, and thus the number of states, is large, then

$$P(\alpha', \Sigma\alpha''(E'',\theta))\,\delta\Omega \doteq 2\left|\langle\alpha''(E',\theta)|V|\alpha'\rangle\right|^2 \rho(E'',\theta)\,\delta\Omega \int_{E''=0}^{E''=\infty} \frac{t^2}{\hbar^2}\left(\frac{1-\cos x}{x^2}\right) dE'' \qquad 1.3/6$$

$$= 2\left|\langle\alpha''(E',\theta)|V|\alpha'\rangle\right|^2 \rho(E'',\theta)\,\delta\Omega\,\frac{t}{\hbar}\int_0^{\infty} \frac{1-\cos x}{x^2}\,dx$$

The integral is known to have the value π. It is seen that the probability of a transition is proportional to t. Thus the probability of a transition per unit time, per unit solid angle, is:

$$\omega(\alpha', \Sigma\alpha''(E',\theta)) = \frac{2\pi}{\hbar}\left|\langle\alpha''(\theta)|V|\alpha'\rangle\right|^2 \rho(E'',\theta) \qquad 1.3/7$$

Consider now $\rho(E'', \theta)$ the density of states per unit energy interval dE" and solid angle $\delta\Omega$. E" is the total energy of the state $|\alpha''\rangle$ and thus the sum of the energies of A" and B". Since the initial state was defined to represent particles with equal and opposite momenta (centre of mass system), the final state will also represent pasticles A" and B" with equal and opposite momenta. Thus the state of one final particle (e.g. A") will define the state of the other (B"). The number of momentum states of particle A", $(dn_{A''})$, in a momentum interval $dp_{A''}$ and solid angle $\delta\Omega$, in a volume U, from a consideration of possible stationary waves is given by

$$dn_{A''} = \frac{4\pi\, U\, \delta\Omega}{(2\pi\hbar)^3\, 4\pi}\, p_{A''}^2\, d|p_{A''}| \qquad 1.3/7$$

This number of states is also the number of momentum states of the whole final system. To obtain the total number of final states the number of spin states of each final particle must also be included. Then

$$\rho(E'',\theta) = (2S_{A''}+1)(2S_{B''}+1)\frac{U}{(2\pi\hbar)^3}\, p_{A''}^2\, \frac{d|p_{A''}|}{dE''_{(A''+B'')}}$$

Relativistically:

$$dE''_{(A''+B'')} = v_{A''}\, dp_{A''} + v_{B''}\, dp_{B''}$$
$$= |\underline{v}_{A''} - \underline{v}_{B''}|\, d|p_{A''}|$$

$$\rho(E'',\theta) = (2S_{A''}+1)(2S_{B''}+1)\frac{U}{(2\pi\hbar)^3}\frac{p_{A''}^2}{|\underline{v}_{A''} - \underline{v}_{B''}|} \qquad 1.3/8$$

The differential cross section for the transition $|\alpha'\rangle \rightarrow |\alpha''\rangle$ is defined in terms of the probability of a transition by

$$P(\alpha' \Sigma \alpha''(\theta))\,\delta\Omega = m_{A'} m_{B'}\, U\, v_{A'B'}\, \sigma(\alpha'\alpha''(\theta))\,\delta\Omega \qquad 1.3/9$$

where $m_{A'}$, and $m_{B'}$ are the particle densities in space, U is the volume considered, and $v_{A',B'}$, the relative velocity between the two initial particles. Since the states have been normalized to represent single particles $m_{A'} = m_{B'} = 1/U$, using the equations 1.3/7, 8 and 9

$$\sigma(\alpha'\alpha'';(\theta)) = \frac{2\pi}{\hbar}\frac{1}{(2\pi\hbar)^3}\cdot U^2\left|\langle\alpha''|V|\alpha'\rangle\right|^2$$

$$\cdot(2S_{A''}+1)(2S_{B''}+1)\ \frac{(p_{A''})^2}{|v_{A'}-v_{B''}|\ v_{A'B'}} \qquad 1.3/10$$

If the states $|\alpha'\rangle$ and $|\alpha''\rangle$ had been normalized to give unit density in space of one particle (A') interacting with the single other particle (B') then U^2 will not appear in this equation. The volume U may then be taken to infinity without complication.

Consider now the reverse interaction $\sigma(\alpha''\alpha'(\theta))$. The angle Θ between initial and final states will remain the same.

$$\frac{\sigma(\alpha'\alpha''(\theta))}{\sigma(\alpha''\alpha'(\theta))} = \frac{|\langle\alpha''|V|\alpha'\rangle|^2}{|\langle\alpha'|V|\alpha''\rangle|^2}\frac{(2S_{A''}+1)(2S_{B''}+1)}{(2S_{A'}+1)(2S_{B'}+1)}\frac{(p_{A''})^2}{(p_{A'})^2}\frac{|v_{A'}-v_{B'}|\,v_{A''B''}}{|v_{A''}-v_{B''}|\,v_{A'B'}} \qquad 1.3/11$$

If either particle A' or B' and A'' or B'' are non-relativistic then

$$|v_{A'B'}| = |v_{A'}-v_{B'}|$$

$$|v_{A''B''}| = |v_{A''}-v_{B''}| \qquad 1.3/12$$

If V is real which implies invariance under time reversal then

$$|\langle\alpha''|V|\alpha'\rangle|^2 = |\overline{\langle\alpha'|V|\alpha''\rangle}|^2 = |\langle\alpha'|V|\alpha''\rangle|^2 \qquad 1.3/13$$

Using equations 1.3/11, 12 and 13,

$$\frac{\sigma(\alpha'\alpha''(\theta))}{\sigma(\alpha''\alpha'(\theta))} = \frac{(2S_{A''}+1)(2S_{B''}+1)}{(2S_{A'}+1)(2S_{B'}+1)} \frac{p_{A''}^2}{p_{A'}^2} \qquad 1.3/14$$

This is the required formula for detailed balance. A modification to it is, however, required if any one of the particles A', B', A", B", is a photon. If, for instance, B" is a photon then although its spin is 1 the number of spin states it can take is only 2. Thus instead of $(2S_{B''} + 1)$ must be written 2.

In the particular case of neutron-capture and photo-disintegration

$$n + p \rightleftharpoons d + \gamma$$

$S_n = \frac{1}{2}$, $S_p = \frac{1}{2}$, $S_d = 1$, and equation 1.3/14 becomes, assuming the deuteron to be non-relativistic

$$\frac{\text{cap}\,\sigma(\theta, E_n)}{d_{1S}\sigma(\theta, E_n)} = \frac{3}{2} \frac{p_\gamma^2}{p_n^2} \qquad 1.3/15$$

Where p_γ = photon momentum, p_n = centre of mass momentum of neutron or proton, θ = angle between the same two particles, one before and one after the interaction, both in the centre of mass system.

Invariance under time reversal, the approximations in first order perturbation theory, and the non-relativistic Schrödinger equation have been assumed. The validity of the latter two

assumptions is well confirmed by experiment. Time reversal is also confirmed by experiment, though less precisely.

The validity of this theory of detailed balance will be assumed in the next section, while the theory of neutron-capture is discussed.

1.4 NEUTRON CAPTURE THEORY.

In this section a few points in the theory of radiative transitions will be mentioned. These will be applied to neutron-capture and thus the approximate angular distribution of the emitted photon derived. The present state of the theory and experiments on photo-disintegration will then be given. In this discussion, the results of detailed balance, that link neutron-capture and photo-disintegration, will be assumed. When referring to the energy of either process it will be the laboratory neutron energy which will be implied.

It is convenient to distinguish processes that can emit radiation by the momentum of the photon emitted and the change in parity that accompany its emission.

'Electric multipole radiation' of order (ℓ, m) is then defined to have angular momentum ℓ, component of angular momentum m, and to give a change in parity $(-1)^{\ell}$. It is called 'electric' because its emission probability may be related to changes in the distribution of charge during the process. Magnetic multipole radiation is similarly defined but gives a parity change $-(-1)^{\ell}$. Its emission probability may be related to changes in the distribution of electric currents. Now it may be shown (Blatt and Weisskopf, chapter XII) that other things being equal: (a) transitions involving higher angular momenta (ℓ) have much

smaller probabilities of occurring, and (b) that for the same ℓ, magnetic multipole radiation is less intense than electric multipole radiation. Since there can be no radiation with $\ell = 0$, the most probable radiations are electric and magnetic dipole ($\ell = 1$) radiations.

These brief considerations of multipole radiation can now be applied to the radiation emitted when a neutron and proton pass from an unbound to a bound state. This is the process of neutron-capture ($n + p \rightarrow \gamma + d$).

At sufficiently low energies the initial state must be pure S wave, with parity +1. It is known that the deuteron is also in an S state with parity +1. Thus, the change of parity with emission of the radiation is +1, and the radiation can be electric multipole with angular momentum $\ell = 2$, or magnetic multipole with $\ell = 1$. Since the emission of photons with higher angular momenta are much less probable the radiation is expected to be magnetic dipole ($\ell = 1$).

At higher energies, however, there is sufficient contribution from P initial states, with parity - 1, to allow the stronger electric dipole emission with ($\ell = 1$, parity = -1) to take place. At energies above about 5 MeV this radiation is found to be much stronger than the magnetic dipole radiation, which has, in fact, become negligible. It may be shown that the angular distribution

of this electric dipole radiation is (Blatt and Weisskopf p.610):

$$_{cap}\sigma(\psi,E) \propto \sin^2\psi \qquad 1.4/1$$

where ψ is the angle between the emitted photon and the initial neutron directions.

Since the agreement of theory and experiment is now to be discussed, photo-disintegration rather than neutron-capture, will be considered. As is generally true of nuclear interactions the photo-disintegration cross sections can be fitted with theory assuming a central nucleon potential, for all energies up to about 10 MeV. At higher energies the angular distribution diverges from a pure $\sin^2\psi$ dependence rather faster than is predicted from a consideration of higher order radiation. The angular distributions at energies up to 200 MeV have, however, been fitted reasonably well assuming the SM potential (de Swart and Marshak, 1958. Phys. Rev. 111, 272)

The polarization of neutron-capture is found to be even more sensitive to the nuclear theory used than the differential cross section.

Several widely differing predictions of the polarization were given at the 'University College Conference on the few nucleon problem' held in the summer of 1959.

In the last section of this chapter the kinematics of the neutron-capture process will be calculated.

1.5 NEUTRON CAPTURE KINEMATICS.

1.5.1 General.

As has been stated, the neutron-capture reaction was produced by bombarding protons in the liquid hydrogen of the bubble chamber, with a neutron beam produced from the Harwell cyclotron. The production of the neutron beam will be discussed in section 2.4. Consider the interaction of a single neutron of kinetic energy E_i with a proton in the liquid. Let the direction of the deuteron produced make an angle Θ with initial neutron direction, and the direction of the photon on angle Ψ .

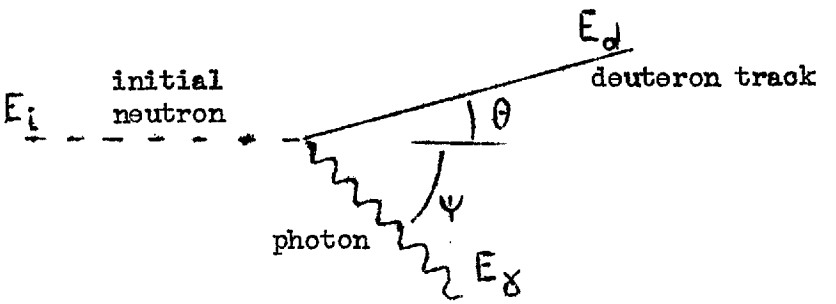

Only the deuteron will leave a track in the chamber; but, if the neutron beam direction is known, the angle Θ may be measured.

First, the relations between the particle energies, angles and track lengths will be calculated. The expected angular distribution of the deuteron tracks will then be derived. Finally the total cross sections for neutron-capture will be calculated from the photo-disintegration cross sections measured

by other workers.

1.5.2 Angle and Energy relations.

In the following calculations the momentum of the proton and neutron in the deuteron will be ignored. This is justified, due to the small deuteron binding energy (B = 2.23 MeV) compared with the laboratory energies considered: (approximately 50 MeV). Relativistic corrections will also be ignored, since the maximum neutron energy used in the experiment were 60 MeV, being 1/15 of the rest energy. In the laboratory system, let:

E_i be the initial neutron kinetic energy,

E_d be the deuteron kinetic energy,

E_γ be the photon energy,

B be the deuteron binding energy,

M_n be the neutron rest energy,

$M_d = 2M_n$, be the deuteron rest energy.

By consideration of energy and momentum:

$$E_i = E_\gamma + E_d + B$$

$$\sqrt{(2M_n E_i)} = \sqrt{(2M_d E_d)} \cos\theta + E_\gamma \cos\Psi \qquad 1.5/1$$

Now $E_d \ll M_d$, $E_\gamma \ll M_d$; and if it is further assumed that $\theta \ll \pi/2$, which will be justified below; then

$$E_\gamma = \frac{E_i}{2} - B \qquad 1.5/2$$

$$E_d = \frac{E_i}{2} \qquad 1.5/3$$

By conservation of momentum:

$$E_\gamma \sin\psi = \sqrt{(2M_d E_d)} \sin\theta$$

$$\theta \leqslant \sin^{-1}\left(\frac{E_\gamma}{(2M_d E_d)^{\frac{1}{2}}}\right) = \hat{\theta}(E_i) \qquad 1.5/4$$

where $\hat{\theta}(E_i)$ is defined by this equation. Then

$$\sin\theta = \sin\psi \cdot \sin\hat{\theta}(E_i) \qquad 1.5/5$$

$$\sin\hat{\theta}(E_i) = \sqrt{\frac{1}{8M_n}\left(E_i - 4B + \frac{4B^2}{E_i}\right)}$$

If $B \ll M_n$

$$\theta(E_i) = \sqrt{\frac{E_i}{8\ M_n}} \qquad 1.5/6$$

In the experiment performed the maximum energy (E_i) was 60 MeV. With M_n = 932 MeV, and using equations 1.5/6 and 1.5/4

$$\theta \leqslant \hat{\theta}(E_i) \leqslant \hat{\theta}(60\ \text{MeV}) = 5{\cdot}4^\circ \qquad 1.5/7$$

The errors due to the approximations in the above calculations are estimated at ± 5%.

The maximum length (or range r_d) of the deuteron in the liquid hydrogen of density 0·058 gm/c.c. may be given by the approximate formula:

$$E_d = 14{\cdot}3\ (r_d)^{{\cdot}548}\ \text{MeV} \pm 1\% \qquad 1.5/8$$

WHERE 1 MeV < E_d < 100 MeV.

For comparison, the range of a proton may be given by:

$$E_p = 10{\cdot}7\ (r_p)^{{\cdot}548}\ \text{MeV} \pm 1\% \qquad 1.5/9$$

where 1 MeV < E_p < 100 MeV. These formulae have been derived

from the data in the 'Berkeley Report No. 2426'.

Thus, given the range of neutron-capture deuteron (r_d) the initial neutron energy (E_i) may be obtained using equations 1.5/8 and 1.5/3.

1.5.3 Angular distribution of deuterons.

The differential cross section for neutron-capture, in terms of the angle ψ has been given above in equation 1.4/1:

$$ {}_{cap}\sigma(\psi, E_i) \propto \sin^2 \psi $$

Therefore

$$ {}_{cap}\sigma(\theta, E_i) \propto \frac{d\psi}{d\theta} \; {}_{cap}\sigma(\psi, E_i) $$

From equation (1.5)5, letting

$$ u = \frac{\sin \theta}{\sin \hat{\theta}(E_i)} = \sin \psi $$

and using $\theta \ll \pi/2$, $\cos \theta \doteq 1$,

$$ {}_{cap}\sigma(\theta, E_i) \propto \frac{u^2}{\sqrt{1 - u^2}} \text{ , approximately.} $$

The number of deuterons in the angle interval $d\theta$ is, therefore

$$ q_d(\theta)\, d\theta \propto \frac{u^3}{\sqrt{1 - u^2}} \, d\theta \qquad 1.5/10 $$

This is plotted on graph (1.5)1 and is seen to be peaked at an angle θ of $\hat{\theta}(E_i)$.

Graph (1.5)2

Distribution of small angle protons

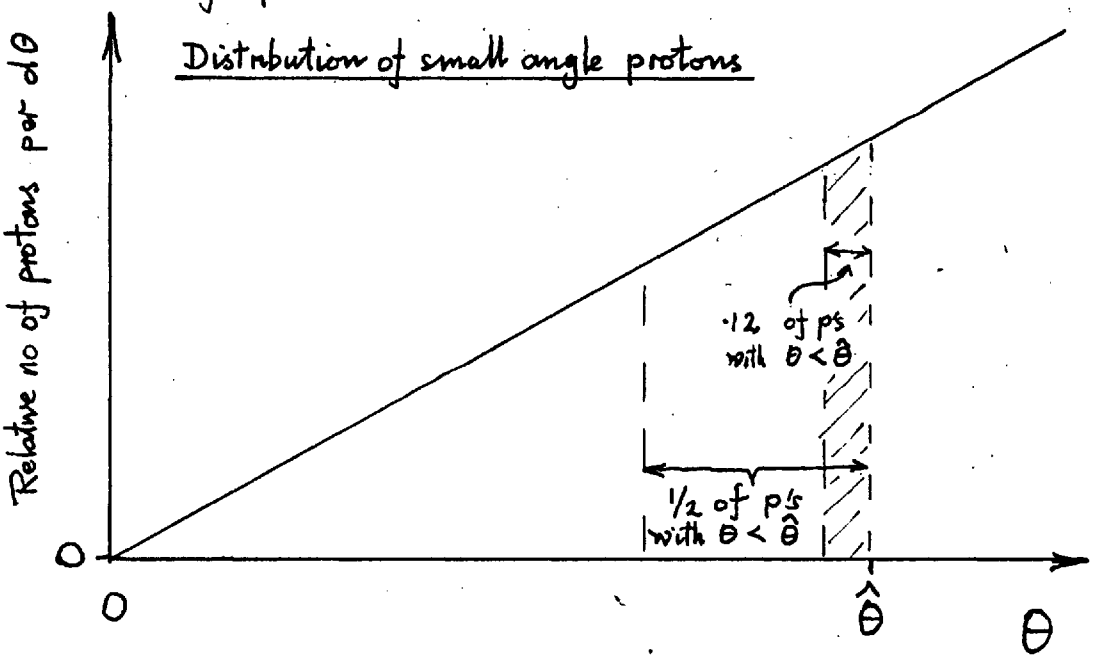

Graph (1·5)1

Angular distribution of deuteron tracks.

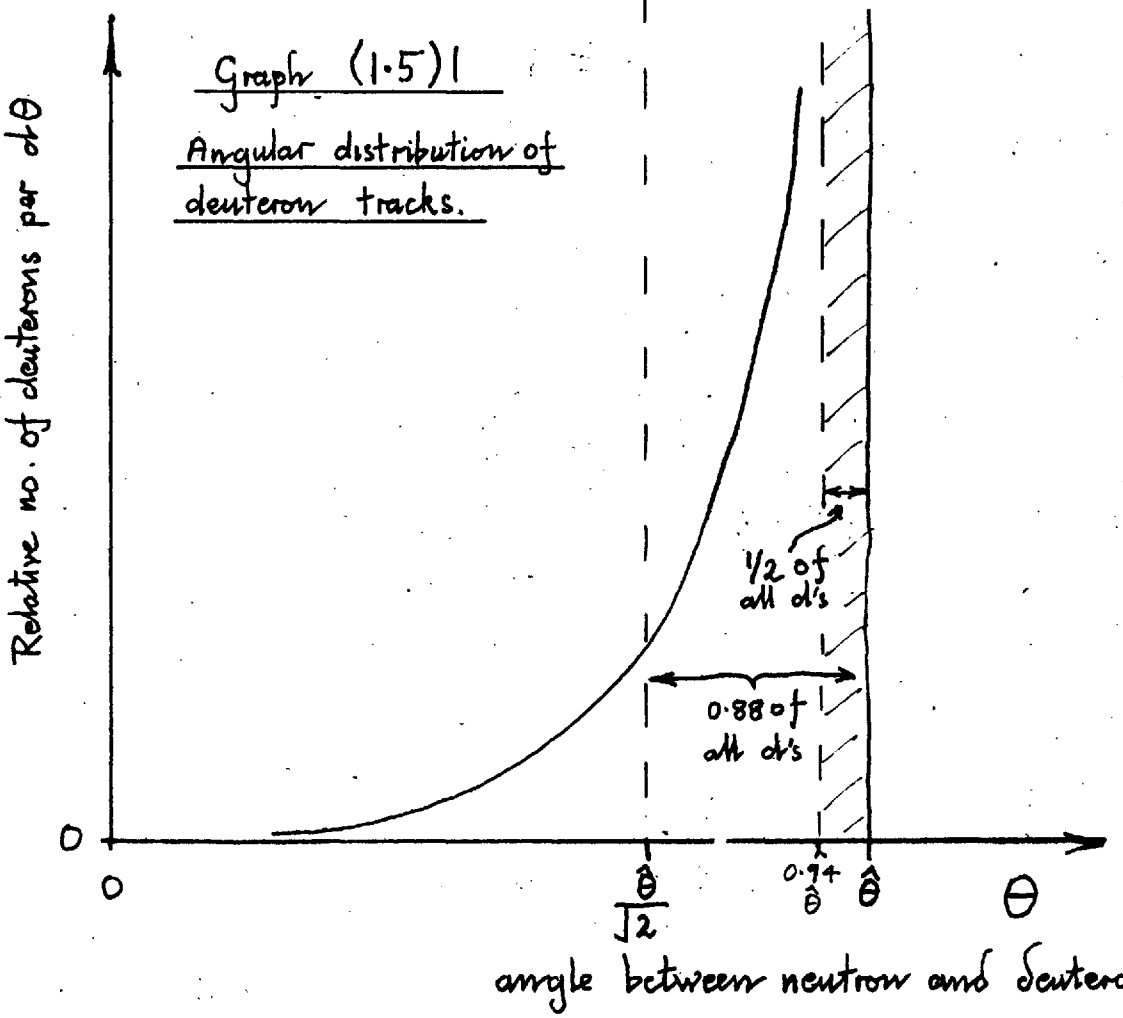

Using the integral

$$\int \frac{u^3}{1-u^2} = -\frac{1}{3}\sqrt{1-u^2}\,(2+u^2),$$

it may be shown that . half the deuterons have angles greater than $0{\cdot}94\ \hat{\theta}(E_i)$.

It is interesting to compare this distribution with an isotropic one for which the number of tracks in $d\theta$ is

$$n_p(\theta)\ d\theta \propto \sin\theta\ d\theta.$$

$n_p(\theta)$ is plotted on graph (1.5)2. Of all such tracks with angles less than $\hat{\theta}(E_i)$ only 1/15 have θ greater than $0{\cdot}94$ whereas half of the deuterons will be found in this interval.

1.5.4 Predicted neutron-capture cross sections.

According to the thoery of detailed balance the neutron-capture total cross section ($_{cap}\sigma_T$) is givon by (1.3/15)

$$\frac{_{cap}\sigma_T}{_{dis}\sigma_T} = \frac{3}{2}\,\frac{p_\gamma^2}{p_n^2}, \qquad 1.5/11$$

where p_γ = the photon momentum

and p_n = the centre of mass nucleon momentum.

Non-relativistically:

$$p_{\gamma} = \frac{E_{\gamma}}{c} ,$$

$$p_n = \sqrt{\frac{M_n E_n}{2c^2}} ,$$

where c = velocity of light,

thus

$$\frac{{}_{cap}\sigma_T}{{}_{dis}\sigma_T} = \frac{(E_{\gamma})^2}{\frac{M_n}{3} E_i} \qquad 1.5/12$$

Experimental values of total photo-disintegration cross sections have been taken from the sources given below and plotted on graph (1.5)3.

Halpern and Weintock, Phys. Rev. 91, 934.

Allen (1955), Phys. Rev. 98, 705.

Keck and Tollsrup (1956) Phys. Rev. 101, 360.

Whalin, Schrivener and Hanson (1956) Phys. Rev. 101, 377.

Using the formulae 1.5/12 and 1.5/2, capture cross sections have been calculated from the above photo-disintegration cross sections and plotted on graph (1.5)4. On graph (1.5)4 are also plotted the ratios of total elastic scattering to total capture cross sections. It is seen that there are relatively fewer capture events at lower energies.

Graph (1.5)4

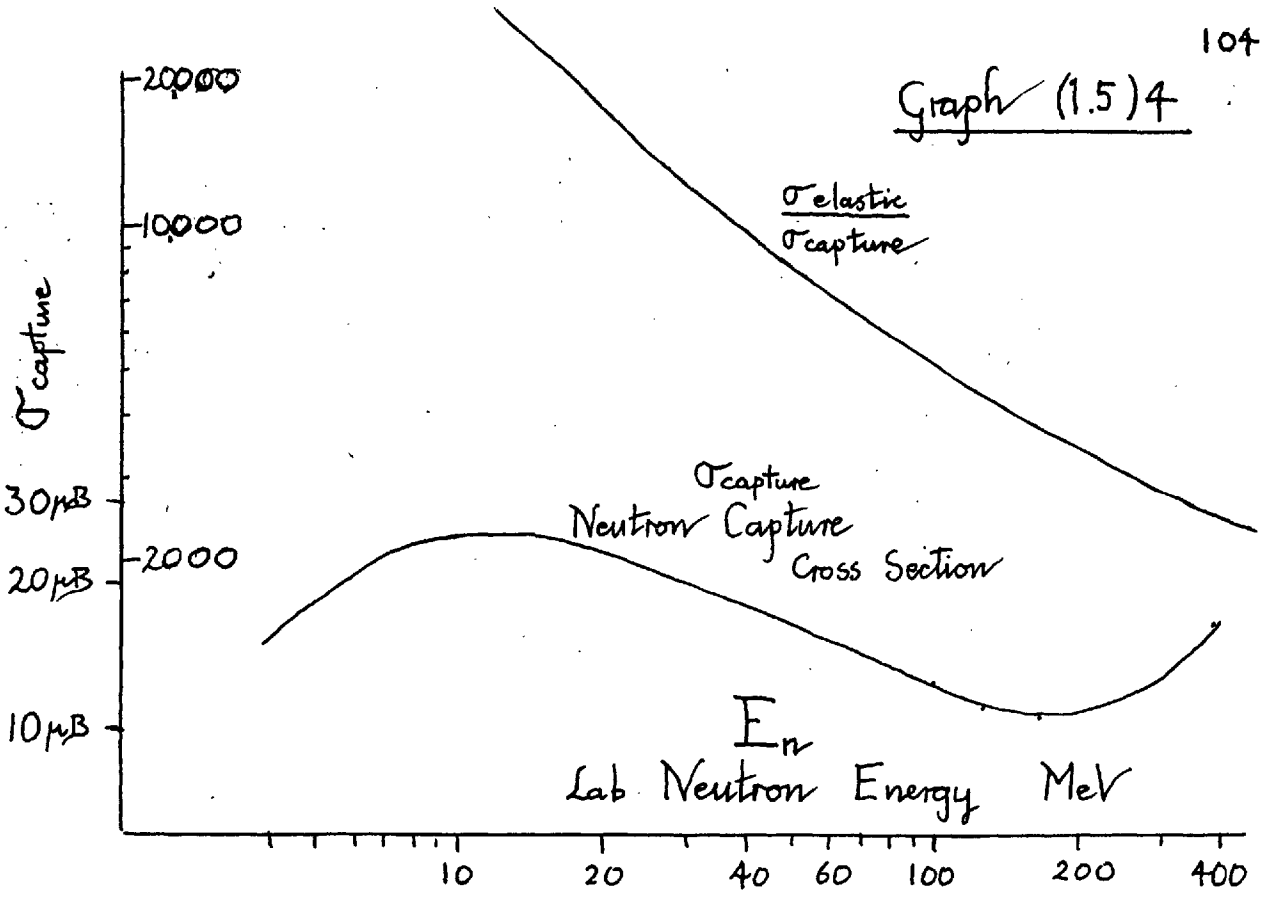

Graph. (1.5)3

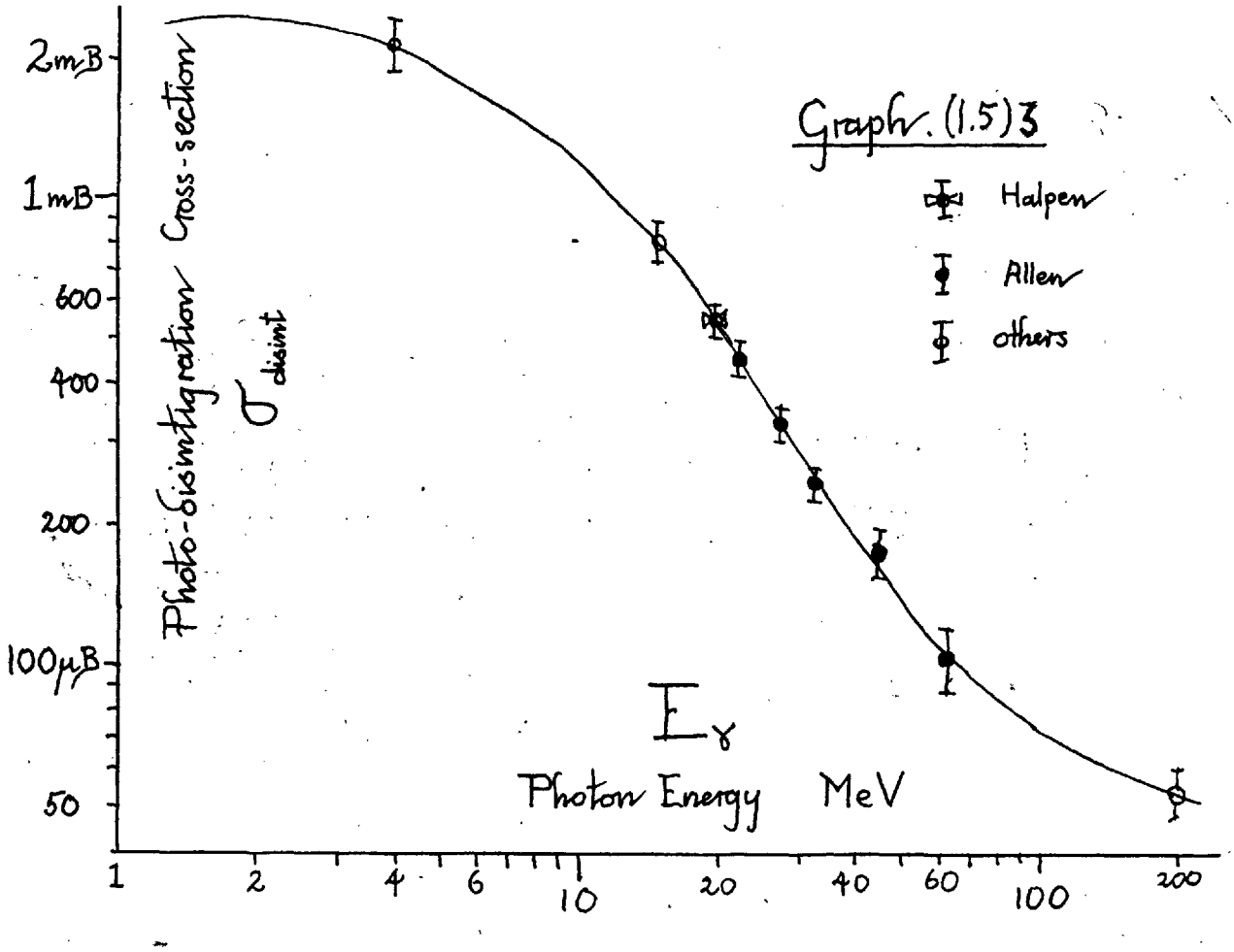

CHAPTER 2

THE EXPERIMENT.

2.1 THE CHOICE OF EXPERIMENT.

The liquid hydrogen bubble chamber, described in part I, was first operated in December, 1957, at Imperial College, London. It was then taken to Harwell in the summer of 1958 where it was tested in the Harwell cyclotron 170 MeV proton beam. It was not until the late spring of 1959 that the chamber was running well enough to undertake a serious experiment. The choice of that experiment will now be discussed. It is necessary, first to mention the characteristics of the bubble chamber and of the Harwell cyclotron.

The illuminated volume of the bubble chamber is approximately a cylinder 7·0 cm. diameter and 8·5 cm. long. It may, in principle, be filled with liquid deuterium or hydrogen. The necessary equipment to fill it with deuterium was not, however, ready in the spring of 1959. The experiment had, thus, to be performed with liquid hydrogen. The chamber was not in a magnetic field; the momenta of the particles passing through the chamber could not, therefore, be determined by measuring the track curvatures.

The Harwell cyclotron has a circulating proton beam with energy up to 170 MeV. From this, polarized and unpolarized proton

beams of near 170 MeV, are extracted with the aid of targets in the circulating beam. Neutron beams, polarized and unpolarized, may also be obtained at various energies up to 170 MeV. The methods of obtaining these will be discussed below in sections 2.4 and 2.5.

For the experiment, therefore, the hydrogen filled chamber could be placed in proton or neutron beams, polarized or unpolarized. The choice of beam was naturally influenced by the nature of the experiments that could be performed with them. There is, however, one general argument in favour of using a neutron, rather than a proton beam, in a small hydrogen bubble chamber. This argument will now be given.

Suppose events, such as scattering, are to be observed. The number of such events recorded in each photograph will depend on the number of primary particles that have passed through the chamber while it was sensitive. In practice one might observe one scattering event for every 200 neutrons or protons passing through the chamber.

If a proton beam were used, its intensity would have to be limited so that there were not too many proton tracks in each photograph. It was found, that if there were more than 50 tracks in a photograph it became difficult to scan and measure. Figure (2.1)2 shows a photograph of just 50 tracks. If then, the proton

beam is limited to give an average of 50 tracks per photograph, there would only be about one scattering event in every four photographs.

Consider the use of a neutron beam; the neutrons of the beam would leave no tracks. The intensity of the beam would have to be limited only by the number of charged tracks, due to a charged contamination in the beam, or due to the events themselves. In practice, the contamination was small and it was practicable to have up to 30 events in each photograph. Thus 120 times more neutron induced events than proton events can be recorded on the same length of film, with a consequent saving in both cyclotron and scanning time.

The main disadvantage in a neutron experiment is the fact that the initial neutron direction is not recorded on the film. The neutron direction has to be obtained from the geometry of the chamber and source, and related to the photographs.

If this disadvantage can be tolerated, and a neutron beam is used, very large numbers of scattering events may be obtained. At the same time, a few events with very small cross sections, compared with the scattering cross section, may be present. One such event is neutron-capture, whose cross section at 50 MeV is 1/10,000 of the total scattering cross section. This event has not previously been observed at medium energies. Mr. B. Rose,

of Harwell suggested that it might be detected in the bubble chamber. The particular interest in observing neutron-capture lies in the possibility of extending the observation to the polarization of neutron-capture. This polarization, as has been stated in chapter 1, is of particular theoretical interest. When the experiment was planned, however, it was not certain if it would be possible to observe neutron-capture at all. Thus, the information that could be obtained from observing other reactions that occurred in the chamber was considered. In all cases more information can, in principle be obtained if a polarized initial neutron beam is used. Unfortunately the intensity and energy spectrum of the polarized neutron beam obtainable, were inferior to those of the unpolarized beam. The reasons for this will be discussed in sections 2.4 and 2.5. For the moment, the information that may be obtained from the reactions in the chamber will be considered for both unpolarized and polarized beams. Later, it will be shown why an unpolarized beam was used. The neutron interactions that may occur in the hydrogen of the chamber will now be listed. In each case the information that may be obatined from their observation will be briefly given.

2.1.1 A single elastic scatter.

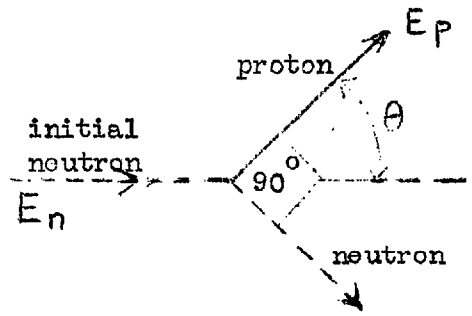

A photograph showing such an event is given in figure (2.1)1. Only the scattered proton is observed, which may or may not stop in the chamber. If it does stop then the proton energy may be obtained from its range r_p using the equation (1.5/11),

$$E_p = E(r_p) \doteq 10{\cdot}7\, r^{0.548}$$

From non-relativistic kinetic theory the energy of the initial neutron (E_n) is given by:-

$$E_n = \frac{E_p}{\cos^2\theta}, \qquad 2.1/1$$

where θ is the angle between neutron and proton directions.

From an observation of such events may be obtained: (a) if the neutron beam is unpolarized: the differential scattering cross section, ${}_{n\text{-}p}\sigma(\theta, E_n)$, and (b) if the initial beam is polarized: the n-p scattering polarization (${}_{n\text{-}p}P(\theta)$).

Fig (2.1)1 n-scattered protons

neutron beam direction →

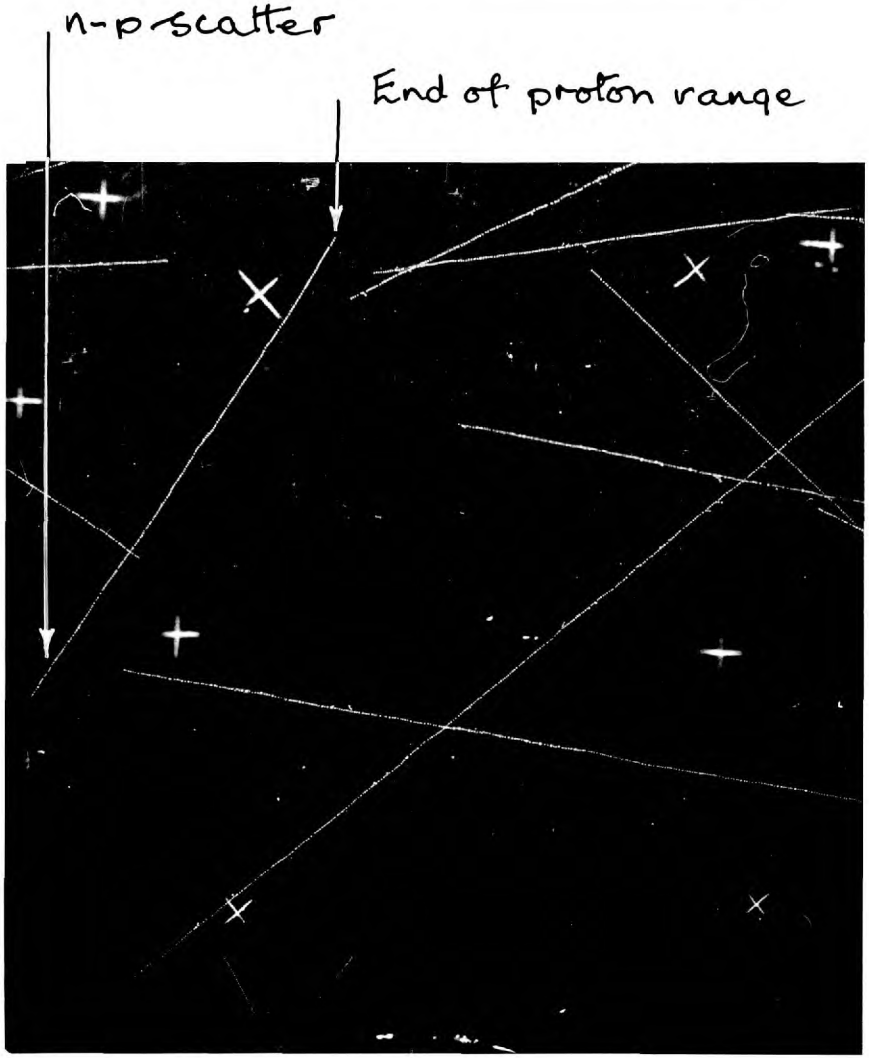

Fig (2.1)2 a p-p, p-p double scatter

proton beam direction →

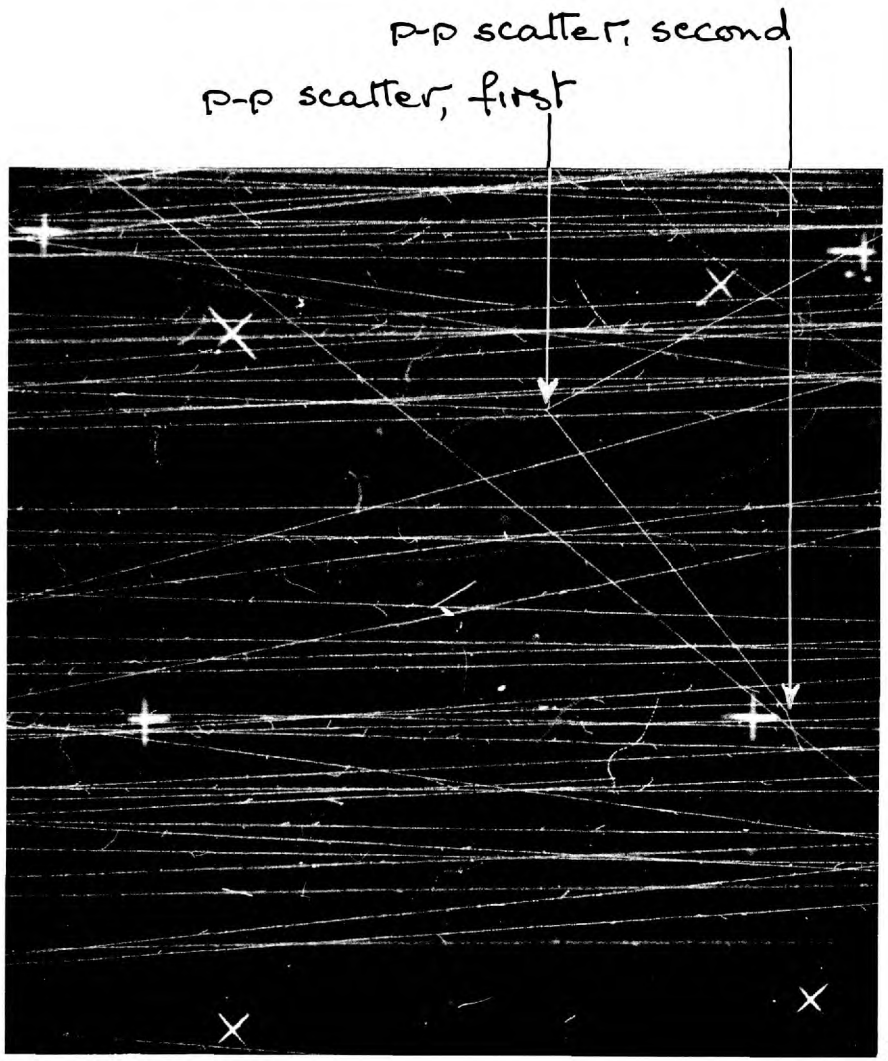

2.1.2 n-p, p-p, double scattor.

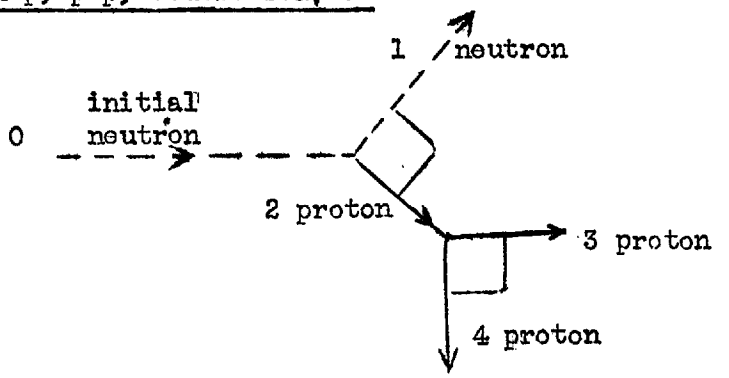

A photograph of such an event is shown in figure (2.1)4. If a polarized neutron beam is used, then, as well as the results given in section 2.1.1, may be obtained two of the 'triple scattering' coefficients referred to in section 1.2.

2.1.3. n-p, n-p double scatter.

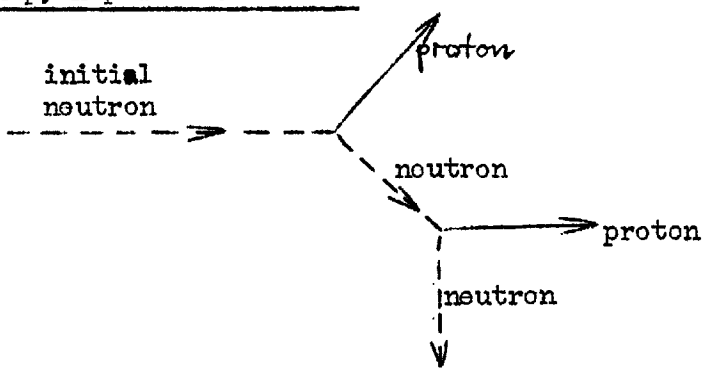

A photograph of such an event, in which the neutron track (3) is very short is shown in figure (2.1)3. If a polarized neutron beam is used, these events may give the same results as the n-p, p-p double scatter referred to above.

Fig (2.1)3. a n-p, n-p double scatter

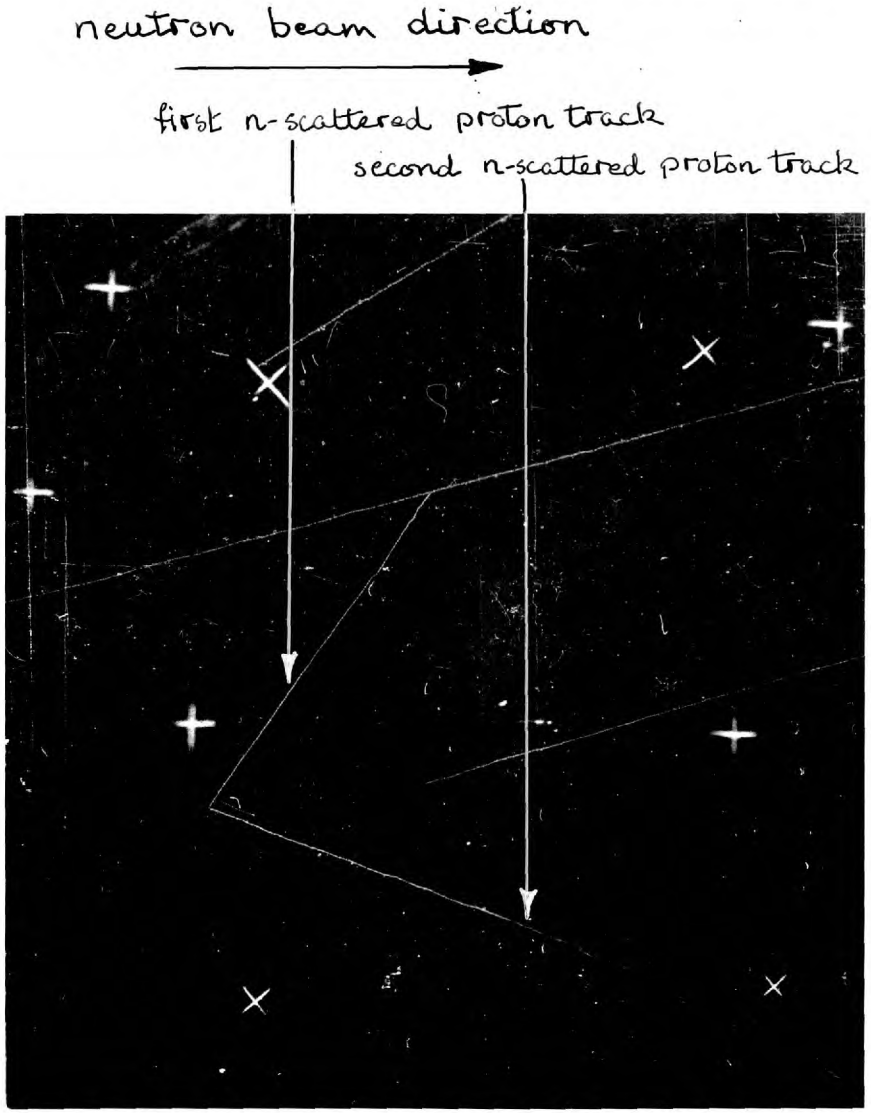

Fig (2:1) 4 a n-p, p-p double scatter

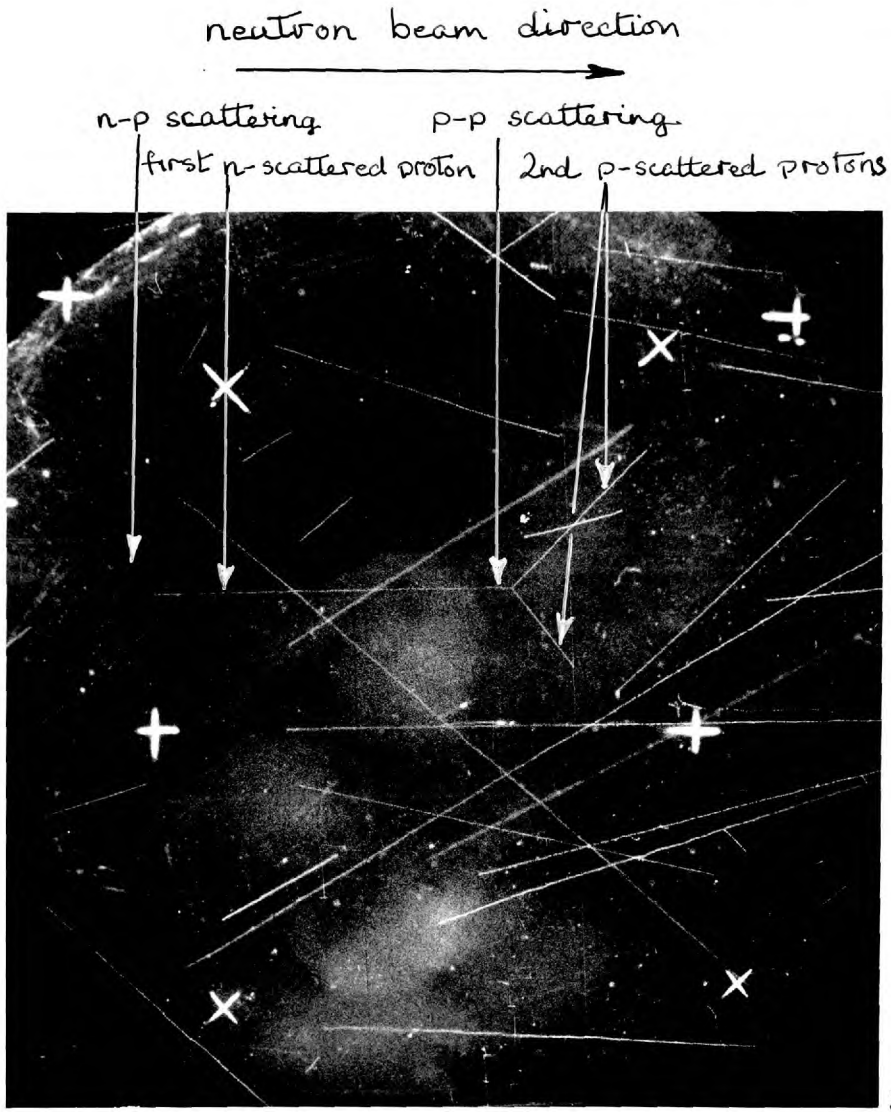

2.1.4 Neutron-capture.

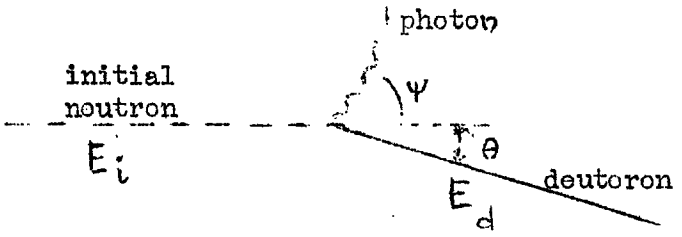

A pair of stereo-photographs of what is probably an example of this event is shown in figure (2.1)5. Only the deuteron gives a track, which makes a small angle 0 with the initial neutron direction. In the stereo-photographs, this small angle is shown by the fact that the two track images are nearly parallel, and in line with the projected neutron direction.

If the deuteron stops in the chamber then the deuteron energy (E_d) and initial neutron energy (E_i) may be obtained from the deuteron range (r_d) in cms., using the following equations derived in chapter 1: the equation numbers given in brackets are those of chapter 1.

$$E_d \doteq 14{\cdot}3\ (r_d)^{{\cdot}548} \quad \text{MeV} \qquad (1.5/8)$$

$$E_i \doteq 2\ E_d \qquad (1.5/3)$$

The angle θ between deuteron and neutron directions has been shown to satisfy the condition:

$$\theta < \hat{\theta}\ (E_i) \qquad (1.5/4)$$

Fig (2.1)5 Stereo photographs of chamber

neutron beam direction

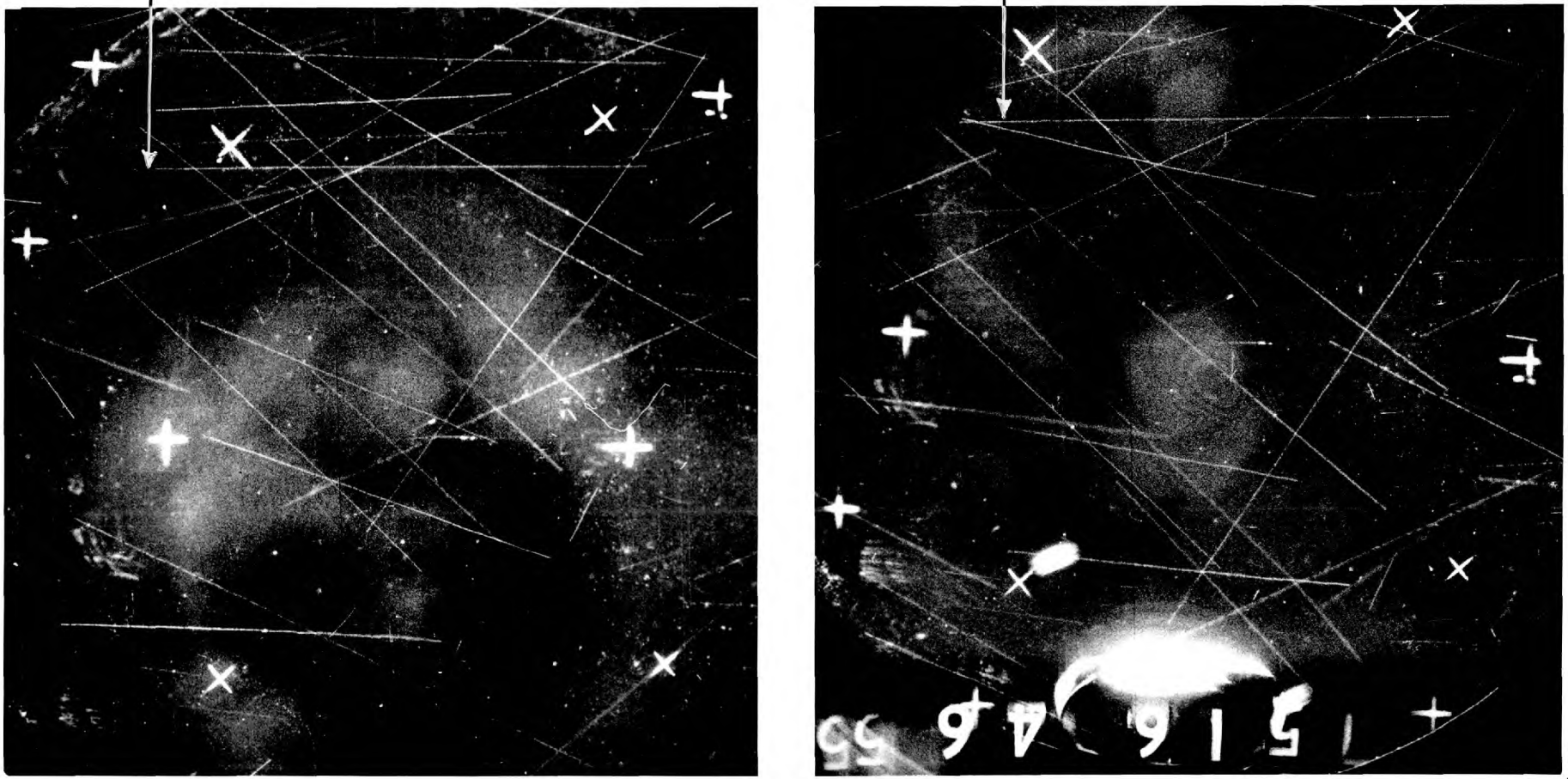

where $$\hat{\theta}(E_i) = \sqrt{\frac{E_i}{8\ M_n}} \qquad (1.5/6)$$

and M_n is the rest energy of the neutron in MeV. From the observation of such events using an unpolarized beam, may be obtained the total cross section for the reaction. If a polarized neutron beam is used then information may be obtained about the polarization of the reaction. This has been discussed in section 1.4.

2.1.5 Radiative Scattering.

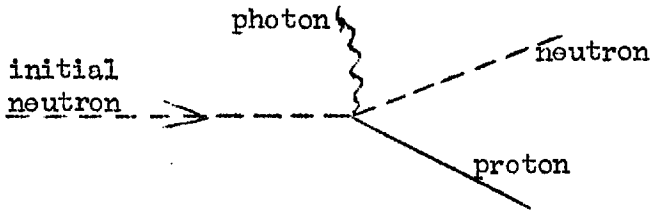

Only the proton will be seen. The cross section for this reaction is negligible compared with the scattering cross section. It will be ignored for the present, but considered again in section 4.5 .

Of the interactions listed above, all are of interest. In chapter 1 it has been shown how results from the double scattering events (2.1.2 and 2.1.3), and neutron-capture (2.1.4), are of particular theoretical interest. It was decided to perform

a neutron experiment with the aim of exploring the possibilities of observing the events listed above. In particular it was hoped to observe the neutron-capture reaction at a medium energy.

It will be shown later (2.3) that the identification of the neutron-capture reaction depended on having a well peaked neutron spectrum. It will also be shown (2.4 and 2.5) that for a given neutron intensity in the chamber a far more peaked neutron energy spectrum could be obtained with unpolarized than polarized neutrons. See figures (2.6)2 and (2.6)3. In practice this meant that a choice had to be made between:- (1) using a polarized beam and being unable to observe the neutron-capture reaction; or (2) using an unpolarized beam and being unable to measure the n-p scattering polarization and triple scattering coefficients.

The determination of triple scattering coefficients did not in any case appear practicable, due to the very small (1%) asymmetries that would have to be observed. The n-p scattering polarization has been determined before and is being determined by the 'time of flight' group at Harwell. It thus appeared sensible to concentrate on a determination of the neutron-capture total cross section, which has not previously been measured. For this purpose it was decided to use an unpolarized neutron beam.

Unpolarized neutron beams could be obtained from the cyclotron with most peak neutron energies between 170 and 50 MeV.

The considerations leading to the choice of a particular energy will now be given.

The bubble chamber used had no magnetic field, and the momentum of a particle in the chamber could not be obtained from its track curvature. The momentum of a particle is related to its ionization, but it was found impracticable to obtain the ionization of a particle from the bubble density of its track. It was also impracticable to determine the momentum of particles from the coulomb scattering of their tracks. The only method of determining the momentum or energy of a particle in the chamber was to measure its range. If the energy of certain particles are required, then only those, whose tracks lie within the chamber, can be considered. In order that there be a reasonable probability that the particle tracks lie within the chamber, the track lengths must be small compared with the chamber dimensions.

If neutron-capture deuterons are to be identified, their energy will certainly be required. If their range is greater than four cms., the probability of their tracks lying within the chamber will be shown in section 4.4.2 to be less than 30%. Using the equations quoted above in section (2.1.4) the energy of a deuteron having a four cm. track is found to be 30 MeV. The energy of the initial neutron producing this deuteron is then 60 MeV. It was decided, therefore, that the maximum neutron beam energy should be 60 MeV.

From graph (1.5)1 it was seen that there were relatively more neutron-capture events, to neutron-scattering events, at higher energies. The neutron-capture polarization is expected to be larger at larger energies, and the theoretical interest in neutron-capture is also greater at higher energies. A beam was therefore required with a maximum energy of 60 MeV, whose spectrum peak was as near this maximum as possible. The chosen experiment may now be summarized:

An unpolarized neutron beam with maximum energy of 60 MeV would be used.

The possible events, listed above (2.1.1 - 2.1.4) should, where possible, be identified, and the following results obtained:-

(1) The n-p differential cross section, to be regarded as a check on the experiment.

(2) The neutron-capture total cross section.

(3) The energy spectrum of the neutron beam. This will be needed for (2).

From the results it was hoped to be able to study the possibility of measuring neutron-capture polarization by this or other methods.

The identification of the listed events will be considered in the next section.

2.2 IDENTIFICATION OF THE EVENTS.

The possible events that may occur in the chamber have been listed above (2.1.1 - 2.1.5). Let tracks in the chamber due to the main neutron beam be classified in the same five categories. A sixth category may be considered in which tracks, not due to the main neutron beam, are classified. These will be known as 'spurious tracks', and will be due to either neutrons or protons entering the chamber in directions other than that of the beam. The identification of the events will be considered in turn.

2.2.1 A single n-p elastic scatter.

Most tracks that have their left hand end (that end nearest the neutron source) inside the chamber will be due to n-p scattering from the beam. The distribution of spurious and other tracks can be estimated and subtracted from the distribution of all such tracks.

2.2.2 n-p, p-p double scatter (see section 2.1.2).

This is identified if it satisfies the following conditions:-

(a) The angle between the two second scattered proton tracks (3 and 4) must be $\pi/2$;

(b) The energies of the two second scattered protons must

be consistent with the angles;

(c) The calculated initial neutron energy must be less than 70 MeV.

2.2.3 n-p, n-p double scatter (see section 2.1.3).

This is identified if it satisfies the following conditions:-

(a) The angle between the first scattered proton and neutron tracks (1 and 2) must be $\pi/2$;

(b) The first scattered proton and neutron directions must be coplanar with the initial neutron direction;

(c) The energies of the two proton tracks, calculated from their ranges, must be consistent with the angles;

(d) The calculated initial neutron energy must be less than 70 MeV.

2.2.4 Neutron-capture.

The properties of neutron-capture events have been derived in section 1.5 and certain results have been quoted in section 2.1.4. Using equations 1.5/8 and 1.5/3, it can be shown that the ranges (r_d) of neutron-capture deuterons from the neutron beam with a maximum energy of 60 MeV must be

$$r_d \leq 4{\cdot}0 \text{ cm.}$$

Similarly from (1.5/4) and (1.5/6)

$$\theta_i \leq \hat{\theta}_i(E_i)$$

$$\hat{\theta}_i(E_i) < 5{\cdot}4^\circ$$

The number of deuterons might be distinguished from the number of neutron-scattered protons by the following methods.

(a) Consider a proton scattered in the forward 5° whose energy is such that its range is 4 cm. The initial neutron will have been scattered through 85° and can be shown to have a final energy of about 1·7 MeV. The cross section of such a slow neutron is high and the probability that it will scatter again in the chamber is about 95%. The 'knock on' proton from such a second scatter will have an energy less than 1·7 MeV and its 'track' will consist of a single bubble. If such a bubble could be observed, then the event would be identified as neutron-scattering, and not neutron-capture. Unfortunately, short bubble growth time, to reduce distortion; and multiple exposures (see section 2.6), had to be used. Under these conditions the photographs were as in figure (2.1)5. In such photographs it proved not possible to identify single bubbles from amongst the background. The method was not successful.

(b) The ionization produced by a deuteron is known to be

about 30% higher than that due to a proton of the same range. In principle, the ionization of a particle is related to the bubble density of the track is produces. From this bubble density and the range of a track, it might be possible to identify it if it were a deuteron. In the bubble chamber used, it was found impossible satisfactorily to relate the bubble density of a track with its ionization. The method was not, therefore, possible.

(c) The coulomb scattering of a particle together with its range will also distinguish whether it is a deuteron or proton. Rough measurements by Dr. Tallini of the apparent scattering of proton tracks of known energy, gave results in excess of the calculated coulomb scattering. This could have been due to distortions resulting from the flow of the liquid in the chamber or variations in the liquid refractive index. The method was abandoned.

(d) Three possible methods of distinguishing a neutron-capture deuteron from a neutron-scattered proton have been given above. All three have been rejected as impracticable. Consider, now, if the number of neutron-capture deuterons can be estimated without identifying the individual tracks.

All the deuteron tracks have ranges less than four cm. and angles θ less than $\hat{\theta}(E_i)$, where $\hat{\theta}(E_i)$ is a function of the track

energy and thus of its range. These limits will be referred to as the 'deuteron limits' (DL).

The number of tracks from all causes, but neutron-capture, inside these limits ($q_{p(DL)}$), may be estimated from the distribution of tracks outside these limits. All that need be assumed is that no track producing process, other than neutron-capture, will give a rapid change in the number of tracks per unit solid angle, between angles above and below $\hat{\theta}(E_i)$. If, from the observed number of tracks within the deuteron limits, ($q_{(DL)}$) the estimated number of non-neutron-capture tracks ($q_{p(DL)}$) is subtracted, then an estimate of the number of neutron-capture deuterons (q_d) is left.

$$q_d = q_{(DL)} - q_{p(DL)}$$

Let the ratio of the number of non-deuteron tracks within the deuteron limits to the number of deuterons be :

$$\alpha = \frac{q_{p(DL)}}{q_d} \qquad 2.2/1$$

If the error in estimating the expected number of non-neutron-capture events is negligible, then the fractional statistical error in determining the neutron-capture cross section is

$$K_{cap\sigma} = \frac{\sqrt{q_{(DL)}}}{q_d} = \frac{1}{\sqrt{q_d}} \cdot \sqrt{1+\alpha} \qquad 2.2/2$$

If the deuterons had been individually identified then the error

would have been:

$$= \frac{1}{\sqrt{q_d}}$$

It is seen that the error introduced by the proposed method is greater than this by the factor $\sqrt{1+\alpha}$. Clearly, a condition for the success of the method is that α be not large; that is, that the number of non-neutron-capture tracks within the deuteron limit be not large compared with the number of deuterons. This condition will be shown in the next section to require that the low energy tail of the neutron energy spectrum be small.

In order to obtain the capture cross sections, the neutron intensity, as well as the number of deuterons will be required. It will also be desirable to know the energy spectrum of these neutrons. The method of obtaining the intensity and spectrum of the initial neutrons, as well as a more detailed account, of the estimation of the number of deuterons, will be given below in section (4.4).

This last method of obtaining the total capture cross section has a number of advantages over the other three methods outlined. It requires only the measurement of track angles, which are easy and rapid to measure compared with curvature, bubble density and scattering. The method is general, in that it could be used in a counter experiment. The method also seems less subject to

experimental bias than the former three methods. If the spectrum condition is satisfied and α is not large then the errors introduced in the neutron-capture cross section are little larger than if the events were identified. The accuracy of the method is then dependent largely on the number of events recorded and thus on the number of photographs taken and scanned.

2.2.5 Radiative scattering.

As stated in section 2.1.5, this reaction will, for the moment, be ignored. It will be considered again in section 4.5

2.2.6 Spurious tracks.

If certain large angle (θ) tracks are assumed to be due to protons scattered by neutrons in the beam; and if, on this assumption the initial neutron energy E_n is calculated, then it is found that $E_n \gg$ 70 MeV. Since there are certainly no neutrons in the beam with energies $E_n \gg$ 70 MeV, the assumption that the tracks are due to protons scattered by the beam must be false. Such tracks must be due to neutrons not in the beam, and can be classed as spurious tracks. From such unequivocably identified large angle spurious tracks, a distribution of spurious tracks over all angles may be estimated. This is done in section (4.2.4).

These methods of identification will be referred to again

when the measurement and reconstruction are discussed in chapter 3 and when the results are discussed in chapter 4. One reason for giving them here, is in order to derive the neutron energy spectrum condition for the determination of the neutron-capture cross section. This condition will be further dealt with in the following section.

2.3 NEUTRON ENERGY SPECTRUM REQUIREMENT.

It has been shown in section 2.2.4 that in order to identify the neutron-capture reaction a certain condition must be satisfied. It was shown that all deuterons produced from neutrons with energies less than 60 MeV have their tracks within certain 'deuteron limits' of range and angle. These deuteron limits are:- (a) that the range of the track be

$$r < 4{\cdot}0 \text{ cm.}$$

(b) that the angle of the track with the neutron direction be

$$\theta < \hat{\theta}(E_i) < 5{\cdot}4^{\circ}$$

The condition that must be satisfied is that the number of non-neutron-capture tracks within these 'deuteron limits' ($q_{p(DL)}$) be not large compared with the number of deuterons (q_d), that is that

$$\frac{q_{p(DL)}}{q_d} = \alpha \gg 1 \quad . \qquad 2.3/1$$

The α in this condition, may be related to the initial neutron energy spectrum. In order to simplify the derivation of this relation, the deuteron limits will be approximated to

$$r < 4 \text{ cm., and } \theta < 5^{\circ} \qquad 2.3/2$$

Here (5°) is a mean of the values of $\hat{\theta}(E_i)$, where E_i varies over the initial neutron spectrum $n(E_i)$. Since θ does not change much over the possible values of r this approximation will make

little difference to the spectrum requirement derived.

Most of the non-neutron-capture tracks will be due to neutron-scattered protons. Consider the number of neutron-scattered protons within the approximate deuteron limits (ADL) given above. The proton energy (E_p) giving a four cm. track is 22·5 MeV. The neutron energy (E_n) giving a scattered proton of 22·5 MeV is given by:

$$E_n = E_p/\cos^2\theta \qquad 2.3/3$$

and if θ is small, $E_n \doteq E_p = 22{\cdot}5$ MeV. Thus the condition that the track length be less than four cm. requires an initial neutron energy less than 22·5 MeV.

At energies of 22·5 MeV and below the neutron-scattered protons are approximately isotropic. Let $q(E_n)dE_n$ be defined as the number of neutron-scattered protons from neutron energies of E_n to $E_n + dE_n$. The number of neutron-scattered protons in the 'approximate deuteron limits' given above is then:-

$$q_{p(ADL)} \doteq \frac{1}{130}\int_0^{22{\cdot}5\ \text{MeV}} q(E_n)\ dE_n \qquad 2.3/4$$

The factor 1/130 is due to the small solid angle below 5°.

The number of deuterons will be approximately

$$q_d \doteq \frac{\text{cap}\,\sigma_T(\bar{E}_i)}{\text{n-p}\,\sigma_T(\bar{E}_n)} \cdot \int_0^{\infty} q(E_n)\ dE_n \qquad 2.3/5$$

where $_{cap}\sigma_T(\bar{E}_i)$ is the total capture cross section, and $_{n\text{-}p}\sigma_T(\bar{E}_n)$ is the n-p scattering cross section, both at the mean neutron

spectrum energy of about 50 MeV. Thus the ratio of the number of protons to deuterons within the approximate deuteron limits (α) is given by:-

$$\alpha = \frac{q_{p(ADL)}}{q_d} = \frac{1/130 \int_0^{22.5\ MeV} q(E_n)\ dE_n}{\frac{cap\sigma_T(\bar{E}_i)}{n\text{-}p\sigma_T(\bar{E}_i)} \int_0^{\infty} q(E_n)\ dE_n} \qquad 2.3/6$$

For convenience, let:

$$\beta = \frac{\int_0^{22.5\ MeV} q(E_n)\ dE_n}{\int_0^{\infty} q(E_n)\ dE_n} \qquad 2.3/7$$

$_{n\text{-}p}\sigma_T/_{cap}\sigma_T$ has been calculated and plotted on graph (1.5)1. At 50 MeV, the mean spectrum energy, it is seen to be 10,000. Substituting this into equation 2.3/6 and using 2.3/7

$$\alpha = 80 \cdot \beta \qquad 2.3/8$$

Now the condition for the success of the neutron-capture determination is that α be not large, or that:

$$80\beta \not> 1 \qquad 2.3/9$$

This expresses the condition in terms of β, which is defined by the spectrum of neutron-scattered protons ($q(E_n)$), where β is the ratio of the number of neutron-scattered protons, from neutrons below 22·5 MeV, to the total number of neutron-scattered protons. The spectrum of these protons $q(E_n)$ is related to the neutron spectrum ($n(E_n)$) by:

$$q(E_n) \propto {}_{n\text{-}p}\sigma_T\ (E_n)\ \ n(E_n).$$

Thus the condition has been related to a requirement of the initial neutron spectrum, as required.

Before discussing the attainment of this requirement, in section 2.6, the method of obtaining the neutron beam must first be described. This will be done in the following two sections.

2.4 THE PRODUCTION OF A NEUTRON BEAM.

In the vacuum case of a cyclotron there is a circulating proton beam. Neutrons can be produced by allowing the protons to make nuclear interactions in a target material.

A few details of the cyclotron must first be given. Methods of bringing the protons into a target will then be discussed with particular reference to the neutron spectrum that will be produced. A discussion of the nuclear interactions in the target material will be left to the next section (2.5).

The cyclotron vacuum tank includes the space between the horizontal facus of the magnet poles, each 110" diameter and about 10" apart. In this gap the proton beam consists of a bunch of particles rotating about the vertical axis of the magnet poles, and spiralling slowly outward. Individual protons perform oscillations about a common equilibrium orbit and thus give the bunch a cross section of about 2" diameter. The mean radius of the bunch increases by about 0·0025" per revolution, as the energy of the protons in the bunch is increased by the radio frequency accelerating field. This radius is plotted against proton energy on graph (2.4)1. In order to focus the beam, the magnetic field falls as the radius increases. As a consequence of this the period of rotation of the protons falls as the radius of their orbit increases. This necessitates a fall in the

Graph (2.4)1. Cyclotron energy - radius relation.

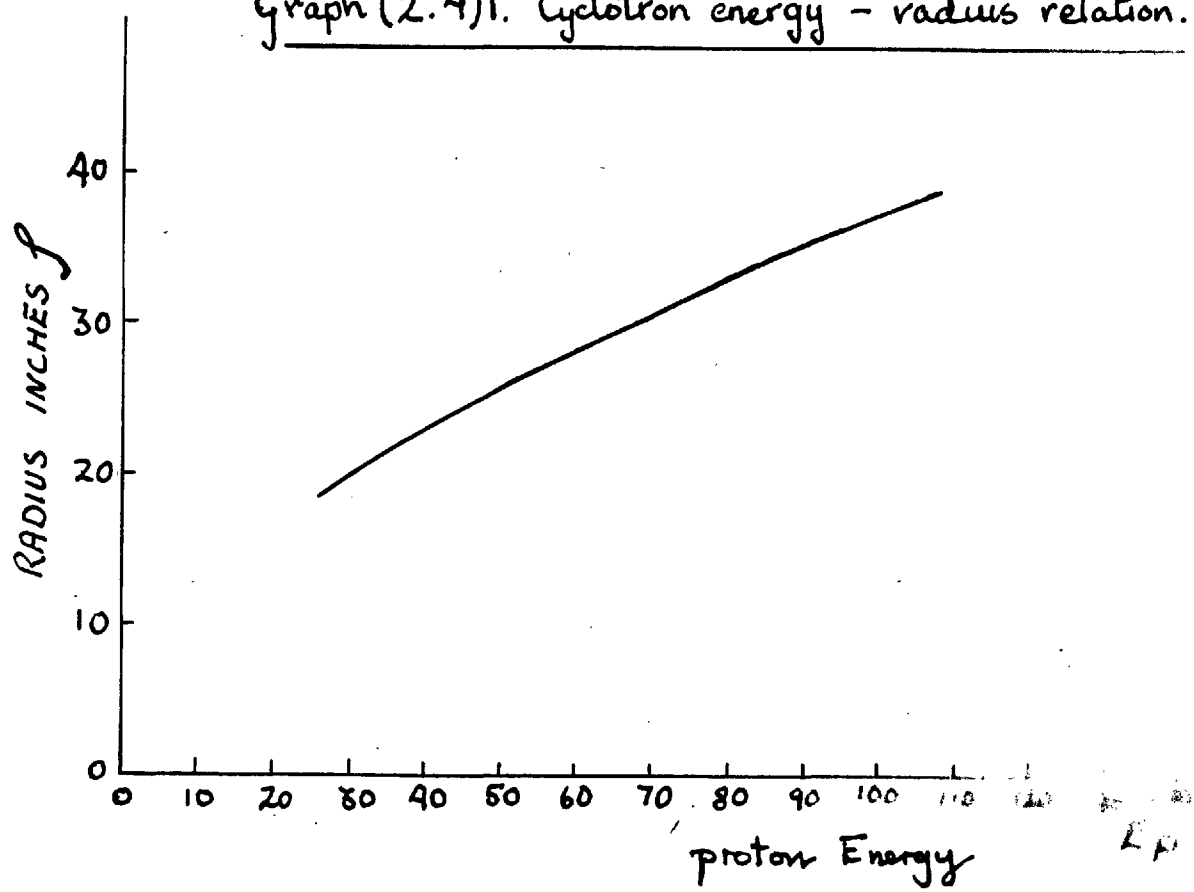

accelerating radio frequency as the proton energy and radius of orbit increases. For a given frequency, only particles with the corresponding period of rotation will be accelerated. For this period of rotation they must have a particular mean radius, and thus energy. The energy of the protons is, therefore, closely related to both the radio frequency and the mean radius of the proton orbit. Due to the radial oscillations, the energy is not so closely related to the actual radius of a proton orbit at any given time.

If protons in the circulating bunch enter a target, then nuclear interactions may occur that produce neutrons. These neutrons may have energies up to that of the protons.

There are two different methods by which the protons in the circulating bunch in the Harwell cyclotron may be brought into a target.

The first and preferable method, is that used by the 'time of flight' group at Harwell, in which the beam is electrostatically deflected on to the target during one revolution of the particles. The protons incident on the target are then effectively monoenergetic. It was not, unfortunately, possible to use this method for technical reasons.

In the second and simpler method, a target is placed in the plane of the circulating bunch at a certain radius. As the

energy of the protons increases so the mean radius of the bunch increases until it is 'peeled off' on the target. All the protons will, eventually, enter the target even if the target height is much less than the vertical spread of the beam. This is because the vertical oscillation of the individual protons are not in phase with their rotations in the vacuum tank.

The neutron spectrum produced by this method is worse than that produced by deflecting the beam on to the target for two reasons:-

(1) As has been stated, the energy of the protons are closely related to the mean radius of the particle orbit. At one moment of time they all have approximately the same energy. Due to the oscillation of protons about their mean radius, the process of 'peeling off' is spread over a period of time during which the mean radius approaches that of the target and the proton energy increases. This causes a spread in the proton energy incident on the target of about 5-10 MeV, and a consequent spread in the final neutron energy spectrum.

(2) The second cause of an inferior neutron spectrum is that the protons make multiple traversals of the target. Each proton that enters the target will be slowed down as it passes through, and may emerge from the other side into the vacuum tank with a reduced energy. Such is the focussing of an approximately constant magnetic field, that such a proton may be brought back

on to the target a second time. The proton will then lose more energy as it passes through the target and may emerge and again be focussed back on to the target. Eventually coulomb scattering, or a nuclear interaction may cause the proton to leave the target in such a direction that, in being focussed back, it passes out of the vacuum case and is lost. The effect of these multiple traversals is to increase the effective thickness of the target, and thus to spread the resultant neutron energy spectrum. It is found that the effective thickness of the target is constant, and such as to reduce the proton energy by about 15 MeV, provided that the actual thickness in MeV is less than this value. If the actual thickness is more than 15 MeV there are few or no multiple traversals, and the effective thickness becomes equal to the actual thickness.

It would appear from the above that the target thickness may be anything less than a certain value. Unfortunately, heating must also be considered in certain target materials, and this affects the choice of thickness. Before discussing this, however, the choice of target material must be considered. This will be done in the next section.

2.5 THE TARGET.

The first object of this section is to discuss the choice of target material to produce the best possible unpolarized neutron energy spectrum. In order to do this, the theory of neutron production must be briefly mentioned. The problem of heating in the target will be considered, and the size of target to be used chosen from these considerations. The mounting and placing of the target will be described. The unpolarized neutron energy spectrum obtained, using the target, will then be given and briefly discussed. Finally the choice of target to obtain a polarized spectrum is considered, and the energy spectrum obtained from this target compared with the unpolarized neutron spectrum.

A proton as it passes through the material of a target may make a nuclear interaction and emit a neutron. Let the angle between the initial proton and final neutron directions be θ, and E_b and E_n the energies of proton and neutron.

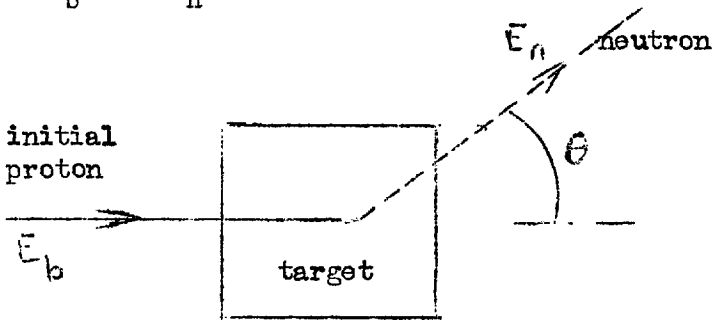

If the nucleons in the target nucleus are few, and if the initial proton energy (E_b) is large compared with the nucleus binding energy (B), i.e.

$$B/E_b = \eta \ll 1 \qquad 2.5/1$$

then the initial proton may be approximately regarded as interacting with one particular free mucleon in the nucleus. This is known as the impulse approximation. If the proton strikes an approximately free neutron, then the emitted neutron would have energy:

$$E_n = \frac{E_b}{\cos^2\theta} \qquad 2.5/2$$

and a polarization $P(\theta, E_n)$. The polarization tends to zero as the angle θ and energy E_b are decreased. At $\theta = 0$ unpolarized neutrons would be emitted.

In the deuterium nucleus there are only two nucleons, and the binding energy (B_d) is only 2·23 MeV. For an initial proton energy E_b of 60 MeV $:\eta = \cdot037 \ll 1$. The conditions for the validity of the impulse approximation are satisfied; and it is found experimentally that it is a good approximation.

Consider a deuterium target placed in a mono-onorgotio proton beam. When $\theta = 0$ a nearly mono-energetic neutron beam is obtained. If placed in a 100 MeV proton beam, then at an anglo θ of 45°, $\sim$ 50 MeV neutron beam with polarization of 20-30% would be expected.

Other elements with larger atomic numbers than deuterium

have more nucleons and larger binding energies. The impulse approximation becomes progressively less valid as the atomic number increases. Consider targets containing such elements placed in a mono-energetic proton beam. At $\theta = 0$ instead of a mono-energetic neutron beam, a peaked spectrum with a finite width of peak and with a low energy tail is obtained (see figure (2.5)1). As the atomic number increases so does the width of the peak and magnitude of the low energy tail. At an angle (θ) other than zero, polarized neutrons may be obtained whose polarization will depend on the energy, angle and element. At 45° and E_n = 100 MeV a polarization of 20% would not be unreasonable.

It is clear that the best target material is deuterium. If the proton beam were external, or if the protons could be deflected on to the target, it might be possible to use deuterium. it does not, however, seem possible to allow a beam to 'peel off' on a deuterium target. The deuterium would have to be contained within some walls. The protons as they spiralled out, by 0·0025" per revolution, would 'peel off' on the wall rather than the deuterium behind it.

If deuterium cannot be used, then other elements must be considered in order of their increasing atomic numbers. After helium which cannot be used for the same reasons as deuterium, comes lithium and then beryllium. Beryllium is a stable metal

and is often used. With 140 MeV mono-energetic protons incident on a thin beryllium target, the neutron energy spectrum of $\theta = 0$ is similar to that given on graph (2.5)1. This spectrum was obtained by the Harwell 'time of flight' group.

Lithium gives a slightly better neutron energy spectrum but is chemically active, and awkward to handle. Lithium deuteride, however, is a moderately stable compound. The neutron spectrum obtained from such a target will be the sum of the lithium spectrum and mono-energetic neutrons from the deuterium. The total number of neutrons produced by the deuterium in lithium deuteride is about half the total number produced by the lithium. Not only is the spectrum obtained from lithium deuteride more peaked than that from beryllium, but for a given loss of proton energy, more neutrons are produced. By hardening, (section 2.6) a final energy spectrum of given intensity may always be improved if more initial neutrons are available. Thus, the use of lithium deuteride instead of beryllium gives a double improvement in the hardened energy spectrum for a given hardened neutron flux.

It has been stated that lithium deuteride is a moderately stable compound. It is normally a fine white powder. It is hygroscopic and it interacts slowly with the oxygen of the atmosphere. It also decomposes if heated for above room temperature. It is highly inflammable. It may be bonded into

Fig (2.5.)1.

neutron energy spectrum from a Lithium hydride target in a mono-energetic proton beam., from Harwell data.

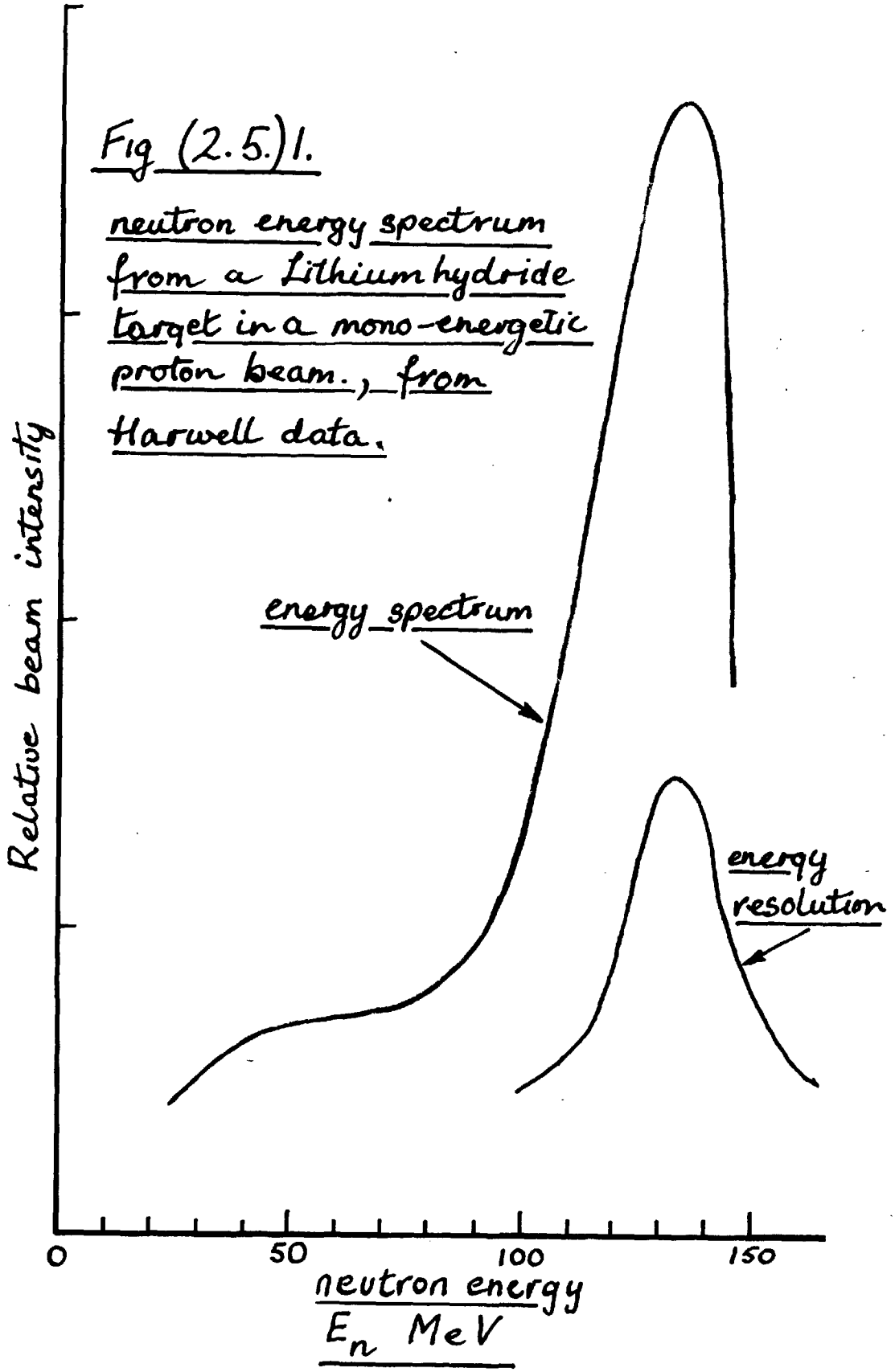

moderately strong greyish blocks with a density of about 0·9. These blocks should not be handled in the atmosphere more than can be helped, but no visible change is seen after they have been left out for periods up to a quarter of an hour. They can be filed or sawn quite easily. A lithium deuteride target was used, despite the inconvenience of handling it, because of the valuable improvement in energy spectrum it gave.

Since lithium deuteride will decompose if heated, it is necessary to consider the dissipation of the beam energy in the target. The cyclotron normally produces about 10^{10} protons 200 times a second. Due to multiple traversals, about 15 MeV is lost by each proton in the target, this represents a heat dissipation of 10 watts in the target. When the full beam was allowed to fall on the target, the lithium dueteride changed from grey to black, became hard and brittle, broke into small pieces and dropped on to the floor of the vacuum case. Two things were done in order to reduce this heating.

(1) The cyclotron was pulsed to give small bursts of only about four beam pulses each time the chamber was expanded, once every three seconds. This reduced the heat dissipation by a factor of about 150. It was not found possible to reduce the burst to less than four beam pulses.

(2) The target was made large, for the following reasons. Due to vertical oscillation of the circulating protons, the

number of protons that enter the target, and thus, the energy dissipated by the proton in a target, is independent of the height (b) (see figure (2.5)2) of the target. Because of multiple traversals, the energy dissipated and the neutron spectrum obtained are independent of the thickness (c) of the target, up to a certain limit. All the energy will be dissipated near (within 0·002") the end surface of the target, where the protons are first 'peeled off'. If this surface area is larger then the energy dissipated per unit area will be less and the heating less. The height (b) must be kept small in order to allow vertical collimation. The thickness (c) may be increased until it equals the effective target thickness due to multiple traversals. If it is further increased the energy dissipated per unit area will no longer be reduced and the neutron spectrum will suffer.

The height (b) chosen was one cm., the thickness (c) was chosen to drop the proton energy by 20 MeV, thus giving a single traversal and minimum heating. This thickness (c) was then two cm. Even with the above precautions the target surface became badly discoloured after exposure and was probably decomposing to some extent.

A bonded block of lithium deuteride two cm. x one cm. x six cm. was obtained. Due to its interaction with the atmosphere, the target was kept in a metal vacuum can. The

target was transferred to a spring loaded holder in the cyclotron vacuum tank just before the tank was pumped down for one of the experimental runs. When the tank was next opened the target was at once returned to the vacuum can. The target holder could be set in the required position by sighting on a wooden dummy target instead of the lithium deuteride. The alignment of the lithium deuteride was, however, always checked before closing the vacuum tank. The spring loaded holder (figure (2.5)2) was designed to ease the otherwise difficult operation of rapidly inserting the target into its holder while the latter was in the cyclotron magnet gap. The target may be moved in or out of the beam by passing a current through a coil (see figure (2.5)2). The coil and lower part of the holder was borrowed from the group at Harwell.

In order to obtain a maximum neutron energy of 60 MeV, the target was placed at a radius of 28", which is the mean radius of 50 MeV protons (see graph (2.4)1). The mean energy of the protons entering the target will be somewhat lower than 60 MeV due to the radial oscillation of the protons. Neutrons were then selected by the collimator whose angles θ were approximately zero. The collimator was, thus , set in line with the target and tangential to the proton beam. The collimation will be described in section 2.7 and is illustrated in figure (2.7)1.

Figure (2.5)2 Target Holder

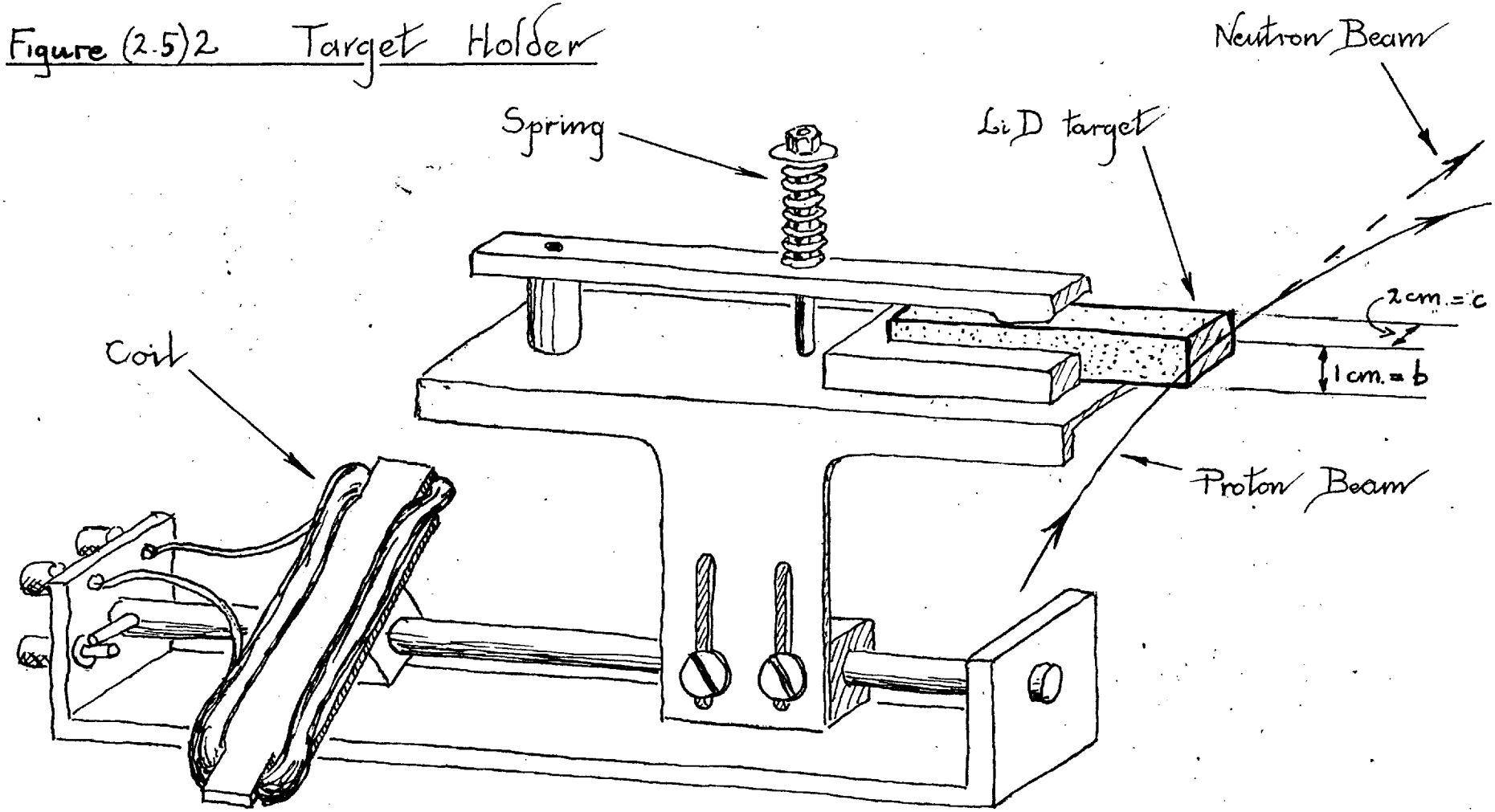

The energy spectrum of the neutrons leaving the target is shown in figure (2.5)3. This spectrum is taken from the results of the experiment and will be derived in chapter 4. It is appropriate to introduce it here since the choice of hardening, which will be discussed in the next chapter, was made after this spectrum was approximately known. The spectrum is seen to have a peak about 20 MeV wide. This is expected due to the thickness of the target. The relative magnitude of the low energy tail in this spectrum is very much larger than in the time of flight beryllium spectrum from 140 MeV. This cannot be entirely accounted for by the difference between the two target materials, or by the effect of multiple traversals. It is probably a direct result of using a lower initial proton energy. This is expected to give a worse neutron spectrum due to the further departure from the impulse approximation condition (2.5/1). The binding energy of lithium (B_{Li}) is approximately 42 MeV. Thus for E_b = 140 MeV, η = 0·3 and for E_b = 60 MeV η = 0·7.

This spectrum clearly does not satisfy the spectrum requirement derived in section 2.3. Since the intensity of neutrons is high however, considerable hardening may be employed. Before considering this hardening, it will be interesting to consider the choice of target for a polarized beam. The polarized spectrum will then be compared with the unpolarized spectrum.

Figure (2.5)3 Unpolarized neutron spectrum using lithium deuteride target, $\theta = 0$.

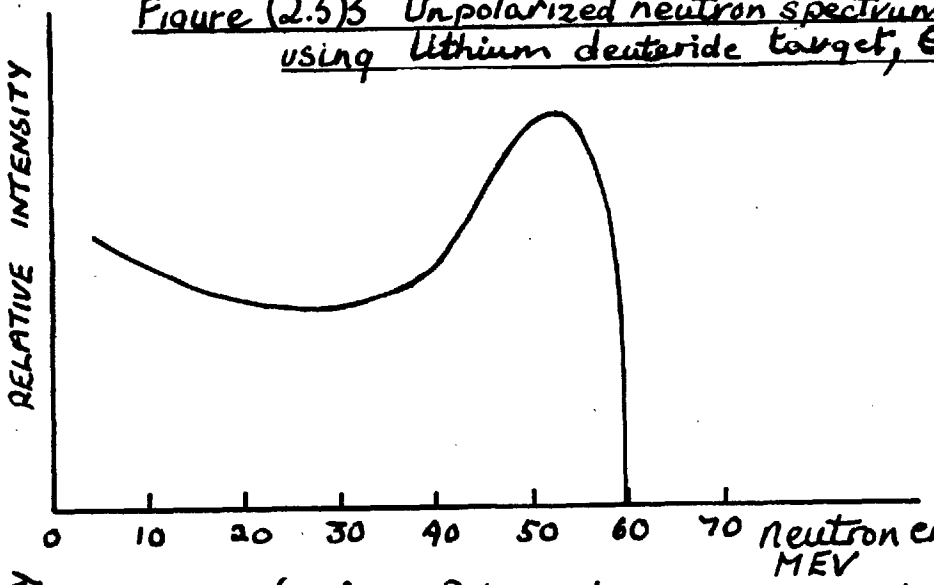

Figure (2.5)4 Polarized neutron spectrum using beryllium target, $\theta = 40°$.

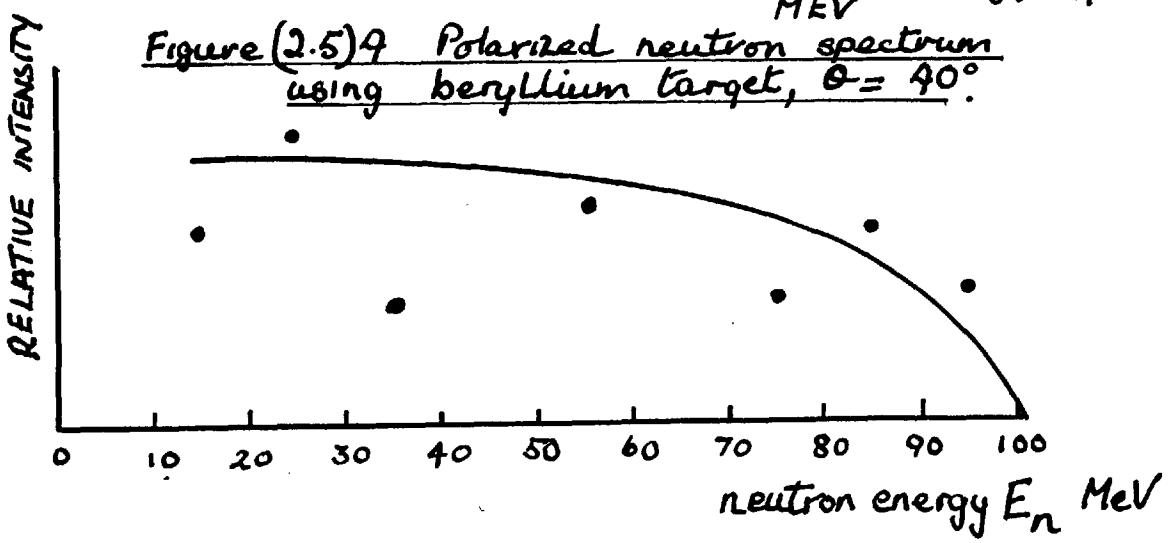

Lithium deuteride is not a suitable target to use to obtain a polarized beam because the polarization of the lithium and deuterium are of opposite sign. A polarized beam was obtained using a beryllium target and selecting neutrons at an angle θ of 40°. The beryllium target was placed at a radius of 37", which is the radius of the orbit of 100 MeV protons. It was so placed that neutrons from it passed down the same collimator as those from the lithium deuteride target. Either target could be brought into the beam by passing currents through the coils on the target holders (figure (2.5)2).

The energy spectrum of the polarized beam is shown on figure (2.5)4. Not only does the spectrum have no peak but the intensity of neutrons in the polarized beam was only 1/3 that in the unpolarized beam. The worse spectrum is due to the lack of deuterium and the further departure from the impulse approximation: B_{Be} = 56 MeV, η = .94. The loss in intensity is due to the larger angle θ and the lower efficiency of beryllium compared with deuterium as a producer of neutrons. As a result of the lower intensity the polarized beam cannot be hardened as much as the unpolarized beam and the difference between the two hardened spectra will be greater than those between those in figures (2.5)3 and (2.5)4. In the next section the effect of hardening on both polarized and unpolarized spectra will be calculated.

2.6 HARDENING.

Several times in the above section it has been stated that the energy spectrum of a neutron beam may be improved by a process of hardening. By an 'improved' spectrum is meant a spectrum in which there are relatively more neutrons with a higher energy. In this section the theory of the process of hardening will be described and its effect on the polarized and unpolarized beam spectra calculated. The final spectra will then be considered in the light of the 'neutron spectrum requirement' derived in section 2.3. From this discussion will follow the reasons for photographing several expansions on the same frame.

First the process of hardening itself will be considered. If a collimated neutron beam is passed through some 'hardening material' then a neutron in the beam will either make one or more nuclear interactions in the material, or pass through without being affected in any way. As a result of any nuclear interactions produced by the beam in the material other neutrons may be emitted. It will be shown in the next section that the probability of such emitted neutrons passing down the beam and entering the chamber, can be, and was, made small. Thus the effect of the hardener is simply to reduce the intensity of the beam entering the chamber by the probability that any given particle heading for the chamber will make a nuclear interaction

in the material. If $n_1(E_n)$ is the number of neutrons heading for the chamber before the hardener and $n_2(E_n)$ is the number that arrive, then it can be shown that

$$n_2(E_n) = n_1(E_n)h(E_n), \qquad 2.6/1$$

where $$h(E_n) = e^{-g\,\sigma_h(E_n)\,\rho\,N_A}$$

and g = length of hardener

$\sigma_h(E_n)$ = total cross section of hardener, per nucleon

ρ = density of hardener

N_A = Avogadro's number.

Consider now a hardening material such that its cross section $\sigma_h(E_n)$ decreases with increasing energy. From equation 2.6/1 and 2.6/2, it then follows that for any initial spectrum ($n_1(E_n)$) the final spectrum ($n_2(E_n)$) may be 'improved' if g is increased. The effect of increasing g is, however, always to reduce the final neutron intensity. It also follows that the improvement is larger if the rate of change of $\sigma_h(E_n)$ with E_n is greater. For comparison, approximate values of $\sigma_h(E_n)$ for various different elements and substances are plotted on graph (2.6)1. It is seen the lighter elements have larger rates of change of $\sigma_h(E_n)$ and are thus more suitable as hardening materials than the heavier elements. Hydrogen is clearly the best hardening material. If the intensity of the neutron beam is known, and the number of events required per

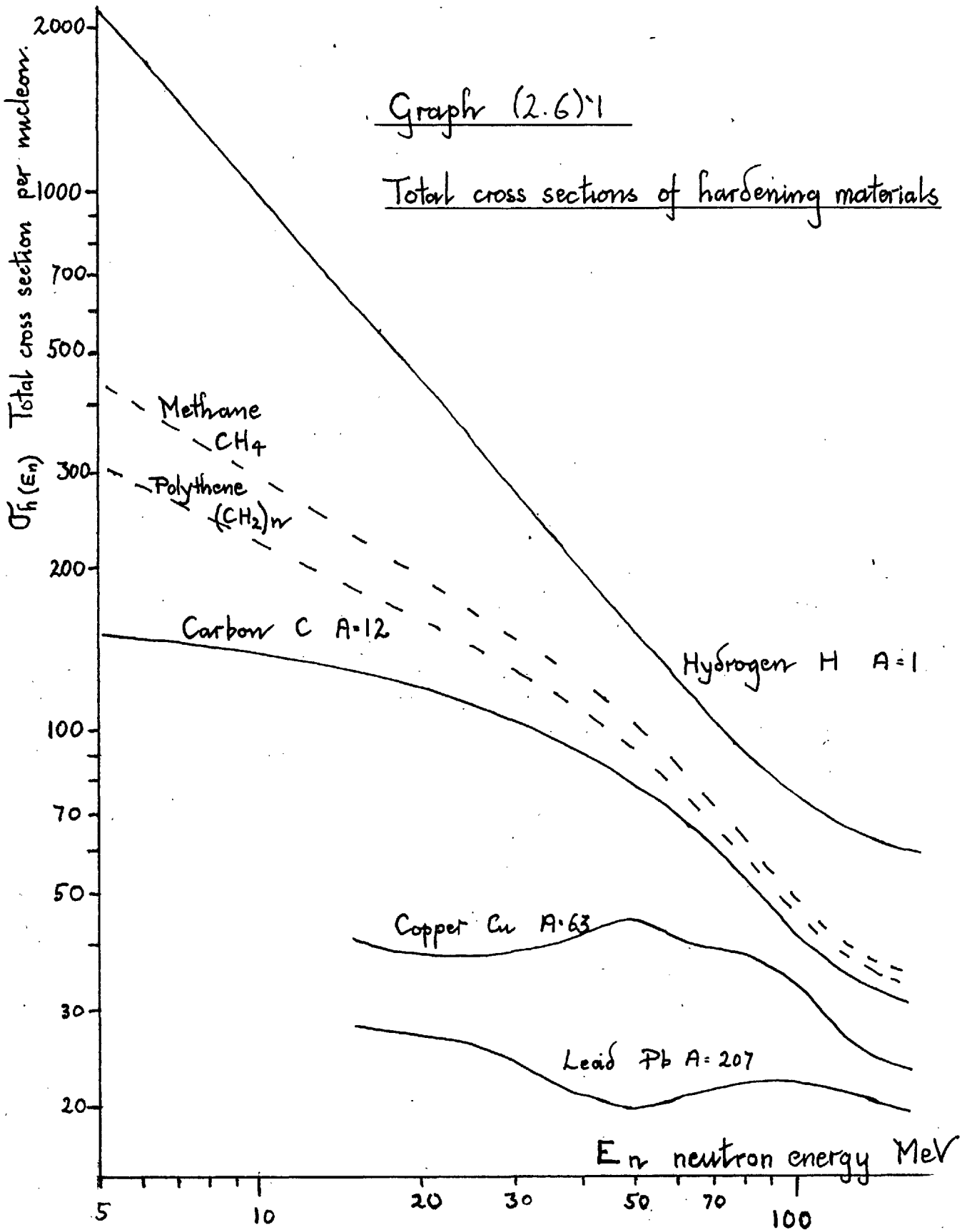
Graph (2.6)-1
Total cross sections of hardening materials
$\sigma_t(E_n)$ Total cross section per nucleon
2000
1000
700
500
300
200
100
70
50
30
20
Methane
CH_4
Polythene
$(CH_2)_n$
Carbon C A=12
Hydrogen H A=1
Copper Cu A=63
Lead Pb A=207
E_n neutron energy MeV
5
10
20
30
50
70
100

expansion is decided, then the correct length (g) of hardening material can be calculated. It works out that for 30 events in each expansion 50 ft. of liquid hydrogen would be required. This is not practicable. As an alternative to hydrogen, polythene $(CH_2)_n$ is often used. There are several other possibilities which listed in order of merit include: lithium deuteride (LiD) and lithium hydride (LiH), both of which would be very good, beryllium, boron hexahydride (B_2H_6), and methane (CH_4). The factor $h(E_n)$ for different lengths of polythene and liquid methane are given in the table below.

Table of $h(E_n) = e^{-g \sigma_h(E_n) \rho N_A}$

(a) For polythene $(CH_2)_n$, $\rho = 0.92$

E_n MeV =	5	15	25	35	45	55	h(15 MeV) / h(55 MeV)
g cm.				$h(E_n)$			
12	·26	·3	·37	·46	·53	·58	0.52
20	·087	·135	·188	·272	·368	·398	0.34
30	·025	·050	·082	·142	·202	·252	0·19
40	·0074	·018	·034	·074	·120	·159	0·11
50	·0022	·0067	·015	·038	·069	·100	0·067
60	·0007	·0025	·007	·020	·040	·063	0·040

(b) For Methane (CH_4) $\rho = ·415$

40	·014	·086	·190	·281	·343	·436	0·197
60	·0015	·025	·087	·153	·223	·317	0·079
80	·0002	·0075	·037	·077	·118	·192	0·039
120		·0006	·007	·023	·050	·078	0·008

Polythene was, in fact, used as a hardener, but the possible use of methane was also considered.

It will be remembered that the maximum number of tracks per photograph, that could reasonably be scanned was about 30. The lengths of polythene hardeners to give this number of tracks from the unpolarized and polarized beams were 20 and 10 cm. respectively. In order to compare the resulting energy spectra with the spectrum requirement derived in section 2.3, the spectra of neutron-scattered protons ($q(E_n)$) that would be obtained from the two beams are plotted on graphs (2.6)2 and (2.6)3.

Consider the spectrum requirement for the unpolarized spectrum. Using the equations (2.3/7) and (2.3/8), and figure (2.6)2,

$$\beta = \frac{\int_0^{22.5} q(E_n)\, dE_n}{\int_0^{\infty} q(E_n)\, dE_n} = \frac{1}{2.5}$$

$$\alpha = 80\beta = 32$$

The coefficient α, defined in section 2.3, is the relative number of protons within the deuteron limits of range and angle, compared with the number of deuterons. It was shown in section 2.2, equation 2.2/2 that if q_d deuterons are present, the resultant error in the proposed determination of capture cross section will be

$$\frac{1}{\sqrt{q_d}} \cdot \sqrt{1+\alpha} = \frac{6}{\sqrt{q_d}}$$

If 3,000 ft. of film were exposed, which was the maximum length that could be considered, only about 23 deuterons would be

Graph (2.6)2

Energy spectrum of n-p scatters from the unpolarized beam with 20 cm of polythene hardening.

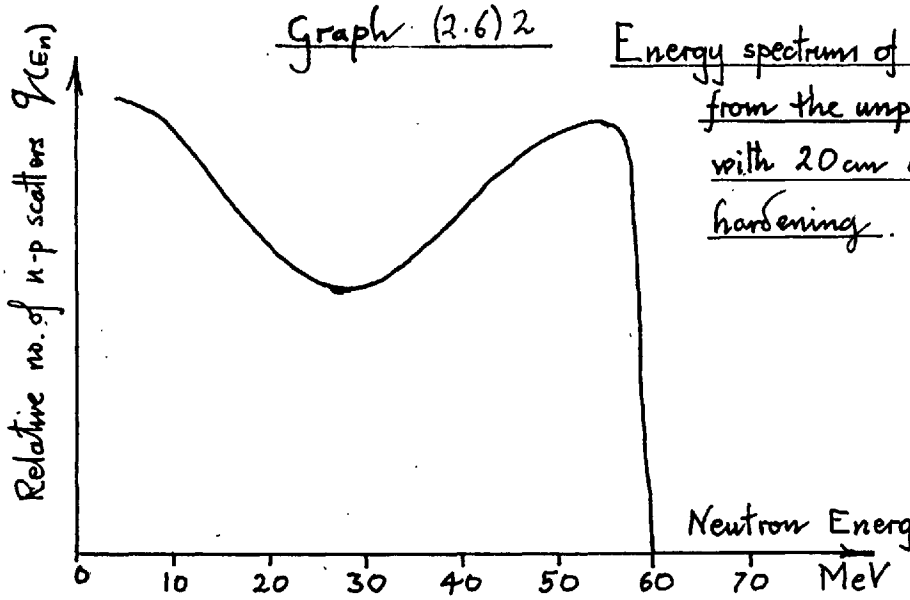

Graph (2.6)3

Energy spectrum of n-p scattering events from the polarized beam with 12 cm of polythene hardening.

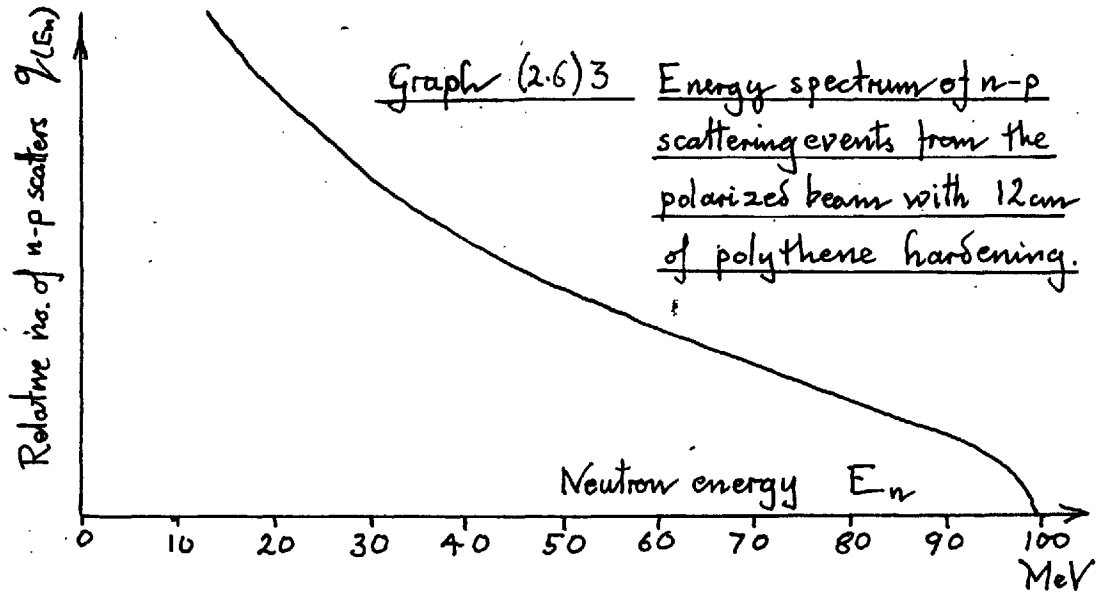

Graph (2.6)4

Energy spectrum of n-p scattering events from the un-polarized beam with 50 of polythene hardening.

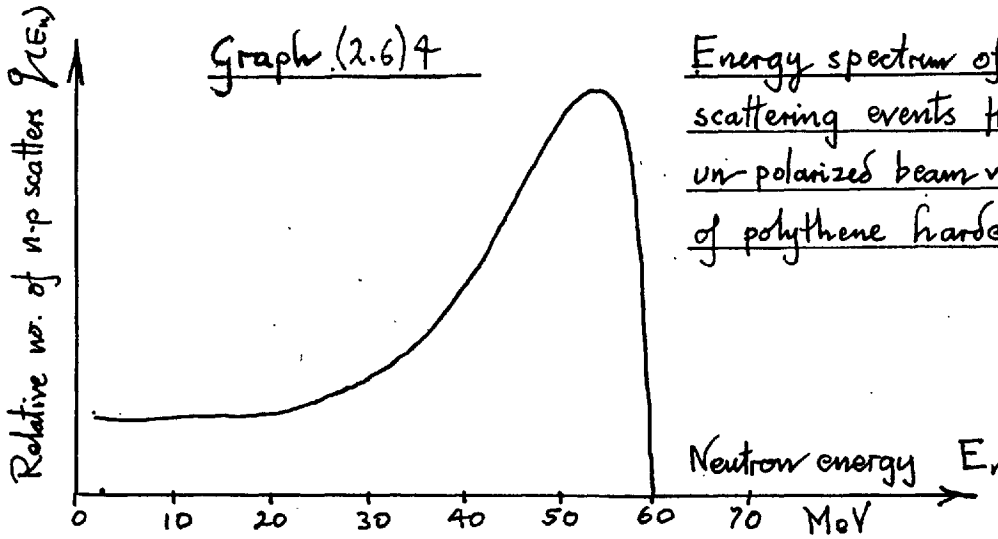

expected and the error in the capture cross section would be 120%. This would not be satisfactory.

The polarized spectrum, being even worse than the unpolarized spectrum, would give even larger errors, and will not, therefore, be considered further.

Various possibilities of improving the situation had now to be considered. If, for instance, a greater length of hardener were employed two effects would follow:

(a) The spectrum would be improved which would tend to reduce the capture cross section error.

(b) The intensity of the neutron beam would be reduced and thus the number of deuterons would be decreased. This would tend to increase the error.

The question is: which of the two effects dominates? Keeping the quantity of film exposed constant, the variation of neutron-capture error ($K_{\sigma_{cap}}$) with thickness of polythene hardener (g) is plotted on graph (2.6)5 (the line marked 'One exposure'). The left hand end of this curve (A) represents the condition where the maximum number of tracks per photograph that can be scanned, and thus the minimum length of hardener, is used. As more hardener is used the spectrum is improved and the number of deuterons reduced. This is seen to result in an increase of the error. It is concluded, that the minimum length of hardener, and thus the maximum number of tracks per

Graph (2.6)5 Variation of capture cross section error with polythene hardening

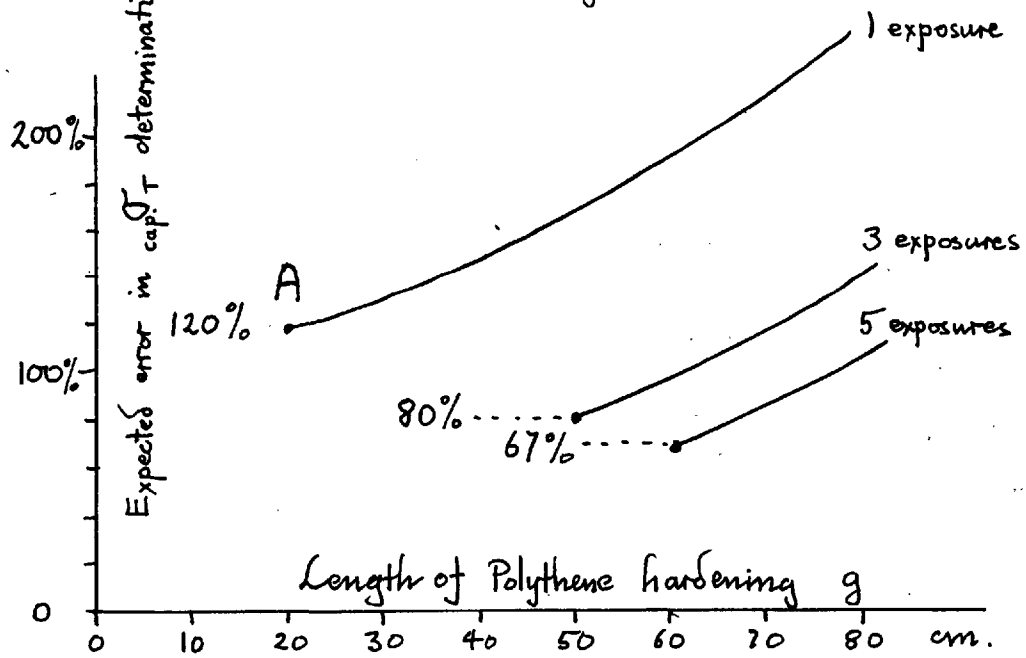

Graph (2.6)6 Variation of capture cross section error with methane hardening

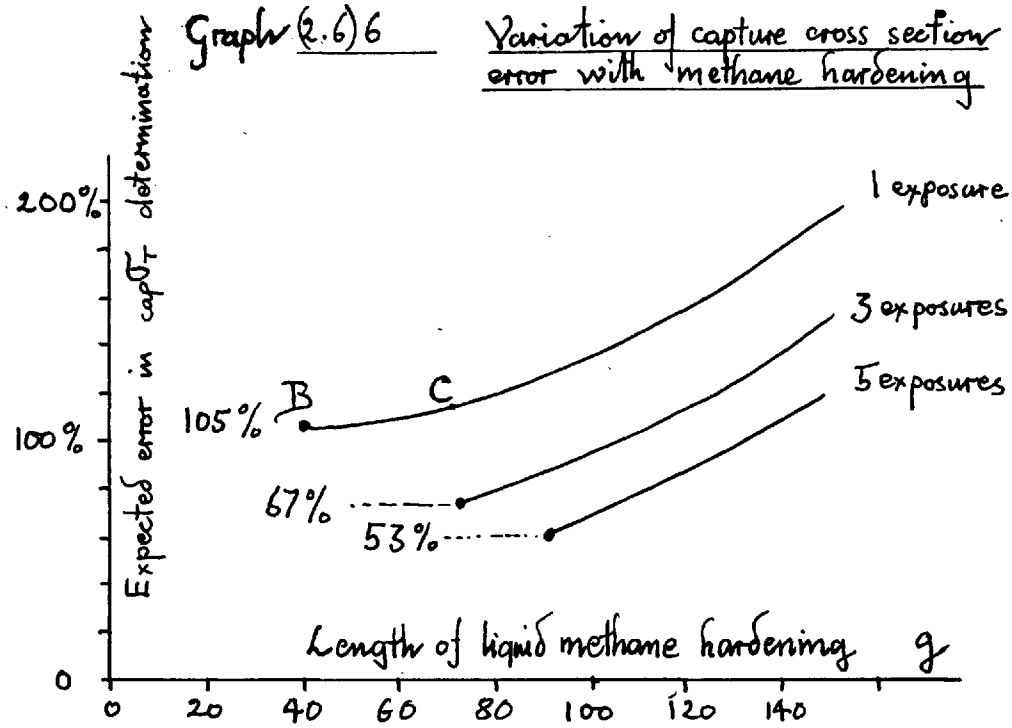

photograph should be used. The second possibility was the use of liquid methane as a hardening material. The curve of error against length of methane is shown in figure (2.6)6 (the curve marked 'one exposure'). It is seen that the minimum error is now lowered to 105%, not a very significant reduction. An interesting effect is that there is no longer any advantage in using the minimum length of hardener, represented in figure (2.6)6 by the point (B). It is seen, that the error does not rise significantly till the length of methane hardener has been increased beyond the point (C).

The third possibility was to photograph several expansions one one frame of the film. The condition that not more than 30 tracks should appear on one photograph would then require fewer tracks in each expansion. Thus more hardener must be used. The number of tracks, and thus of deuterons, on a given length of film need not, however, be changed. Thus the spectrum factor α can be improved while the number of deuterons q_d is left the same. The resultant error will be reduced. In order to expose the same length of film, more cyclotron time was required, but this presented little difficulty since the major labour was not in running the chamber, but in scanning the film. The expected errors in capture cross section have been calculuted assuming that the same 3.000 foot of film is exposed, first with three expansions to each photograph and then

with five. The results are also plotted on graphs (2.6)5 and (2.6)6.

It is seen that in all cases now, irrespective of which hardener is used, it is desirable to use the minimum length of hardener. Using polythene the minimum errors are reduced from $\pm$ 120% to $\pm$ 80% with three expansions per photograph, and to 67% for five expansions.

The maximum number of expansions per photograph was limited by the background illumination, since at each exposure this added up while the intensity of a track remains what it would be in a single exposure. If a photograph with three exposures, e.g. figure (2.1)4, is compared with a photograph with one exposure, e.g. figure (2.1)3, the increase in background is tolerable. If more exposures were given this was not so. It was decided, therefore, to give three exposures to each photograph. 50 cm. of polythene hardener were used, which gave approximately 25 scattering events in each photograph. The spectrum $q(E_n)$ obtained, has been given on graph (2.6)4. This curve was, of course, taken from the results that will be given in chapter 4. In this case $\beta = \frac{1}{6}$, $\alpha = 13$.

The placing of the hardener and the collimation will be described in the next section. In particular the assumption that a negligible number of neutrons emitted from interactions in the hardener reach the chamber, will be checked.

2.7 COLLIMATION.

The objectives of the collimation will first be stated. The final arrangement will then be described and the reasons for its choice briefly discussed. The condition that a negligible number of neutrons scattered in the hardener enter the chamber, will then be checked. The method of aligning the collimators and the chamber will be described and finally an experimental check of this alignment given.

The main object (I) of the collimation is to limit the cross section of the beam. The beam must fill the required part of the chamber but not extend so as to enter and scatter in other parts of the apparatus. In particular the beam had to be kept from entering the heavy brass chamber window clamping rings, 3·7 cm. apart, either side of the beam (see figure (2.7)1).

In arranging the collimators, a second (II) important consideration must be borne in mind. The direction of neutrons that produce events in the chamber must be taken from a knowledge of the beam direction. Since the target is small and a large way from the chamber, this direction is well defined, but only so long as most of the neutrons entering the chamber do come, directly from the target, and not, after being scattered in the defining collimator.

As has been mentioned in the last section, another source

Figure (2.7)1 Collimation

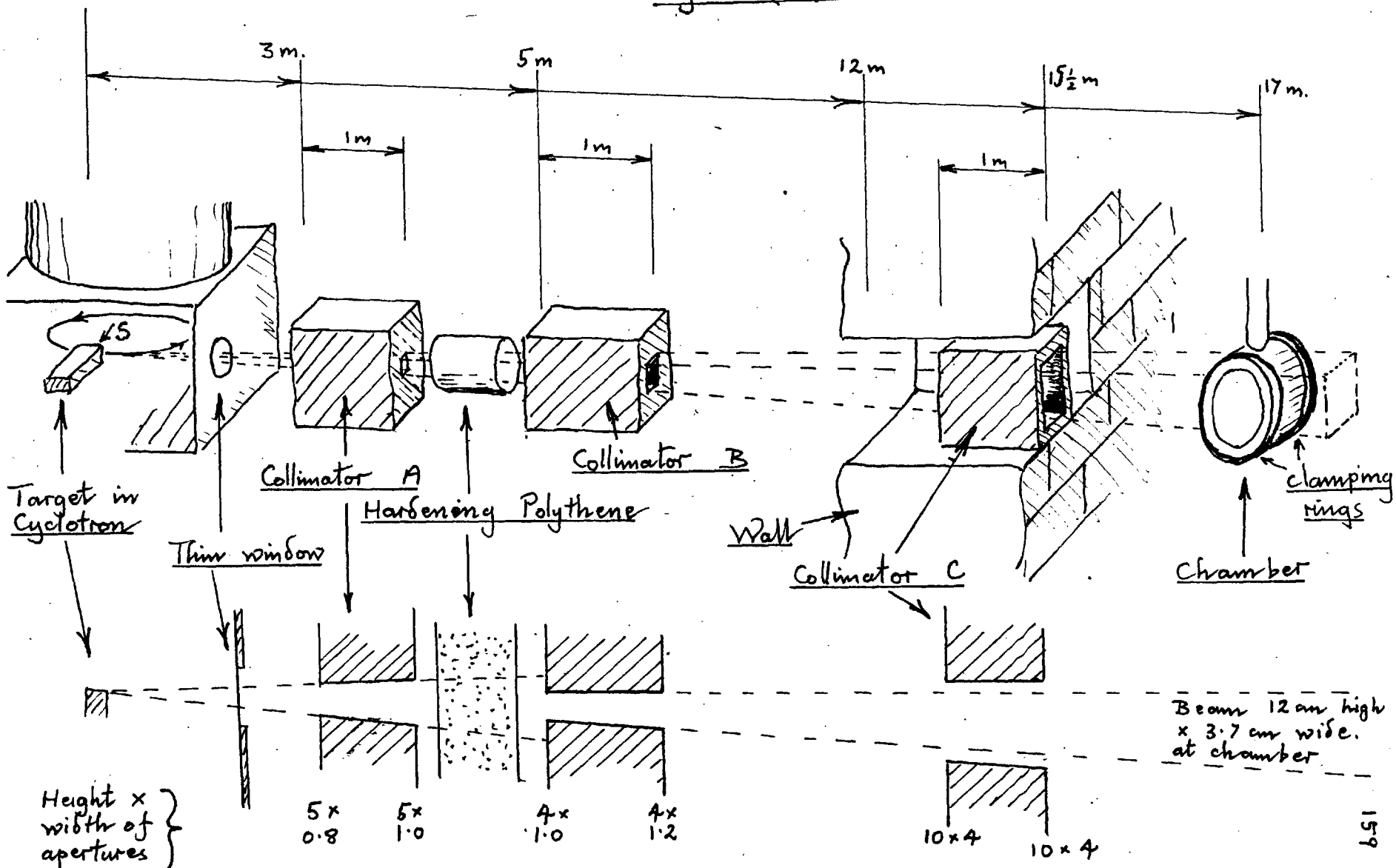

of neutrons, other than direct from the target will be the hardening material through which the beam must pass. The collimation must, therefore, also (III) be such that as few excess neutrons pass through the hardener as possible, and that by placing the hardener a long way from the chamber, few of the emitted neutrons enter the chamber.

Consider the arrangement of hardener and collimators illustrated in figure (2.7)1. The source of scattered neutrons will be near the end surface (s) of the target. Viewed from the chamber this will appear like a thin vertical line one cm. in height. The boundaries of the beam were only to be accurately defined in the horizontal direction, to avoid the clamping rings; the vertical collimation being of much less importance. Thus, the source could be regarded effectively as a point.

The first collimator (A) was chosen to limit the flux entering the hardener to a cross section only slightly greater than that required to fill the succeeding collimator. Both it and the hardener were placed as far from the chamber as possible, in accordance with requirement III.

The second collimator (B) was the defining collimator. It was set so that, at the chamber the beam should have the required cross section - a rectangle 3·7 cm. wide and approximately 12 cm. high (requirement I). This collimator (B) was placed as

far as possible, from the chamber, in order that the probability of neutrons scattered in its walls, entering the chamber be small, in accordance with requirement III.

A third clearing collimator was set in a concrete shielding wall near the chamber. Its dimensions were such that neutrons from the target, defined by the second collimator (B), should just not touch it. Its purpose was to stop neutrons scattered by the hardener or collimators from entering other parts of the bubble chamber and apparatus.

From the dimensions of the arrangement shown in figure (2.7)1 it is now possible to calculate the proportion of neutrons entering the chamber that come from interactions in the hardener. Let n_o be the number of neutrons after the collimator (A) entering the hardener. Let the proportion of these that would pass through the defining collimator (B) and enter the chamber, if there were no hardener, be ζ ; and with the hardener be ζ' . Thus the number of neutrons in the chamber coming direct from the target is:

$$n_2 = n_o \zeta \zeta'$$

If every interaction in the hardener emits one neutron, then the number of these that will enter the chamber cross section A at a distance ℓ from the hardener is:

$$n_3 = n_o (1 - \zeta') \cdot \frac{\sigma \text{ forward}}{\sigma \text{ total}} \cdot \frac{A}{\ell^2}$$

Now the cross sections (Van Zyl, 1956, Phil. mag. 1, 1003)

$$\frac{\sigma \text{ forward}}{\sigma \text{ total}} < 2$$

$$\xi = 1/100$$

$$\zeta = 1/4$$

$$A = 26 \text{ cm}^2$$

$$\ell = 1{,}200 \text{ cm.}$$

From which the proportion of emitted neutrons is:

$$\frac{n_1}{n_2} \leqslant 1\%$$

which will be regarded as a negligible proportion.

The collimation system described above was set up with the aid of a 1¼" theodolite. The errors in alignment of the main collimator B were ± 1 mm. This could cause errors in the bounds of the beam in the chamber of the order of 3 mm. Experimentally, the width of the beam, as found from the observed distribution of neutron induced events in the chamber, was correct to within these limits. Before discussing this distribution further, the method of positioning the chamber will first be described.

As has been stated, the only method of knowing the direction of a neutron that makes an interaction in the chamber, is from a knowledge of the relative position of the chamber and neutron

beam. As will be discussed in section (3.1) directions in the chamber were given with respect to three axes, x, y, z. These axes were defined with respect to the film and lens positions (see figure (3.1)1). It was convenient, therefore, to have the neutron beam parallel with one of these axes. The axis chosen was the (z) axis, which was defined as the perpendicular to the plane including the two lens axes. This was, approximately, perpendicular to the side of the stereo camera. In order to align the beam direction to this axis the following procedure was followed. A mirror was mounted on the front of the vacuum case so as to cut across the required path of the beam. With the aid of engineering measuring equipment, this mirror was set parallel with the side of the camera. A cross was marked on the face of the mirror, where the beam axis should cut it. The theodolite was placed so that it looked down the beam axis to where the chamber would stand. The chamber was then brought into position. Looking through the theodolite, the cross on the mirror and a reflection of the theodolite were seen. The chamber position was adjusted till the cross on the mirror and the image of a cross in front of the theodolite coincided on the eyepiece fiducial. The axis of the theodolite was then perpendicular to the mirror and thus, parallel to the (z) chamber axis. The errors introduced in the alignment with the theodolite were of the order of 0.1°. In the mechanical placing

of the mirror parallel with the camera side, the errors were of the order of $0{\cdot}5^{\circ}$. The alignment of the side of the camera with the lens axes was probably better than $0{\cdot}2^{\circ}$. The total angular error in alignment of the beam and chamber (z) axis was thus less than $0{\cdot}7^{\circ}$. The errors in placing the cross on the mirror, and thus of the lateral positioning of the beam were of the order of $\pm$ 3 mm. These errors in positioning the cross were rather large because of a movement of the chamber, due to the squashing of gaskets, when the vacuum case was pumped down. The measurements on the chamber position had to be made without a vacuum and these movements could only be guessed. The problem of measuring the position of the chamber will arise again when the optics are discussed in section 3.5.

Although strictly belonging to the chapter 4 on results, an experimental check on the above alignments will now be described. As has been said, the width of the collimated beam and the relative position of this beam in the chamber can be checked by observing the distribution of neutron-induced events in the chamber. On figure (2.7)2 the positions with respect to the beam axis of left hand ends or 'starts' of tracks in the chamber are given. On graph (2.7)3 are given the horizontal distribution of these 'starts'. The positions of the two brass rings, 3·7 cm. apart are marked by dotted lines. It is seen that the number of 'starts' falls off rapidly at the line

Figure (2·7)2 Distribution of 'starts' of tracks in the cross section of the beam.

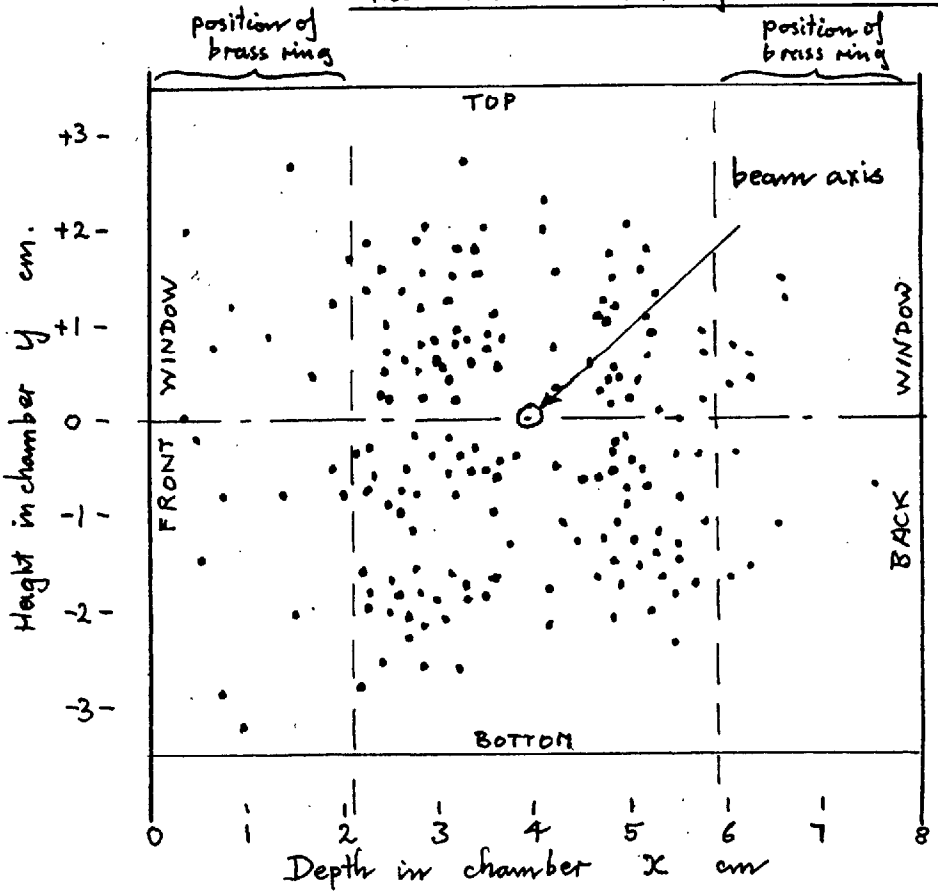

Fig(2·7)3 Distribution of starts in chamber depth

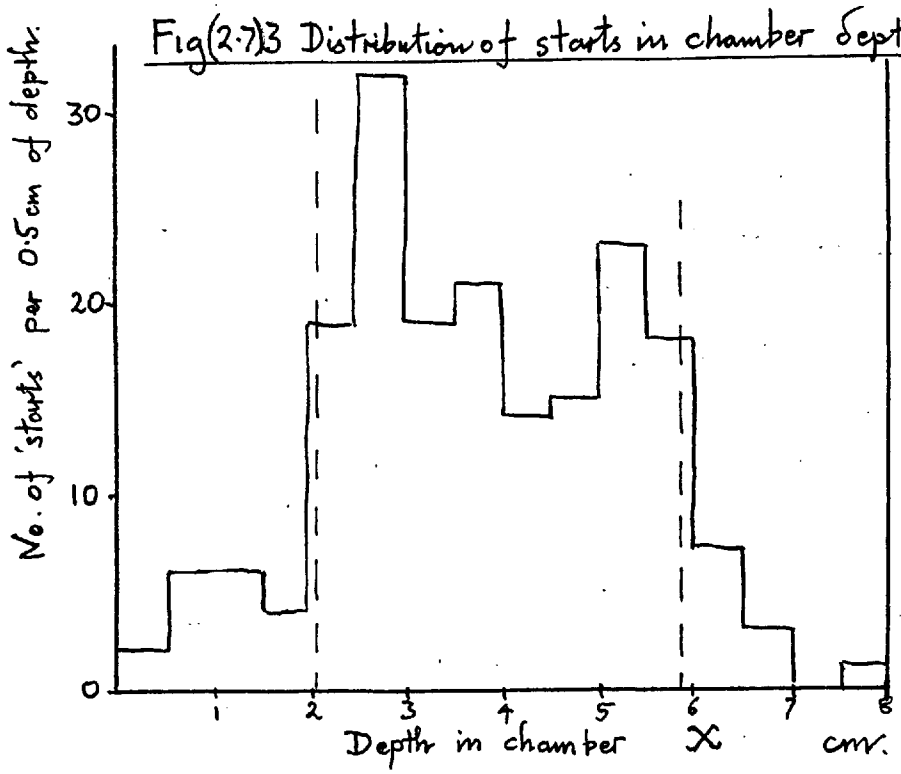

indicating the edge of a brass ring, but that there are still a considerable number beyond it. The rapid drop in intensity at the two edges of the brass rings indicate that the collimation had provided a beam of the correct width and that the position of the chamber in this beam was also correct. The number of events beyond the edges of the rings, about 15% of the total, are presumably due to neutrons that have been scattered in the metal of the vacuum case, shields and chamber wall. The tracks they produce, since they are from neutrons not in the beam are 'spurious' tracks according to the definition of section 2.2.6. In the experiment, only tracks with their 'starts' within the intended beam cross section will be selected, and the 15% of tracks whose 'starts' lie outside it, will be rejected. Some of the tracks considered may still have come from similar scatterings in the vacuum case etc., and thus be spurious tracks. If it is assumed that the spatial distribution of 'starts' of spurious tracks is uniform, then in the selected tracks there will be another estimated 15% of these spurious tracks. In chapter 4 the spurious tracks will be considered again and a similar figure of about 15% given for their proportion of the total number of selected tracks.

A second experimental check one would like to make, is of the alignment of the beam direction with the chamber z axis. The neutron direction cannot be obtained accurately from the

spatial distribution of neutron-scattered protons since this is roughly isotropic. Only the neutron-capture deuterons are likely to provide the check. Ideally, as has been shown in section 1.6, the distribution of deuteron tracks should be peaked at a small angle of about 4°. If the directions of measured tracks are marked on a θ, χ, polar graph then the marks corresponding to deuterons should lie in a ring of 4° radius, while the marks corresponding to neutron-scattered protons should be evenly distributed.

Due to an insufficient number of deuterons and too low an accuracy, no ring was observed. There was, however, a general increase in the number of tracks at angles less than 5°, and this was approximately centred on $\theta = 0$, or the z axis. (see figure 4.4.4) and the further discussion of this distribution in section (4. 4)). The accuracy of alignment of the beam and z axis had, thus, to be assumed equal to the previous estimate of $\pm 0{\cdot}7^{\circ}$, since the above check only confirmed that no gross error of alignment greater than two or three degrees had occurred.

2.8 THE EXPERIMENTAL RUNS.

The arrangement of targets in the cyclotron, of the collimation, and placing of the chamber have already been discussed. In this section the actual experimental runs will be described. Considerable time and effort were involved in preparing the chamber, clearing space for it in the beam, and positioning the apparatus and collimators. It was, therefore, desirable to have few, but reasonably long periods of cyclotron time, and it is these periods that are referred to as 'runs'. Before each run, which lasted for three or four days, the chamber was operated, out of the beam, in order to check that the chamber was working satisfactorily. Despite these preliminary tests, it was, in practice, found that the first two days of a run were usually devoted to clearing difficulties and faults arising both out of the chamber and cyclotron.

Two runs were performed with the modified chamber during the summer of 1959. The particular object of the first, in May, was to determine the spectra of, and proton contamination in, the polarized and unpolarized neutron beams. In fact during the first run considerable difficulties were encountered, and only about 5,000 expansions were performed. The results were sufficient, however, to show how bad the spectra were. Only then was the hope of using the polarized beam abandoned and the

photography of several expansions on one film proposed.

The results that will be given in chapter 4 were all derived from the second, and main, experimental run. Again difficulties were met with, and it was only possible to expose 2,000 ft. of film, instead of the 3,000 ft. hoped for. On this film, about 6,000 useful stereo-pairs of photographs of 18,000 expansions were obtained. So far 1,756 of these photographs have been scanned for neutron-capture events, and smaller numbers scanned for the neutron energy spectrum and n-p differential cross section. The remaining photographs will be scanned during the coming year. The methods of scanning and measuring will be described in chapter 3, and the results obtained given in chapter 4.

CHAPTER 3.

MEASUREMENTS ON THE FILM.

3.1 CORRESPONDING AND NON-CORRESPONDING METHODS OF RECONSTRUCTION.

During the main experimental run of the bubble chamber in an unpolarized neutron beam, approximately 6,000 stereo-pairs of photographs were taken. These had then to be looked at, or scanned, and particular tracks measured. From these measurements the lengths and directions of the original tracks in the bubble chamber were reconstructed. Finally information, such as the initial neutron energies, was calculated from these lengths and angles. The calculations were all preformed by an electronic computer. In this chapter the methods used and calculations performed will be described.

The reconstruction of lengths and angles in the chamber, from measurements of the stereo-photographs will first be considered. It will be convenient to consider positions in the chamber with respect to a coordinate system x y z, with the y axis vertical. Directions of tracks in the chamber will be referred to by the angle θ, between the track and the z axis, and χ, between the projection of the track on z = 0 plane, and the y axis, (see figure (3.1)1). The chamber was photographed

Figure (3.1)1 Coordinate system

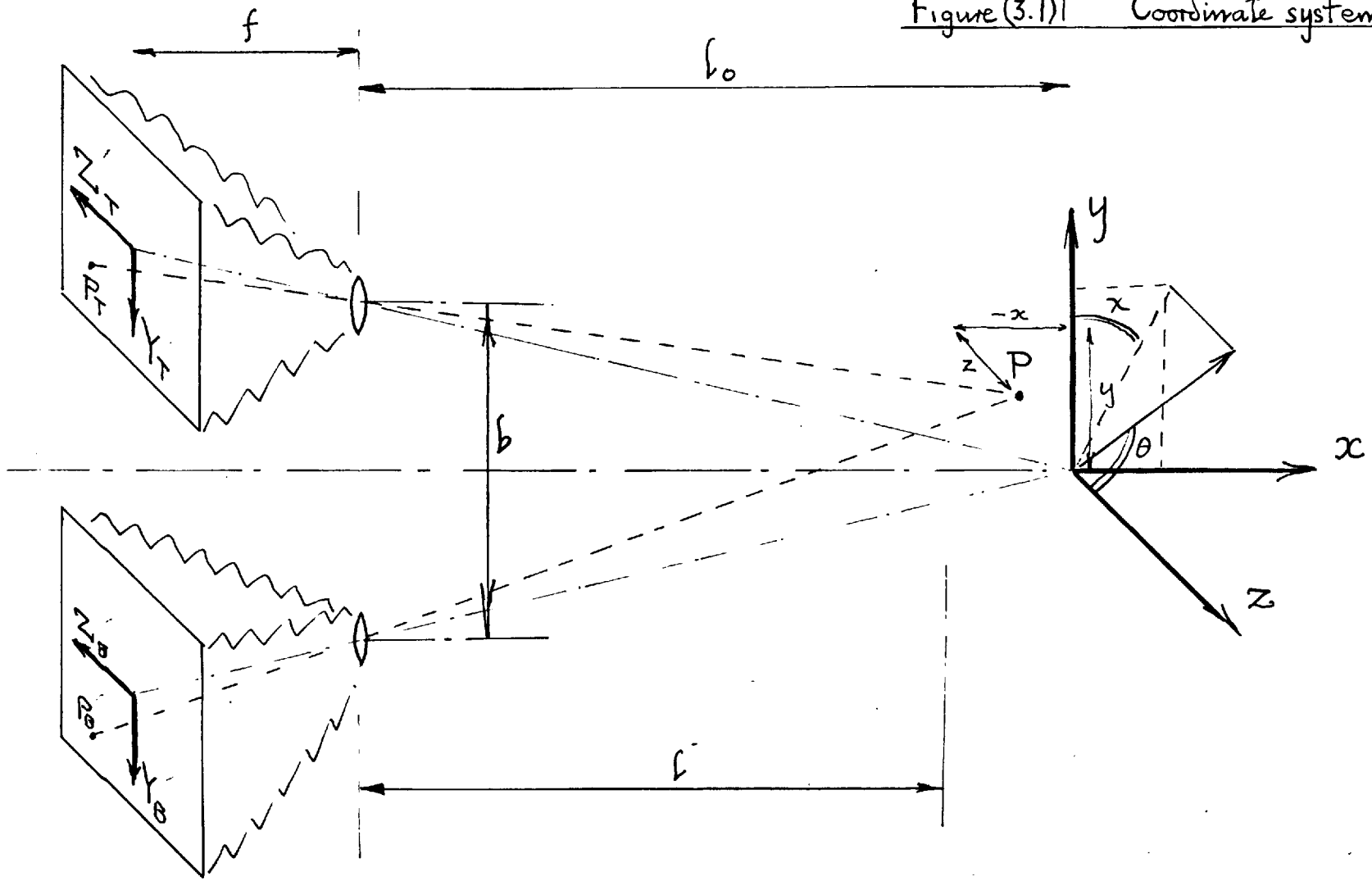

by two cameras, whose lenses, with respect to the chamber, were symmetrically above and below the negative x axis. Let the images of the y and z chamber axes on the film provide Y'_T and Z'_T film coordinate axes for the top film; and similarly Y'_B, Z'_B, for the bottom film. Consider now the images of a point P(x, y, z) on the two stereo films. It can be shown, assuming no lens distortions, that the coordinates x, y and z may be obtained from the film coordinates of these images using the following relations.

Let

$$\ell = \frac{bf}{(Y'_T - Y'_B) + \frac{bf}{\ell_o}}$$

$$x = \ell - \ell_o \qquad 3.1/1$$

$$y = \frac{\ell}{f} \cdot \frac{(Y'_B + Y'_T)}{2}$$

$$z = \frac{\ell}{f} \cdot Z'_B = \frac{\ell}{f} Z'_T$$

where ℓ_o is the perpendicular distance of the origin of chamber coordinates, to the appropriate principal plane, common to the two lenses; b is the distance between the lens axes; and f is the distance between the plane of the film and the other principal plane common to the two lenses.

It is seen that the Z' coordinates of the images in the two stereo-photographs are the same. This is important, since, if there are many points in the chamber, it enables the pairs

of stereo images of each point to be identified. If there are a number of tracks, both of whose ends are in the chamber, then these ends may be treated as points. Thus from the film coordinates of the ends of the images of the tracks, may be obtained the coordinates of the ends of the tracks in the chamber, and the lengths and angles of the tracks. This method of reconstructing the lengths and angles is known as a corresponding method, since it employs measurements on corresponding points on the two photographs.

If the ends of a track are not in the chamber, then any two points may be arbitrarily chosen on the track in one of the stereo-photographs. The corresponding points on the image of the track in the other stereo-photograph may then be determined by the fact that their Z' coordinates must be the same. The coordinates in the chamber of these two arbitrary points on the track may then be calculated, and thus the direction of the track determined. It is impossible, however, to select such corresponding points on the other stereo-photograph if the track lies parallel to the y axis. In this case all the points on the images of such a track have the same z coordinates. This method of reconstructing the directions of a track can be modified so that only the angles and one coordinate of each of the stereo-images is measured. The method of reconstruction is then known as a non-corresponding method.

The errors in determining directions in space, using corresponding and non-corresponding methods of reconstruction will now be compared. Allowance must be made for the fact that the error in determining the position of the end of a track image, in the direction of the track, will be greater, by a factor λ, than the error in determining the lateral position of a track. In the present case this factor (λ) was about two. Let K_ℓ be defined as the error in determining the lateral position of a track. The error K_{ϕ_T} in determining the angle ϕ_T between the track image and the Z axis depends on the two independent random errors in measuring the lateral positions of the track near its ends.

Thus,

$$K_{\phi_T} = \frac{\sqrt{2}\ K_\ell}{R_T}$$

where R_T is the length of the image of the track in the upper photograph. A similar relation holds for errors in measurements on the bottom photograph.

In order to estimate the errors in the reconstructed direction of a track due to the above errors in measurement the following approximation was made. The distance between the stereo-lenses was assumed small compared with their distance from the chamber. The difference between the angles ϕ_T and ϕ_B is them small and the mean of the two angles is approximately equal to the angle ϕ, between the projection of a track on the

x = 0 plane, and the z axis.

Then $$K_{\phi} \doteq K_{\phi_T} \quad .$$

Using this approximation it is shown in appendix C that the error K_{Ω} in measuring any angle in space using (a) a corresponding method, is (equation C2/6):

$$K_{\Omega(c)} \leqslant \hat{K}_{\Omega(c)} = K_{\phi}\left(\lambda^2 + 2\frac{\ell_o^2}{b^2}\left(\cos^2\phi + \lambda^2 \sin^2\phi\right)\right)^{1/2}, \qquad 3.1/3$$

(b) a non-corresponding method, is (C3/6)

$$K_{\Omega(NC)} \leqslant \hat{K}_{\Omega(NC)} = K_{\phi}\left(\tan^2\phi + 2\frac{\ell_o^2}{b^2} - \frac{1}{\cos^2\phi}\right)^{1/2} \qquad 3.1/4$$

$\hat{K}_{\Omega(c)}$ and $\hat{K}_{\Omega(NC)}$ are plotted against ϕ on graph (3.1)2, for $\frac{\ell_o}{b} = 3$. In the present case, $\frac{\ell_o}{b} = 3$ and $\lambda = 2$. It is seen that there is, in this case little advantage in using a non-corresponding method. A corresponding method usually could be and was, therefore, used.

An estimate of the error $K_{\Omega(c)}$ in any angle averaged over all directions in space is given in the appendix, equation C2/7:

$$K_{\Omega(c)} = 4 K_{\phi} \qquad 3.1/5$$

This will approximately equal the error $K_{\theta(c)}$ averaged over all directions. An estimate for the error in θ averaged over all χ but only for small θ is also given in the appendix,

Figure (3.1)2 Maximum errors in determining directions in the chamber ($\mathcal{E}_\Omega$). with stereo-ratio = S = 3

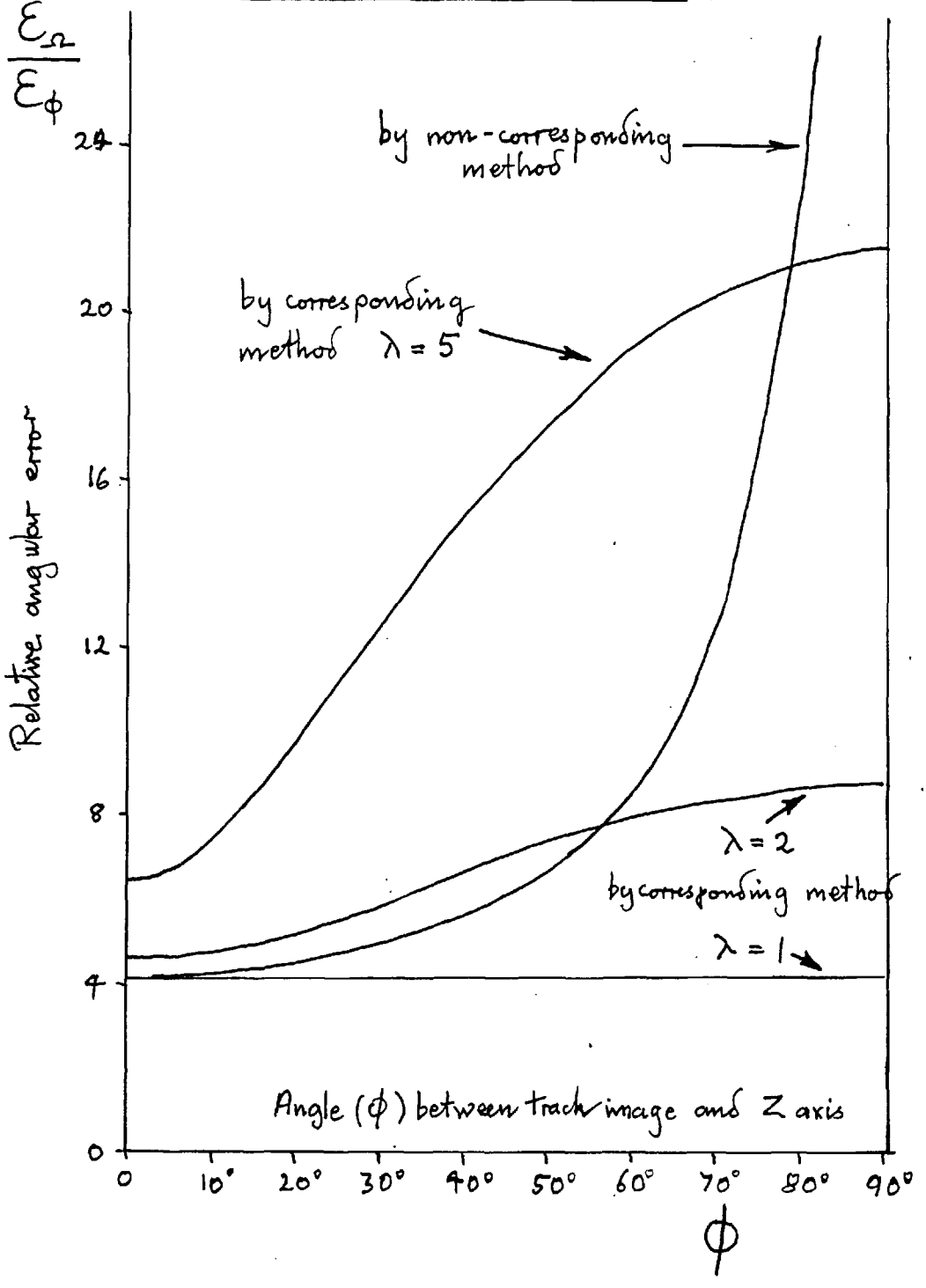

equation C2/9:

$$(\text{small } \Theta)\ K_{\Theta(c)} \doteqdot 3\ K_{\phi}$$

Thus it is seen that the estimated error in determining a large angle Θ is greater than that in a small angle Θ.

It is interesting to note that if a'measuring machine' had been used λ would probably have been equal to five, or more. It is then seen from the graph ((3.1)2) that there would be an advantage in using a combination of both corresponding and non-corresponding methods.

3.2 MEASUREMENT AND SCANNING.

The film was scanned and particular events selected by eye. When a required event had been selected, its coordinates were, at once, measured. This measurement will be described first and then different criteria of selection will be given in turn.

3.2.1 Measurement.

Three methods of measuring the film might have been used. The two stereo-photographs could have been projected simultaneously and the position where the two projected images of a track coincided measured three dimensionally. This method, which would avoid any reconstruction calculation, was rejected because of the long time required to make a measurement. Ideally, the film could have been measured on a high speed 'measuring machine', in which the film is moved, and the track positions measured photo-electrically. Such a machine was not available. The method used, was to project the stereo-photographs, one at a time on to a horizontal table. The arrangement was built by the Imperial College cloud chamber group under Dr. B. French. The ends of the tracks were then measured with respect to a coordinate system (Y, Z) marked on a card on the projection table. The method used to measure these coordinates will now be described.

The coordinate system (Y, Z) with respect to which the projected tracks were measured differed from the film coordinates (Y', Z') defined in the last section only by scale and origin. The card, on which this coordinate system was marked, was located with respect to the projected images of fiducial marks on the inside of the rear chamber window. The origin of chamber coordinates was taken to be in this plane and the distance (ℓ_o) became the distance from the camera lenses to this reference window. The card was marked, as shown in figure (3.2)1, with scaled lines drawn parallel to the Y axis at 10 cm. intervals. A draughtman's pantograph was used to hold a short, 10 cm. ruler parallel with the Z axis. If the left hand end of this ruler was placed on a point P, then the Y coordinate of that point could be read on the scaled line the ruler crossed. The Z coordinate could be obtained by adding the Z coordinate of this scaled line to the distance of the point from it. This distance could be measured with the same short ruler held by the pantograph. Figure (3.2)2 shows the details of this ruler.

The coordinates of track ends, read by the above method, were spoken out loud, and either written down by a second worker, or typed by him directly on to punched tape, ready to be fed into the computor. Which procedure was used, depended on how frequently measurements were made and thus on the type of events being scanned for. This scanning will now be described.

Figure(3.2)1 Reprojection Table

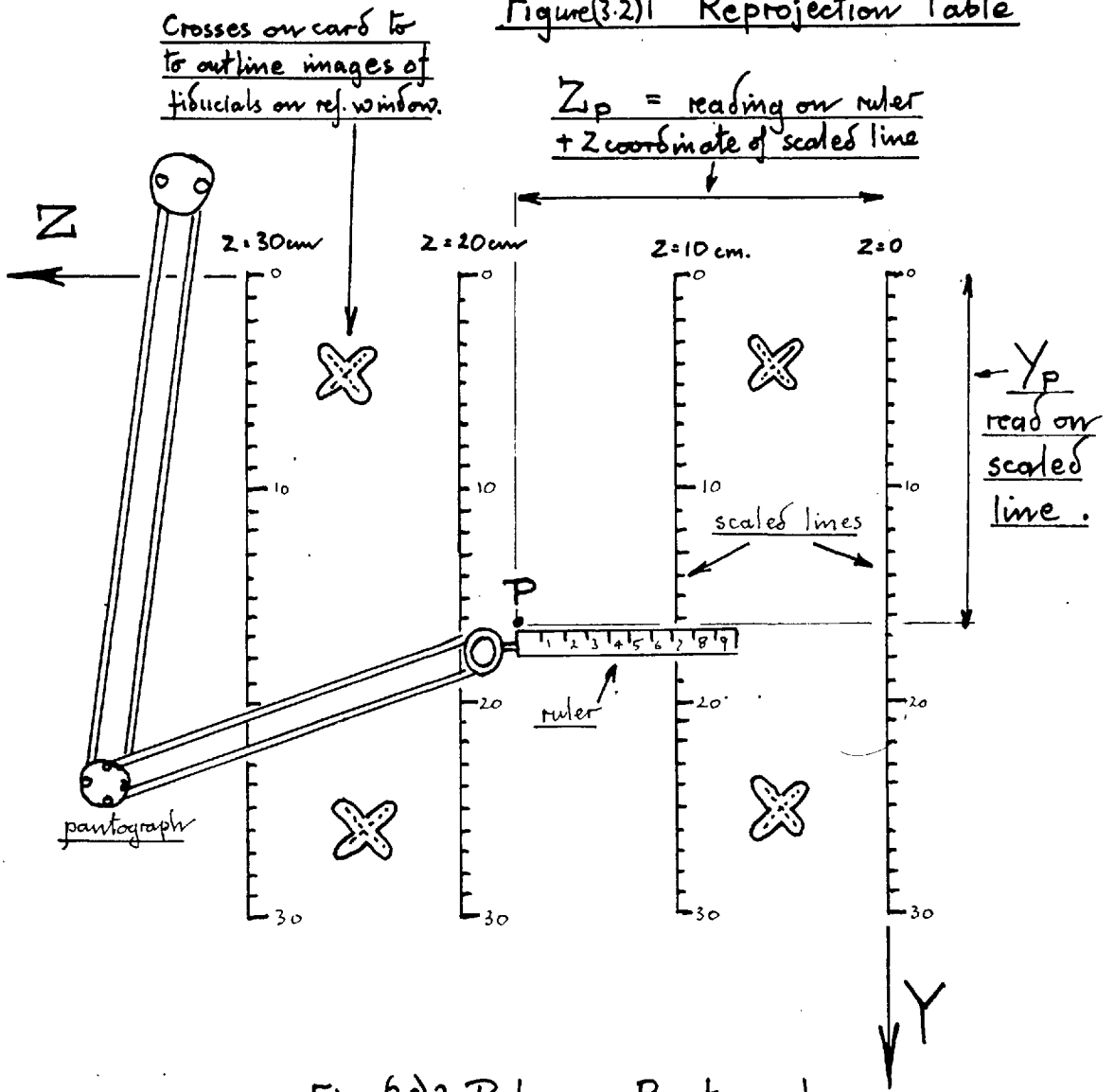

Figure(3.2)2 Ruler on Pantograph

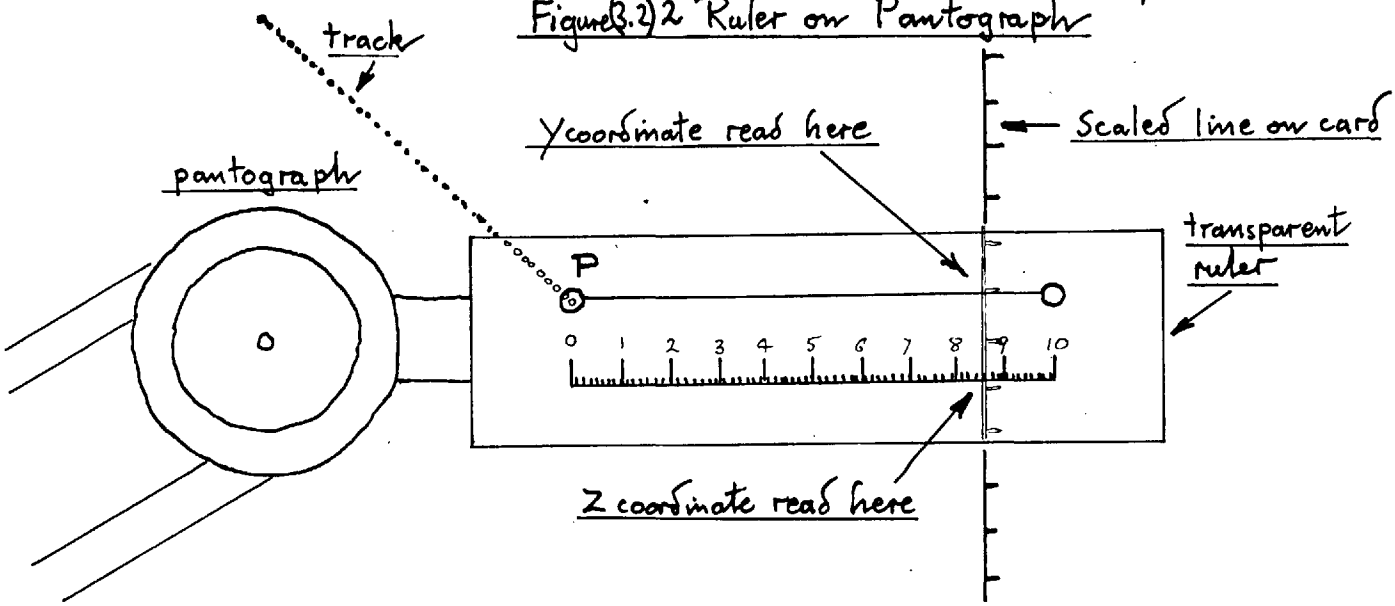

3.2.2 Small angle track scan.

Different amounts of film were scanned in different ways, in order to obtain data that would be used to derive particular experimental results.

In order to determine the small neutron-capture cross section, as much film as possible had to be scanned, but only tracks that might be neutron-capture deuterons needed to be measured. It was shown in section 1.5 that all the neutron-capture deuterons will have angles (θ) less than $5{\cdot}4^{\circ}$. The images of such small angle tracks will make small angles (Φ_T and Φ_B) with the Z projection axes, such that

$$\Phi_T \leqslant 5{\cdot}4^{\circ}, \quad \Phi_B \leqslant 5{\cdot}4^{\circ}$$

To ensure that all deuteron tracks were selected, all tracks with projected angles in both stereo-photographs less than the larger angle, $7{\cdot}5^{\circ}$, were measured. That is, those with

$$\Phi_T \leqslant \varepsilon = 7{\cdot}5^{\circ}, \quad \Phi_B \leqslant \varepsilon = 7{\cdot}5^{\circ}. \qquad 3.2/1$$

Some tracks with θ greater than $7{\cdot}5^{\circ}$, that dipped away from the camera, also satisfied these conditions and were inevitably measured.

With the aid of lines drawn on the porjection card at angles $7{\cdot}5^{\circ}$ to the Z direction, tracks on one stereo-photograph for which Φ was less than $7{\cdot}5^{\circ}$ were selected by eye, and their ends marked. The second stereo-photograph was then projected,

the corresponding image of the marked track found, and only if it, too, made an angle less than $7°5^{o}$ with the Z direction, were both stereo-images measured. One pair of stereo-photographs could be scanned, in this way, in approximately one minute. Measurements were made on about one photograph in ten.

3.2.3 'Starting and stopping tracks scan'

In order to derive the neutron-capture cross section from measurements of possible capture events, a knowledge of the initial neutron energy spectrum is also required. Almost all the tracks that start in the chamber will be neutron-scattered protons. By measuring all of their tracks that also stop in the chamber the neutron spectrum may be obtained. It was not possible to measure all the tracks, that started and stopped in the chamber, in as many photographs as could be scanned for small angle tracks, but the measurements on individual tracks could be made more rapidly. It was not necessary, for instance, to locate the stereo-pairs of tracks with the aid of markers. The tracks in each stereo-photograph were measured separately and it was left to the electronic computor to select the corresponding tracks and note when there was any ambiguity. It was when these 'starting and stopping tracks' were being measured that the coordinates were typed directly on to punched tape.

With the above aids it was found possible to measure one

track in both photographs, involving the determination and recording of eight four figure numbers in an average of one minute.

Besides the 'small angle track scan' and this 'starting and stopping track scan', two other scans were made in order to provide data that would check the present experiment and explore the possibilities of others. The first involved measuring all tracks that started in the chamber; and in the second, 'charged particle scatterings', were searched for.

3.2.4 All starting tracks scan.

The results of this scan were used to give an estimate of the differential n-p scattering cross section at the peak spectrum energy. Tracks that started and stopped in the chamber were measured as in the 'starting and stopping tracks scan', those tracks that did not stop in the chamber were measured by a partially 'non-corresponding' method. The coordinates of the starts of the tracks were made in the normal way. Having identified the stereo-pair of track images, points with the same Z coordinate were selected on these two track images, near where the track left the chamber. The Y coordinates of these corresponding points were then measured. These measurements were not as rapid as those in the starting and stopping tracks scan due to the necessity of relating corresponding stereo-images.

3.2.5 Charged particle scattering scan.

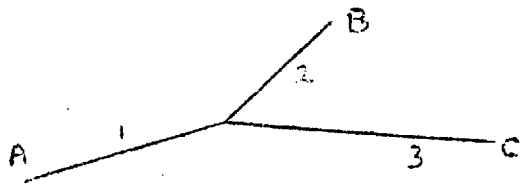

In this scan, tracks whose images appeared as shown above were measured, providing that the point A and at least one of points B and C appeared to be inside the chamber.

All the calculations performed on the results of the scans will be described in the following sections. The results obtained from them will be given in chapter 4.

3.3 RECONSTRUCTION FORMULAE.

In the last section it was explained how the positions of images of tracks were measured in terms of projection coordinates (Y, Z). The positions in space of the tracks had to be calculated from these projection coordinates.

Equations 3.1/1 give the derivations of coordinates in the chamber from a given set of film coordinates, that were defined in section 3.1. They assume that no plates of glass or liquid hydrogen are present between the camera and the chamber. It will be shown below, to a first approximation, that the effects of glass and hydrogen can be allowed for by replacing the real distances ℓ_o and f, that appear in the above equations, by apparent distances ℓ'_o and f'.

When allowance has been made for the change of coordinate system, the formulae 3.1/1 become:

Where:

$$\ell = \frac{bmf'}{Y_B - Y_T + \frac{bmf'}{\ell'_o}} ,$$

$$x = \ell - \ell'_o \qquad 3.3/1$$

$$y = \frac{\ell}{2mf'} (Y_B + Y_T - {}_oY_B - {}_oY_T) ,$$

$$z = \frac{\ell}{2mf'} (Z_B + Z_T - {}_oZ_B - {}_oZ_T) ,$$

Where b = distance between the lenses;

m = magnification of projector;

ℓ'_o = the apparent distance of the appropriate principal plane, of the two lenses, to the reference window;

f' = apparent distance of the appropriate principal plane, of the two lenses, to the film; and

${}_oY_B$, ${}_oY_T$, ${}_oZ_B$, ${}_oZ_T$: are the projection coordinates of the images of the points where the lens axes cut the film.

ℓ'_o and f' must now be related to the previously (section 3.1) defined 'real' values ℓ_o and f.

Consider first the effect of a glass plate of thickness t, and refractive index μ, between the cameras and chamber. Let the plane of this plate be tilted by a small angle γ from the perpendicular to the lens axes. See figure (3.3)1. It will be shown in appendix D1 that to a first order, the plate will produce an apparent contraction ($\delta\ell$) in the distance between the chamber and cameras and a lateral shift in the apparent position of the chamber. The lateral shift will have no effect on either directions or lengths in the chamber and will, therefore, be ignored. The contraction is shown in appendix D.1 to be:

$$\delta\ell = t(1 - 1/\mu) \qquad 3.3/2.$$

The errors introduced by the approximation will be considered below. Correct coordinates in the chamber would be obtained

Figure (3.3)1 The effect of a glass plate

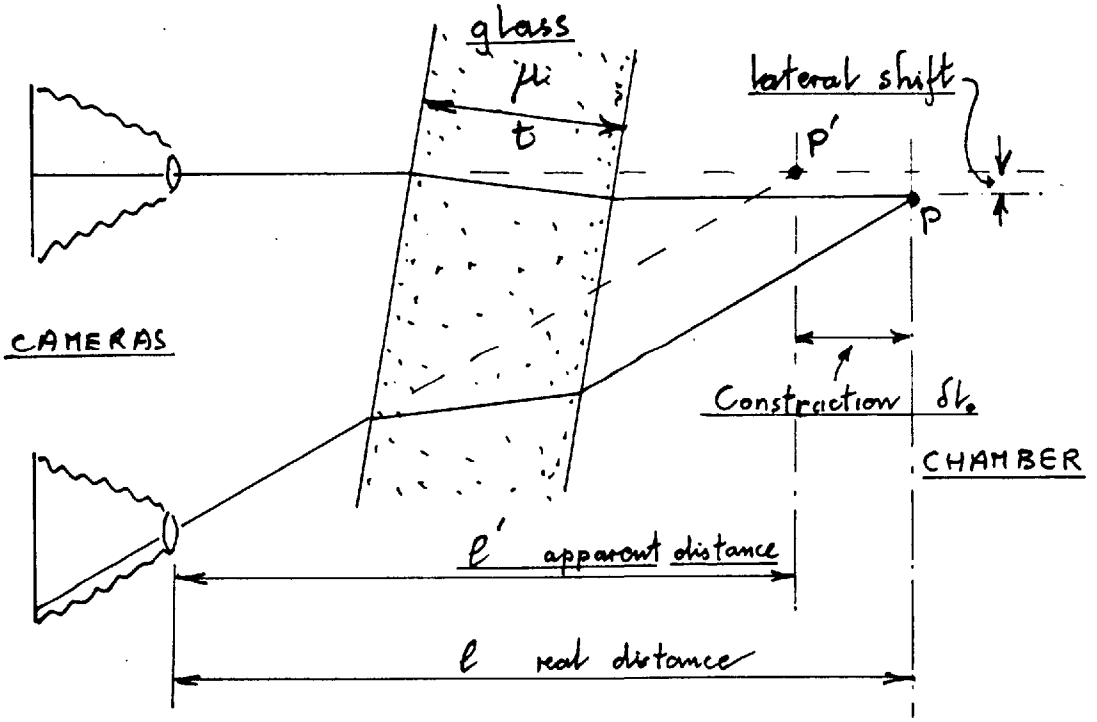

Figure (3.3)2 The effect of liquid Hydrogen

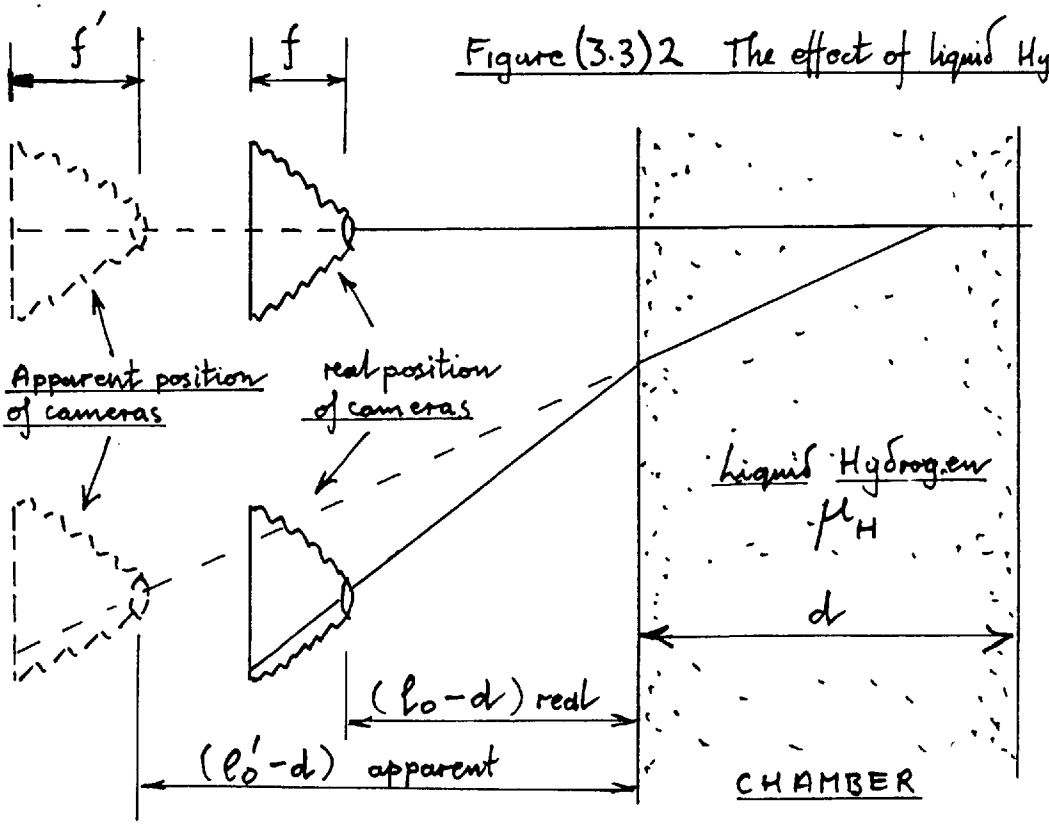

using formulae 3.3/1 if:

$$\ell'_o = \ell_o - t(1 - 1/\mu). \qquad 3.3/3$$

Ignoring the effects of the glass plate, consider now the effect of the refractive index μ_H of the hydrogen in the chamber, from the point of view of an observer inside the liquid hydrogen, looking out at the cameras. (see figure (3.3)2). The effect is shown in appendix D.2 to give an apparent increase of 'depth' to all objects outside the hydrogen, by an approximate factor of μ_H. To a first approximation there is no effect on the apparent dimensions in a direction parallel to the liquid surface. Thus the effect is to increase the apparent lengths ℓ_o and f without affecting the size of images on the film. Correct coordinates would, therefore, be obtained using formulae 3.3/1 if:

$$\begin{aligned} \ell' - d &= \mu_H (\ell - d), \\ f' &= \mu_H f , \end{aligned} \qquad 3.3/4$$

where d is the depth of the chamber.

Considering now the combined effect of a number of glass plates each of thickness t_i and of refractive index μ_i, and of the effect of liquid hydrogen, correct chamber coordinates will be obtained if:

$$\ell'_o \doteq \ell_o \left\{ \mu_H + \Sigma_i \left(t_i \left(1 - \frac{1}{\mu_i} \right) \right) \right\} \qquad 3.3/5$$

$$f' = f\mu_H$$

The maximum errors in the determination of an angle θ in the chamber, due to the above approximations, have been estimated in appendix D.2 and are:

For all θ : $K_\theta \doteqdot 0{\cdot}3^\circ$

for small θ: $K_\theta \doteqdot 0{\cdot}15^\circ$

Thus the coordinates in the chamber could be calculated with the aid of formulae 3.3/1, and 3.3/5, and the constants b, m, f, ℓ_o, ${}_oY_T$, ${}_oZ_T$, ${}_oY_B$, and ${}_oZ_B$. The derivation of these constants will be considered later in section 3.5. The other calculations performed by the computor will now be described.

3.4 THE CALCULATION PROGRAMME.

Not only did the reconstruction calculation, given in the last section, have to be performed, but also a number of checks and searches that will be described below. Some of the calculations and searches would have been impracticable if an electronic computor had not been used. A Ferranti 'Mercury' high speed electronic computor at the University of London Computing Centre was available, and programmes for it were written in 'auto-code'. Not only did this computor perform the calculations rapidly, but also faultlessly. The computor programme, constants and the data from the scans were all punched on tape and read by the computor. After calculation, the results were then punched by the computor on to output tape, which could later be printed out to give a page of tabulated results.

A single computor programme was written to deal with the data from any of the 'scans' referred to in section 3.2. In the form of the data, or with the aid of short 'command' tapes, the computor was 'told' which of its calculations to perform. In the following description of these calculations it will be understood that each calculation is only performed when relevant. The computor programme will be given in Appendix E.

In the data from the 'stopping tracks scan', the projection coordinates of track images from the top stereo-photograph were

not paired with the corresponding coordinates from the bottom photograph. The computor had, therefore, to search for, and select stereo-pairs whose Z coordinates agreed within a certain tolerance (0·55 cm.).

For the 'small angle scan', the angles (Φ_T and Φ_B) of the track images with the Z projection axes were calculated, and a check of equation 3.2/1 made. The position and direction of each track was then calculated with the aid of formulae 3.3/1; using the constants that had been read in.

Four checks on the location of the track could then be made.

(a) It was determined if any track appeared to start or stop on a wall or window, where the track might have been passing in or out of the chamber. Such tracks should not be considered when track lengths are to be interpreted as ranges.

(b) A check was made to see that the start of a track was in the beam cross section. The reason for this check was given in section 2.7. Tracks starting outside the beam cross section must have been produced by scattered neutrons whose directions were not that of the beam. Tracks produced from such neutrons have been defined as 'spurious' in section 2.2, and are not of interest.

(c) A check could be made to see if both ends of a track were in a defined rectangular volume (V'), inside the chamber, As will be shown in section 4.2.2 , the probability of tracks

from a given neutron energy lying in such a rectangular volume may be calculated. From the number of tracks that are found in this volume, therefore, the beam intensity at any energy, that is its spectrum, may be calculated. The whole volume of the chamber was found to be both too ill defined, and too complicated for this purpose.

(d) It was possible to determine whether tracks had lengths greater than a certain value (0·25 cm.). The direction in space and range of very short tracks could not be accurately measured. It was convenient, therefore, to be able to exclude them in certain cases.

After making the above checks on the coordinates of any tracks that were read in, the computor then calculated the appropriate direction cosines, angles, lengths, and energies. The formulae used, have been derived in chapter 1 and given or quoted in section 2.2 and will not be quoted again here. In the case of a starting and stopping track; θ, χ, the track length r, E_n, E_p and E_d were all calculated, where: E_n is the initial neutron energy assuming the track to be a proton scattered by the beam, and E_p and E_d are the energies of the particle producing the track assuming the particle to be a proton or deuteron. After any given number of 'starting and stopping tracks' had been calculated, a spectrum of the number of tracks, satisfying given conditions, in ranges of angle and initial

neutron energy, could also be printed out.

In the case of data from the 'charged particle scattering scan', the appropriate angles and energies were also calculated and printed out. The details and definitions of those parts of the output required, will be given when the results are discussed in chapter 4.

A search could be made amongst the data from the 'starting and stopping tracks scan' for n-p, n-p double scatters, using the criteria given in section 2.2.3. When a pair of proton tracks were found that satisfied the data within certain limits the relevant angles and energies were calculated and printed out. Since the search, as will be shown in section 4.3.3 , was unsuccessful, no further details of it will be given here.

The reasons behind some parts of the computor programme will be dealt with more fully when the results are discussed in the next chapter. Before this, however, the derivations of the constants used in the reconstruction calculation must first be described.

3.5 DERIVATION OF RECONSTRUCTION CONSTANTS.

The reconstruction of directions of tracks in the chamber was performed with the formulae 3.3/1. In these formulae the following constants: b, mf', ℓ'_o, and ${}_oY_T$, ${}_oZ_T$, ${}_oY_B$, ${}_oZ_B$ defined in section 3.3, were used.

The effects of errors in the latter four constants on derived lengths and directions in the chamber are very small, and thus the derivation of these constants, from the camera geometry, need not be further discussed.

The first three constants may be derived entirely from a knowledge of the geometry of the optical system, using the formulae (3.3/5) for the 'apparent' distances (f' and ℓ'_o). There are two disadvantages in doing this. Firstly a knowledge is required of the positions of the principal planes in the lenses. The second disadvantage arises out of the difficulty in measuring the relative positions of the chamber and camera. In order to make this measurement, the vacuum case windows have to be removed, and thus the measurement has to be made with no vacuum in the vacuum case. Now, it is found that, due to the presence of rubber gaskets, the chamber moves when the case is pumped down, and the measurements made in the absence of a vacuum are no longer applicable.

As an alternative to using a knowledge of the optical

geometry, the three constants may be derived indirectly from measurements of fiducial marks at known positions in the chamber. Let M_o be the magnification of distances between points on the back, reference, window, when projected on to the table. Let M_F be the corresponding magnification from the front window. If d is the distance between the windows, ${}_FY_T$ and ${}_FY_B$ are the projection coordinates of a point on the front window, and if

$$\Delta Y = {}_FY_T - {}_FY_B,$$

then

$$b = \Delta Y \quad M_o \frac{M_o}{M_F - M_o} \quad , \qquad 3.5/1$$

$$\ell'_o = d \frac{M_F}{M_F - M_o}$$

$$mf' = M_o \ell'_o$$

The disadvantage, here, is the dependence of all the constants on the relatively small difference term $(M_F - M_B)$ which cannot be determined to a high accuracy. An alternative method was used, therefore, which relied on a mixture of direct and indirect measurements:

$$b = b \text{ (direct)} ,$$

$$\ell'_o = d\left(\frac{bM_o}{\Delta Y} + 1\right) , \qquad 3.5/2$$

$$mf' = M_o \ell'_o \ ;$$

The value of M_F could then be checked against direct measurement:

M_F (from above) = 9·728 ± ·02 cm.

M_F (direct) = 9·753 ± ·02 cm.

which agree within the errors. ℓ_o and f could not be checked without a knowledge of the positions of the principal planes.

CHAPTER 4.

RESULTS.

4.1 MEASUREMENT ERRORS.

4.1.1 Accuracy of determination of angles and lengths in the chamber.

The accuracy of any of the results calculated in this chapter will depend on the accuracy of measurements of lengths and angles in the chamber. The causes of errors in these measurements will now be considered.

Due to coulomb scattering the paths of ionizing particles are not quite straight and their range is not exactly related to their energy; thus an inevitable error is introduced in the determination of energies and angles at the event. Errors in angle from this cause can be shown to be

$$K_{\theta} < 0{\cdot}2^{\circ} \qquad 4.1/1$$

Errors in the determination of angles in space could be due to the following causes:-

(a) Distortion of tracks due to movement of the liquid, and thus of the tracks, between the time when the particles passed through the chamber and the time when they were photographed.

(b) Optical distortion of the tracks due to local

variations of temperature in, and thus of the refractive index of, the liquid hydrogen.

Errors due to the above two distortions were only estimated from a determination of the total errors due to all causes, see section 4.1.2.

(c) The optical distortions due to imperfections in the camera lenses and projection system were almost certainly negligible.

(d) The optical distortions due to the presence of glass plates between the camera and chamber and due to the finite refractive index of the liquid hydrogen have been estimated in appendix D, where it was shown that the maximum error in determining any direction is

$$K_{\Omega} < \pm 0{\cdot}3^{\circ}, \qquad 4.1/2$$

and the error in determining a small angle θ:

$$K_{\theta}, \text{ (small } \theta) < \pm 0{\cdot}15^{\circ}, \qquad 4.1/3$$

where θ is the angle which a track makes with the beam direction.

(e) In the particular case of a determination of the angle (θ) of a track with the beam direction, there is an error due to the imperfect knowledge of the beam direction. This fixed error was estimated in section 2.7 to be less than $0{\cdot}7^{\circ}$. The results given in section 4.2.4 suggest that its actual value was somewhat less than this.

(f) The accuracy with which the coordinates of a projected track could be measured depended on the finite size of the bubbles, their distribution about the true path of the particle and on the accuracy of the equipment used to measure the tracks.

In section 3.1 it has been shown that if

K_ℓ = error in determining the lateral position of a projected track

λK_ℓ = error in determining the longitudinal position of a projected track end,

$\lambda = 2$, and

$$K_\Phi = \frac{\sqrt{2}\, K_\ell}{R} \qquad 4.1/4$$

then the error in determining any angle in space K_Ω is

$$K_\Omega \doteq 4\, K_\Phi \,, \qquad 4.1/5$$

and the error in determining a small angle θ is

$$K_{\theta\ (\text{small})} \doteq 3\ K_\Phi \quad . \qquad 4.1/6$$

4.1.2 Experimental determination of the accuracy of angle measurement.

If the events selected in the 'charged particle scattering scan' (section 3.2.5) are n-p, p-p double scattering events (section 2.1.2) then the angle between two of the tracks (2 and 3

in the figure below), θ', is 90°.

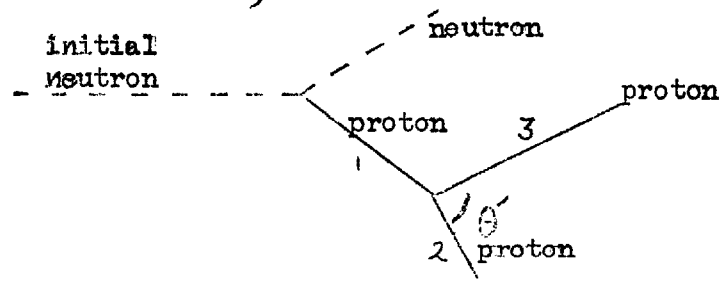

900 photographs were scanned and 91 events selected. In these events, except those in which one of the tracks 2 and 3 was less than 0·5 cm. in length and large errors might be expected, it was found that the measured angle, θ', was $90^\circ \pm 5^\circ$. The events were, therefore, assumed to represent the second scatterings of scattered protons. The R.M.S. variation of the measured angle θ' from 90°, $K_{\theta'}$, then gave a determination of the accuracy of measurement of the directions of the two tracks. On graph (4.1)1 $K_{\theta'}$ is plotted against the length (r') of the shorter of the two tracks (2 and 3 in the figure above). It is seen the variation, $K_{\theta'}$, is very much larger if r' is small, presumable due to the much larger error in measuring the short track. If one of the tracks was less than 0·5 cm. long, it was generally true that the other track was much longer than 0·5 cm. The error in measuring θ' will then primarily depend on the larger error in measuring the shorter track. If, therefore, K_{Ω} is defined as the error in determining the direction of any track, of length r, then

$$K_{\Omega} \doteq K_{\theta'} \qquad 4.1/7$$

when r is taken as the length (r') of the shorter track and when r' is less than 0·5 cm.

When the length of the shorter track (r') was above 2 cm., then the difference in length between the two tracks was not, in general, large. The error K_θ, was then caused approximately equally by the random direction errors in the two tracks, and

$$K_\Omega \doteq \frac{1}{\sqrt{2}} \quad K_{\theta'} \qquad 4.1/8$$

when r is taken as the length, r', of the shorter track, and when r' is grater than 2 cm. On graph (4.1)1, K_Ω as obtained from equations 4.1/7 and 4.1/8 has been plotted for the ranges of r for which these equations are valid. A smooth curve has been interpolated in the range between 0·5 cm. and 2 cm., where neither equation 4.1/7 or 4.1/8 is valid.

Assuming that the error K_Ω is entirely due to the measurement errors (see (f) in section 4.1.1), then from the values of K_Ω, the error K_ℓ in measuring the lateral position of a projected track may be calculated from 4.1/4 and 4.1/5. These calculated errors, K_ℓ, are plotted on graph (4.1)2. Over most of the range of R, K_ℓ is seen to be constant and equal to a value (0·4 mm.) that is somewhat less than the estimate of 0·5 mm. This result suggests that causes of error other than those resulting from errors in measurements of the coordinates of projected tracks, may legitimately be ignored. Using this fact,

Graph (4.1)1 Errors in determining angles in the chamber.

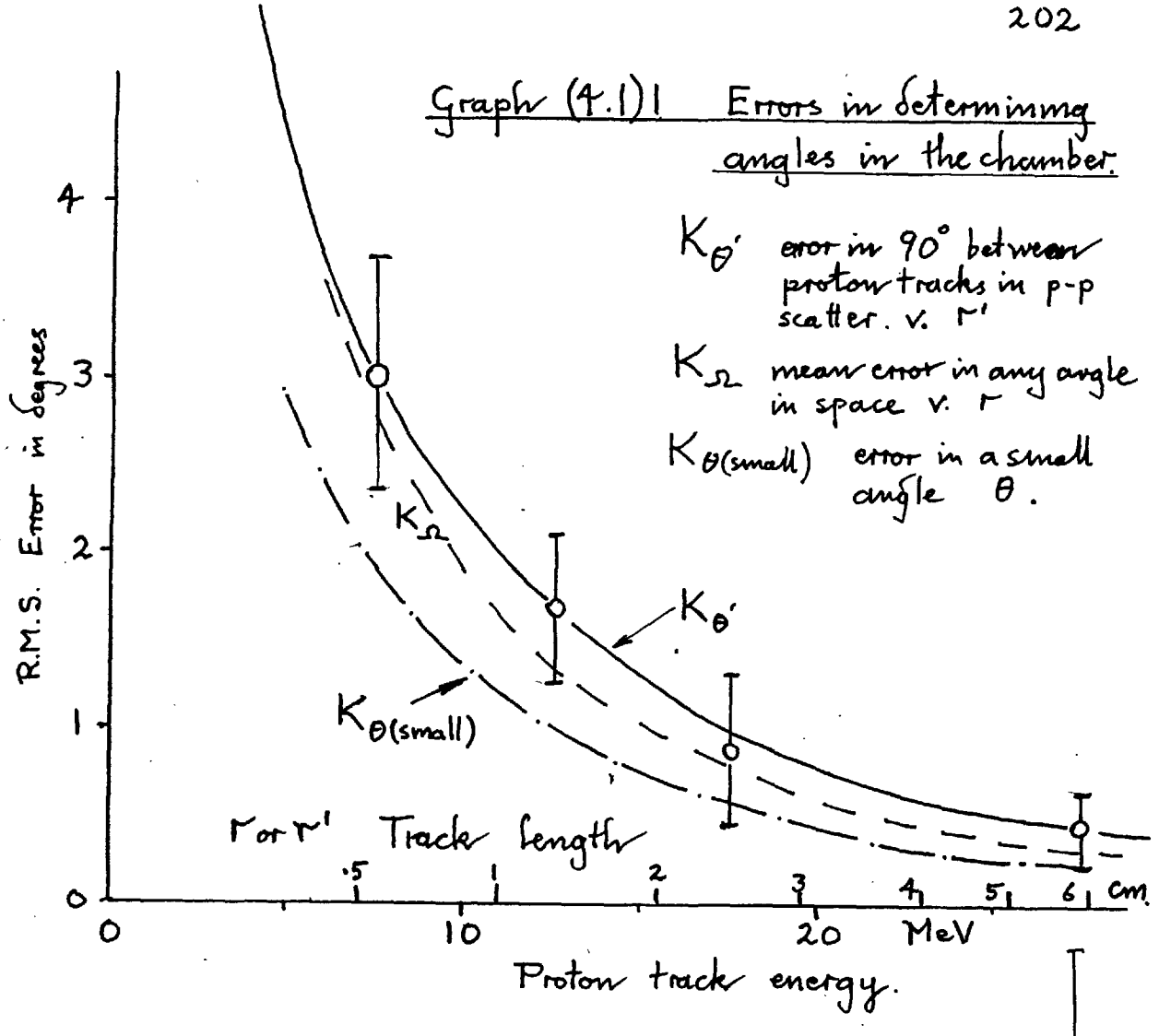

Graph (4.1)2 Error in determination of lateral position of projected track

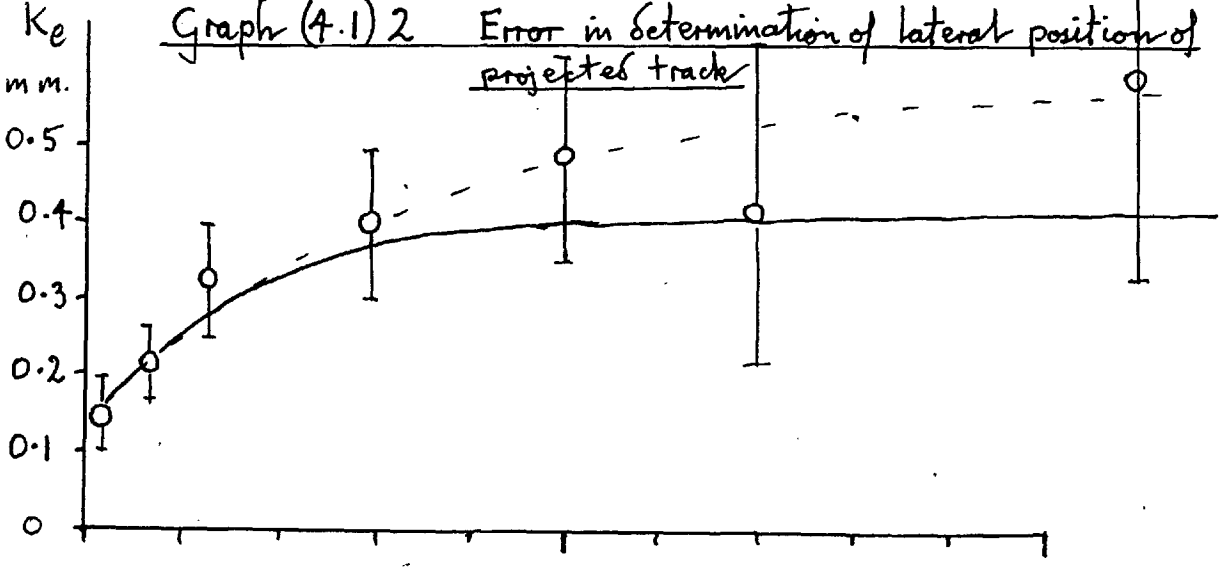

the error $K_{\theta(small)}$ in determining a small angle θ, has been calculated and plotted on graph (4.1)1.

4.2 NEUTRON ENERGY SPECTRUM.

4.2.1 Basic Equations.

Let a beam scattered proton be defined as a proton which is scattered in the chamber by a neutron in the beam. In this case the energy of the neutron may be calculated from the range and angle of the track of the proton (equation 1.5/9 and 2.1/1). Hence from the tracks of these beam scattered protons, the energy spectrum of the neutron beam may be calculated.

Let $q(\theta, E_n)\ \delta\theta, \delta E_n$, be defined as the number of beam scattered proton tracks starting in a volume V', with angles and energies in the intervals $\delta\theta, \delta E_n$. The spectrum of initial neutrons , that may be derived from the above distribution, will be defined by the number $n(E_n)\ \delta E_n$ of neutrons per cm^2 of beam cross section, per burst of particles from the cyclotron, with energies in the interval δE_n. $n(E_n)$ may be obtained from $q(\theta, E_n)$ using the relation,

$$q(\theta, E_n) = N\ V'\ \rho\ N_A\ \left({}_{n-p}\sigma'(\theta, E_n)\right)\left(n(E_n)\right)\left(2\pi \sin 2\theta\right) \qquad 4.2/1$$

where N = number of cyclotron bursts considered,

V' = volume in which tracks start,

ρ = density of the liquid hydrogen,

N_A = Avogrado's number.

The distribution of starting tracks $q(\theta, E_n)$ may be obtained from the distribution of tracks selected from the 'starting and stopping tracks scan' (section 3.2.3).

Let $p(\theta, E_n)\ \delta\theta\ \delta E_n$ be the number of tracks selected in this scan with angles and energies in the intervals $\delta\theta$ and δE_n. $p(\theta, E_n)$ will differ from previously defined $q(\theta, E_n)$ in two ways. Firstly $p(\theta, E_n)$ will include the distribution of spurious tracks (section 2.2.6) caused by neutrons other than those in the beam. The number of these spurious tracks may be estimated and subtracted from $p(\theta, E_n)$ to give a corrected distribution $P''(\theta, E_n)$. The second difference which is still present between $q(\theta, E_n)$ and $p''(\theta, E_n)$ is a consequance of the conditions applied in selecting the tracks in the scan. These conditions will be given in the next section. Let the probability that a track starting in the volume V', with angle θ, from energy E_n, is selected by these conditions, be $G(\theta, E_n)$. Then

$$p''(\theta, E_n) = G(\theta, E_n)\ q(\theta, E_n) \qquad 4.2/2$$

Defining the distributions $p''(E_n)$, $q(E_n)$ and the probability $P(E_n)$ by

$$p''(E_n) = \int p''(\theta, E_n)\ d\theta$$

$$q(E_n) = \int q(\theta, E_n)\ d\theta$$

$$P(E_n) = \int_0^{\pi/2} G(\theta, E_n)\ \frac{n\text{-}p\sigma(\theta, E_n)}{n\text{-}p\sigma_T(E_n)}\ 2\pi \sin 2\theta\ d\theta \qquad 4.2/3$$

then from 4.2/1

$$q(E_n) = NV' \rho N_A \left({}_{n-p}\sigma_T(E_n) \right) \left(n(E_n) \right) \qquad 4.2/4$$

and from 4.2/2

$$p''(E_n) = P(E_n) \; q(E_n). \qquad 4.2/5$$

$p''(E_n) \delta E_n$ is the corrected number of selected tracks in the interval δE_n. From $p''(E_n)$ using 4.2/4 and 4.2/5 the energy spectrum $n(E_n)$ may be obtained.

In the next section $P(E_n)$ will be calculated; then $p(E_n)$ will be given and the corrections applied to it. Finally in 4.2.5 the calculated spectrum $n(E_n)$ will be given.

4.2.2 Probability of selection.

Tracks measured in the 'starting and stopping tracks scan' (section 3.2.3) were only selected (section 3.4) if they satisfied certain conditions.

(a) Tracks were rejected if they started ourside the beam cross section. The reason for this was given in section 2.7. Tracks outside the cross section must be caused by neutrons scattered from the beam and the tracks will thus be spurious tracks (2.2.6). Tracks were in fact only selected if they started inside a volume V', which was everywhere inside the beam, and also inside the visible part of the chamber.

(b) The range of a particle and thus E_n could not be obtained if the particle's tracks did not stop in the chamber. Tracks were, therefore, only selected if they stopped in a volume V which was larger than V' but also inside the visible part of the chamber (see figure (4.2)1).

(c) Finally, very short tracks with lengths less than r_c (0·25 cm.), were rejected, because they could not be measured with sufficient accuracy.

The probability of selecting a track with angle Θ, and E_n, $G(\Theta, E_n)$, will depend on the shapes of V' and V, and on the value of r_c. This probability $G(\Theta, E_n)$ may be derived as follows. Let $D(\Theta, \chi, E_n, x, y, z)$ have the value unity if a track with Θ, χ and En, that starts at the point x, y, z satisfies the selection conditions (b) and (c) given above; and let $D(\Theta,\chi,E_n,x,y,z)$ have the value zero if these conditions are not satisfied. Then

$$G(\Theta, E_n) = \frac{\iiint_{V'} \int_{\chi=0}^{2\pi} D(\Theta, \chi, E_n, x, y, z)\, d\chi\, dx\, dy\, dz}{\iiint_{V'} \int_{0}^{2\pi} d\chi\, dx\, dy\, dz} \qquad 4.2/6$$

Figure (4.2) 1 Selection Volumes

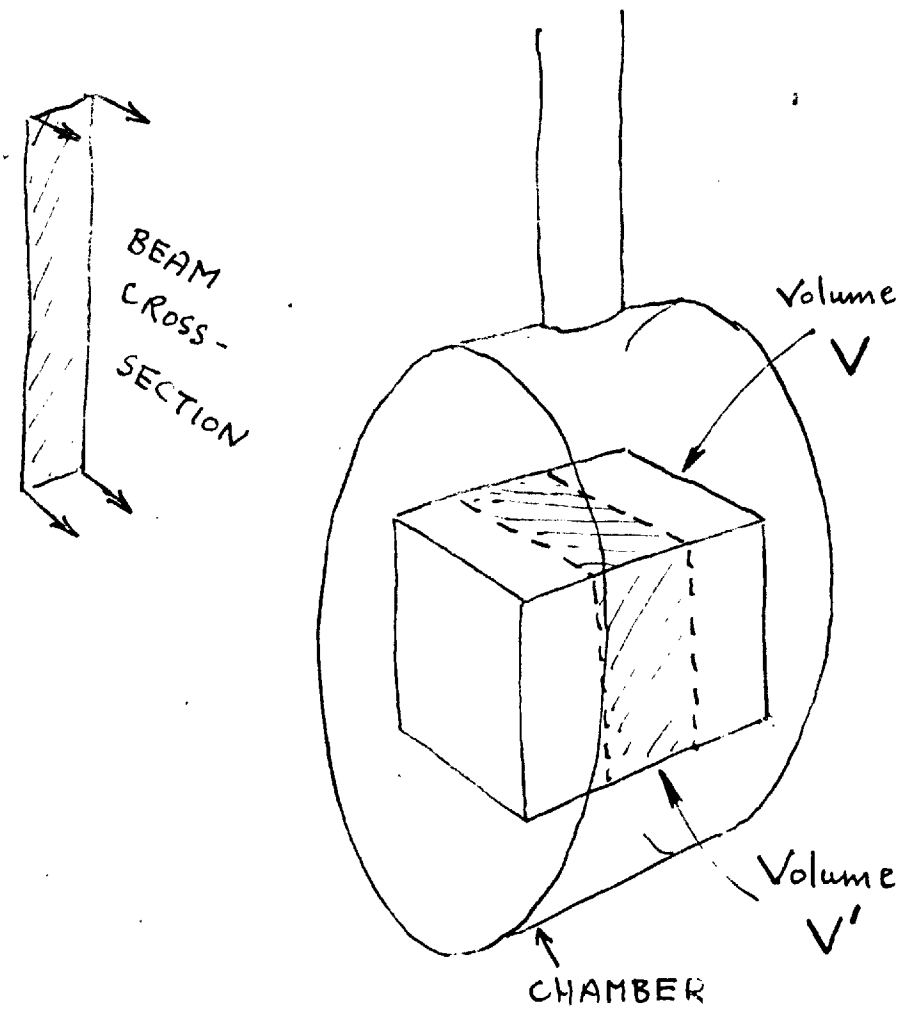

This can, in practice, only be solved exactly for very special cases. Even numerical integration, with the aid of an electronic computor, is very slow unless fairly simple shapes V and V' are chosen. Thus for V, instead of using the complete illuminated volume of the chamber (a polygonal truncated cone, see figure (4.4)1), a rectangluar volume was used. The volume V' was then taken to be that part of V that also lay within the beam cross section. Since the beam cross section was rectangular the volume V' was rectangular also. The volumes V and V' with respect to the chamber are illustrated in figure (4.2)1.

The calculation of $G(\theta, E_n)$, and hence of $P(E_n)$ (see equation 4.2/3), were performed numerically with the help of the Mercury Computor referred to in section 3.4. The theory and programme will be given in appendices F and G. The calculated values of $G(\theta, E_n)$ and $P(E_n)$ are given in appendix F. $P(E_n)$ is also plotted on graph (4.2)7. From equations 4.2/1 and 4.2/2,

$$p''(\theta, E_n) \propto 2\pi \left(\sin 2\theta\right)\left(G(\theta, E_n) \right)\left(\sigma_{n-p}(\theta, E_n) \right) \quad 4.2/7$$

At the energies used, $\sigma_{n-p}(\theta, E_n)$ is approximately independent of θ. The angular distribution of selected beam scattered protons is then approximately given by

$$p''(\theta, E_n) \propto 2\pi \sin 2\theta \;\; G(\theta, E_n),$$

which for various values of E_n is plotted on graph (4.2)2.

Graph (4.2)2 Selection Probability for starting and stopping tracks scan, $E_c = 5$ MeV

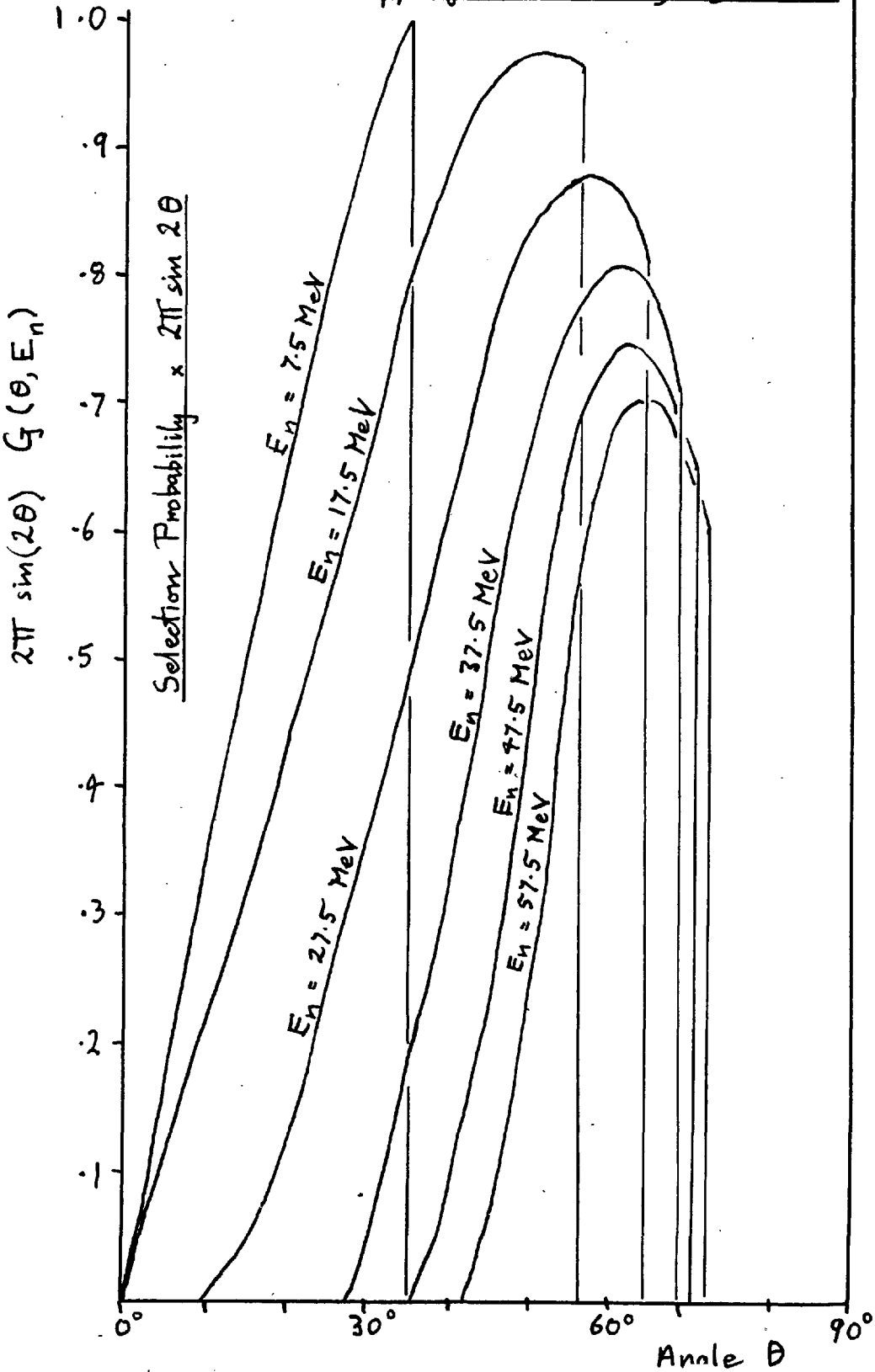

4.2.3 Energy distribution of starting and stopping tracks.

In the starting and stopping tracks scan, described in section 3.2.3, 72 pairs of stereo-photographs were scanned and 324 tracks found that satisfied the selection conditions given above. The numbers if these tracks $p(E_n)\,\delta E_n$ in neutron energy intervals δE_n of 5 MeV are plotted on graph (4.2)3. The fractional error (K_p) in $p(E_n)\,\delta E_n$ marked on this graph is the purely statistical error,

$$K_p = \frac{1}{\sqrt{p(E_n)\,\delta E_n}}$$

The error (K_E) in determining the initial neutron energy E_n was estimated as follows.

Using equations (1.5)9 and 2.1/1

$$E_n = 10{\cdot}7\ \frac{(r)^{0{\cdot}548}}{\cos^2\theta} \qquad \text{MeV}$$

Therefore $$\frac{dE_n}{E_n} = 0{\cdot}548\ \frac{dr}{r} - 2\tan\theta,\ d\theta$$

Since the R.M.S. errors in r and θ, K_r and K_θ, are independent,

$$\frac{K_E}{E_n} = \sqrt{\left(0{\cdot}55\ \frac{K_r}{r}\right)^2 + \left((2\tan\theta)\,K_\theta\right)^2}.$$

K_r arises from the two longitudinal errors in determining the position of the ends of a track in space. Using the definition

Graph (4.2)3 Number of selected tracks per interval of E_n

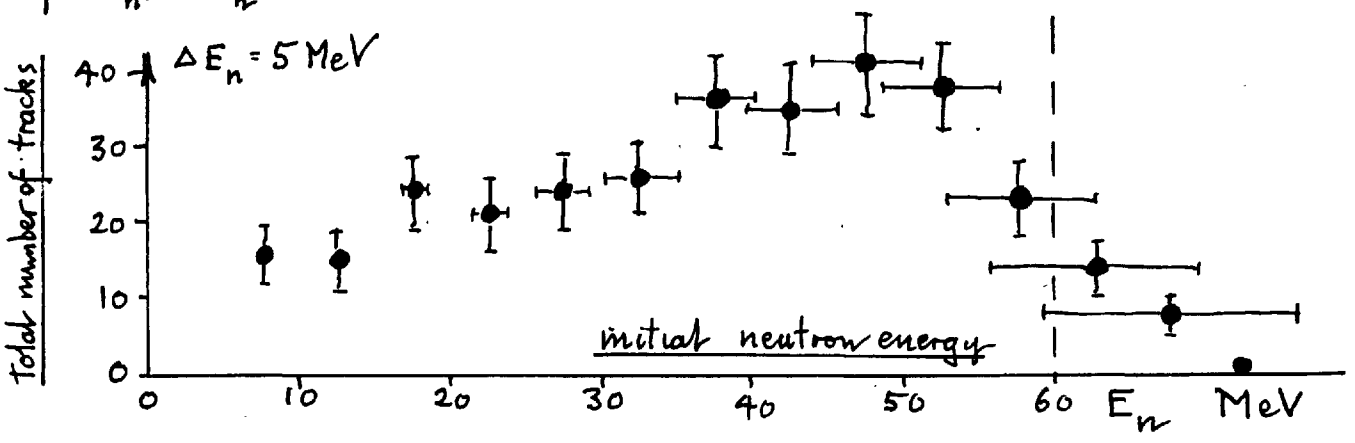

Graph (4.2)4 selected tracks corrected for maximum E_n = 60 MeV

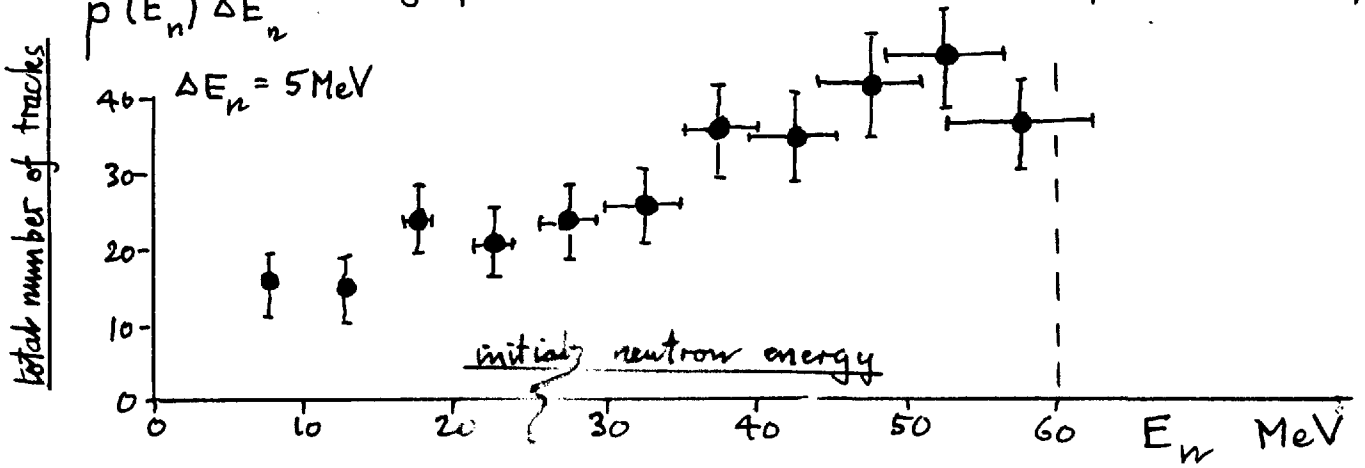

of K_{Ω} (which has been plotted on graph (4.1)1) and of λ , given in section 4.1.1 (f),

$$\frac{K_r}{r} = \lambda K_{\Omega} ,$$

and since θ may be any angle,

$$K_{\theta} = K_{\Omega} ,$$

thus

$$\frac{K_E}{E_n} = K_{\Omega} \sqrt{1{\cdot}2 + 4 \tan^2 \theta} \qquad 4.2/8$$

K_{Ω} is a function of the track range r. The mean range of selected tracks was found to be approximately independent of the neutron energy E_n, and equal to about 1·3 cm. K_{Ω} for r = 1·3 cm. taken from graph (4.1)1 is 1·5°. The mean value of θ for selected tracks varied considerably with E_n. Using the approximate angular distribution of tracks given on graph (4.2)2, mean values, $\bar{\theta}$, of θ have been estimated and given in the table below. Values of K_E calculated from equation 4.2/8 when the estimate of K_{Ω} and $\bar{\theta}$ are substituted in the equation are also given in the table.

E_n	10	20	30	50	70 MeV
$\bar{\theta}$	20°	40°	50°	60°	70°
K_E/E_n	3·0	5·0	6·5	8·3	13 %
K_E	·3	1·0	2·0	4·2	9·1 MeV

These errors are marked on graph (4.2)3.

It is seen on the graph (4.2)3 that a number of events are recorded with energies higher than 60 MeV. Since there was, in fact, no source of neutron higher than 60 MeV, all of these events must be accounted for by the estimated error K_E. In fact, their distribution beyond 60 MeV agrees well with the estimated error K_E of 9 MeV. A better approximation to the true distribution of tracks is obtained when the numbers of events with E_n apparently higher than 60 MeV are folded back about 60 MeV. The resulting distribution, $p'(E_n) \delta E_n$, is plotted on graph (4.2)4. A further correction will be given in the next sub-section.

From 4.1 it will be remembered that the estimated value of K_{Ω} did not include errors caused by any lack of alignment of the beam with the z direction. The agreement between the estimated error K_E derived from K_{Ω} with the distribution of tracks above 60 MeV is an indication that any errors due to lack of beam alignment were negligible.

4.2.4 Spurious Tracks.

Spurious proton tracks (see section 2.2.6) due to neutrons not in the beam may be identified by the distribution of tracks whose calculated E_n is far in excess of 60 MeV. The presence of such tracks is not shown up by the distribution $p(\theta, E_n)$ since the value of E_n for a spurious track may tend towards infinity.

On graphs (2.2)5 the numbers of selected tracks $p_h(\theta, E_h(\theta,E_p))\delta\theta\delta E_p$ in intervals of angle and proton energy, $\delta\theta$ and δE_p have been plotted. The tracks represented in the shaded portion of the graph all have calculated values of E_n in excess of 100 MeV, and cannot be explained by measurement errors on tracks produced by the beam.

If the spurious tracks are caused by neutrons that have previously been scattered from the neutron beam, it can be shown that the angular distribution of the spurious tracks will be approximately isotropic in angle and proton energy up to a proton energy of about 30 MeV. Thus if $q_s(\theta, E_n(\theta,E_p))\delta\theta\delta E_p$ is the number of spurious tracks in the intervals $d\theta$ and dE_p, then

$$q_s(\theta,E_n(\theta,E_p)) = B \cdot 2\pi \sin\theta \qquad 4.2/9$$

where B is a constant. The magnitude, B, of the distribution has been calculated from the observed number of tracks with E_n greater than 100 MeV. Let $p_s(\theta, E_n)\,\delta\theta\,\delta E_n$ be the number of selected spurious tracks in the intervals $\delta\theta$, δE_n, then from 4.2/9,

$$p_s(\theta, E_n) = B \quad N \quad G(\theta, E_n) \quad 2\pi \sin\theta \cdot \cos^2\theta,$$

and the number of spurious tracks, $p_s(E_n)dE_n$, selected in an interval dE_n will be given by

$$p_s(E_n) = B\,N \int_0^{\frac{\pi}{2}} G(\theta, E_n)\, 2\pi \sin\theta \cos^2\theta \, d\theta, \qquad 4.2/10$$

The integral was evaluated graphically. The resultant energy distribution of spurious tracks is plotted on graph (4.2)6.

Graph (4.2)5

Number of selected tracks with proton energy E_p in given interval of θ, $\Delta\theta = 10^\circ$ & interval $\Delta E_p = 5$ MeV

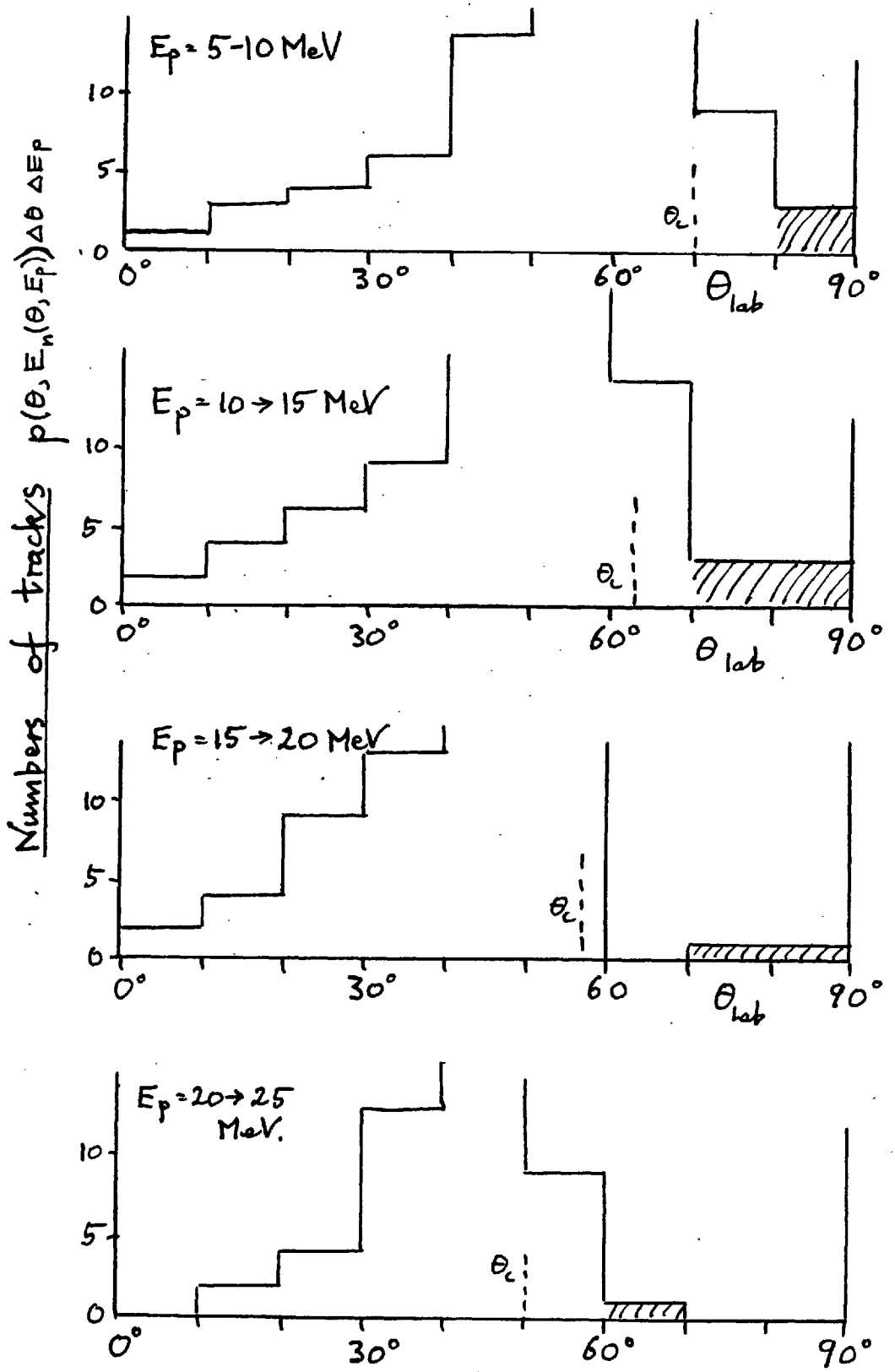

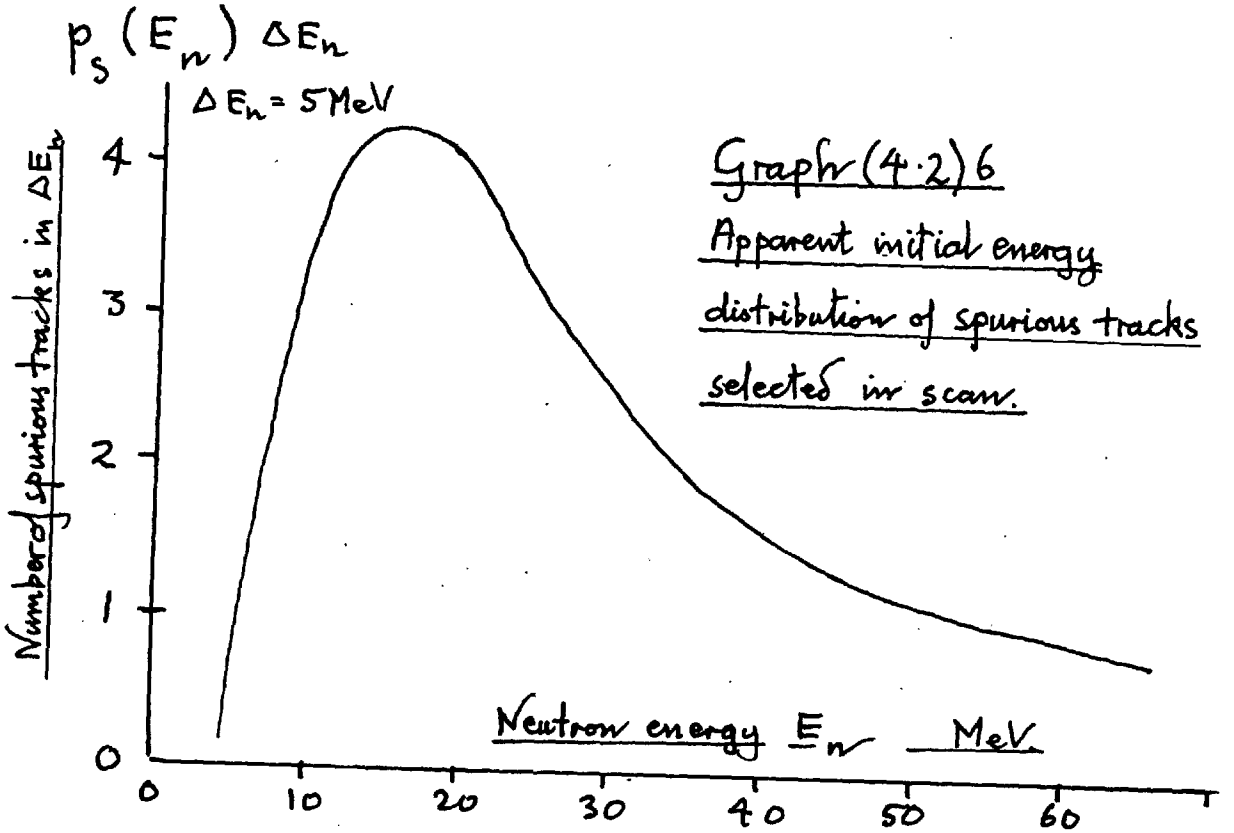

Graph (4.2)6

Apparent initial energy distribution of spurious tracks selected in scan.

Graph (4.2)7 selected tracks corrected for spurious tracks

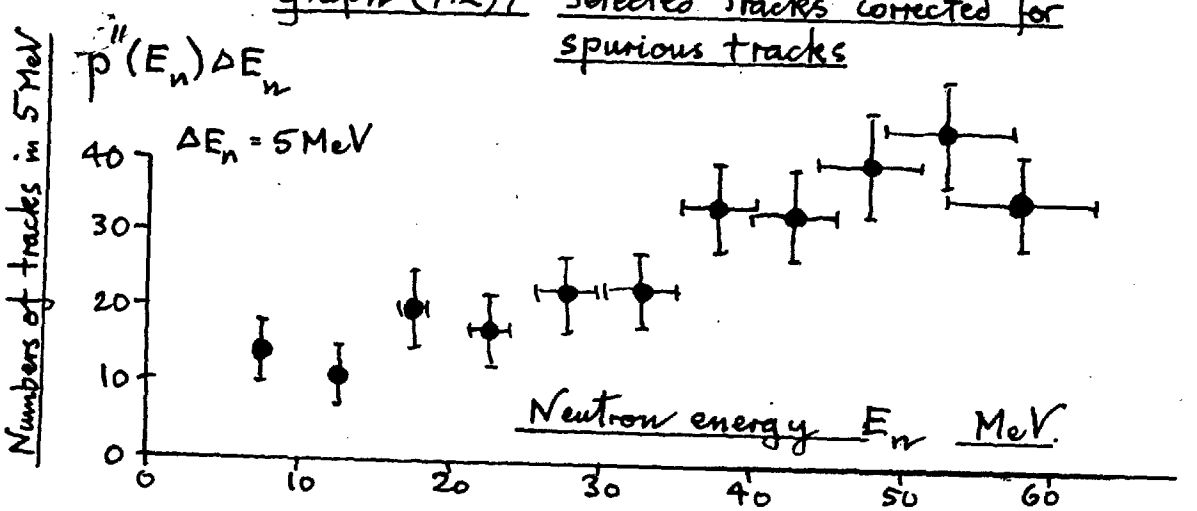

When this distribution of spurious tracks is subtracted from the corrected total distribution of tracks, $p'(E_n)$, an estimate $p''(E_n)$ of the true distribution selected tracks of beam scattered protons, is obtained. $p''(E_n)\,\delta E_n$ for $\delta E_n = 5$ MeV is plotted on graph (4.2)7.

Before deriving the initial neutron energy spectrum a brief consideration will be given to the number and causes of the spurious tracks. From equation 4.9/9, the number of spurious tracks has been calculated to be 15% of the total number of selected tracks.

A similar estimate of 15% for their number was made in section 2.7, from the distribution in space of starts of tracks, in and out of the defined beam. Yet a third estimate of the number of spurious tracks may be made by considering the possible causes of scattered neutrons in the chamber. From the known thickness of metal in front of the chamber, the number of spurious tracks was estimated to be only 5% of all tracks. The number of tracks from neutrons that were scattered in the hydrogen of the chamber, was estimated to be 6% of all tracks. The difference between the total of these rough estimates (11%) and the observed (15%) proportion of spurious tracks is not significant.

4.2.5 Neutron energy spectrum.

From the corrected observed distribution of selected beam scattered proton tracks, $p''(E_n)$, the neutron flux, or energy spectrum, $n(E_n)$ may be obtained. A knowledge of the selection probability $P(E_n)$, and a knowledge of the total scattering cross section ${}_{n-p}\sigma_T(E_n)$ are required. $P(E_n)$ calculated in appendix F is plotted on graph (4.2)8. The total cross section, taken from Harwell data (unpublished) is plotted on graph (4.2)9. Using these, and equation 4.2/5, the calculated neutron flux per burst of particles, in the chamber, in energy intervals 5 MeV wide $(n(E_n)\,\delta E_n)$ neutrons per cm^2, is plotted on graph (4.2)1 The fractional errors in this distribution of flux are taken to be the same as those of the distribution of selected tracks $p(E_n)\,\delta E_n$. The errors involved in the numerical integration used to derive $P(E_n)$ were less than 1% and therefore negligible; and the errors in the cross section were also negligible. The errors in the correction for spurious and high energy tracks may be ignored since both corrections were themselves less than the statistical and energy errors in the flux.

Graph (4.2)8

Probability of selection of tracks in 'starting and stopping tracks scan'

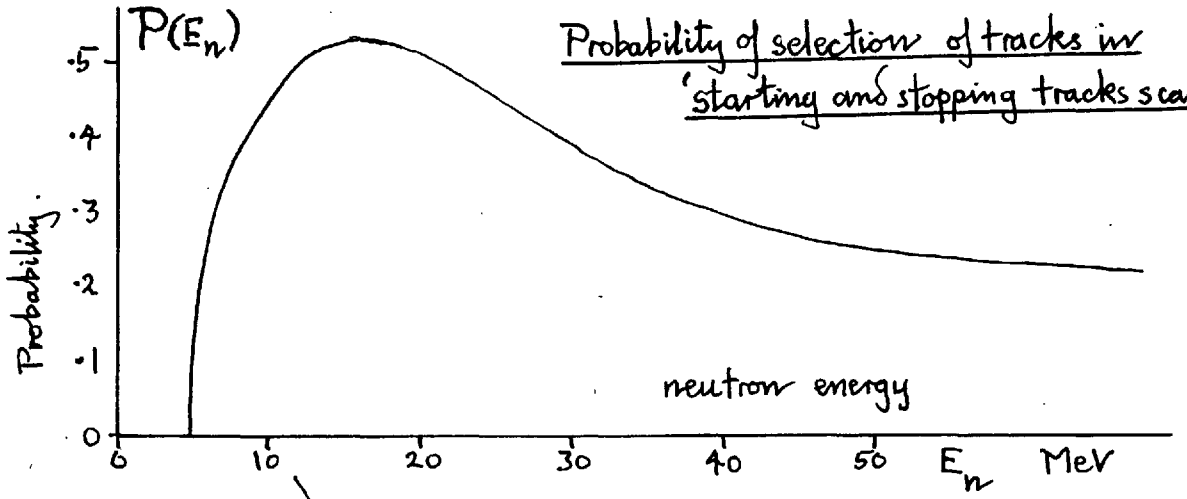

Graph (4.2)9

n-p total scattering cross-section.

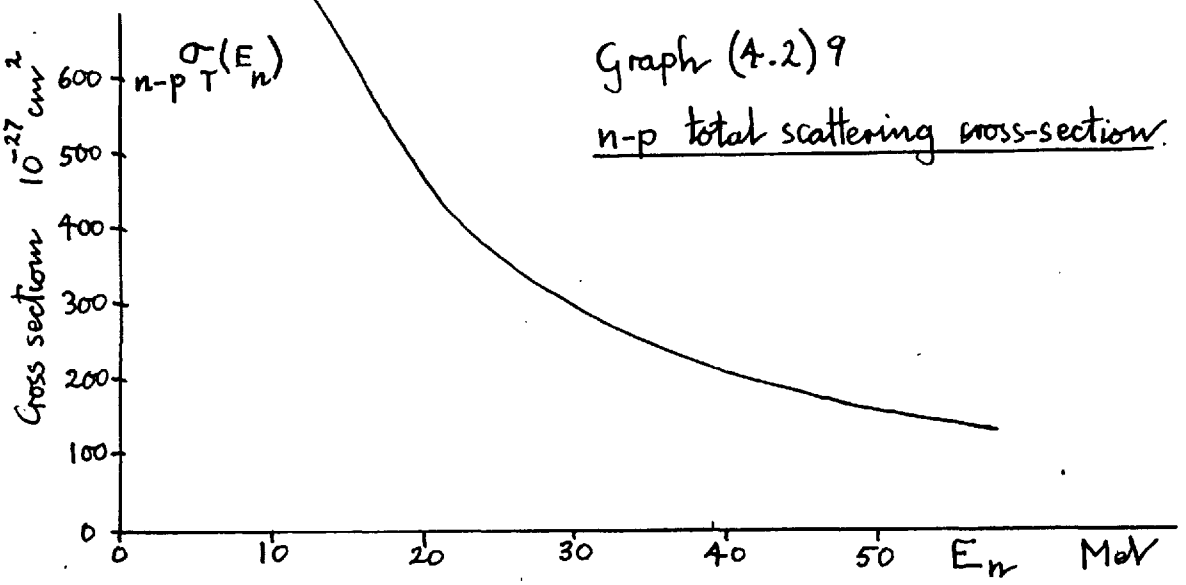

Graph (4.2)10

Hardening factor using 50cm. of polythene.

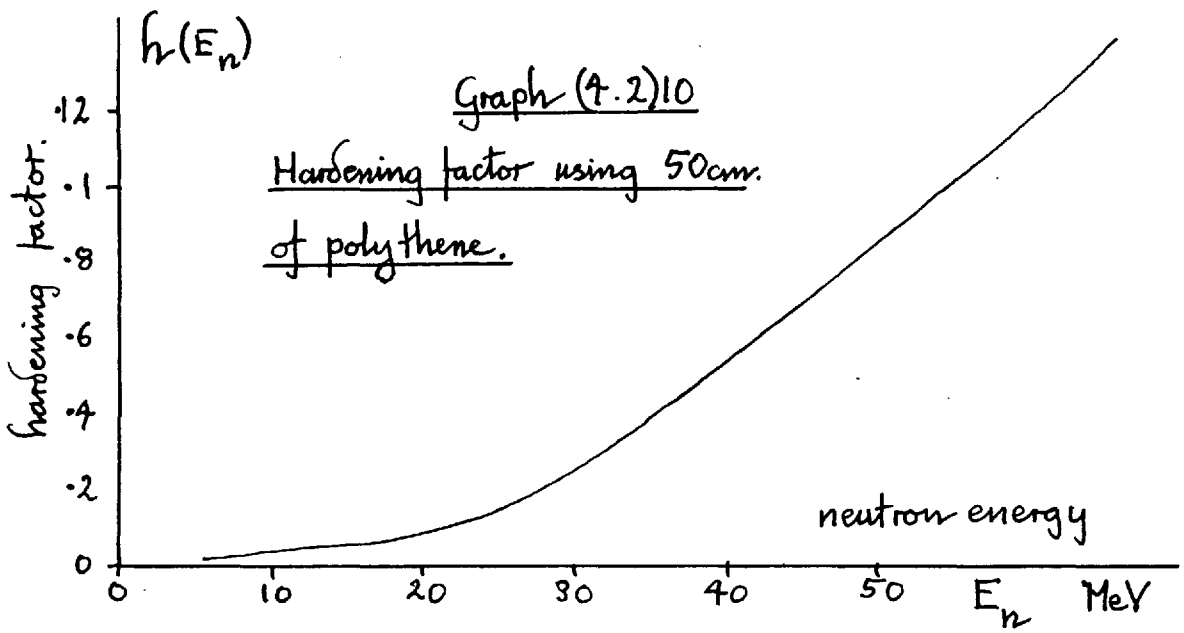

Graph (4·2)11 Number of tracks starting in V'

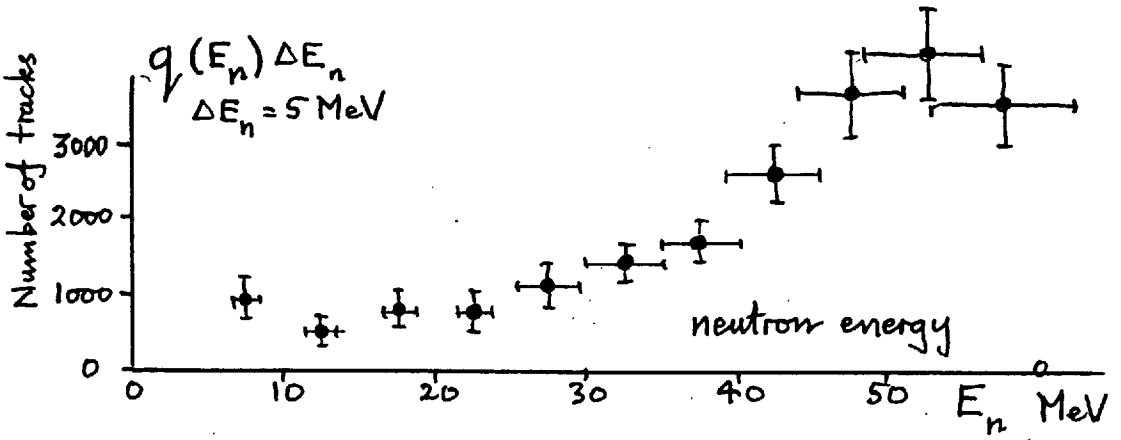

Graph (4·2)12 Neutron Flux after hardening

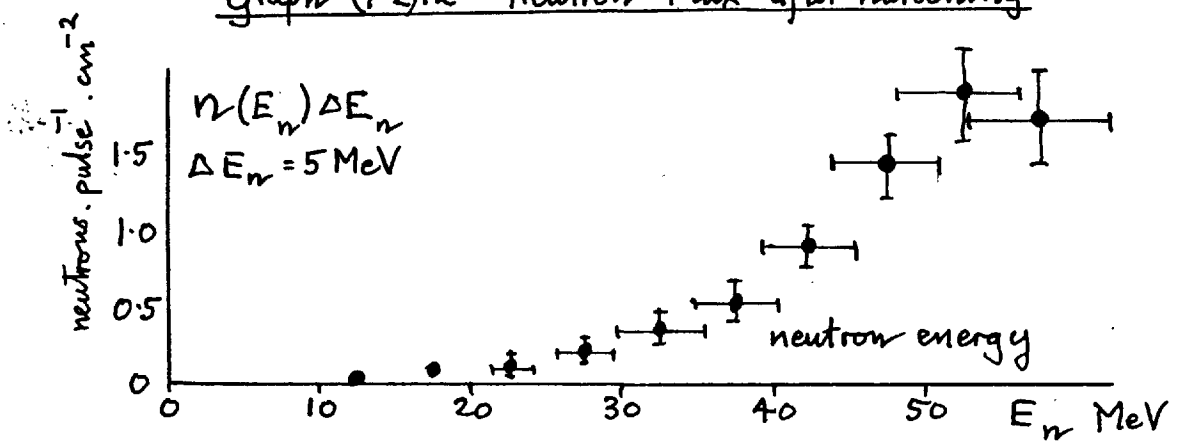

Graph (4·2)13 Neutron flux before hardening.

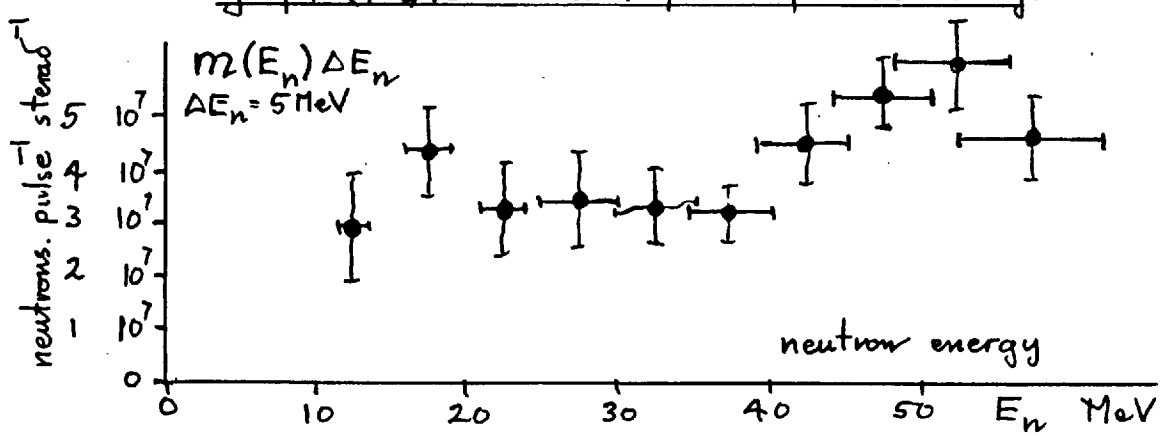

The estimated total number of beam scattered proton tracks, starting in the volume V' (see section 4.2.2) whether selected or not, with energies in the interval $\delta E_n, (q(E_n)\ \delta E_n)$, derived from the equation 4.2/5, is plotted on graph (4.2)12.

The flux of neutrons, per unit solid angle, per burst of particles, leaving the target, before hardening, with energies in the interval $\delta E_n, (m(E_n)\ \delta E_n)$, was also calculated, using the equation:

$$m(E_n) = \frac{n(E_n)}{h(E_n)} \cdot (\ell_c)^2 \qquad 4.2/12$$

where ℓ_c = distance from chamber to target and $h(E_n)$ = hardening factor, defined and calculated in section 2.6, and plotted on graph (4.2)10. The estimated values of $m(E_n)\ \delta E_n$, where δE_n = 5 MeV, are plotted on graph (4.2)13.

4.3 ANCILLARY RESULTS.

4.3.1 Determination of neutron-proton differential cross-sections (1).

Before giving the results of the neutron-capture cross section determination, certain other experimental results and observations will be described.

One of the objects of the experiment, proposed in section 2.1, was to measure the n-p elastic differential cross section, with a view to using the results as a check on the experimental methods.

From equation (4.2)7 the angular distribution of selected protons is given by

$$p''(\theta, E_n) \propto 2\pi(\sin 2\theta)(G(\theta, E_n))({}_{n-p}\sigma(\theta, E_n),)$$

from which the variation of ${}_{n-p}\sigma(\theta, E_n)$ with θ may be obtained. It is seen, however, from graph (4.2)2 that $G(\theta, E_n)$ has values other than zero only over limited ranges of θ and thus the variation of the differential cross section can only be obtained over these ranges. Using the results of the 'starting and stopping tracks scan' without correction for spurious tracks approximate variation of ${}_{n-p}\sigma(\theta, E_n)$ have been derived and plotted on graph (4.3)1. The continuous lines are results from Harwell data whose errors are very much less than those of the

Graphs (4.3)1 Differential n-p scattering cross-sections

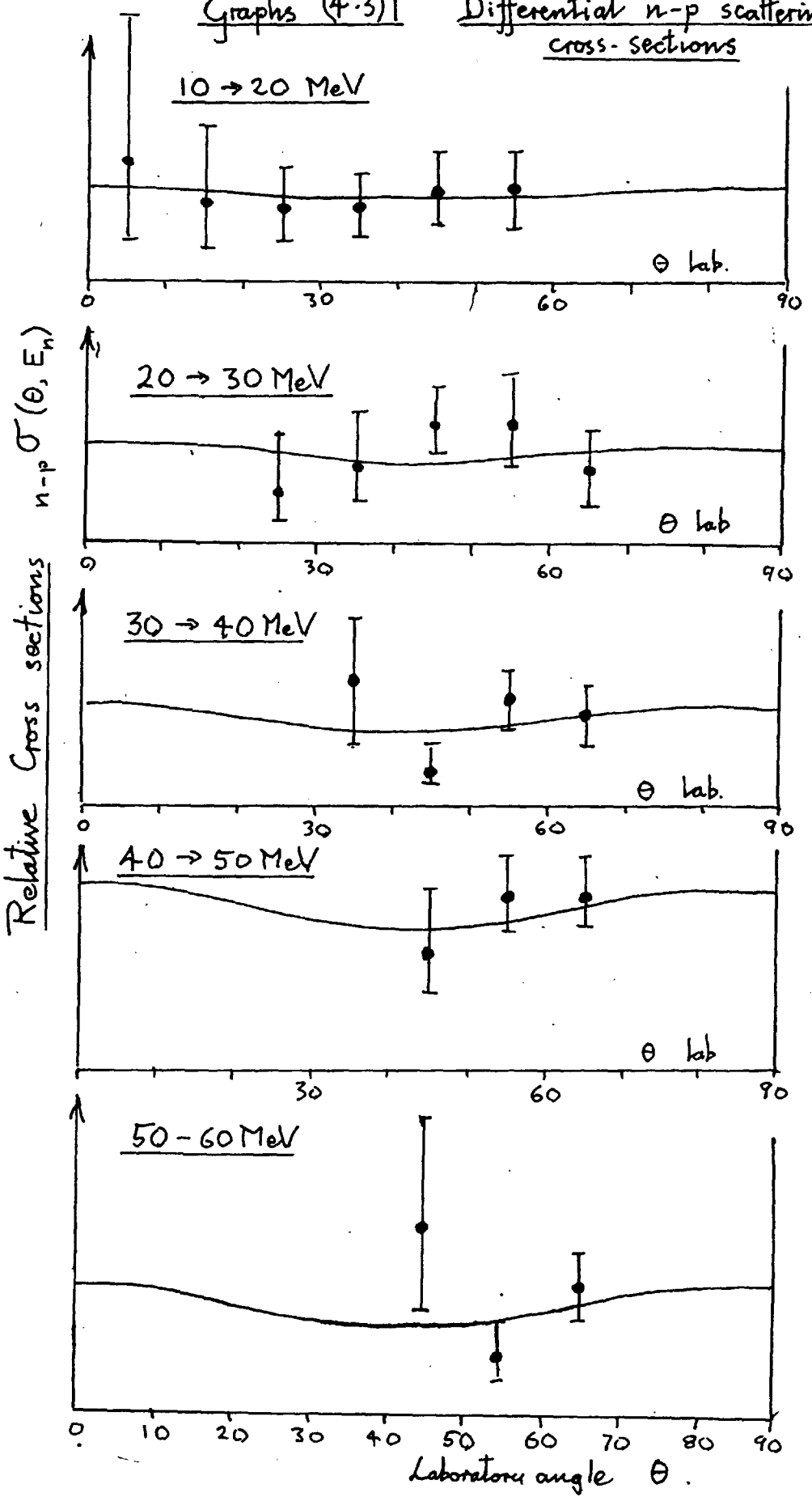

present determination. The satisfactory agreement with the Harwell data may be regarded as a confirmation of the calculated values of the selection probability ($G(\theta, E_n)$), and evidence of freedom from scanning biases.

4.3.2 Determination of neutron-proton differential cross section (2).

As an alternative to the above method, the relative n-p differential cross section could be obtained from the results of the 'all starting tracks scan'; (see section 3.2.4). In this scan, the total number $\left(\int q(\theta, E_n)\, dE_n \right) \delta\theta$ of tracks that started in the defined volume V' and which had track lengths greater than 0·25 cm. and whose angles (θ) were in the interval $\delta\theta$, was determined. The energy, E_n, of the neutrons knocking on protons that did not stop in the chamber could not be obtained from the proton track ranges. However, from the results of the 'starting and stopping tracks scan' (graph(4.2)12), it is seen that the number of events ($q(E_n)$) per unit interval of initial neutron energy (E_n) is peaked at approximately 50 MeV. To a first approximation, therefore, it may be assumed that all events are due to an initial neutron energy of 50 MeV.

For θ less than that angle (θ_c) at which the range of a scattered proton from a 50 MeV neutron would be 0·25 cm.,

Graph (4.3)2 Numbers of events, in angle intervals, selected in 'starting tracks scan'

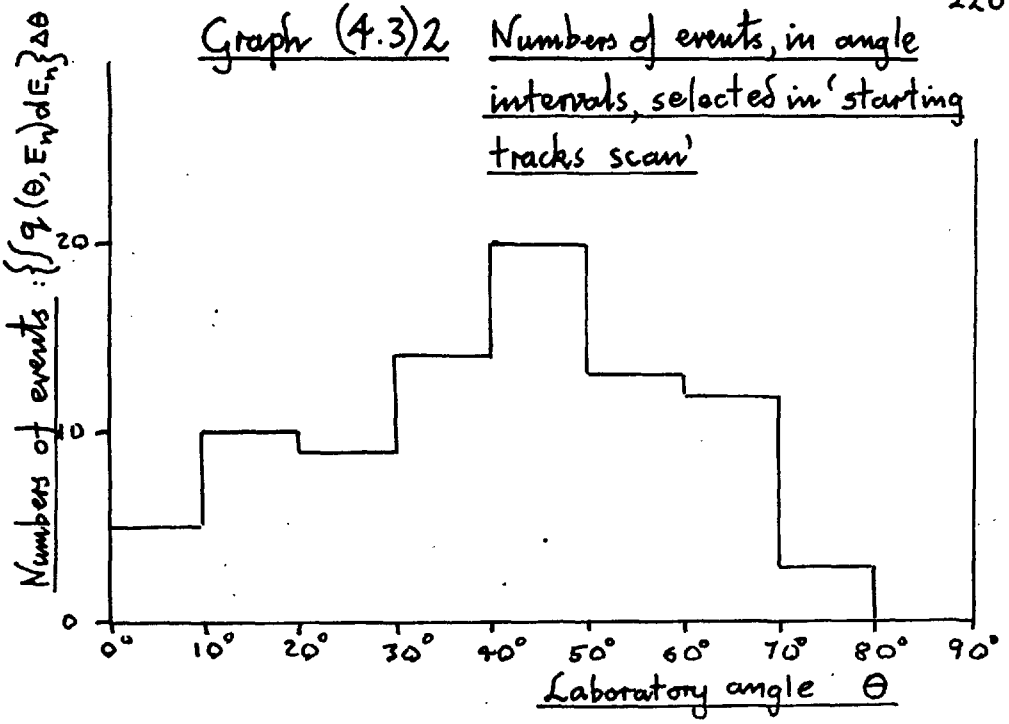

Graph (4.3)3 Relative differential cross-sections for n-p scattering at 45 ± 15 MeV.

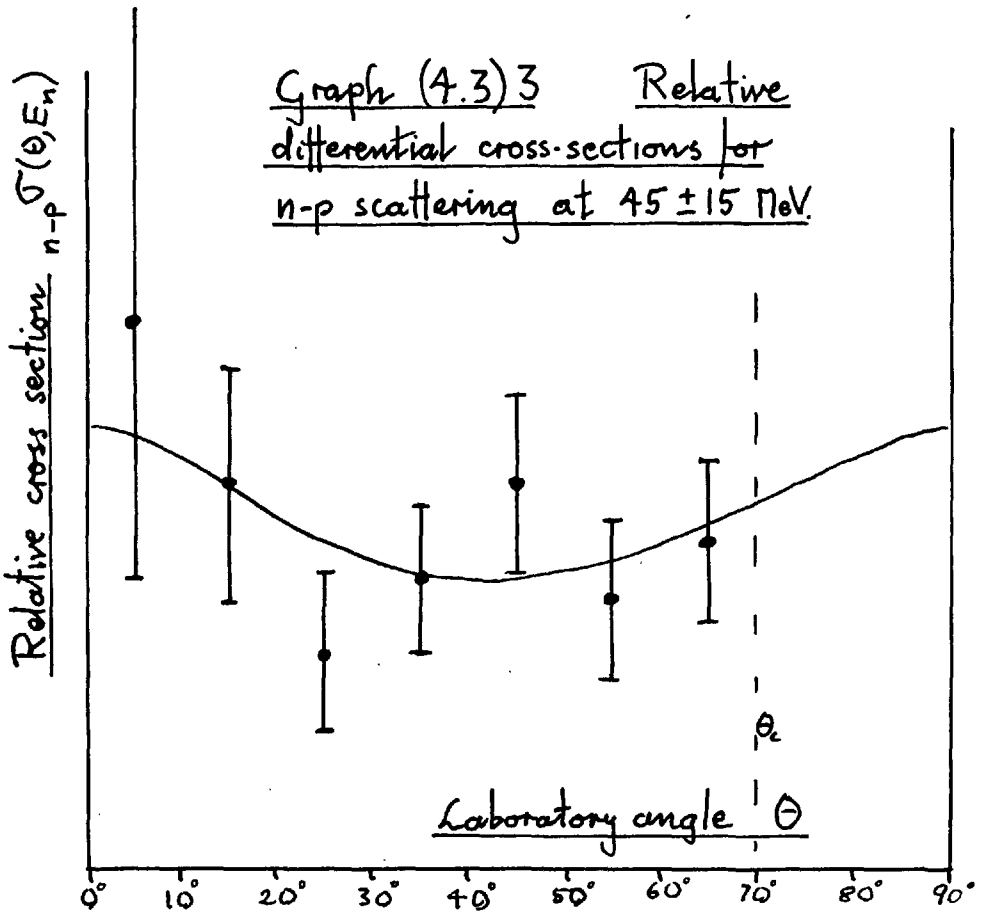

$$\left\{\int_0^\infty q(\theta, E_n)\, dE_n\right\}\delta\theta \propto (\text{approx.})\ 2\pi . \sin 2\theta .\ {}_{n\text{-}p}\sigma(\theta, 45\,\text{MeV})\,\delta\theta$$

The observed values of $\left(\int q(\theta, E_n)\, dE_n\right)\delta\theta$, for $\delta\theta = 10^\circ$, from this scan, and the derived relative differential cross sections are plotted on graphs (4.3)2 and (4.3)3.

The continuous line in graph (4.3)3 is again from Harwell data, and the satisfactory agreement with this data provides confirmation of freedom from scanning bias.

4.3.3 n-p, n-p Double scattering.

Half the results from the 'starting and stopping tracks scan', (about 170 photographs) were searched, with the help of the computor, for measurements of double n-p, n-p elastic scattering events (see section 2.1.3). All possible pairs of tracks on one pair of stereo-photographs were considered in turn, and the selection conditions given in section 2.2.3 applied to them. The tolerances used in applying these conditions were made wide enough to include not only all possible true double scattering events, but also some pairs of tracks, which by coincidence, appeared to correspond to double scattering events. From the 170 frames scanned, 19 pairs of tracks were selected, of which only about half were expected to represent true double

scattering. It was hoped, on further consideration of the 19 selected pairs, that they would fall into two categories: those representing true double scattering that would fit the selection conditions well, and those which because they were not true double scattering events would not fit the conditions so well. In fact the errors in measurements were such that it was not possible to distinguish the better fits of the double scattering events, and the method had to be abandoned.

4.4 DETERMINATION OF THE NEUTRON CAPTURE CROSS SECTION.

4.4.1 Basic equations.

The method of determining the number of neutron capture deuterons has been outlined in section 2.2.4. It relies on the fact that the distribution, in angle and range, of neutron capture deuteron tracks, is fundamentally different from the distribution, in angle and range, of neutron scattered proton tracks produced by the same neutron beam. From a determination of the distribution of both deuteron and proton tracks, therefore, it is possible to make separate estimates of the number of deuterons and the number of protons, that have contributed to the combined distribution.

Let E_n be the initial neutron energy, on the assumption that a track represents a particle that has been scattered by the beam. E_n is given as a function of the range r and angle θ of a track by equations 1.5/9 and 1.2/1. The term E_n will still be defined by these equations, as a function of range and angle, even if the track is known to represent a deuteron. E_i will be defined as the initial neutron energy, on the assumption that a track represents a neutron capture deuteron. For the same track, therefore, $E_i \neq E_n$. Consider that part of the total distribution of tracks due to neutron - capture deuterons. From

From equation 1.5/7, the angle θ of the deuteron track must be less than $5{\cdot}4^{\circ}$. E_n will, therefore, be given approximately by:

$$E_n = \frac{10{\cdot}7\ (r)^{{\cdot}548}}{\cos^2\theta} \doteq 10{\cdot}7(r)^{{\cdot}548}.$$

Using equations 1.5/8 and 1.5/3 the initial neutron energy, if the particle is a deuteron, E_i, is given by:

$$E_i = 2 \quad 14{\cdot}3\ (r)^{{\cdot}548} \doteq 2{\cdot}67\ E_n \qquad 4.4/1$$

In section 4.2 various terms (e.g. $G(\theta, E_n)$, $p(\theta, E_n)$, etc.) have been defined which apply to the 'starting and stopping tracks scan'. In this section corresponding terms will be defined, that apply to the 'small angle tracks scan'. These corresponding terms will be denoted by the same letters, but with an underline, (e.g. $\underline{G}(\theta, E_n)$, $\underline{p}(\theta, E_n)$.

Let the probability that tracks be selected from the small angle scattering scan be $\underline{G}(\theta, E_n)$. Then the number of selected tracks in the intervals $d\theta$ and dE_n, $\underline{p}(\theta, E_n)\ d\theta\ dE_n$, will be given by

$$\underline{p}(\theta, E_n) = \underline{G}(\theta, E_n)\ \ \underline{q}(\theta, E_n), \qquad 4.4/2$$

where $\underline{q}(\theta, E_n)\ d\theta\ dE_n$ is the total number of tracks in the intervals $d\theta$, dE_n, that start in the volume V' of the chamber.

Let $$\underline{p}(E_n) = \int \underline{p}(\theta, E_n)\ d\theta$$

and $$\underline{q}(E_n) = \int \underline{q}(\theta, E_n)\ d\theta.$$

Let those parts of these distributions due to neutron capture deuterons be, similarly, $\underline{q}_d(\theta, E_n)$, $\underline{p}_d(\theta, E_n)$ etc; and those parts due to scattered protons and spurious tracks be $\underline{q}_p(\theta, E_n)$, $\underline{p}_p(\theta, E_n)$ etc.

By the definitions of the cross sections at the same initial energy (E_i) and using equation 4.4/1: $E_i = 2{\cdot}67\, E_n$

$$\frac{\underline{q}_d(E_n)}{\underline{q}_p(2{\cdot}67E_n)} = \frac{{}_{cap}\sigma_T(E_i)}{{}_{n-p}\sigma_T(E_i)} = \frac{{}_{cap}\sigma_T(2{\cdot}67\, E_n)}{{}_{n-p}\sigma_T(2{\cdot}67\, E_n)} \qquad 4.4/3$$

It will be shown, in appendix H, that for all angles ($\theta < 5{\cdot}4^\circ$) in which deuterons may be found, $\underline{G}(\theta, E_n)$ is approximately independent of θ and therefore, equal to $\underline{G}_g(r)$. Using this fact and equation 4.4/2 it follows that:

$$\underline{p}_d(E_n) = \underline{N}\ \underline{G}_g(r)\ \frac{{}_{cap}\sigma_T(2{\cdot}67\, E_n)}{{}_{n-p}\sigma_T(2{\cdot}67E_n)}\ \underline{q}_p(2{\cdot}67E_n) \qquad 4.4/4$$

Thus from a knowledge of the numbers of deuterons selected by the small angle scan in intervals δE_n, $\underline{p}_d(E_n)\,\delta E_n$, and from the number of neutron scattered protons starting in the volume V', in an interval δE_n, $\underline{q}_p(E_n)\,\delta E_n$, may be obtained the ratio of the neutron capture, to scattering, cross sections. The determination of the selection probability $\underline{G}(\theta, E_n)$ will be considered in the next sub-section. $\underline{q}_p(E_n)$ will be derived in section 4.4.3, and the number of deuterons $\underline{p}_d(E_n)$ in section 4.4.4.

4.4.2 Probability of selection.

Since all deuterons have tracks less than $5{\cdot}4^{\circ}$, tracks were selected in the 'small angle tracks scan' that satisfied the conditions (equation 3.2/1),

$$\bar{\Phi}_T \leqslant \quad \varepsilon \quad = 7{\cdot}5^{\circ}$$
$$\Phi_B \leqslant \quad \varepsilon \quad = 7{\cdot}5^{\circ}$$

A further geometrical condition selected only tracks that started in volume $\underline{V}$'and stopped in volume $\underline{V}$, where $\underline{V}$'was that part of the visible chamber that was inside the beam cross section, and where $\underline{V}$ was the visible part of the chamber except that part within 3 mm. of a wall or window, (see figure (4.4)1). The selection probability will depend on the form of the volumes $\underline{V}$ and $\underline{V}$' and can, in principle be derived from a four fold integral similar to that of equation 4.2/5. It was not found possible to integrate such an expression, even numerically, with the truncated polygonal cones that defined $\underline{V}$ and $\underline{V}$'. It would have been more convenient to have defined rectangular volumes $\underline{V}$ and $\underline{V}$'as was done for the corresponding volumes V and V' used in the 'starting and stopping tracks scan'. This would, however, have reduced the number of deuterons selected by a factor of two. Accurate knowledge of $\underline{G}(\theta, E_n)$ is, however, only required for small angles and this enables an approximate determination of $\underline{G}(\theta, E_n)$ to be made. It will be shown in appendix H that the probability be written:

$$\underline{G}(\theta, E_n) \doteqdot \underline{G}_g(r) \quad \underline{G}_a(\theta) \qquad 4.4/5$$

Figure (4.4)1 'small angle tracks scan' selection volumes V and V'

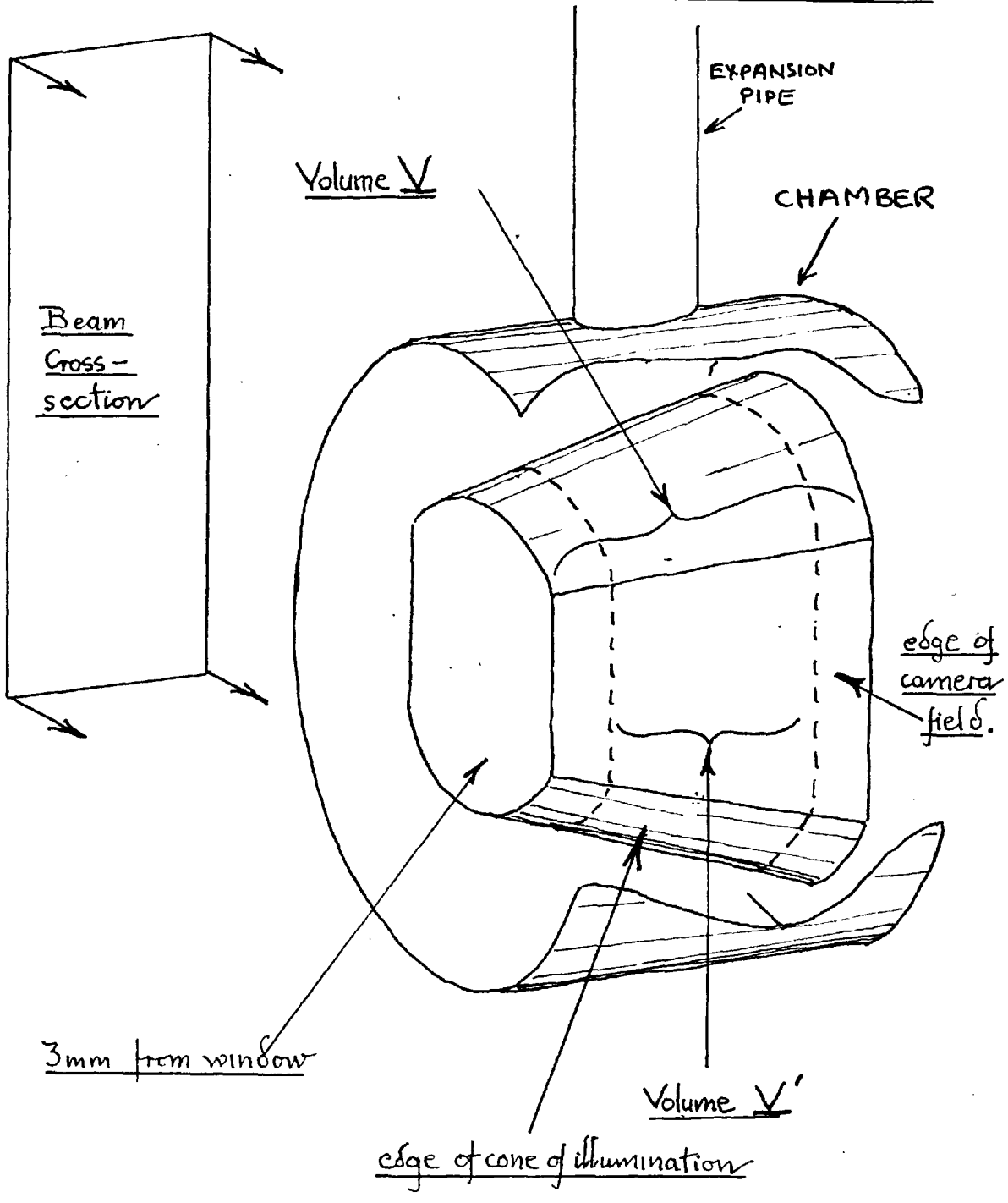

where $G_a(\theta)$ depends only on the small angle conditions, and $G_a(0) = 1$; and where $G_g(r)$ depends only on the geometrical condition and is equal to $G(0, E_n(0, r))$. $G_g(r(\theta, E_n))$ as a function of θ and E_n is plotted on graph (4.4)2 and $G_a(\theta) \cdot 2\pi \sin 2\theta$ is plotted on graph 4.4.2 .

4.4.3 Numbers of n-p events.

$q_p(E_n)\, dE_n$ has been defined as the total number of proton tracks in the interval dE_n, starting in the volume V' during the 'small angle tracks scan'. The distribution $q(E_n)$ obtained in section 4.2.5 differs from $q_p(E_n)$ in that it represented numbers of tracks observed during 'starting and stopping tracks scan', and also in that only tracks starting in the smaller volume V' were considered. If neither the neutron energy spectrum nor the mean neutron intensity changed between the two scans, then

$$q_p(E_n) = \frac{V}{V} \frac{N}{N} q(E_n), \qquad 4.4/6$$

where N and N are the numbers of cyclotron bursts of particles in the 'small angle' and 'starting and stopping' scans. The only possible cause of a change in spectrum would have been the slow continuous decomposition of the lithium deuteride target (see section 2.5). Since the neutron energy spectra determined before and after the small angle scan were not significantly different, this decomposition will be assumed small and the

Graph (4·4)2 Geometrical part of 'small angle tracks scan' selection probability.

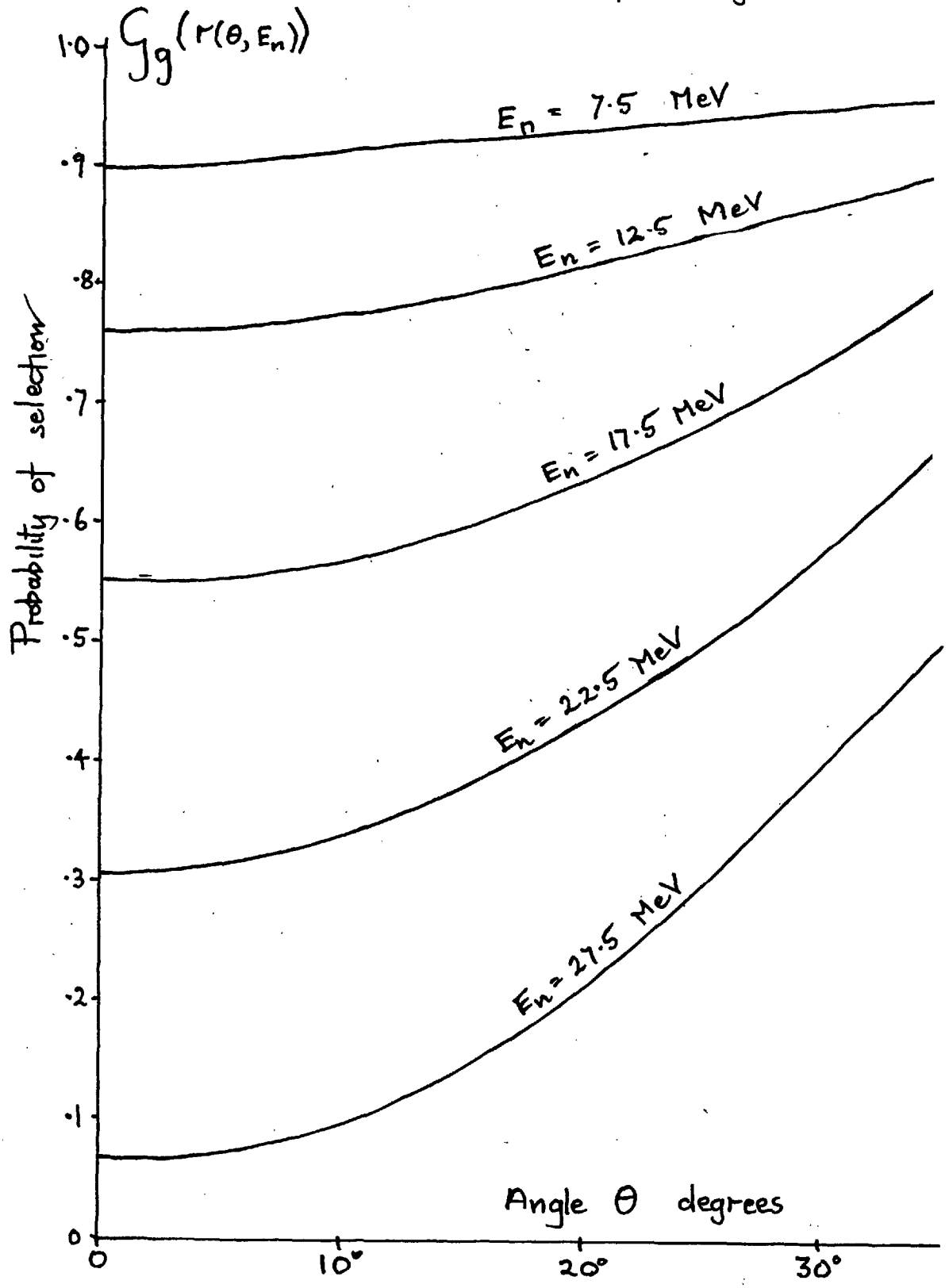

Graph (4.4)3 Small angle part of 'small angle tracks selection' probability x $2\pi \sin 2\theta$.

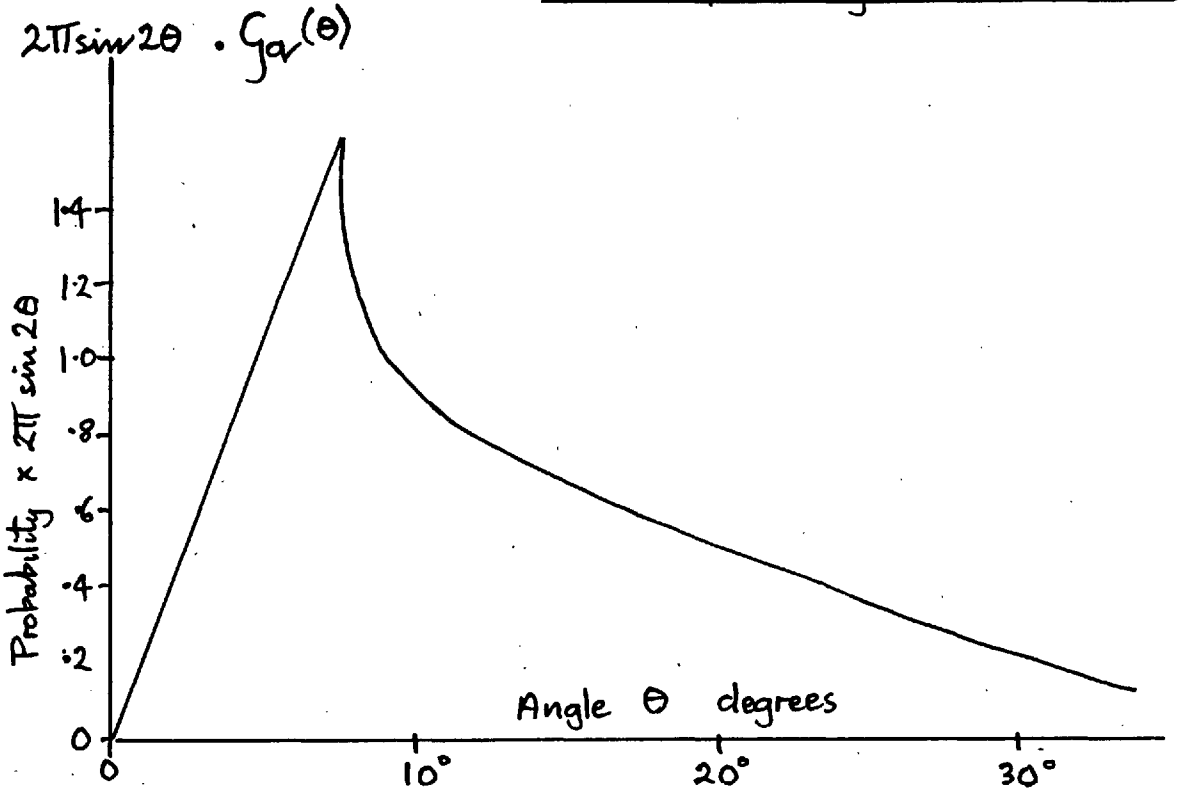

spectrum will be assumed to have remained constant.

The mean neutron intensity, however, did fluctuate and thus the equation 4.4/6 must be modified by the addition of a normalization factor to give:

$$\underline{q}_p(E_n) = \mu \frac{\underline{N}\ \underline{V}}{N\ V} q(E_n) \qquad 4.4/7$$

where:

$$\mu = \frac{\text{mean neutron intensity during 'small angle tracks scan'}}{\text{mean neutron intensity during 'starting and stopping tracks scan'}}$$

The mean number $s_{(SATS)}$ of starting tracks per frame in the 'small angle tracks scan' was obtained by counting, without measurement, the number of starting tracks in five groups of 40 photographs each, spread evenly through the scanned film. The mean number ($s_{(SASTS)}$) of starting tracks in the 'starting and stopping tracks scan' was obtained by similarly counting the tracks in all the film scanned. Then

$$\mu = \frac{s_{(SATS)}}{s_{(SASTS)}} = \frac{20{\cdot}5}{20{\cdot}0} = 1{\cdot}03 \pm 15\% \qquad 4.4/8$$

4.4.4 Determination of neutron-capture total cross section.

From equations 1.5/4 and 1.5/6 and 4.4/1 the angle (θ) of a deuteron track from an initial energy E_i and with E_n defined from the tracks range (r), must satisfy:

$$\theta < \hat{\theta}(E_i) = \sqrt{\frac{E_i}{8\ M_n}} = \sqrt{\frac{2{\cdot}67\ E_n}{8\ M_n}} = \theta(E_n) \qquad 4.4/9$$

The measured θ may be in excess of $\hat{\theta}(E_n)$ because of errors of measurement, K_θ. Let

$$\hat{\hat{\theta}}(E_n) = \hat{\theta}(E_n) + K_\theta \qquad 4.4/10$$

$\hat{\hat{\theta}}(E_n)$ for different values of E_n taking K_θ from graph (4.1)1 are then:-

E_n	7·5	12·5	17·5	22·5 MeV
$\hat{\theta}(E_n)$	3·3°	4·0°	4·6°	5·4°
K_θ	1·7°	1·0°	0·5°	0·3°
$\hat{\hat{\theta}}(E_n)$	5·0°	5·0°	5·1°	5·7°

Since most of the neutrons in the beam are in the energy range 30 - 60 MeV, (see graph (4.2)11, most of the neutron capture deuterons will have E_i in this range and thus E_n in the range.

$$\frac{30}{2{\cdot}67}\ \text{MeV} < E_n < \frac{60}{2{\cdot}67}$$

or approximately

$$10\ \text{MeV} < E_n < 25\ \text{MeV}$$

Thus only tracks in this energy range will be considered.

Consider now the distribution of selected tracks ($\underline{p}(\theta, E_n)$) in the range

$$10 \text{ MeV} < E_n < 25 \text{ MeV}.$$

At angles just above $\hat{\hat{\theta}}(E_n)$ all the selected tracks will be protons scattered by the neutrons in the low energy tail of the neutron spectrum. Just below $\hat{\hat{\theta}}(E_n)$ there will be a similar number of protons, but also a distribution of deuterons. In section 1.5.3 it was shown that this distribution of deuterons is highly peaked at angles, θ, just below $\hat{\theta}(E_n)$ (approximately $4{\cdot}5^{\circ}$). A (θ, χ) plot of observed selected tracks with angles below 10° is given in figure (4.4)4. Although there is a general increase in density of points at angles less than 5° there is no apparent concentration around $4{\cdot}5^{\circ}$. This is presumably caused partly by errors in measurement and partly by lack of statistics. The general increase in numbers of events below 5° is, however, assumed to be due to neutron-capture deuterons and from this increase the capture cross section will now be calculated.

Consider the number of selected proton tracks, $\underline{p}_p(\theta, E_n)\delta\theta\delta E_n$ in the intervals $\delta\theta$, δE_n, due to a neutron flux $\underline{n}(E_n)$. Ignoring spurious tracks, then,

$$p(\theta, E_n)\Delta\theta\delta E_n = \int_{\theta-\frac{\Delta\theta}{2}}^{\theta+\frac{\Delta\theta}{2}} \underline{\varepsilon}_a(\omega)\underline{\varepsilon}_g(r(\theta, E_n))\, 2\pi \sin 2\omega\, \underline{N}\, \underline{V}'\, \rho\, N_A\, \underline{n}(E_n)\, {}_{n\text{-}p}\sigma(\omega, E_n)\, \delta E_n\, d\omega$$

Figure(4.4)4 Angular distribution of 'small angle tracks' with ranges of 1 - 4cm, ie E_n = 10 - 22.5 MeV.

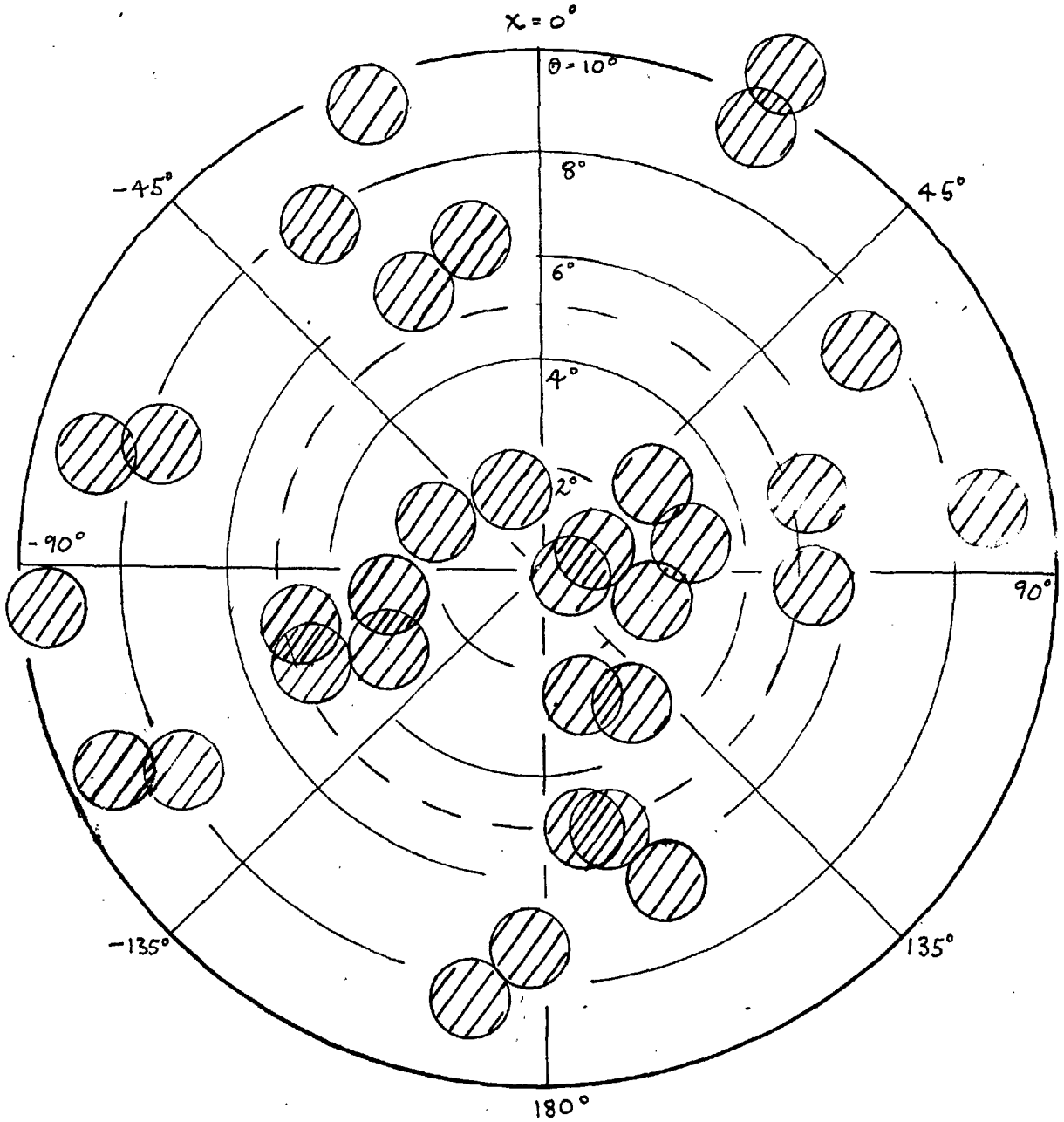

Sense of directions as though looking into the beam

The only terms in the integral that varies rapidly with ω is $G_a(\omega)$ and $\sin(2\omega)$, therefore

$$\underline{\rho}_p(\theta, E_n)\,\Delta\theta\,\Delta E_n = \left(\int_{\theta-\frac{\Delta\theta}{2}}^{\theta+\frac{\Delta\theta}{2}} \underline{G}_a(\omega)\, 2\pi \sin 2\omega \, d\omega \right) \underline{G}_g(r(\theta, E_n))\, \underline{N}\, \underline{V}\, \rho\, N_A\, \underline{n}(E_n)\, {}_{n-p}\sigma(\theta, E_n)\,\Delta E_n \qquad 4.4/11$$

Values of $\underline{n}(E_n)$ obtained from the observed number of tracks in given intervals of angle and energy are plotted on graphs (4.4)5 and (4.4)6. Those values of $\underline{n}(E_n)$ marked with a cross on this graph were obtained using the angle interval 0 to $\hat{\hat{\theta}}(E_n)$, in which all possible deuteron tracks should appear. It is seen from graph (4.4)6, where the energy interval is 10 - 25 MeV, that $\underline{n}(E_n)$ is approximately constant for all angles above $\hat{\hat{\theta}}(E_n)$ but is significantly higher than the mean value for the angle range below $\hat{\hat{\theta}}(E_n)$. This rise is interpreted as representing the presence of neutron capture deuterons. The mean values of $\underline{n}(E_n)$ taken over all angles above $\hat{\theta}(E_n)$ for different values of E_n, are marked as dotted lines on graphs (4.4)5, and are plotted on graph (4.4)7 together with the values $n(E_n)$ obtained from the 'starting and stopping tracks scan'.

When the mean of values of $\underline{n}(E_n)$ taken over angles above $\hat{\hat{\theta}}(E_n)$ is substituted into equation 4.4/11, an estimate may be

Graphs (4·4)5 The initial neutron flux derived from the small angle scan, ignoring deuterons and spurious tracks.

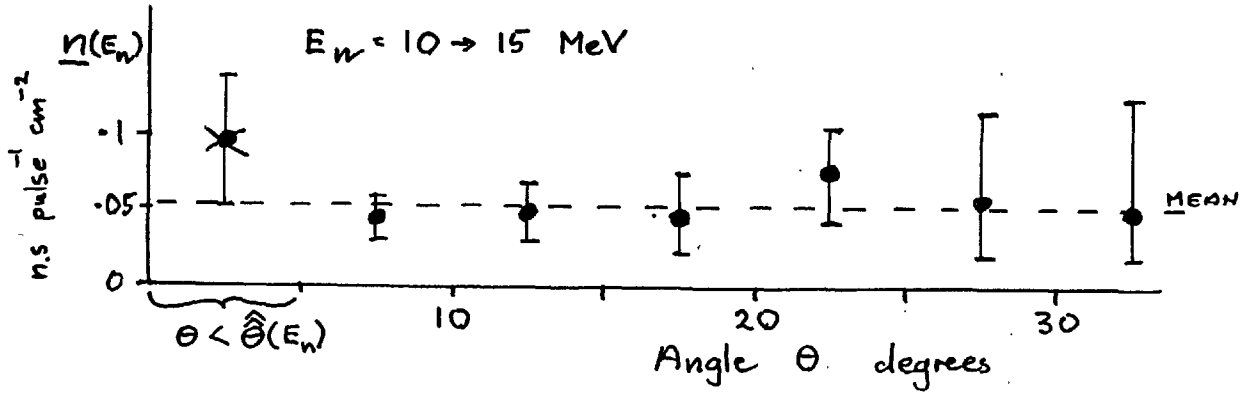

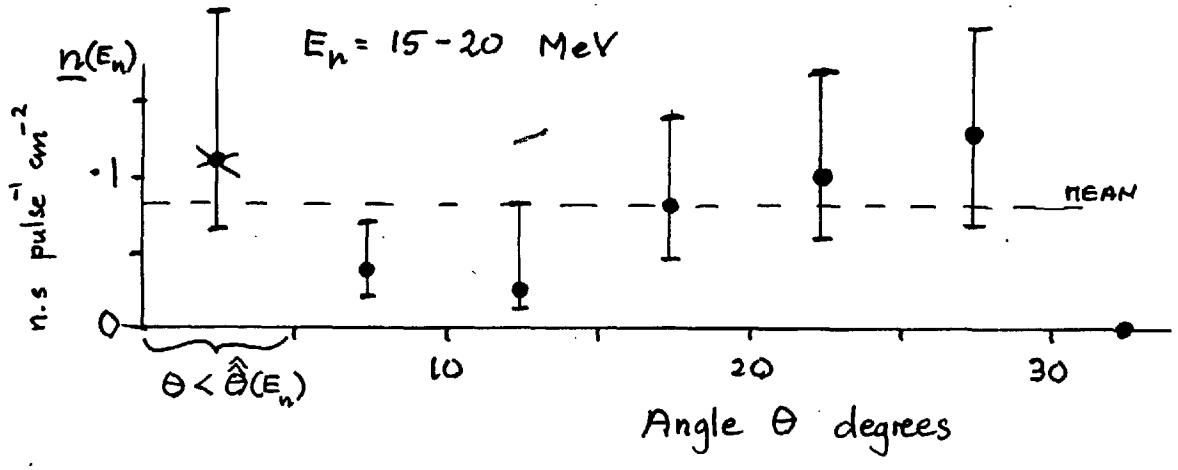

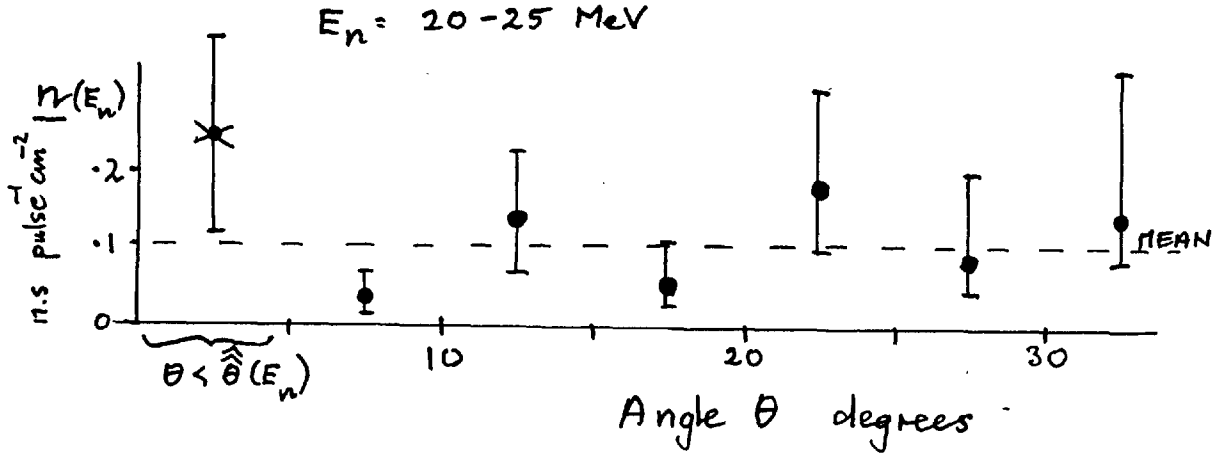

Graph (4.4) 6 Variation of $\underline{n}(E_n)$ with angle. Above $\hat{\hat{\theta}}(E_n)$ $\underline{n}(E_n)$ should be constant. Below $\hat{\hat{\theta}}(E_n)$ the presence of neutron capture deuterons may increase $\underline{n}(E_n)$.

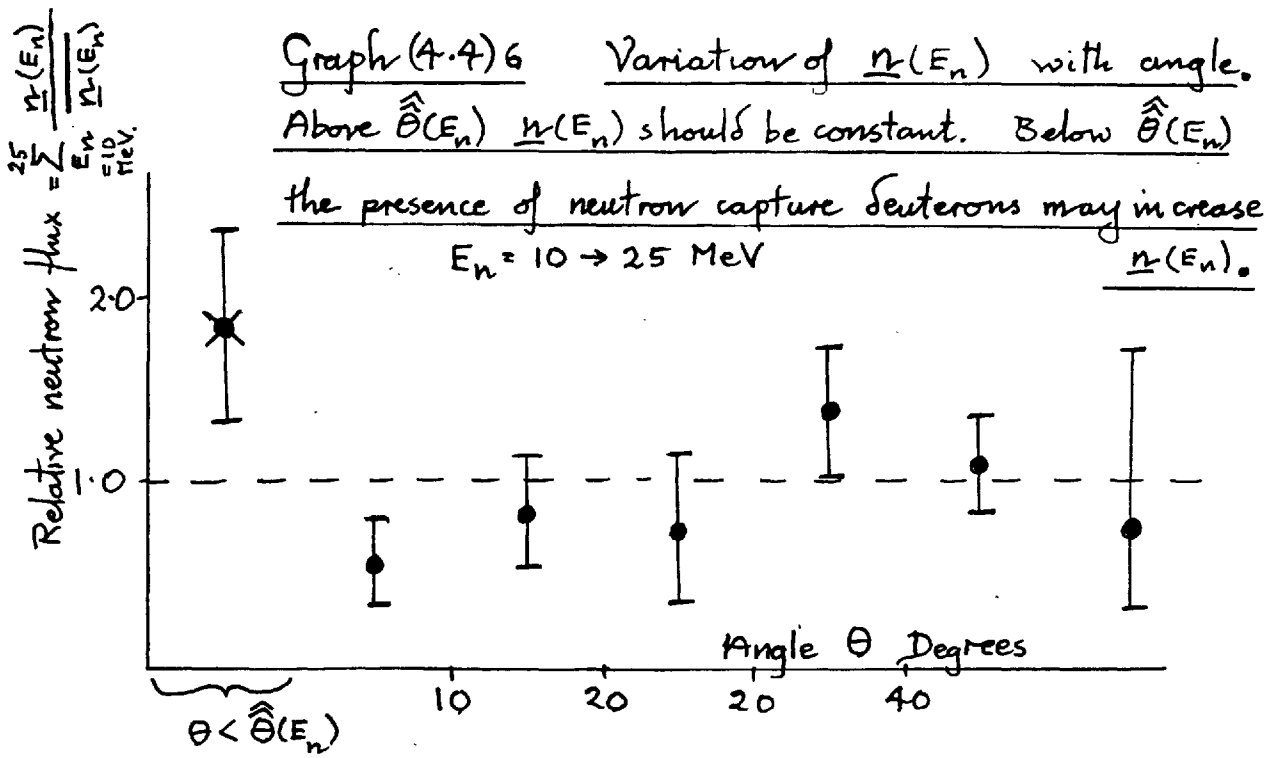

Graph (4.4) 7

hardened beam intensity derived without correction for spurious tracks, from:

1) 'small angle tracks scan' :

2) 'starting and stopping tracks scan' :

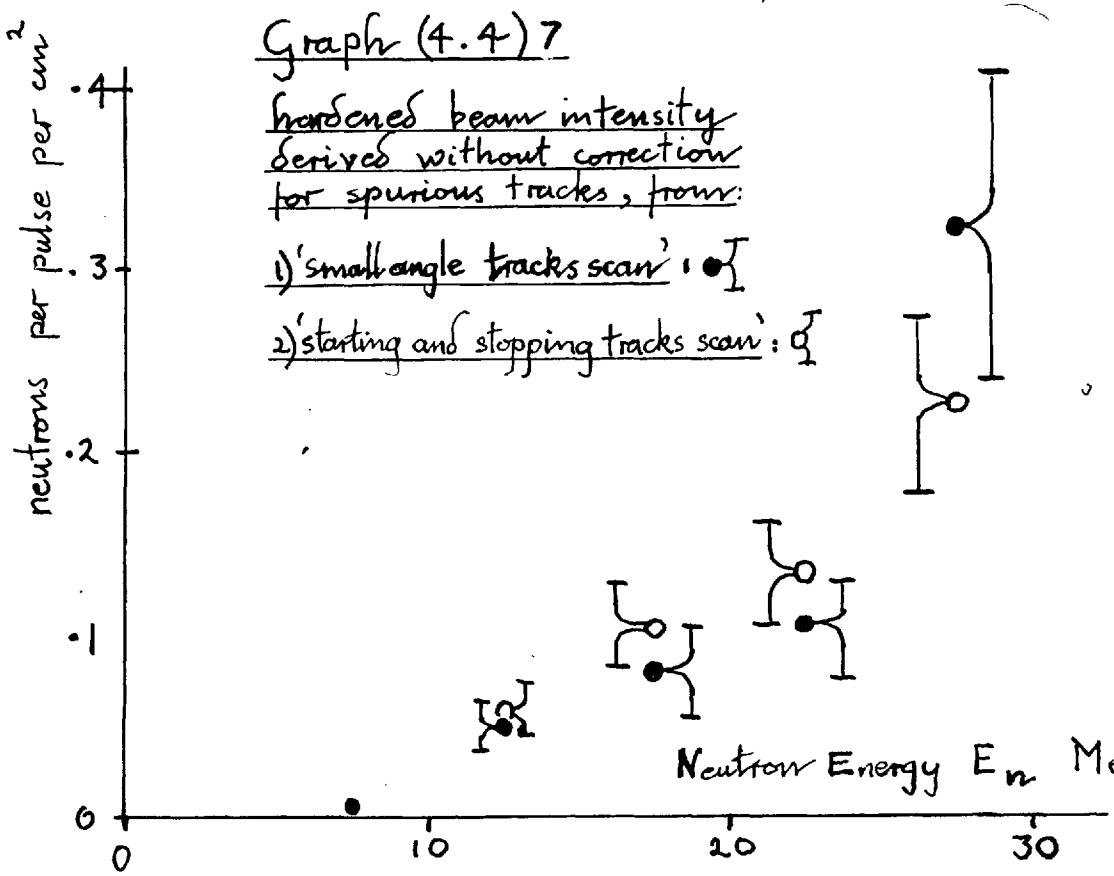

made of the number of protons in the range less than $\hat{\hat{\theta}}(E_n)$. This estimated number of protons, in the energy interval ΔE_n shall be referred to as $\underline{p}_{p(DL)}(E_n)\,\Delta E_n$. No correction for spurious tracks were made either in $\underline{n}(E_n)$ or in $\underline{p}_{p(DL)}(E_n)$ derived from it. The number of deuterons in an energy interval ΔE_n, $\underline{p}_d(E_n)\,\Delta E_n$, may thus be estimated from the observed number of deuteron and proton tracks below $\hat{\hat{\theta}}(E_n)$, $(\underline{p}_{(DL)}(E_n)\,\Delta E_n)$ using:

$$\underline{p}_d(E_n) = \underline{p}_{(DL)}(E_n) - \underline{p}_{p(DL)}(E_n) \qquad 4.4/12$$

deuterons — total observed — protons calculated

The values of $\underline{p}_{(DL)}(E_n)\,\Delta E_n$, $\underline{p}_{p(DL)}E_n)\,\Delta E_n$ and the calculated number of deuterons $\underline{p}_d(E_n)\,\Delta E_n$ are given in the table below.

E_n	10 - 15	15 - 20	20 - 25	MeV
$p_{(DL)}(E_n)\ \Delta E_n$	5 ± 5	3 ± 3	4 ± 2	
$p_{p(DL)}(E_n)\,\Delta E_n$	2·7	2·3	1·6	
$p_d\ (E_n)\ \Delta E_n$	2·3	0·7	2·4	

The total estimated number of deuterons is seen to be

$$5{\cdot}4 \pm 3{\cdot}6$$

From equations 4.4/4, 4.4/5 and 4.4/7,

$$p_d(E_n)\,\Delta E_n \doteq \mu \frac{V}{V'} \underline{N}\, G_g(\gamma) \frac{\text{cap}\,\sigma_T(2{\cdot}67E_n)}{n\text{-}p\,\sigma_T(2{\cdot}67E_n)} \int_{(E_n-\frac{\Delta E_n}{2})2.67}^{(E_n+\frac{\Delta E_n}{2})2.67} q\ (E'_n)\ dE'_n \qquad 4.4/13$$

taking $G_g(r(\theta, E_n))$ from graph (4.4)2 $\pm$ 10%

$n\text{-}p\ \sigma_T(E_n)$ from graph (4.2)9

$q\ (E_n)$ from graph (4.2)11

and using:

$\underline{V}' = 144$ c.c. $\pm$ 5%

$V' = 105$ c.c. $\pm$ 5%

$N = 5268$ bursts

$\mu = 1{\cdot}03$ $\pm$ 15%

Values of the neutron-capture cross section obtained are given in the table below.

E_n	10 - 15	15 - 20	20 - 25	MeV
E_i	27 - 40	40 - 54	54 - 67	MeV
$G_g(r)$	·76	·55	·31	units
$\int q\ (E_n)\, dE_n$	·88	1·81	1·09	$cm.^{-2}$
$n\text{-}p\ \sigma_T(E_i)$	265	170	130	$10^{-27} cm.^2$
$\underline{p}_d(E_n)\ \Delta E_n$	2·3	·76	2·36	
$cap\ \sigma_T(E_n)$	122	17·5	120	$10^{-30} cm.^2$

A weighted mean of the results given as the neutron capture cross section at approximately 50 MeV:

$$cap\ \sigma_T(50\ \text{MeV}) \doteq 66\ \mu B.$$

The errors are dominated by the statistical errors in the numbers of small angle tracks observed. Other errors were,

however, included in obtaining the total R.M.S. error of $\pm$ 72% giving

$$_{cap}\sigma_{T}(50\ \text{MeV}) = 66 \pm 46\ \mu B \left(10^{-30}\ \text{cm}^2\right)$$

This results will be briefly discussed in the next and final section.

4.5 CONCLUSION.

The primary object of the experiment was to observe the neutron-capture process at medium energies. The experimental difficulties in the observation of the neutron-capture reaction arise from its small cross section compared with the cross section of neutron proton scattering (1 : 10,000). There is considerable theoretical interest in the polarization of the reaction (section 1.2). Because of the small reaction cross-section, however, not only has this polarization not been measured, but the reaction itself had not previously been observed. In the present experiment the reaction has been observed.

The total cross-section for neutron capture, determined in the present experiment at a neutron energy of 45 ± 15 MeV, is

$$66 \pm 46 \quad \mu B \quad (10^{-30} \text{ cm.}^2).$$

The total capture cross-section, at the same energy, calculated by detailed balance (section 1.3) from measured photo-disintegration cross-sections (section 1.5) is

$$17{\cdot}5 \pm 3 \quad \mu B \quad (10^{-30} \text{ cm.}^2).$$

The rather high value (66 μB) of the capture cross-section determined in the present experiment may be partly caused by the presence of the radiative scattering reaction (section 2.1.5),

which has been ignored. In the absence of a reliable theory of radiative scattering it is not possible to make corrections for its presence. Dr. R.J.N. Phillips, of Harwell, has, however, estimated that corrections to the present measurement of the capture cross-section, due to radiative scattering, should not be more than 40%.

The large errors (72%) in the present determination of the capture cross-section are almost entirely due to the small number of deuterons observed. In order to obtain an accuracy of 10% in the capture cross-section 100,000 photographs would have had to be taken and scanned. In order to measure the polarization of the reaction to 10%. approximately 1,000,000 photographs would be required, the scanning of which would not be practicable. The method used to identify the neutron-capture reaction, used in the present experiment, might be used in a counter experiment, and measurement of the polarization might then be possible.

APPENDIX A.

WORK DONE DURING CYCLE.

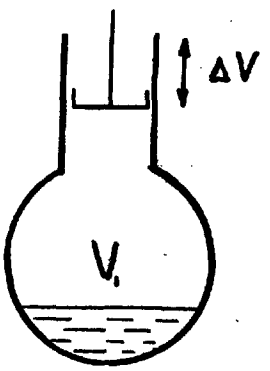

Let the initial pressure be p_1 and the initial volume V_1. Consider then a rapid expansion of the volume to $V_1 + \Delta V$ where $\Delta V \ll V_1$. A small amount of gas of volume U' at pressure p_1 is introduced due to boiling of the liquid. The volume of the system is then rapidly compressed to its initial value of V_1.

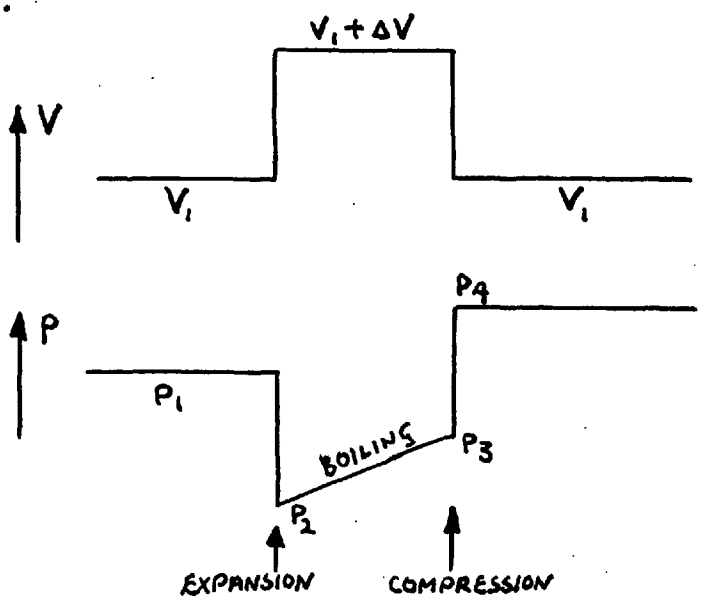

Denoting the pressures as in the above figure, and assuming the complete cycle to be adiabatic,

$$p V^{\gamma} = \text{CONSTANT}$$

$$P_2 = P_1\left(1 - \gamma \frac{\Delta V}{V_1}\right)$$

$$P_3 = P_1\left(1 - \gamma\frac{\Delta V}{V_1} + \frac{U'}{V_1} + \frac{\gamma U'\Delta V}{V_1^2}\right)$$

$$P_4 = P_1\left(1 + \frac{U'}{V_1}\right)$$

the work done $= \int p\, dV = W$

which for $p V^{\gamma}$ = constant, gives

$$W = \frac{1}{\gamma - 1}\ \Delta(pV)$$

Therefore W_1 (during expansion) $= \frac{1}{\gamma-1}\left(P_2V_2 - P_1V_1\right)$

$$= \frac{P_1V_1}{\gamma-1}\left(-\gamma\frac{\Delta V}{V_1} + \frac{\Delta V}{V_1} - \gamma\frac{\Delta V}{V_1^2}\right)$$

W_2 (during compression) $= \frac{1}{\gamma-1}\left(P_4V_4 - P_3V_3\right)$

$$= \frac{P_1V_1}{\gamma-1}\left(+\frac{U'}{V_1} + \gamma\frac{\Delta V}{V_1} - \frac{U'}{V_1} + \gamma\frac{U'\Delta V}{V_1^2} + \frac{\Delta V}{V_1} - \frac{\gamma\Delta V^2}{V_1^2} + \frac{U'\Delta V}{V_1^2}\right)$$

Total work done on the system

$$W_1 + W_2 - \frac{P_1\, U'\Delta V}{V_1}$$

but $$\frac{\Delta V}{V_1} = \frac{1}{\gamma} \frac{P_1 - P_2}{P_1} = \frac{1}{\gamma} \frac{\Delta P}{P_1}$$

$$\therefore \quad W_1 + W_2 = W = \frac{1}{\gamma} U' \Delta P$$

APPENDIX B.

ELECTRONIC CIRCUITS.

Figure(B)1 Light flash circuit

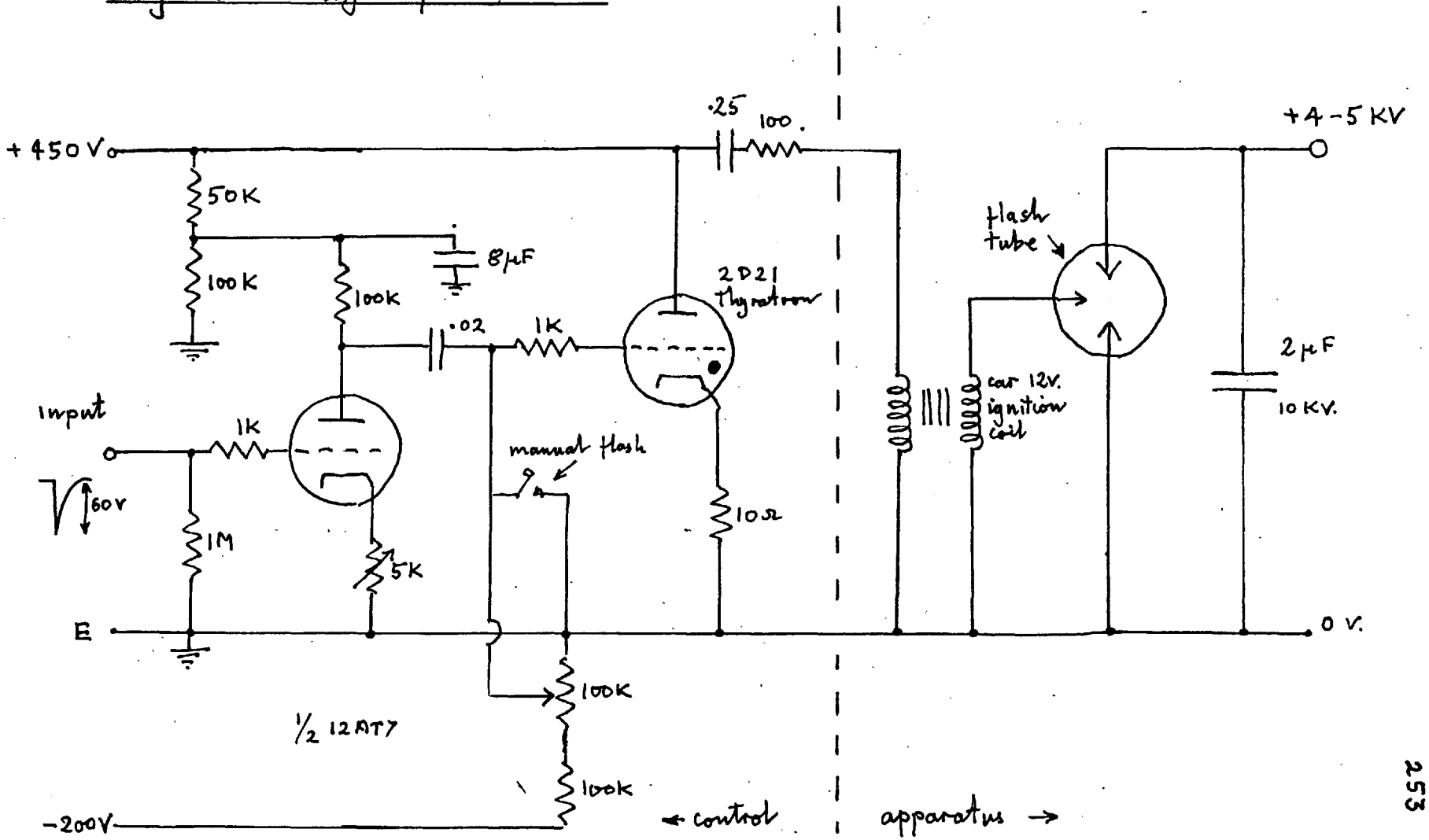

Figure(B)2 Discharge circuit to operate exp. and comp. valves

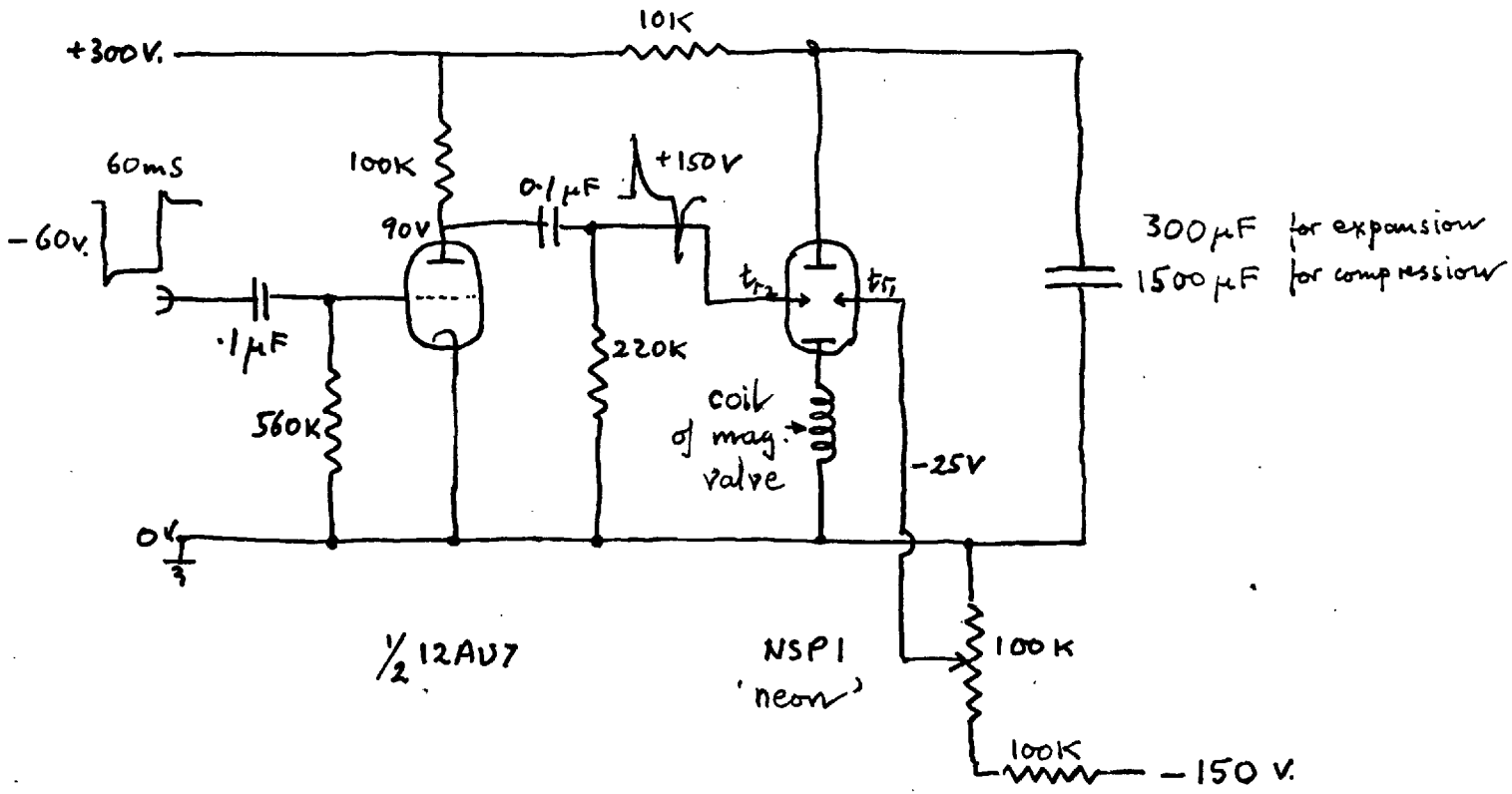

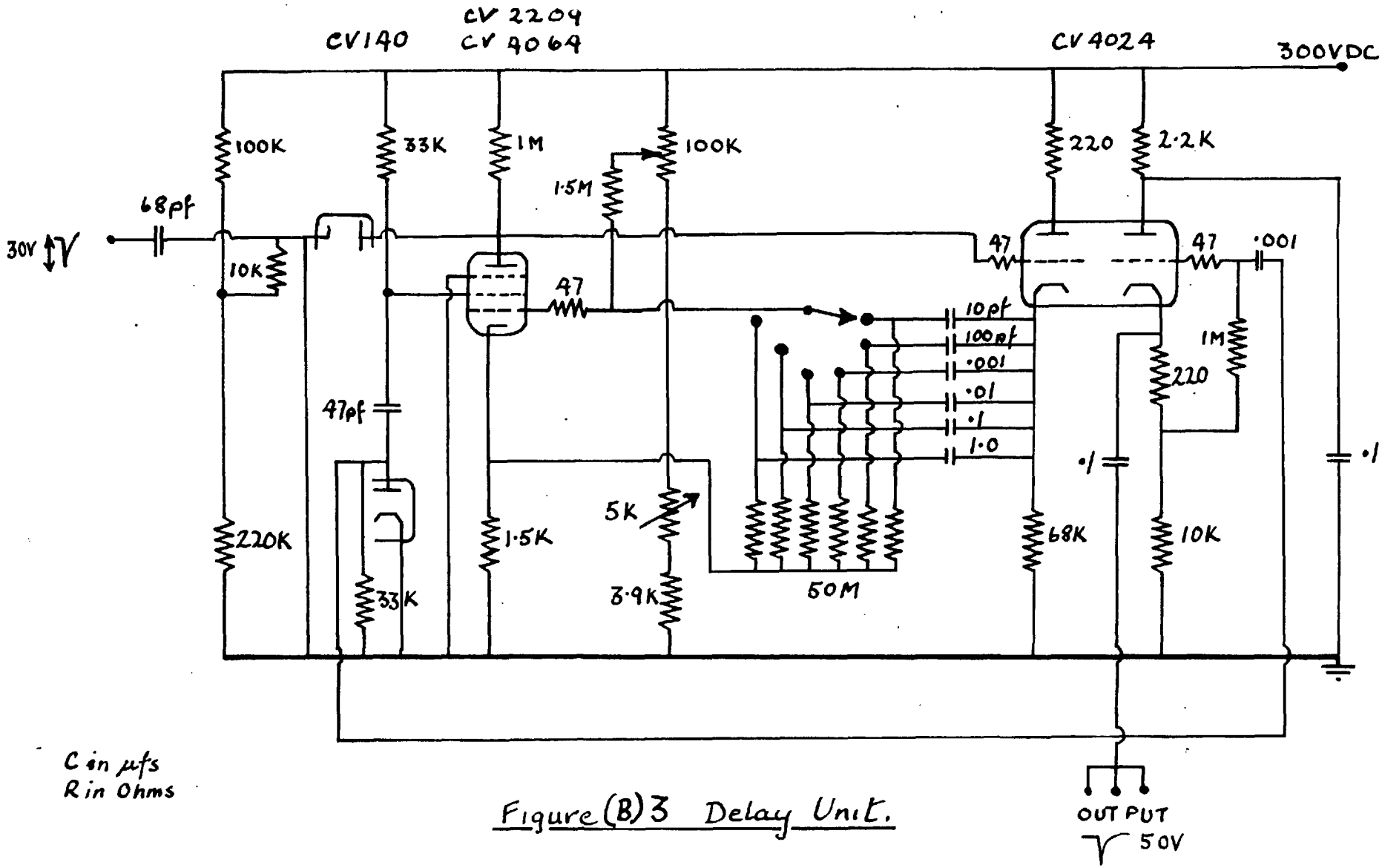

C in μfs
R in Ohms

Figure (B) 3 Delay Unit.

Figure (B) 4. Pulse lengthener

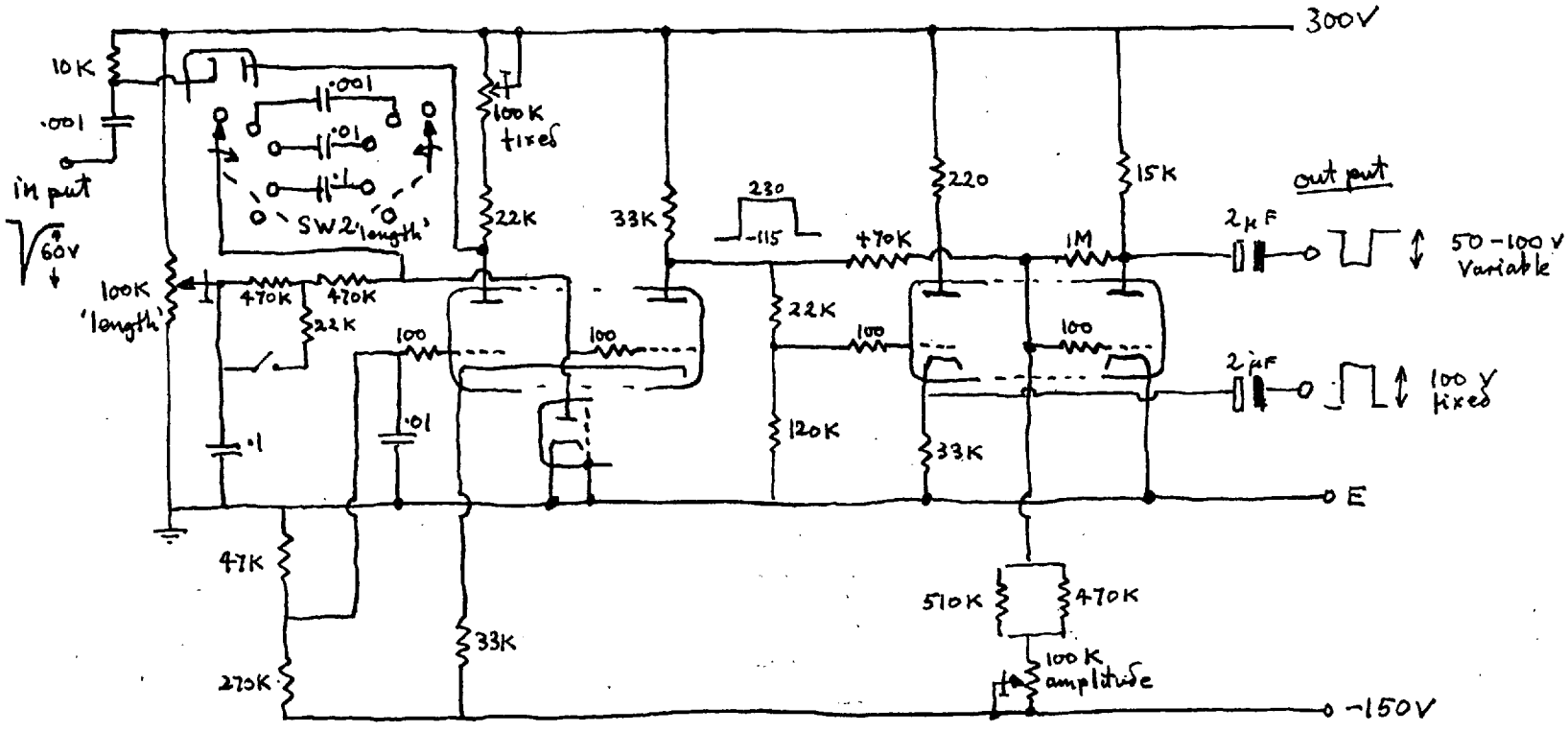

Figure (B)5 Pulse lengthener and gate

all resistance values in Ω's and condenser values in μF unless stated.

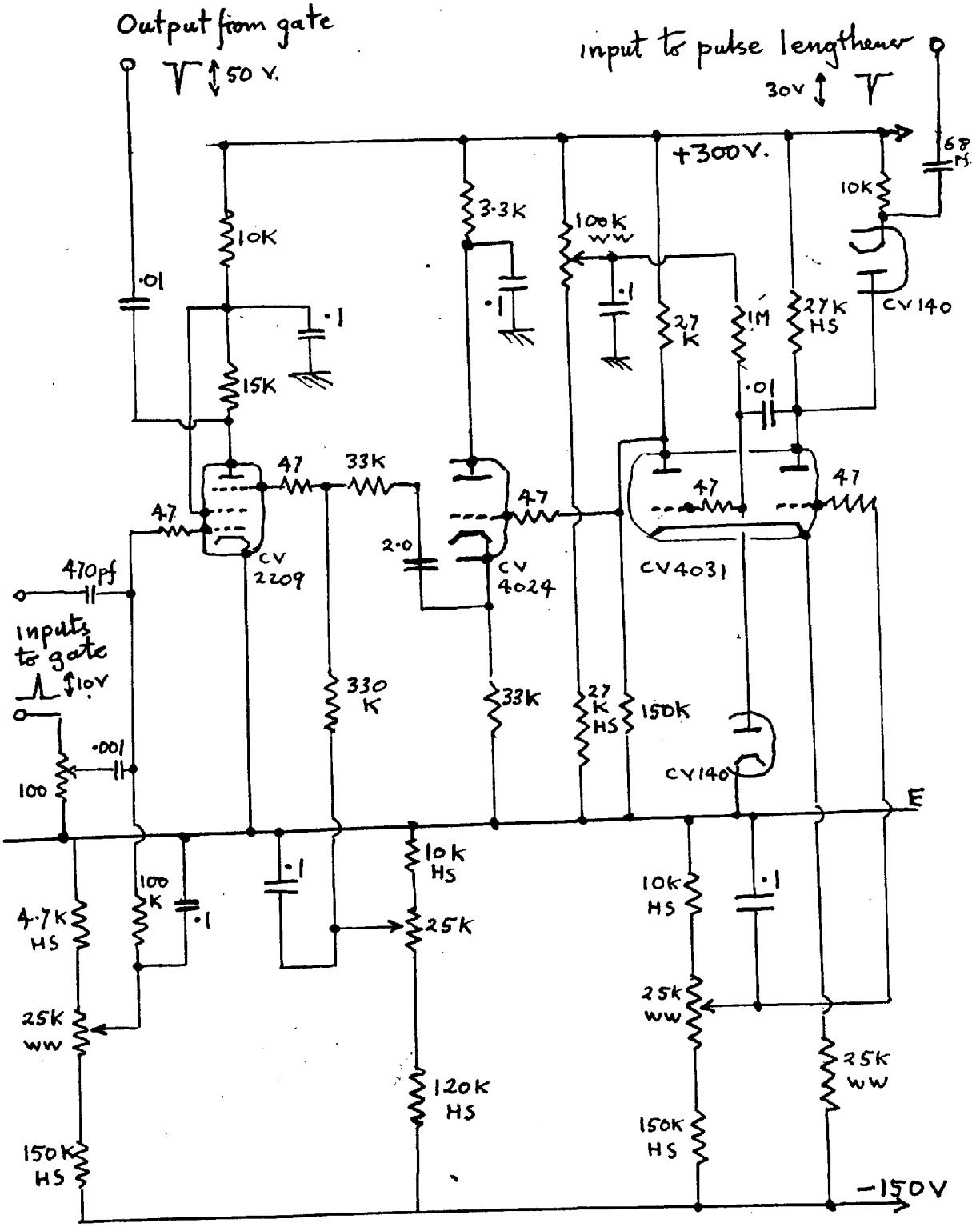

Figure (B)6 Pressure Indicator

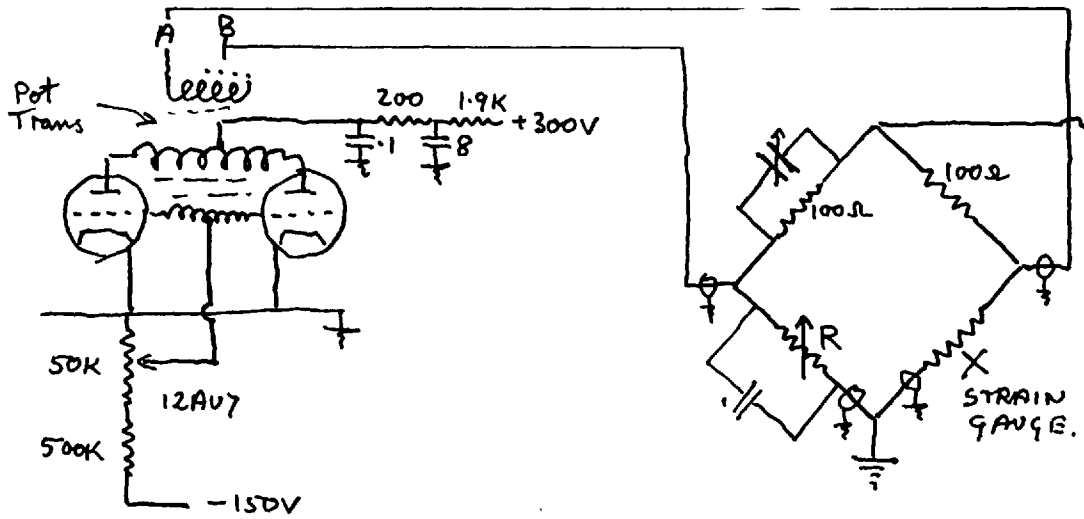

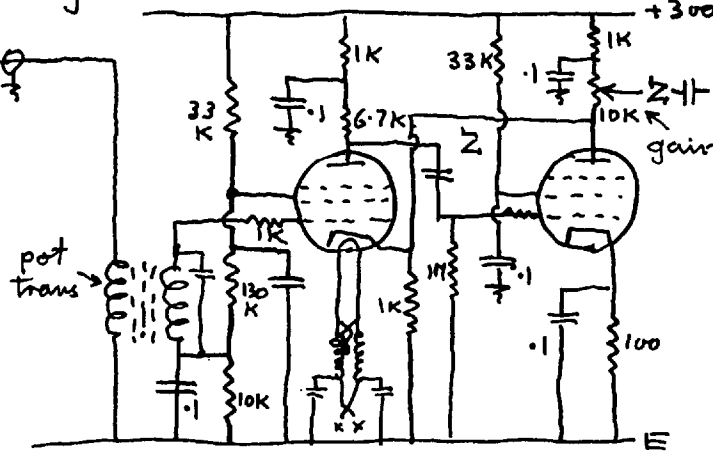

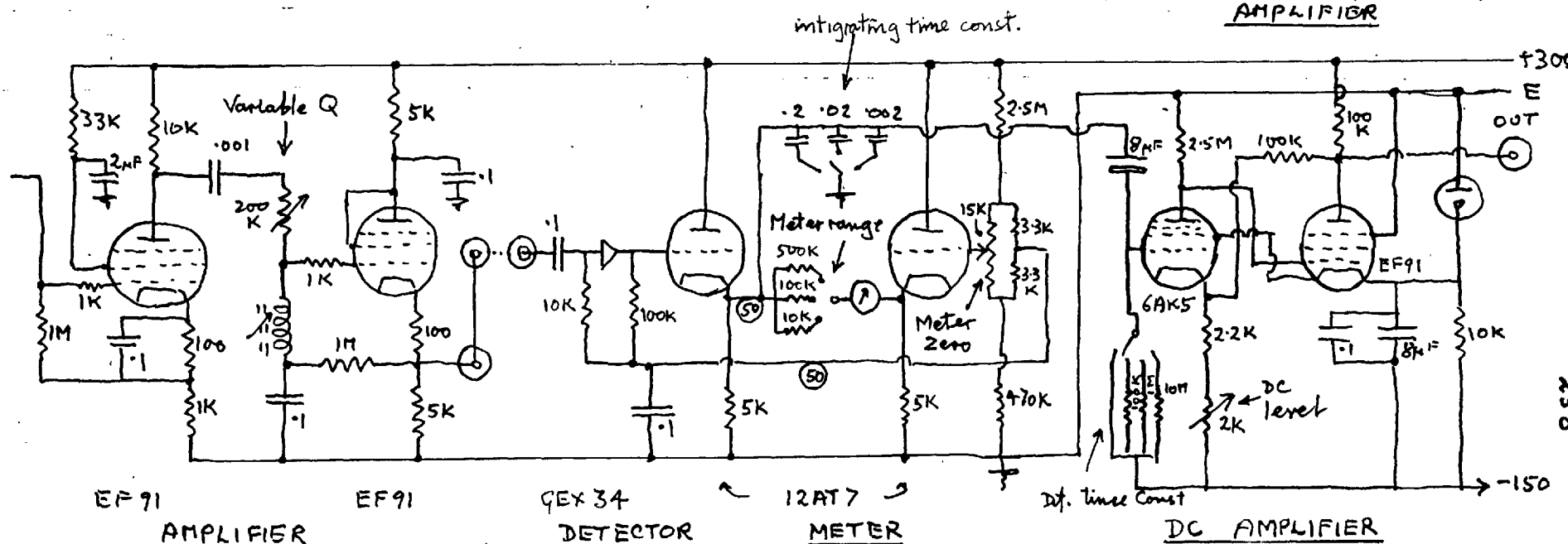

Figure (B)7 Mixer and Pulse Lengthener

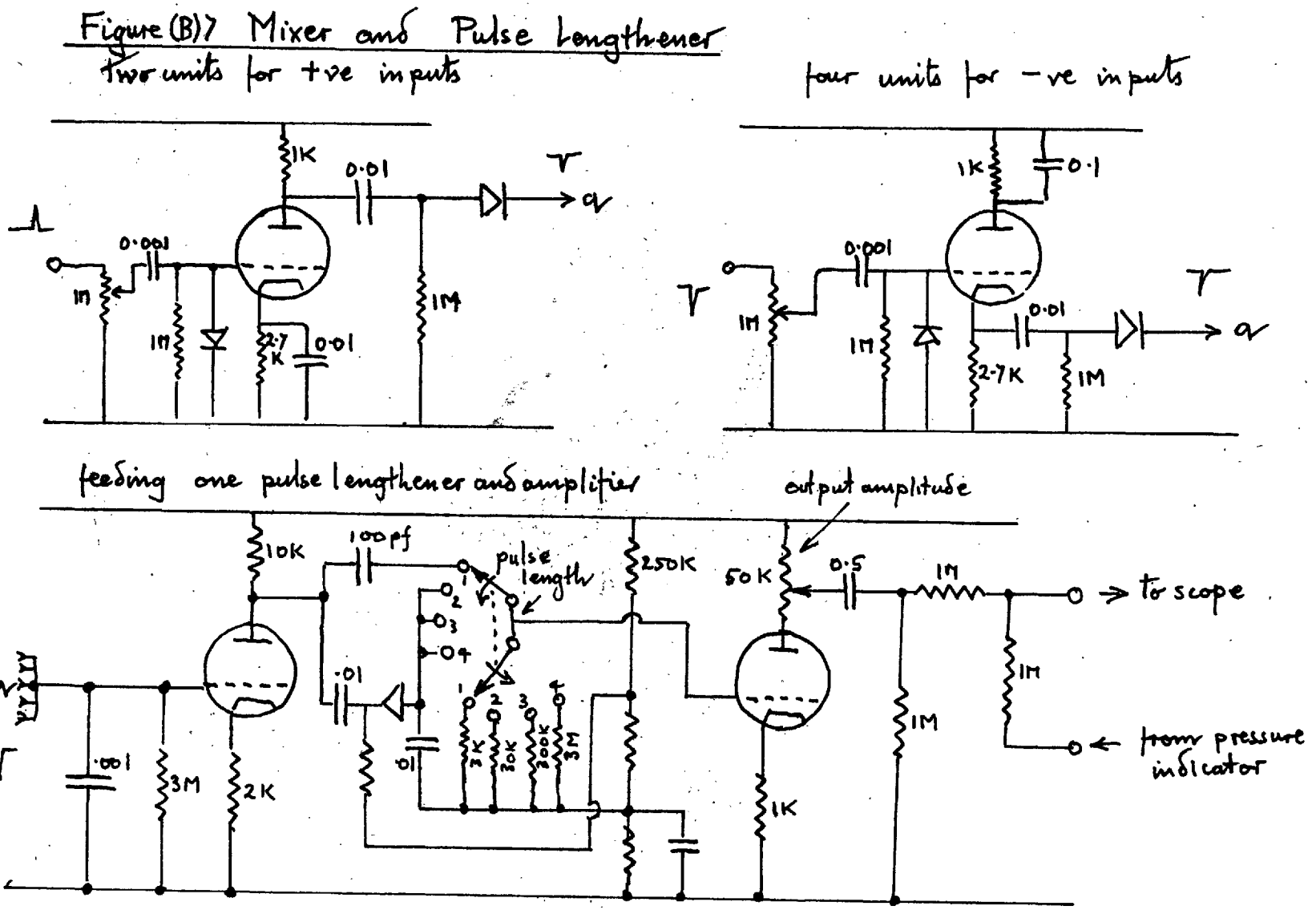

Figure(B)8 Automatic filling and depth gauge circuit

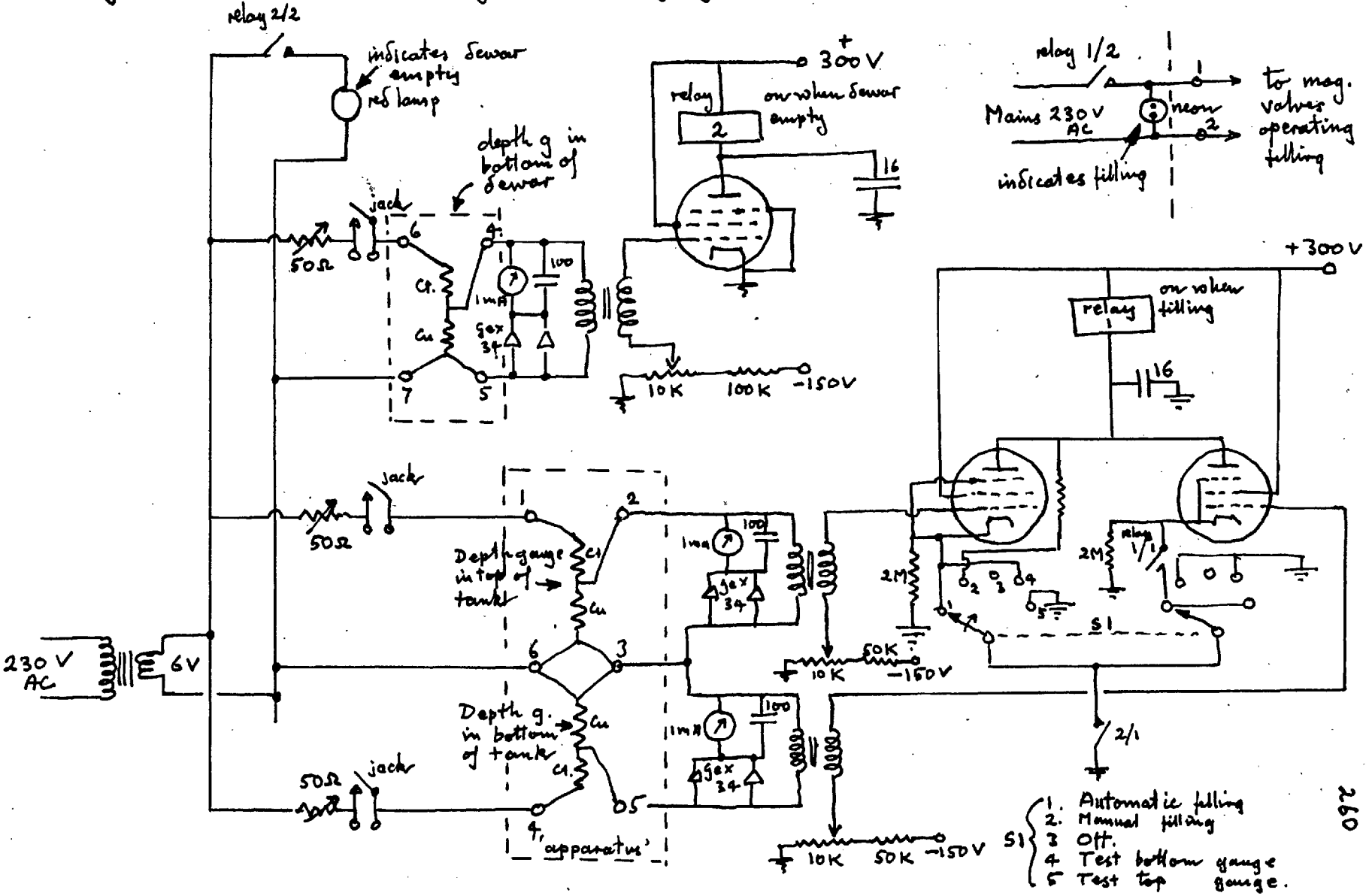

APPENDIX C.

RECONSTRUCTION ERRORS.

In this appendix the errors in the determination of angles in the chamber from measurements on the film will be estimated. In the first section these errors will be related generally to the errors in determining the coordinates of points on the film. In the second section they will be calculated for a 'corresponding' method of reconstruction, and in the last section for a non-corresponding method.

Terms defined in section 3.1 will be used here without further definition, their meaning should be clear from the figures. All calculations assume that the chamber is small, a long way from the cameras, and that the stereo ratio

$$S = \ell_o/b \ll 1$$

The term K_x will always denote the root mean square error in a determination of x.

C.1. General

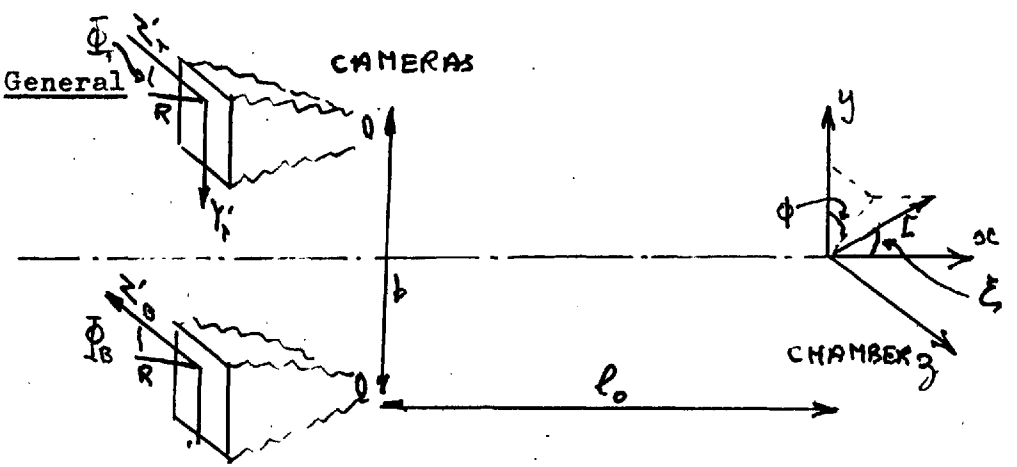

The reconstruction formulae of 3.1/1 give approximately:

$$x \doteq \frac{l_o}{f} S(Y_T' - Y_B') \qquad \frac{K_x}{\rho} \doteq \frac{K_{Y'}\sqrt{2}}{R'} S$$

$$y \doteq \frac{l_o}{f} Y' \qquad \text{C.1/1} \qquad \frac{K_y}{\rho} \doteq \frac{K_{Y'}}{R'} \qquad \text{C.1/2}$$

$$z \doteq \frac{l_o}{f} Z' \qquad \frac{K_z}{\rho} \doteq \frac{K_{Z'}}{R'}$$

$$\frac{K_\rho}{\rho} \doteq \frac{K_{R'}}{R'}$$

where ρ is the length of a track projected on to the x = 0 plane and R' is the length of its image in the photographs.

Let there be a system of polar coordinates in the chamber: r, ξ, ϕ; where ξ is the angle between the track and the x axis, and ϕ the angle between the projection of the track on the x = 0 plane and the z axis. Then:

$$\tan \xi = \frac{\rho}{x}$$

$$\frac{1}{\cos^2 \rho} d\xi = \frac{d\rho}{x} - \frac{\rho}{x^2} dx$$

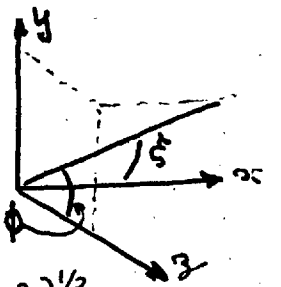

From which

$$K_\xi = \sqrt{2}(\cos^2 \xi)\left\{\left(\frac{1}{x} K_\rho\right)^2 + \left(\frac{\rho}{x^2} K_x\right)^2\right\}^{1/2} \qquad \text{C.1/3}$$

The $\sqrt{2}$ arises from the independent errors in determining the two ends of a track. From equation section 3.1:

$$K_\phi \doteq K_\xi$$

where K_Φ is the error in determining the angle of a projected track.

A second system of polar coordinates (r , θ , χ) was defined in section 3.1. If θ is small then $\xi \doteqdot \pi/2$

$$\theta^2 \doteqdot \phi^2 + \cos^2 \xi$$

$$d\theta \doteqdot \frac{\phi}{\theta} d\phi - \frac{\frac{\pi}{2} - \xi}{\theta} d\xi$$

$$K_\theta = \sqrt{(\cos^2\chi) K_\phi^2 + (\sin^2\chi) K_\xi^2}$$

C.1/4

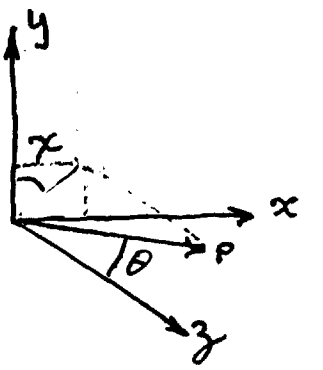

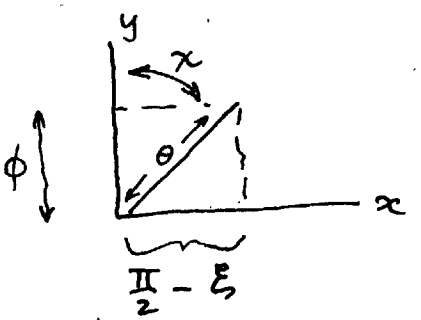

C.2 Corresponding Method.

The longitudinal error in determining the end point of a track was defined in section 3.1 to be λ times the lateral error. These errors are given in the figure.

$$K_{Y'(c)} = \frac{R' K_{\Phi}}{\sqrt{2}} \sqrt{\cos^2\phi + \lambda^2 \sin^2\phi}$$

$$K_{Z'(c)} = \frac{R' K_{\Phi}}{\sqrt{2}} \sqrt{\sin^2\phi + \lambda^2 \cos^2\phi}$$

$$K_{R'(c)} = \frac{\lambda K_{\Phi} R'}{\sqrt{2}} \qquad C.2/1$$

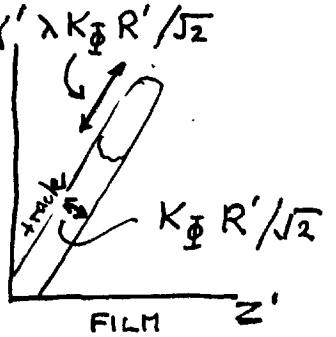

using c1/2

$$K_{x(c)} = \frac{\sqrt{2}\,\rho S K_{\Phi}}{\sqrt{2}} \sqrt{\cos^2\phi + \lambda^2 \sin^2\phi}$$

$$K_{y(c)} = \frac{\rho}{\sqrt{2}} K_{\Phi} \sqrt{\cos^2\phi + \lambda^2 \sin^2\phi}$$

$$K_{z(c)} = \frac{\rho}{\sqrt{2}} K_{\Phi} \sqrt{\sin^2\phi + \lambda^2 \cos^2\phi}$$

$$K_{\rho(c)} = \frac{\rho \lambda}{\sqrt{2}} K_{\Phi}$$

using c1/3

$$K_{\xi(c)} = K_{\Phi} \left((\lambda \sin 2\xi)^2 + \left(\sqrt{2} S \sin^2\xi \sqrt{\cos^2\phi + \sin^2\phi} \right)^2 \right)^{1/2}$$

for all ξ

$$K_{\xi(c)} \leq K_{\Phi} \left(\lambda^2 + 2S^2 (\cos^2\phi + \lambda^2 \sin^2\phi) \right)^{1/2} \qquad C.2/4$$

and since $S > 1$

$$K_{\xi} > K_{\Phi} \qquad C.2/5$$

Now ξ and ϕ are orthogonal coordinates, from equation C.2/5 it follows that any error, $(K_{\Omega(c)})$, in the determination of any

angle of the track in the chamber will be less than $K_{\xi,(c)}$.

$$K_{\Omega(c)} < K_{\Phi} \sqrt{\left(\lambda^2 + 2S^2(\cos^2\phi + \lambda^2 \sin^2\phi)\right)} \qquad C2/6$$

An estimate of the value of $K_{\Omega(c)}$ averaged over all angles and directions of a track, may be obtained from C.2/3 and K_{Φ}. Letting $\lambda = 2$, $S = 3$:

$$K_{\Omega(c)} \doteq 4 K_{\Phi} \qquad C2/7$$

The error in determining a small angle θ may be derived more directly, using equations C.1/4 and C.2/3:

$$K_{\theta(\text{small})} \doteq K_{\Phi} \sqrt{\cos^2\chi + 2S^2 \sin^2\chi} \qquad C2/8$$

Averaging over χ and letting $\lambda = 2$, $S = 3$:

$$K_{\theta(\text{small})} \doteq 3 K_{\Phi} \qquad C2/9$$

C.3 Non-corresponding method.

In a non-corresponding method the Z coordinates of a point are selected arbitrarily. The errors in the Y coordinate and length are then:

$$K_{Y'} = \frac{K_{\Phi} R'}{\sqrt{2}} \frac{1}{\cos\phi}$$

$$K_{R'} = \frac{K_{\Phi} R'}{\sqrt{2}} \tan\phi \qquad C3/1$$

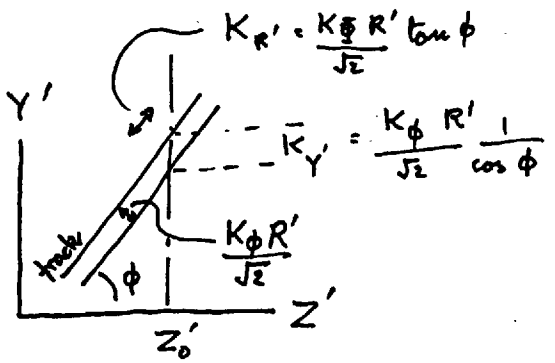

Using (C. 1/2)

$$K_{x(NC)} = \frac{\rho\sqrt{2}\ S\ K_\Phi}{\sqrt{2}} \cdot \frac{1}{\cos\phi}$$

$$K_{y(NC)} = \frac{\rho\ K_\Phi}{\sqrt{2}} \cdot \frac{1}{\cos\phi} \qquad C3/2$$

$$K_{z(NC)} = 0$$

$$K_{p(NC)} = \frac{\rho\ K_\Phi}{\sqrt{2}} \cdot \tan\phi$$

Using (C. 1/3)

$$K_{\xi,(NC)} = K_\Phi \sqrt{(\sin 2\xi \cdot \tan\phi)^2 + \left(\sqrt{2}\,S \sin^2\xi \frac{1}{\cos\phi}\right)^2} \qquad C3/3$$

for all ξ

$$K_{\xi,(NC)} \leq K_\Phi \sqrt{\tan^2\phi + \frac{2S^2}{\cos^2\phi}} \qquad C3/4$$

since $S > 1$

$$K_{\xi,NC} > K_\Phi$$

and by the same argument as used for the corresponding method, section C.2,

$$K_{\Omega(NC)} < K_\Phi \sqrt{\tan^2\phi + \frac{2S^2}{\cos^2\phi}}$$

APPENDIX D.

THE EFFECT ON RECONSTRUCTION OF GLASS WINDOWS AND LIQUID HYDROGEN.

D.1 EFFECT OF A WINDOW.

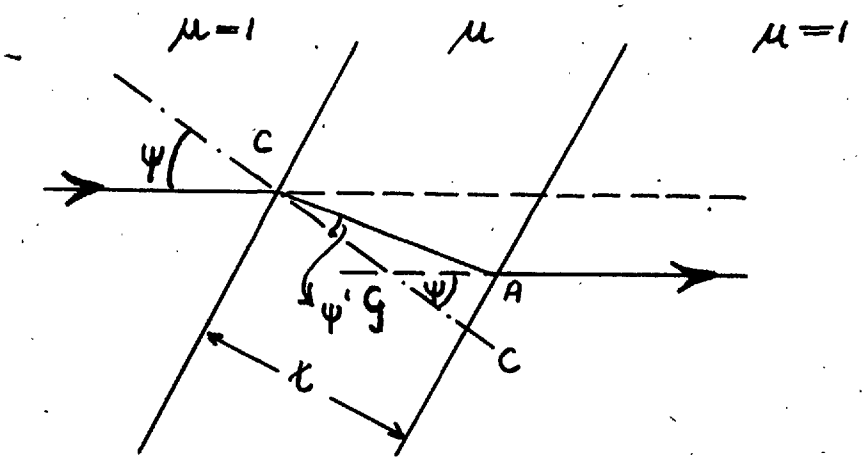

Consider a ray of light passing through a parallel sided plate of glass, of refractive index μ. Defining terms as in the above figure, and using

$$\sin\psi' = \frac{1}{\mu}\sin\psi$$

it follows that

$$\delta = t\left(1-\frac{1}{\mu}\,\frac{\cos\psi}{\cos\psi'}\right)\sin\psi. \qquad D1/1.$$

To a first approximation for $\psi \doteq \frac{\pi}{2}$

$$\delta = t\left(1-\frac{1}{\mu}\right)\sin\psi \qquad D1/2$$

and to second approximation,

$$\delta = \left\{t\left(1-\frac{1}{\mu}\right)+\frac{t\psi^2}{2\mu}\left(1-\frac{1}{\mu^2}\right)\right\}\sin\psi \qquad D1/3$$

Thus the error (K_ρ) in ρ, caused by the first approximation, is given by,

$$K_\rho = \left\{ \frac{t\psi}{2\mu} \left(1 - \frac{1}{\mu^2}\right) \right\} \sin\psi \qquad D.1/4$$

Consider now the shift in apparent stereo position of a point P in the chamber, caused by a glass plate on angle γ from the vertical.

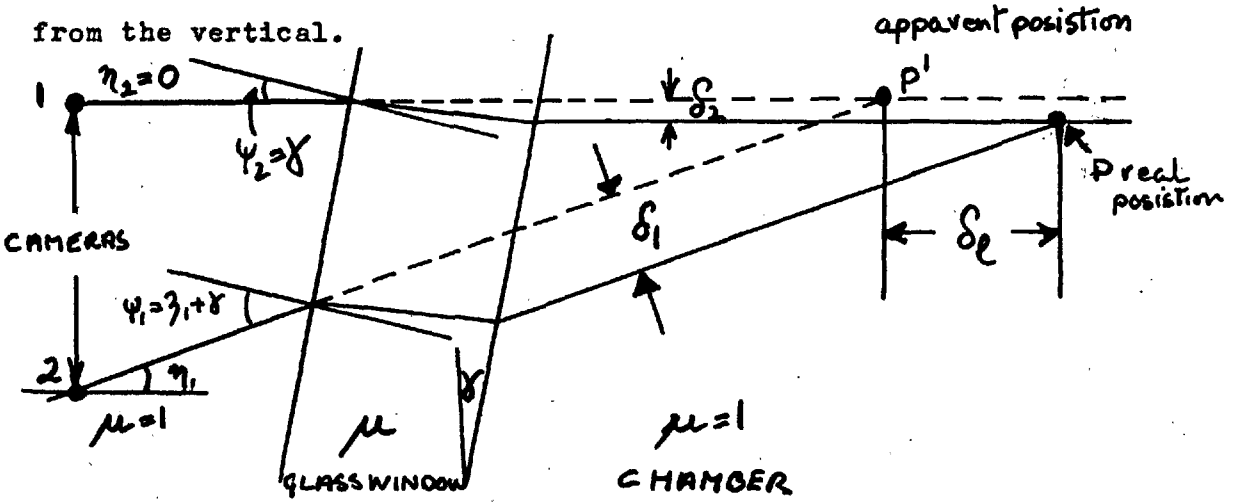

Defining terms as in the above figure, then, using equation D.1/2, to first order approximation,

$$\delta_2 = t\left(1 - \frac{1}{\mu}\right) \sin\gamma$$

$$\delta\ell = t\left(1 - \frac{1}{\mu}\right) \frac{\sin(\eta_1 + \gamma)}{\sin\eta_1} - t\left(1 - \frac{1}{\mu}\right) \frac{\sin\gamma}{\tan\eta_1}$$

IF $\gamma \ll 1, \eta \ll 1$

$$\delta\ell = t\left(1 - \frac{1}{\mu}\right) \qquad D.1/5$$

Thus, to first approximation, the effect of the glass plate is to

produce a longitudinal shift of apparent position (δl) of a point P, which is independent of the position of P, and independent of the angle of the glass plate. Together with this longitudinal shift of apparent position, there is a lateral shift (δ_2) which is independent of the position of P. The longitudinal shift is such as to increase the apparent distance of the point P from the cameras.

Assuming $\gamma \doteq 0$ and using equation D.1/4 it may be shown that the maximum error in determining a stereo position in the chamber is of the order of

$$+ \frac{t\varphi^2}{2\mu}\left(1-\frac{1}{\mu^2}\right)$$

The maximum error (K_Ω) in determining any angle in the chamber is given by

$$K_\Omega = \frac{K_{l_1} - K_{l_2}}{r},$$

where K_{l_1} and K_{l_2} are the errors in position at either end of a track of length r. If

distance to the chamber = l = 30 cm.

maximum length in the chamber = 8 cm.

refractive index, μ = 1·5

thickness of glass, t = 4 cm.,

then, for a vertical track the maximum difference of Ψ between the ends is 15°, and

$$K_{\Omega} = 0{\cdot}47^{\circ} \qquad \text{D.1/6}$$

For a horizontal track with small angle θ, the maximum difference of Ψ between the ends is $7{\cdot}5^{\circ}$ and the error in the small angle θ is given by

$$K_{\theta(\text{small})} = 0{\cdot}23 \qquad \text{D.1/7}$$

D.2 EFFECT OF LIQUID HYDROGEN.

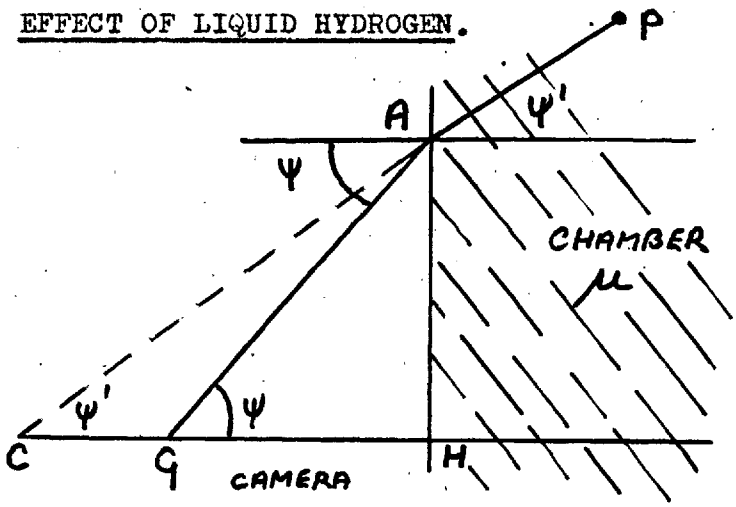

Defining the terms as in the above figure, and using,

$$\sin\psi' = \frac{1}{\mu}\sin\psi,$$

it follows that to first approximation when $\psi \doteq \pi/2$,

$$\frac{GH}{CH} = \frac{1}{\mu} = \frac{\text{real depth}}{\text{apparent depth}}, \qquad D.2/1.$$

and to a second approximation,

$$\frac{GH}{CH} = \frac{1}{\mu} - \frac{\psi^2}{2\mu}\left(1 - \frac{1}{\mu^2}\right) \qquad D.2/2.$$

The effect is to decrease the apparent distance from the cameras to a point P (the opposite effect to that of the glass plates).

The maximum errors due to the first order approximation may be estimated from equation D.2/2 and found to be; for any angle track

$$K_{\Omega} = \cdot 33^{\circ} \qquad D.2/3$$

for a small angle θ

$$K_{\theta(\text{small})} = \cdot 16^{\circ} \qquad \text{D.2/4}$$

It follows from equations D.1/3 and D.2/2 that the errors introduced in the first order approximations for the effects of the hydrogen and the effects of the glass plates, are of opposite sign. The total errors caused by both approximations are estimated to be:

$$K_{\Omega} = \cdot 3^{\circ} \qquad \text{D.2/5}$$

$$K_{\theta(\text{small})} = \cdot 15^{\circ} \qquad \text{D.2/6}$$

APPENDIX E RECONSTRUCTION COMPUTOR PROGRAMME

written in 'Mercury' Autocode

```
TITLE
NOPER 2  ( R.P.PALMER  1.2 )
CHAPTER1
U=50
V=50
W=50
G=50
E=25
X=50
Y=50
Z=50
D=50
F=45

1)NEWLINE
PRINT(3939)6.1
15)ROOT
NEWLINE
NEWLINE

2)NEWLINE
READ(A)
PRINT(A)4.6
CHECK(A,11111.1.45)
CHECK(A,22221.1.41)
CHECK(A,55559.1.43)
CHECK(A,44441.1.4)
CHECK(A,77777.1.5)
CHECK(A,66666.1.43)
JUMP6

4)ACROSS2/5
5)ACROSS3/5

40)N=0(1)45
READ(FN)
REPEAT
F17=F15/F14
F15=XTAN(F15/F14)
JUMP2
41)N=15(1)35
READ(FN)
NEWLINE
PRINT(FN)1.2
REPEAT
F17=F17/F14
F15=XTAN(F15/F14)
JUMP2
42)400=X15(0.399)
JUMP2
43)0=X11(0.400.399)
JUMP2
```

read all constants
read some constants $F_{15} \rightarrow 35$
store spectrum
spectrum → 0
print spectrum
restore spectrum from store

} commands

} read in constants

```
6)READ(A)
PRINT(A)3.3
50)NEWLINE
NEWLINE
K=0(1)50
READ(YK)          Z_T
YK=YK/F16
JUMP7,YK>887      Y_T
READ(XK)
XK=XK/F18
JUMP7,XK>887
REPEAT
PRINT(191919)6,0
HOOT
JUMP50
7)N=0(1)50
READ(DN)          Z_B
DN=DN/F16
JUMP8,DN>998
READ(ZN)          Y_B
ZN=ZN/F18
JUMP8,ZN>998
REPEAT
PRINT(292929)6,0
NEWLINE
NEWLINE
HOOT
JUMP7
8)JUMP2,K=0
JUMP2,N=0
A=XPARITY(K)
JUMP1,0>A
A=XPARITY(N)
JUMP1,0>A
J=K-2
M=N-2
```

read in projection coords written →

No
No
} ref.

top photo
$Z_1 Y_1 Z_2 Y_2$
$Z_1 Y_1 Z_2 Y_2$
$Z_1 Y_1 Z_2 Y_2$
etc

8888

bottom photo
$Z_1 Y_1 Z_2 Y_2$
$Z_1 Y_1 Z_2 Y_2$
$Z_1 Y_1 Z_2 Y_2$
etc

9999

new frame
No
No
$Z_1 Y_1 Z_2 Y_2$
etc

```
Q=0
K=0(2)J
R=0
N=0(2)M
JUMP57,K=0
JUMP57,N=0
JUMP13,0>X(K-2)
JUMP13,0>Z(N-2)
57)CHECK(YK,DN,F22,9)
JUMP13
9)CHECK(Y(K+1),D(N+1),F22,10)
JUMP13
10)JUMP54,0.5>F29
PRINT(YK-DN)2,2
PRINT(Y(K+1)-D(N+1))2,2
NEWLINE
54)JUMP11,1>R
EQ=3
E(Q-1)=3
JUMP12
11)EQ=0
12)S=2Q
US=XK
VS=YK
WS=ZN
GS=DN

S=S+1
US=X(K+1)
VS=Y(K+1)
WS=Z(N+1)
GS=D(N+1)
CHECK(VS,V(S-1),0.0001,60)
CHECK(GS,G(S-1),0.0001,60)
A=XDIVIDE(US-U(S-1),VS-V(S-1))
B=XDIVIDE(WS-W(S-1),GS-G(S-1))
CHECK(A,0,F15,58)
JUMP60
58)CHECK(B,0,F15,59)
JUMP60
59)EQ=EQ+5000
60)Q=Q+1
JUMP3,Q>25
JUMP56,XK>0
EQ=EQ+0.1
K=K+2
N=N+2
JUMP10
56)JUMP55,K=0
JUMP55,N=0
JUMP55,X(K-2)>0
EQ=EQ+0.1
K=K-2
N=N-2
55)R=R+1
13)REPEAT
REPEAT
JUMP2,Q=0
T=S%
```

selection of stereo pairs

check $\Phi_T < \alpha$
$\Phi_B < \alpha$

```
S=o(1)T
DS=GS
GS=o
JUMP14,DS>88.7
A=xMOD(WS)
B=xMOD(US)
C=xMOD(DS+VS)
XS=xDIVIDE(F1,A-B+F1/F2)
YS=A+B-F4
YS=o.5YSXS/F3
ZS=C-2F5
ZS=o.5ZSXS/F3
XS=XS-F2
14)REPEAT
ACROSS19/2
3)PRINT(494949)6,o
JUMP15
PSA
CLOSE

**
```

Reconstruction of x, y, z in chamber of ends

```
CHAPTER2
VARIABLES1

19)S=o(1)T
JUMP78,o>DS
JUMP51,DS>88.7
X=XS-F6
Y=YS-F7
Z=ZS-F8
F=xRADIUS(Y,Z)
CHECK(X,o,F13,14)
G=xPARITY(S)
JUMP14,o>G
GS=GS+20
14)CHECK(Y,o,F11,15)
GS=GS+100
JUMP16
15)CHECK(Z,o,F12,16)
GS=GS+100
16)CHECK(F,o,F10,77)
GS=GS+300
JUMP8
77)CHECK(X,o,F9,8)
GS=GS+300
8)JUMP1
78)GS=GS+1000
JUMP1
51)GS=GS+3000
1)REPEAT
```

check start inside V'
stop inside V

```
A=T
T=xINTPT(A/2)
17)Q=o(1)T
S=2Q
GS=GS+EQ
G(S+1)=G(S+1)+EQ
JUMP18,US>o
ACROSS1/4
18)JUMP28,D(S+1)>88.7
M=o

I=S+1
R=S
DOWN1/6
A=Dn
B=En
C=Fn
U=Hn
W=xARCTAN(B,A)

JUMP50,0.5>F32
NEWLINE
PRINT(A)1,3                    direction cosines
PRINT(B)1,3
PRINT(C)1,3
50)F=F41A+F42B+F43C
V=xSQRT(1-FF+0.0000001)        } χ
V=xARCTAN(F,V)
F=FF+0.000001
F=1/F
A=xLOG(U)
E=xEXP(AF39)                   } Ep
E=F38E
A=xEXP(AF39)
A=2F40A
EQ=EF
28)VQ=V
WQ=W
UQ=E

JUMP29,0.5>F30
NEWLINE
G=GS+G(S+1)
PRINT(G)3,1        (G) indicator
JUMP2,0.5>F27
JUMP49,9999>G
2)JUMP45,0.5>F28
PRINT(10DS)3,0     } Z1, Z2 from input
PRINT(10D(S+1))3,0 }
45)JUMP46,0.5>F25
PRINT(10XS)2,0     } xyz of start
PRINT(10YS)2,0     }
PRINT(10ZS)2,0     }
NEWLINE
```

} output

```
46)JUMP29,D(S+1)>88.7
PRINT(VF14)2,2          θ
PRINT(WF14)3,1          χ
JUMP47,0.5>F26
PRINT(U)1,3             ν
PRINT(E)2,1             Ep
NEWLINE
47)JUMP48,0.5>F27
B=XSQRT(0.125A/F37)
PRINT(F14B)1,2          θ̂(En)
PRINT(A)3,1             Ed
48)PRINT(EQ)3,1         En
49)NEWLINE
29)REPEAT
NEWLINE
NEWLINE

JUMP44,F17>0.1
ACROSS4/5
44)ACROSS1/3

*100)PRINT(595959)6,0
ACROSS15/1

XSQRT
XARCTAN
XLOG
PSA
XEXP
PSA
CLOSE

***
```

output

```
CHAPTER3
VARIABLES1
1)Q=0(1)T
S=2Q
JUMP5,XS>999
M=0
I=S+1
R=S
DOWN1/6
D=Dn
E=En
F=Fn
```

Search for n-p n-p double scattering.

```
P=o(I)J
JUMP5,XP>999
JUMP5,P=S
JUMP5,DP>88.7
JUMP5,D(S+I)>88.7
R=S+I
JUMP5,P=R

An=XP-XS+o.oooo1
Bn=YP-YS+o.oooo1
Cn=ZP-ZS+o.oooo1
H=xSQRT(AnAn+BnBn+CnCn+o.ooooooI)
G=I/H
An=GAn
Bn=GBn
Cn=GCn

C=DBn-EAn
CHECK(C,o,FI7,2)
JUMP5
2)Gn=DAn+EBn+FCn
CHECK(Gn,o,FI7,3)
JUMP5
3)A=ECn-FBn
B=FAn-DCn

G=xPARITY(P)
G=P+G
I=xINTPT(G+o.I)
G=P
K=xINTPT(o.5G+o.2)

R=P
DOWNI/6
X=Hn

Hn=AnDn+BnEn+CnFn
JUMP5,o>Hn
G=EQCnCnHnHn/UK
CHECK(G,I,FI9,4)
JUMP5
4)Un=BCn-CBn
Vn=CAn-ACn
Zn=ABn-BAn
```

```
Xn=BnFn-CnEn
Yn=CnDn-AnFn
Zn=AnEn-BnDn

H=xARCTAN(AXn+BYn+CZn,UnXn+VnYn+WnZn)
Y=xSQRT(1-HnHn)
Hn=xARCTAN(Hn,Y)

Y=xSQRT(AA+BB+CC)
Z=xSQRT(1-GnGn)
Gn=xARCTAN(GnX,Z)

PRINT(GS+G(S+1))3,0
PRINT(GI+GP)3,0
NEWLINE
PRINT(10DS)3,0
PRINT(10D(S+1))3,0
PRINT(10DP)3,0
PRINT(10DI)3,0
NEWLINE
PRINT(A/Y)1,3
PRINT(B/Y)1,3
PRINT(C/Y)1,3
NEWLINE
PRINT(GnF14)3,1
PRINT(G)1,1
PRINT(X)1,2
NEWLINE
PRINT(VQF14)2,1
PRINT(WQF14)3,1
NEWLINE
PRINT(HnF14)3,1
PRINT(HF14)2,1
NEWLINE
PRINT(EQ)2,1
PRINT(UQ)3,1
PRINT(EQCnCn)3,1
PRINT(UK)2,1
NEWLINE
NEWLINE
5)REPEAT
REPEAT
NEWLINE
NEWLINE

ACROSS4/5
100)PRINT(696969)6,0
ACROSS15/1
xSQRT
PSA
xARCTAN
PSA
CLOSE
```

```
xxxx


CHAPTER4
VARIABLES1

1)NEWLINE
PRINT(GS)3,0
PRINT(G(S+1))3,0
PRINT(G(S+2))3,0
PRINT(G(S+3))3,0
NEWLINE
PRINT(10DS)3,0
PRINT(10D(S+1))3,0
PRINT(10D(S+2))3,0
PRINT(10D(S+3))3,0
NEWLINE
M=1
I=S+1
R=S
DOWN1/6
An=Dn
Bn=En
Cn=Fn
U=Hn

JUMP5,DS>88.7

W=F41An+F42Bn+F43Cn
Gn=XSQRT(1-WW+0.0000001)
Gn=XARCTAN(W,Gn)
PRINT(F14Gn)2,1
Gn=WW
W=XARCTAN(Bn,An)
PRINT(F14W)3,1
NEWLINE

xx5)I=S+2
R=S+1
DOWN1/6
D=Dn
E=En
F=Fn
V=Hnxx

I=S+3
R=S+1
DOWN1/xx6
```

Calc. of charged particle scattering

```
W=AnD+EBn+FCn
G=WW
X=xSQRT(1-G*+0.0000001)
X=xARCTAN(W,X)
PRINT(F14X)2,1
W=AnDn+BnEn+CnFn
H=WW
X=xSQRT(1-H+0.0000001)
X=xARCTAN(W,X)
PRINT(F14X)2,1
W=DDn+EEn+FFn
X=WW
JUMP10,X>0.00001
W=0.000001
X=0.0000001
10)X=xSQRT(1-X)
X=xARCTAN(W,X)
PRINT(F14X)2,1

A=F42Cn-F43Bn
B=F43An-F41Cn
C=F41Bn-F42An
Un=BCn-CBn
Vn=CAn-ACn
Wn=ABn-BAn
Xn=EFn-FEn
Yn=FDn-DFn
Zn=DEn-EDn
W=xARCTAN(AXn+BYn+CZn,UnXn+VnYn+WnZn)
PRINT(F14W)3,1
NEWLINE

PRINT(V)1,3
PRINT(Hn)1,3

B=xSQRT(XnXn+YnYn+ZnZn)
JUMP4,DS>88.7
PRINT(U)1,3
4)NEWLINE
PRINT(Xn/B)1,3
JUMP9,DS>88.7
JUMP3,0.5>F33
9)PRINT(Yn/B)1,3
PRINT(Zn/B)1,3
NEWLINE
3)JUMP2,DS>88.7
W=XnAn+YnBn+ZnCn
W=W/B
PRINT(W)1,3
NEWLINE
```

```
JUMP6,o>D(S+2)
JUMP7,o>D(S+3)
JUMP7,V>Hn
6)A=3
V=Hn
G=H
JUMP8
7)A=2
8)PRINT(A)1,o
V=xLOG(V)
V=xEXP(VF39)
V=F38V
PRINT(V)2,1
V=V/G
PRINT(V)2,1
V=xLOG(V/F38)
V=xEXP(V/F39)
V=xLOG(V+U)
V=xEXP(VF39)
***PRINT(VF38/Gn)3,1
2)NEWLINE
NEWLINE
XS=1000
X(S+1)=1000
X(S+2)=1000
X(S+3)=1000
Q=Q+1
ACROSS29/2
100)PRINT(797979)3,6
ACROSS15/1

PSA
xSQRT
xARCTA*N
xEXP
xLOG
PSA
CLOSE
```

```
*****

CHAPTER5
U→50
V→50
W→50
G→50
E→25
X→198
A→4
F→45

1)N=0(1)198
XN=0
REPEAT
X7(0)X0,199
X7(200)X0,199
ACROSS2/1

3)NEWLINE
X6(0)X0,199
I=0(1)10
PRINT(0.5F21+1F21)2,1
NEWLINE
N=0(1)1
C=0
O=0(1)8
R=91+O+100N
JUMP16,F23>0.5
XR=XR+X(R+100)
16)PRINT(XR)2,0
C=C+XR
REPEAT
SPACE
PRINT(C)3,0
NEWLINE
JUMP17,0.5>F23
REPEAT
17)NEWLINE
A=1
JUMP2,A>F24
REPEAT
```

Summation of spectrums

} set spectrum = 0

} print spectrum

```
X6(200)X0,199
I=X1(1)21
PRINT(0.5F21+1F21)2,1
NEWLINE
N=0(1)1
C=0
O=0(1)8
R=91-99+O+100N
JUMP18,F23>0.5
XR=XR+X(R+100)
18)PRINT(XR)2,0
C=C+XR
REPEAT
SPACE
PRINT(C)3,0
NEWLINE
JUMP19,0.5>F23
REPEAT
19)NEWLINE
A=1
JUMP2,A>F24-0.01
REPEAT
2)NEWLINE
NEWLINE
ACROSS2/1

4)JUMP8,0.0001>F20
X6(0)X0,199
Q=0(1)T
S=2Q
G=GS+G(S+1)
JUMP14,9999>G
G=G-10000
14)JUMP7,G>0.001
O=XINTPT(F14VQ/F20)
I=XINTPT(EQ/F21)
JUMP12,0>O
O=8
12)JUMP7,F31>UQ
JUMP7,I>10
5)R=91+O
W=XMOD(WQ)
G=0.5E
JUMP6,W>G
XR=XR+1
JUMP7
6)X(R+100)=X(R+100)+1
7)REPEAT
X7(0)X0,199
```

print spectrum

add terms to spectrum

```
X6(200)X0,199
Q=0(1)T
S=2Q
G=GS+G(S+1)
JUMP15,9999>G
G=G-10000
15)JUMP11,G>0.001
0=XINTPT(F14VQ/F20)
1=XINTPT(EQ/F21)
JUMP13,9>0
0=8
13)JUMP11,F31>UQ
JUMP11,10>1
JUMP9,21>1
1=21
9)R=91+0-99
W=XMOD(WQ)
G=0.5£
JUMP10,W>G
XR=XR+1
JUMP11
10)X(R+100)=X(R+100)+1
11)REPEAT
X7(200)X0,199
8)ACROSS2/1

PSA
CLOSE
```

```
******

CHAPTER6
VARIABLES1

1)Dn=X1-XR+0.0001
En=Y1-YR+0.0001
Fn=Z1-ZR+0.0001
Hn=xSQRT(DnDn+EnEn+FnFn+0.000001)
G=1/Hn
Dn=GDn
En=GEn
Fn=GFn
JUMP3,M=0

X=88.7
JUMP2,DS>X
JUMP3,0.5>F34
JUMP4
2)JUMP4,R≠S
Dn=F41
En=F42
Fn=F43
JUMP3
4)PRINT(Dn)1,3
PRINT(En)1,3
PRINT(Fn)1,3
NEWLINE
3)UP
100)PRINT(898989)6,0
ACROSS15/1

xSQRT
PSA
CLOSE

CHAPTER0.
ACROSS2/1
CLOSE

**********
```

calculation of direction cosines

APPENDIX F.

PROBABILITY OF SELECTION USED IN THE STARTING AND STOPPING TRACKS SCAN.

In section 4.2.3 it was shown that the probability of selection of a track could be given by

$$\zeta(\theta, E_n) = \frac{\iiint_{x} \int_{0}^{2\pi} D(\theta, \chi, E_n, x, y, z)\, dx\, dy\, dz\, d\chi}{\iiint\int dx\, dx\, dy\, dz} \qquad F/1$$

where $D(\theta, \chi, E_n\ x,y,z) = +1$ if the track, starting at x, y, z, stopped in the volume V', and had a range greater than r_c; and where the expression had the value zero if these conditions were not satisfied. θ, χ and E_n are as defined in section 1.5 and x, y, z are as defined in section 3.1. The integrals in the expression with respect to x, y and z are taken over the volume V', and that with respect to χ, over angles 0 to 2π. Since the integration is not taken over θ and E_n, these, for convenience, will be left out of the expressions for functions. Thus, $D(\theta, \chi, E_n, x, y, z)$ shall be written $D(\chi, x, y, z)$.

It will be convenient here to define a function: δ' (condition), such that $\delta' = 1$ if the condition is satisfied;

and $\delta' = 0$ if it is not. Let the volumes V (a x b x c) and V' (j x b x c) be as defined in section 4.2.3 and illustrated in figures (4.2)1 and (F)1. Let r be the range of the track derived from θ and E_n using equation 1.5/9 and 2.1/1 and let

$$H = r \sin\theta$$

Then

$$D(\chi, x, y, z) = D_1(z) \cdot D_2(x,y,\chi) \quad D_3 \qquad F/2$$

where

$$\left.\begin{aligned} D_1(z) &= \delta'\left(-\tfrac{c}{2} < z + r\cos\theta < \tfrac{c}{2}\right) \\ D_2(x,y,\chi) &= \delta'\left\{\begin{aligned} -\tfrac{a}{2} &< H\sin\chi + \tfrac{a}{2} - x < \tfrac{a}{2} \\ -\tfrac{b}{2} &< H\cos\chi + y < \tfrac{b}{2} \end{aligned}\right\} \\ D_3 &= \delta'(r > r_c) \end{aligned}\right\} F/3$$

and using F/1.

$$G(\theta, E_n) = D_3 \cdot \frac{\int_{-\frac{c}{2}}^{+\frac{c}{2}} D_1(z)\, dz}{\int dz} \cdot \frac{\int_{-\frac{a+j}{2}}^{-\frac{a-j}{2}} \int_{-\frac{b}{2}}^{+\frac{b}{2}} \int_0^{2\pi} D_2(x,y,\chi)\, d\chi\, dy\, dx}{\int d\chi \iint dx\, dy} \qquad F/4$$

The second term is given by

$$\frac{\int_{-c/2}^{+c/2} D_1(z)\, dz}{\int_{-c/2}^{+c/2} dz} = \left(1 - \frac{r\cos\theta}{c}\right) \delta'(c > r\cos\theta) \qquad F/5$$

Consider the third ferm. The integral of D_2 for given x, y over χ (see figure (F)1 view B) is equal to the sum of the sector angles of those parts of a circle of radius H($H = r \sin\theta$) that lie inside the rectangle, $0 > x > -a$, $-b/2 < y < b/2$ (e.g. $\chi_1 + \chi_2$ in figure (F) 1, view B).

Figure (F)1 Selection Volumes V and V'

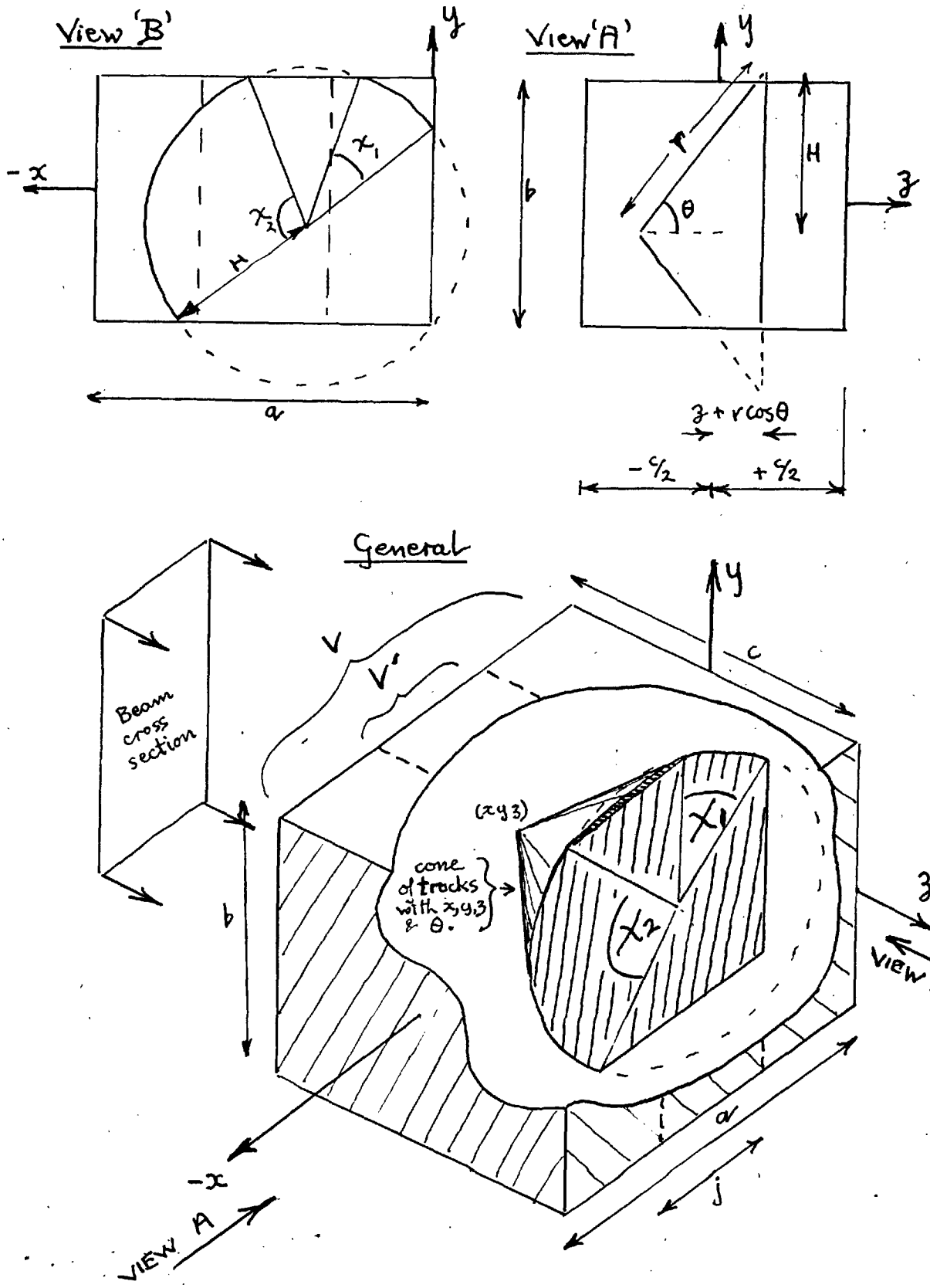

The following simplification may be made due to the symmetry of V and V' about the x axis and the $x = \frac{a}{2}$ line. The integral of D_2 with respect to χ may be taken over the range $0 \rightarrow \frac{\pi}{2}$ instead of $0 \rightarrow 2\pi$, without affecting the result. Physically this means that the probability of selection of tracks that only go 'up', is the same as those that go 'down', and similarly the probability is the same for left and right. This now means that the integral of D_2 over the range $0 \rightarrow \frac{\pi}{2}$ is equal to the sector angle (χ_i) of that part of a quadrant of a circle that lies inside the rectangle. See the illustrations below. According to the values of x and y so the expression for χ_i will vary. Using the function defined above and letting

$$x'' = -x$$

and

$$y' = \frac{b}{2} - y$$

F/6

then

$$\int_0^{\pi/2} D_2(x,y,\chi)\,d\chi = J(x,y) =$$

$$0 \quad + \quad$$

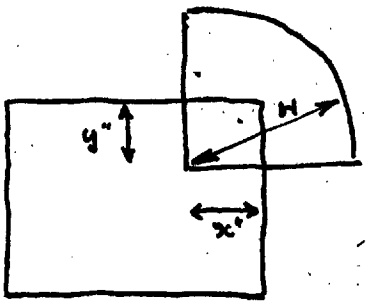

$$\left\{\frac{\pi}{2} - \cos^{-1}\left(\frac{x''}{H}\right) - \cos^{-1}\left(\frac{y''}{H}\right)\right\} \cdot \delta'\begin{Bmatrix} H < \sqrt{x''^2 + y''^2} \\ H > x'' \\ H > y'' \end{Bmatrix} +$$

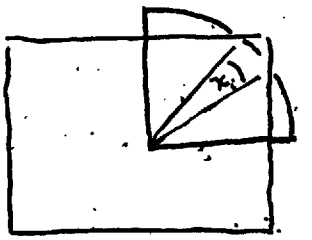

$$\left\{\frac{\pi}{2} - \cos^{-1}\left(\frac{x''}{H}\right)\right\} \cdot \delta'\begin{Bmatrix} H > x'' \\ H < y'' \end{Bmatrix} +$$

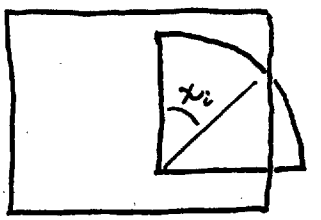

$$\left\{\frac{\pi}{2} - \cos^{-1}\left(\frac{y''}{H}\right)\right\} \delta'\begin{Bmatrix} H > y'' \\ H < x'' \end{Bmatrix} +$$

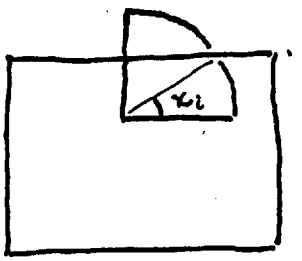

$$\frac{\pi}{2} \quad \delta'\begin{Bmatrix} H > y'' \\ H > x'' \end{Bmatrix}$$

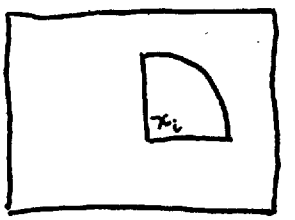

Since $\int_0^{\pi/2} \chi = \pi/2$

and $\int_{-\frac{a+j}{2}}^{-\frac{a-j}{2}} \int_{-\frac{b}{2}}^{+\frac{b}{2}} dx\,dy = jb$

then using F/3, F/4, F/5, and F/7:

$$G(\theta, E_n) = \left(\delta'(r > r_c)\right)\left((1 - \frac{r\cos\theta}{c})\,\delta'(c > r\cos\theta)\right)\left(\frac{1}{\frac{\pi}{2}ab}\int_{-\frac{a+j}{2}}^{-\frac{a-j}{2}}\int_{-\frac{b}{2}}^{+\frac{b}{2}} J(x,y)\,dy\,dx\right) \qquad F/8$$

The integration of J(x, y) was performed numerically using the Mercury Computor referred to in section 3.4. The programme used (NOPEG 1/1) is given in appendix G. The calculation was performed for:

$a = 7{\cdot}2$ cm.,

$b = 5{\cdot}4$ cm.,

$c = 5{\cdot}4$ cm.,

$j = 3{\cdot}6$ cm.,

On graph (F) 2 the calculated probability $G(\theta, E_n(\theta, E_p))$ is plotted as a function of θ and E_p. $G(\theta, E_n) \cdot 2\pi \sin 2\theta$ is plotted on graph (4.2)2.

The probability $P(E_n)$, calculated numerically from

$$P(E_n) = \int_0^{\pi/2} G(\theta, E_n)\,\frac{{}_{n-p}\sigma(\theta, E_n)}{{}_{n-p}\sigma_T(E_n)}\,2\pi\sin 2\theta\,d\theta \qquad F/9$$

by the computor, is plotted on graph (F)3. The values of ${}_{n-p}\sigma(\theta, E_n)$ were taken from Harwell data. The computor programme (NOPEG 1/2) is given in Appendix G.

Graph (F)2 Probability of a track being selected in starting and stopping tracks scan.

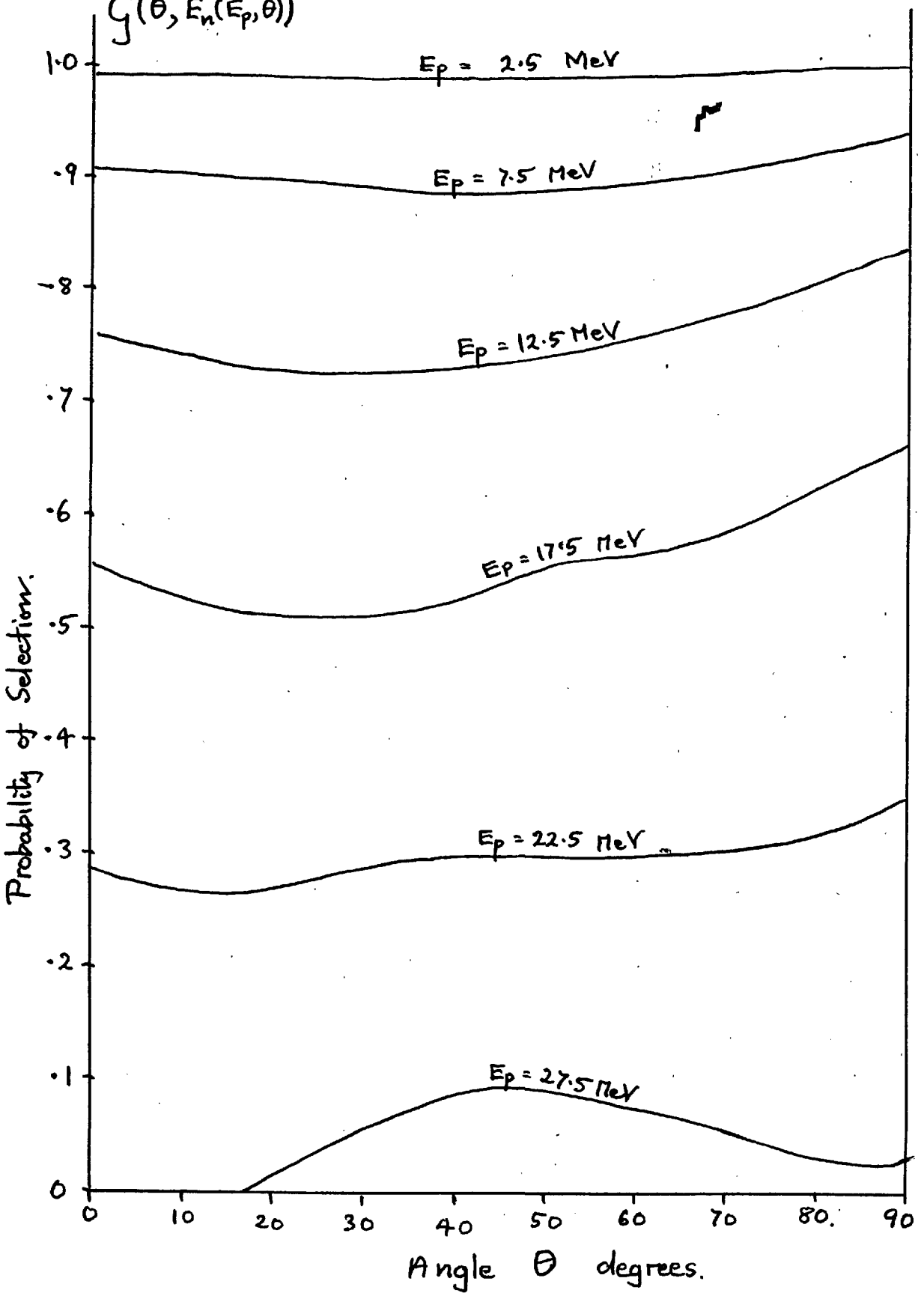

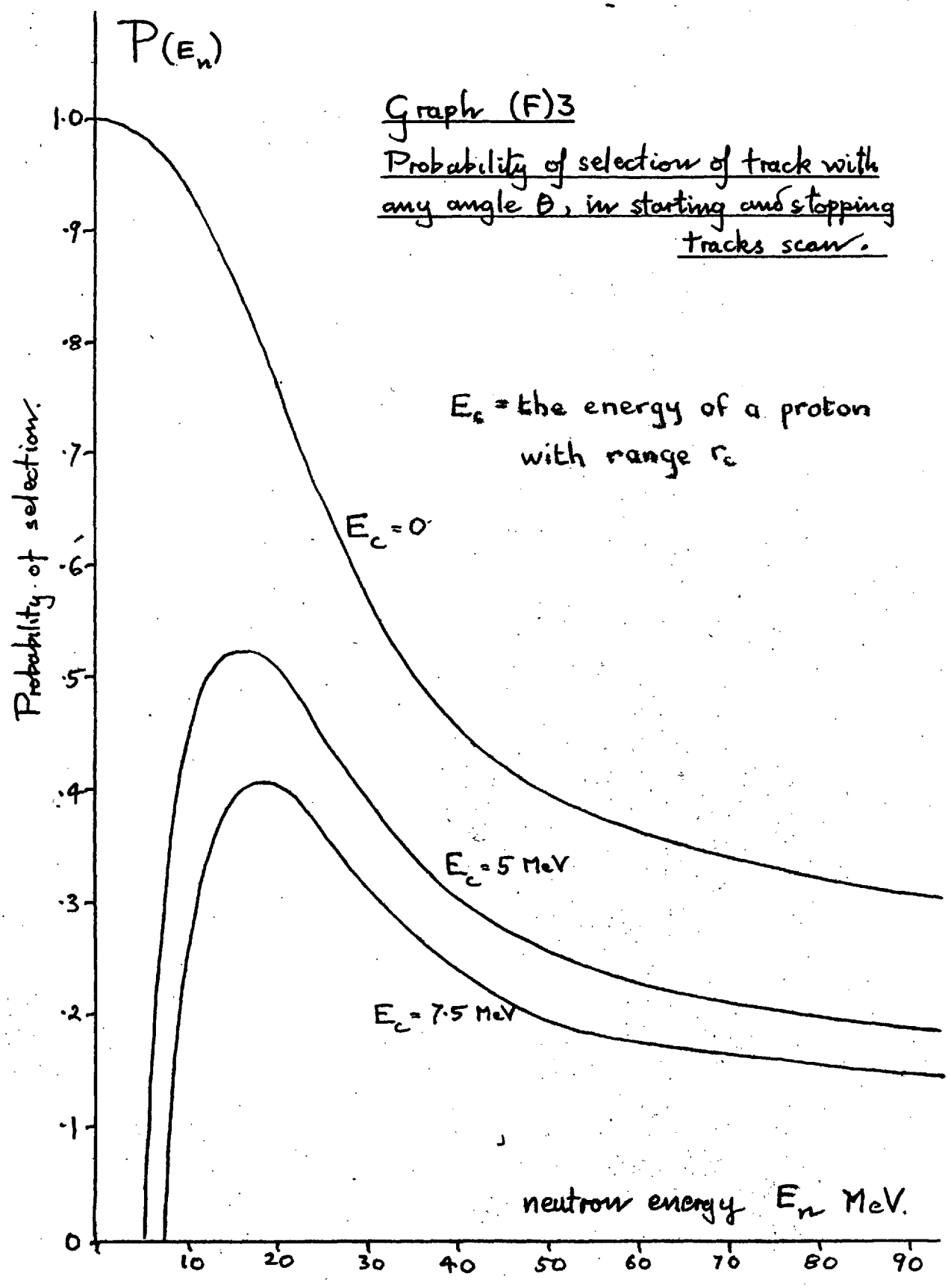
P(E_n)
Graph (F)3
Probability of selection of track with any angle θ, in starting and stopping tracks scan.
E_c = the energy of a proton with range r_c
E_c = 0
E_c = 5 MeV
E_c = 7·5 MeV
Probability of selection.
neutron energy E_n MeV.
1·0
·9
·8
·7
·6
·5
·4
·3
·2
·1
0
10
20
30
40
50
60
70
80
90

APPENDIX G PROBABILITY OF SELECTION PROGRAMMES

NOPEG 1/1 Calculation of $G(\theta, E_n)$

```
TITLE
NOPEG 1/1    (ROBERT PALMER 1...)
CHAPTER1
V→20
E→20

1)NEWLINE
NEWLINE
N=1(1)4                    } read dimensions of V and V'
READ(EN)
PRINT(EN)1,3
NEWLINE
REPEAT
N=0(1)30
SPACE
REPEAT
NEWLINE
NEWLINE
READ(E5)                   } read integral step E5
PRINT(E5)1,6
NEWLINE
J=xINTPT(E2/E5+0.5)
L=xINTPT(E4/E5+0.5)
E11=JL
E12=10.7                   } energy range relation
E13=1.83

NEWLINE
22)READ(E)                 read En
PRINT(E)3,1
NEWLINE
NEWLINE
U=0
N=0(1)17
W=NE/36+E/72               W = θ angle
C=xCOS(W)
D=xSIN(W)
Z=ECC
Z=xLOG(Z/E12)              Z = r range
Z=xEXP(E13Z)
A=ZC/E3                    A = 1 - r cos θ / c
A=1-A
JUMP21,0>A
F=8EDCAE/36
H=ZD
A=xRADIUS(0.5E1+0.5E4,E2)
JUMP21,H>A
```

```
G=0
P=I(1)L
Q=I(1)J
X=0.5E1+0.5E4-PE5+0.5E5
Y=E2-QE5+0.5E5
JUMP4,0.000001>Y
JUMP4,0.000001>X
C=XRADIUS(X,Y)
JUMP9,Y>H
B=XDIVIDE(HH,YY)
B=XSQRT(B-1)
B=XARCTAN(1,B)
B=2B/£


9)JUMP4,H>C
3)JUMP5,X>H
A=XDIVIDE(HH,XX)
A=XSQRT(A-1)
A=XARCTAN(1,A)
A=2A/£
JUMP6,Y>H
G=G+1-A-B
JUMP4
5)JUMP7,Y>H
G=G+1-B
JUMP4
6)G=G+1-A
JUMP4
7)G=G+1
4)REPEAT
REPEAT
G=G/E11

G=FG
JUMP20
21)G=0
20)PRINT(G)1,6
NEWLINE
8)REPEAT
NEWLINE
NEWLINE
NEWLINE
JUMP22
100)PRINT(888888)6,0
NEWLINE
PRINT(P)2,1
PRINT(Q)1,1
PRINT(H)0,6
PRINT(W)0,6
HALT
XSQRT
XARCTAN
PSA
CLOSE
```

$X = x'$

$Y = y'$

calculation of $J(\theta, E_n)$

output

```
CHAPTERo
ACROSSI/I
CLOSE

******

7•2
5•4
5•4
3•6

0•225

2•5
7•5
12•5
17•5
22•5
27•5
32•5
37•5
42•5
47•5
52•5
57•5
62•5
67•5
72•5
77•5
82•5
87•5
92•5
97•5
110
130
150
170
190

→

**************
```

dimensions: a / of : b / VL V' : c / : J — INPUT DATA

integral step

Values of E_w

NOEG 1/2 Programme for obtaining $P(E_n)$ from $G(\theta, E_n)$

$$P(E_n) = \int_0^{\pi/2} G(\theta, E_{n'}) \frac{n\text{-}p\,\sigma(\theta, E_n)}{n\text{-}p\,\sigma_T(E_n)} \cdot 2\pi \sin 2\theta \, d\theta$$

```
TITLE
NOPEG 1/2
CHAPTER1
U→20
V→20
E→20
G→400
1)E12=10.7
E13=1.83

READ(A)
PRINT(A)1,3
NEWLINE
NEWLINE*
NEWLINE
K=0(1)19
READ(A)
N=0(1)17
R=18K+N
READ(GR)
REPEAT
REPEAT
X7(0)G0,400
HALT
J=0
2)READ(E)
CHECK(E,99999,1,5)
K=XINTPT(E/5)
JUMP3,19>K
K=19
3)N=0(1)17
R=18K+N
READ(GR)
REPEAT
JUMP4,J≥K
I=K=1
L=J(1)I
N=0(1)17
S=18L+N
R=18K+N
GS=GR
REPEAT
REPEAT
4)J=K+1
JUMP2
5)X7(400)G0,400
```

step used in 1/1

read in energy followed by $G(\theta, E_n)$

read in Energy followed by $_{n\text{-}p}\sigma(\theta, E_n)$

```
x6(o)Go,400
6)READ(E6)
PRINT(E6)2,2
READ(EI4)
PRINT(EI4)I,o
NEWLINE
NEWLINE
K=o(I)I9
x6(I8K+400)Vo,I8
V=o
N=o(I)I7
W=N£/36+£/72
C=xCOS(W)
D=xSIN(W)
V=V+8£DCVN£/36
REPEAT
E=2.5+5K
PRINT(E)3,I
Z=xLOG(E/EI2)
Z=xEXP(EI3Z)
PRINT(Z)3,2
G=o
N=o(I)I7
R=I8K+N
W=N£/36+£/36
C=xCOS(W)
Z=ECC
JUMP7,E6>Z
UN=GRVN/V
JUMP9
7)D=xCOS(W-£/36)
Y=EDD
JUMP8,Y>E6
UN=o
JUMP9
8)A=xDIVIDE(Y-E6,Y-Z)
UN=GRVNA/V
```

} cut off energy $E_c = E_6$

} $E_{14} = 0$ short output
$E_{14} = 1$ full output.

} calc of $_{n\text{-}p}\sigma_T(E_n)$

} calc of $P(E_n)$

} cut off

```
9)G=G+UN
JUMP*10,0.5>E*4
NEWLINE
W=N£/36+£/72
C=xCOS(W)
D=xSIN(W)
PRINT(180W/£)2,1
PRINT(ECC)2,1
Z=xLOG(ECC/E*2)
Z=xEXP(E*3Z)
PRINT(Z)1,2
PRINT(10000VN/V)4,0
H=xDIVIDE(36GR,8£DC£)
PRINT(H)1,4
PRINT(GR)1,4
PRINT(100000GRVN/V)4,0
PRINT(100000UN)4,0
PRINT(100000UNC)4,0
NEWLINE
10)REPEAT
JUMP*11,0.5>E*4
NEWLINE
NEWLINE
11)PRINT(G)1,6
NEWLINE
NEWLINE
NEWLINE
NEWLINE
REPEAT
NEWLINE
NEWLINE
NEWLINE
NEWLINE
NEWLINE
JUMP6

xCOS
xLOG
xEXP
PSA
CLOSE

CHAPTER0
ACROSS*/*
CLOSE

→

**********
```

output

APPENDIX H.

PROBABILITY OF SELECTION OF SMALL ANGLE TRACKS.

H.1 General

The conditions of selection used in the small angle tracks scan were given in section 4.4.2. They could be considered in two parts:

(i) the small angle condition, and (ii) the geometrical condition. To a first approximation at small angles, θ, the probability ($\underline{G}\ (\theta, E_n)$) of satisfying the conditions, may be separated into a geometrical and a small angle part. It will be shown (H.3), that considering only the small angle condition, the probability of selection is a function of the angle θ only ($\underline{G_a}(\theta)$). The geometrical condition is that tracks starting in $\underline{V}$'must stop in $\underline{V}$. The volumes $\underline{V}$'and $\underline{V}$, defined in section 4.4.2, and not very different from those volumes, V' and V used in the 'starting and stopping tracks scan' selection. Thus the present geometrical selection probability is expected to behave in a not very different way from the 'starting and stopping tracks scan' selection probability ($G(\theta, E_n)$). If this probability is written

$$G(\theta, E_n) = G(\theta, E_n(\theta, r)) = G(0, E_n(0, r)) \cdot G'(\theta, r) \qquad \text{H.1/1}$$

then it is found that (G'(θ, r)) for fixed range is given by (see graph (H.1)1):

$$G'(\theta, r) \doteq 1 \qquad \pm 8\ \%$$

when $0.5\,cm < r < 4\,cm$

and $\theta < 30^\circ$

and thus from H.1/1

$$G(\theta, E_n) \doteq G(0, E_n(0, r)) \ .$$

It is assumed that this starting and stopping tracks selection probability, and the geometrical part of the small angle tracks selection probability are, in fact, similar; then this latter probability may be assumed to be also approximately independent of angle and it may be written as $\underline{G}_g(r)$, in the ranges

$$0.5cm < r < 20\,cm \quad , \quad \theta < 30^\circ$$

Thus the total small angle tracks selection probability may be written

$$\underline{G}(\theta, E_n) = \underline{G}_a(\theta) \cdot G_g(r) \qquad \text{H.1/2}$$

in the above ranges.

Graph (H.1) 1. Term in starting and stopping track scan selection probability, $G(\theta, E_n(r))$ when $G(\theta, E_n(r)) = G(0, E_n(r)) \cdot G'(\theta, r)$

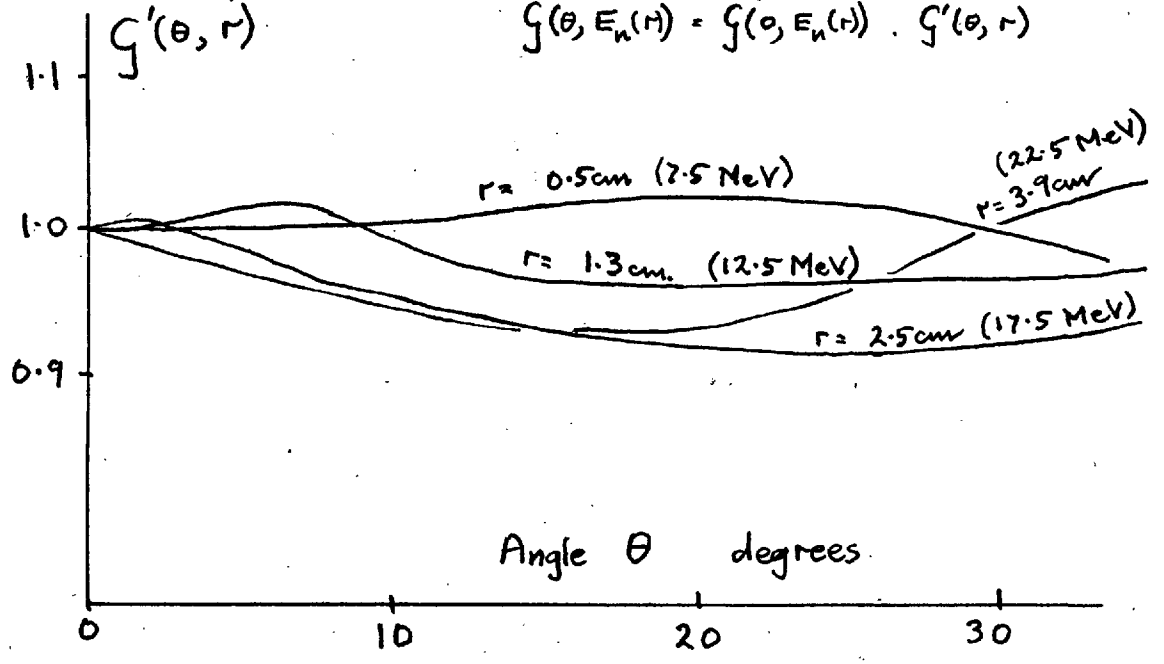

Graph (H.2) 1

Probability of track being selected by geometrical condition in 'small angle track scan.'

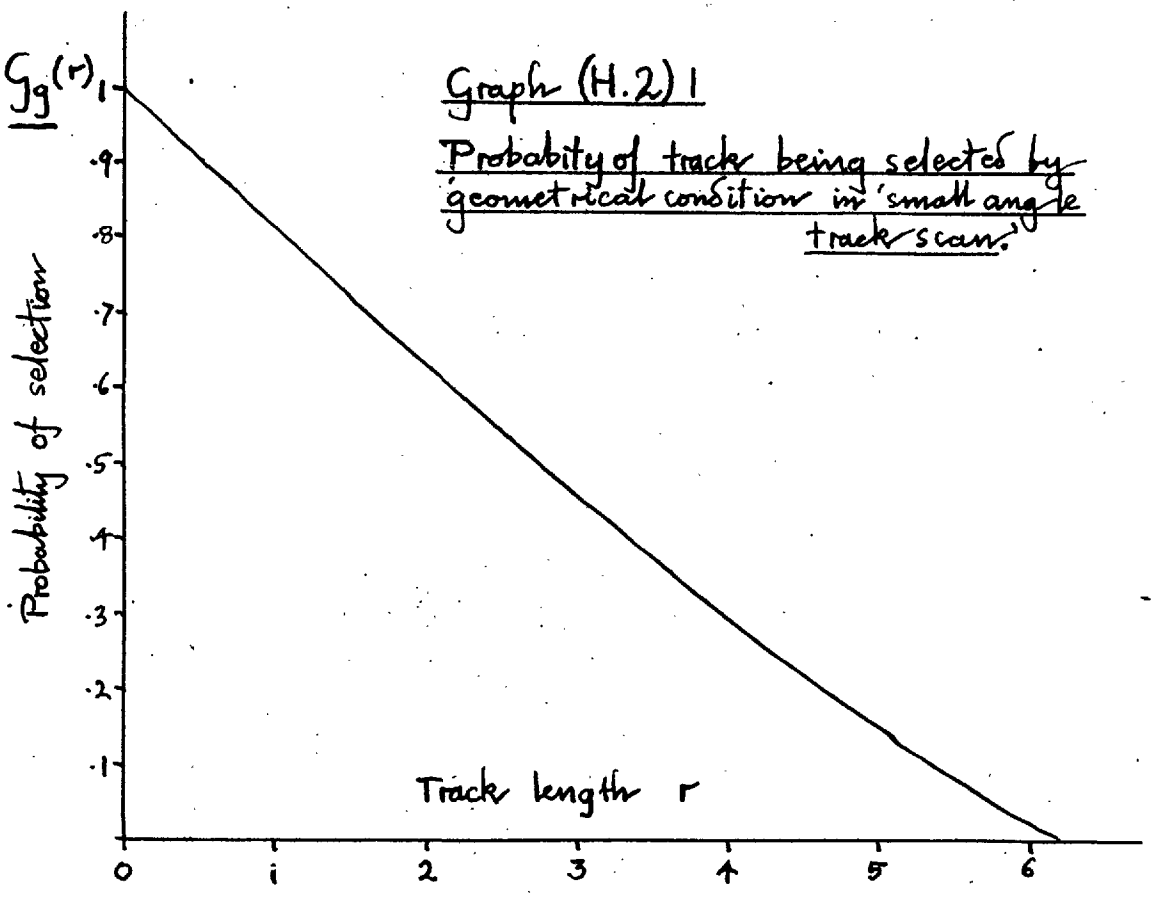

H.2 Geometrical factor.

$G_g(r)$ may be defined as the probability that a track with $\theta = 0$, and range r, that starts in the volume $\underline{V}'$, stops in the volume $\underline{V}$ (see section 4.4.2). Such are the volumes $\underline{V}$ and $\underline{V}'$ (see figure (4.4)1) that for a track with $\theta = 0$, the above condition requires that the track must both start and stop in the volume $\underline{V}'$. The form of $\underline{V}'$ is shown below

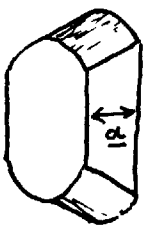

This form of $\underline{V}'$ may be closely approximated by a prism of height, a, and base equal to the mean cross section of the above truncated cone. The dimensions of this base are shown below.

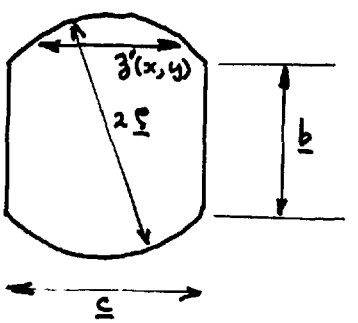

b = 4·13 cm

ρ = 3·72 cm

a = 3·6 cm

If z'(y, x) is the length inside $\underline{V}'$ in the z direction at y, x; then the probability of a track that starts in $\underline{V}'$ also stopping

in $\underline{V}$'is given by:

$$\underline{C_g}(r) = \frac{\iint_{V'} \left(1 - \frac{r}{z'(x,y)}\right) dx\, dy}{\int dx\, dy}$$

which, for the case of the prism, becomes:

$$\underline{C_g}(r) = \frac{\int \left(1 - \frac{r}{z'(y)}\right) z'(y)\, dy}{\int z'(y)\, dy} \qquad \text{H.2/1}$$

Defining $\underline{\rho}$ and $\underline{b}$ by the above figure, the integrations give, when

$$\eta = \frac{r}{2\underline{\rho}}\,, \quad \alpha = \sqrt{1-\eta^2}\,, \quad \zeta = \frac{\underline{b}}{2\underline{\rho}}\,, \quad \beta = \sqrt{1-\zeta^2}$$

$$\underline{C_g}(r) = \frac{2\underline{\rho}^2\left(-\cos^{-1}\alpha - \alpha\eta + \cos^{-1}\zeta - \zeta\beta + 2\zeta\eta\right) + \underline{b}\,\underline{c}\left(1 - \frac{r}{\underline{c}}\right)}{2\underline{\rho}^2(\cos^{-1}\zeta - \zeta\beta) + \underline{b}\underline{c}}$$

Calculated values of this function are given on graph (H.2)1

H.3 Angular selection probability $G_a(\theta)$.

$G_a(\theta)$ has been defined as the probability of a track with angle θ being selected by the 'small angle conditions',

$$\Phi_T < \varepsilon = 7.5^\circ$$
$$\Phi_B < \varepsilon = 7.5^\circ \qquad \text{H.3/1}$$

Consider the case of a track with angles χ and θ that cuts the z = 0 plane at the centre of the chamber (P_o).

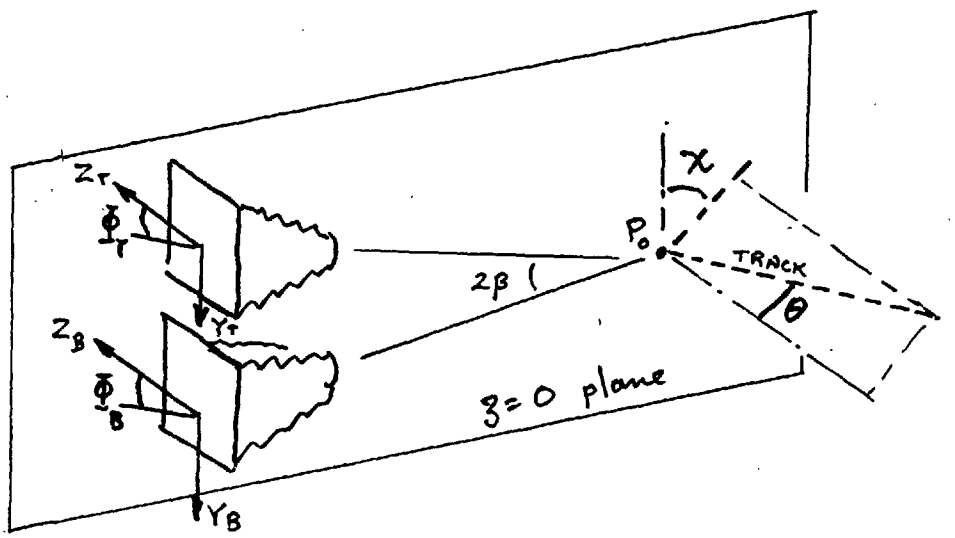

Defining β by the above figure, and letting

$$\chi' = \chi + \pi/2$$

then (see figure below)

$$\Phi_T = \tan^{-1}\left(\tan\theta \cdot \sin(\chi' - \beta)\right)$$
$$\Phi_B = \tan^{-1}\left(\tan\theta \cdot \sin(\chi' + \beta)\right) \qquad \text{H.3/2}$$

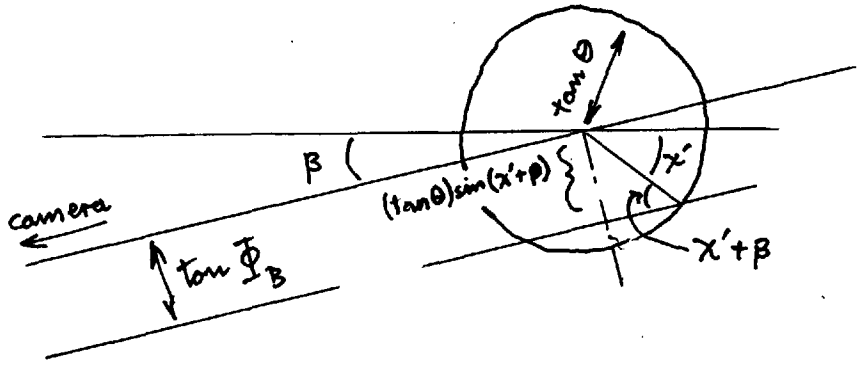

(The above figure, represents the projection of a track of unit length on the z = θ plane.) Thus the condition (H.3/1) requires:

$$\tan\varepsilon > \tan\theta \sin(\chi' - \beta)$$
$$\tan\varepsilon > \tan\theta \sin(\chi' + \beta)$$

Let $$\lambda = \sin^{-1}\frac{\tan\varepsilon}{\tan\theta}$$

then the condition requires

$$\lambda > |\chi' - \beta| \qquad \text{H.3/3}$$
$$\lambda > |\chi' + \beta|$$

The ranges of χ' for which these conditions are satisfied, χ'_i, are

a) if $\lambda < \beta$	$\Sigma\chi'_i = 0$	H.3/4
b) if $\beta < \lambda < \frac{\pi}{2} - \beta$	$\Sigma\chi'_i = 4(\lambda - \beta)$	
c) if $\frac{\pi}{2} - \beta < \lambda$, $\varepsilon < \theta$	$\Sigma\chi'_i = 4(2\lambda - \frac{\pi}{2})$	
d) if $\theta < \varepsilon$	$\Sigma\chi'_i = 2\pi$	

The probability of selecting a track with random χ that passes through P_o is given by:

$$\text{Probability}_o = \frac{\Sigma \chi'_i}{2\pi}$$

For fixed ε and θ, $\Sigma\chi'_i$ is only a function of β. Thus $\Sigma\chi'_i = f(\beta)$.

Consider tracks cutting the z = 0 plane at points (P') other than the centre of the chamber. The probability of selection of these tracks is approximately $f(\beta')$, where β' is the angle subtended by the camera lenses at P'. The mean value of the probability over all possible tracks in the chamber is approximately $f(\beta)$ where β is again the angle subtended by the cameras at the centre of the chamber. Therefore,

$$\underline{G_a}(\theta) = \frac{\Sigma \chi'_i}{2\pi} \qquad \text{H.3/5}$$

where χ'_i is taken from equations H.3/4.

In the present case:

$\beta = 9.2°$ = approx $\frac{1}{2}$ the stereo angle

$\varepsilon = 7.5°$

$\underline{G}_a(\theta)$ is plotted on graph (H.3)1.

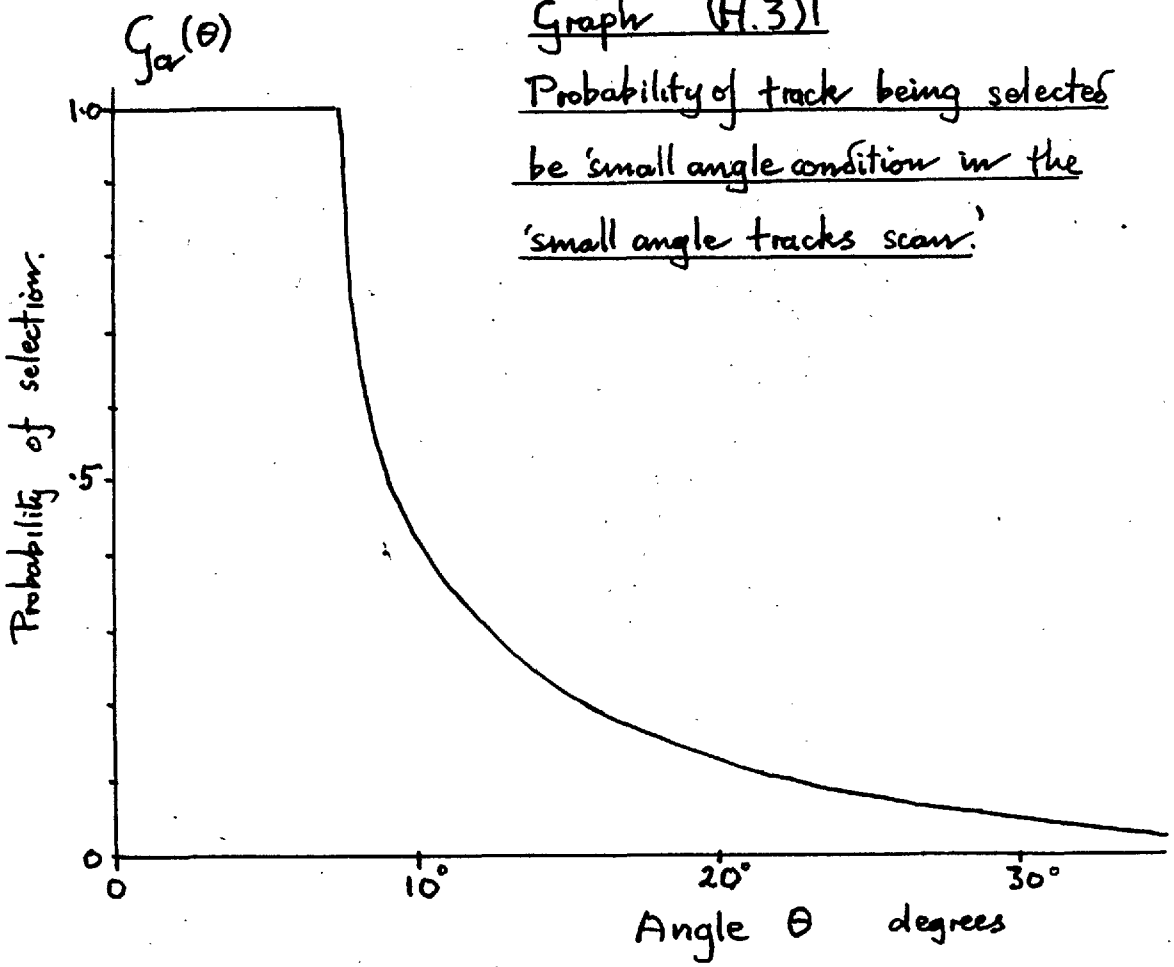

Graph (H.3)1

Probability of track being selected be 'small angle condition in the 'small angle tracks scan'.

APPENDIX I

NOTATION USED IN PART II CHAPTERS 3 and 4.

x, y, z	:	Coordinates in the chamber. See figure (3.1)1 page 171.
θ	=	angle of track with z axis
χ	=	angle of projection of track on z = 0 axis, with y axis.
r	=	length of track in the chamber.
θ'	=	see page 200
Y_T Z_T / Y_B Z_B	:	Coordinates on the projection table from top ($_T$), and bottom ($_B$) stereo-photographs. See figure (3.2)1 page 171.
Y'_T Z'_T / Y'_B Z'_B	:	As above but measured on the film.
Φ_T / Φ_B	:	Angle between projected track from top ($_T$) or bottom ($_B$) stereo-photograph with Z_T or Z_B axes.
R_T, R_B	:	length of projected track.
ℓ_o, b, m, f	:	optical constants, see page 172
ℓ'_o, f',	:	optical constants, see page 185.

K_{Σ} : The root mean square error in Σ .

K_{Ω} : The root mean square error in determining any angle in space.

K_{ℓ} : The root mean square error in determining the lateral position of a projected track.

λ : see page 199 .

ξ : see page 232 .

$_{n\text{-}p}\sigma(\Theta, E_n)$: n-p scattering differential cross-section.

$_{n\text{-}p}\sigma_T(E_n)$: n-p scattering total cross-section .

$h(E_n)$: hardening factor, see page 151.

$E_p = E_p(r)$: energy of a track assuming it to be a proton, calculated from its range.

$E_d = E_d(r)$: as above assuming it to be a deuteron

$E_n = E_n(\Theta, r)$: Initial neutron energy, calculated from the range and angle of a track, assuming the track to represent a proton scattered by a neutron in the beam.

$E_i = E_i(\Theta, r)$: Initial neutron energy, calculated from the range and angle of a track, assuming the track to represent a neutron-capture deuteron from a beam neutron.

All the following terms apply to the 'small angle tracks scan' if underlined, and to the 'starting and stopping tracks scan' if not underlined.

$G(\theta, E_n)$: Probability of selection of tracks.

$P(E_n)$: Probability of selection of tracks of all angles.

V' : Selection volume in which tracks must start.

V : Selection volume in which tracks must stop.

In the following terms, the subscript

$(_p)$ implies numbers of protons,

$(_d)$ implies numbers of deuterons,

Neither subscript implies total numbers. The subscript $(_{DL})$ implies numbers of tracks within the deuteron limits of range and angle. See page 123.

The following definitions are of numbers of events of some kind in the intervals given, (e.g. $p(E_n)\,\delta E_n$ is the number of tracks in an interval of E_n, namely δE_n.)

$p(\theta, E_n)\,\delta\theta\,\delta E_n$ = Number of selected tracks.

$p(E_n)\,\delta E_n$ = Number of selected tracks of any angle θ.

$q(\theta, E_n)\,\delta\theta\,\delta E_n$ = Total number of tracks, selected or not, that start in the volume V'.

$n(E_n)\,\delta E_n$ = Number of neutrons per burst, per cm^2 in hardened neutron beam.

$n'(E_n)\ \delta E_n$:
$n''(E_n)\ \delta E_n$: corrected approximations to $n(E_n)\ \delta E_n$.

$m(E_n)\ \delta E_n$: number of neutrons per burst, per sterad, before hardening.

ACKNOWLEDGEMENTS.

The author wishes to thank Mr. N.C. Barford for initiating the development of the hydrogen bubble chamber described, and for his helpful advice and direction concerning the work done under his supervision. Thanks are also due to Mr. B. Rose who suggested the neutron-capture experiment and to Dr. R.J.N. Phillips for his discussion of the experiment. The author's thanks are due to Mr. D. Reed who worked with the author on the development of the chamber, and to Dr. B. Tallini who worked on both the chamber and on the scanning of the film. The author is indebted to Dr. A. Curzon for his help in the preparation of this thesis, and to the Department of Scientific and Industrial Research for a maintenance grant.